NUMERICAL MODELING OF LARGE DEFORMATION BEHAVIOUR OF OFFSHORE PIPELINES AND RISERS IN SOFT CLAY SEABEDS

by

© Sujan Dutta

A Thesis submitted to the

School of Graduate Studies

in partial fulfillment of the requirements for the degree of

Doctor of Philosophy

Faculty of Engineering and Applied Science

Memorial University of Newfoundland

October, 2017

St. John's Newfoundland Canada

ABSTRACT

Deepwater oil and gas development activities have increased significantly in the last few decades to meet the global demand for energy. One of the key components of these developments is the oil and gas transportation pipeline. Deepwater pipelines are often laid on the seabed and may vertically penetrate into the seabed sediment (primarily clay) or remain suspended in the case of uneven seabed profiles. Partially embedded pipelines might displace laterally during operation due to changes in internal pressure and temperature. The displacement of the pipeline depends on soil resistance, which is also related to the initial embedment. The suspended pipelines might also be impacted by soil blocks moving out from submarine landslides. Moreover, in deepwater, steel catenary risers (SCR)—a long pipe of 150–600 mm typical diameter—are often used to transport hydrocarbon from the seabed production system to floating production facilities. The interaction between soil, water and pipes (partially embedded, suspended or SCR) involves significant large deformations, which cannot be modeled properly using traditional Lagrangian-based finite element (FE) techniques and therefore improved numerical modeling is required for safe and economic design.

In the present study, simulations of the large deformation behaviour of deepwater pipelines and SCRs are performed using two numerical approaches. First, simulation is performed using the Coupled Eulerian-Lagrangian (CEL) approach available in the Abaqus FE software. In CEL, the soil is modeled as an Eulerian material that flows through the fixed mesh and therefore numerical issues related to mesh distortion at large displacements are avoided. Simulations are performed for undrained loading conditions implementing a strain-rate and strain-softening dependent undrained shear strength model for clay in Abaqus CEL through user subroutines. For partially embedded pipelines, numerical simulations are performed for vertical penetration and

subsequent lateral displacements. In addition, dynamic penetration of the pipeline into a deepwater soft clay seabed is simulated. The penetration and lateral resistances are compared with the results of previous physical model tests, and numerical and analytical solutions.

Recognizing the limitations of Abaqus CEL and other FE modeling techniques to simulate the role of water, ANSYS CFX—a finite volume software—is used in the second approach for numerical modeling. A technique is developed to implement strain-rate and strain-softening dependent undrained shear strength of clay in ANSYS CFX. The comparison between penetration resistances obtained from CEL and CFX shows that the latter approach can simulate the effect of water in the cavity formed behind the pipe when it penetrates to a sufficiently large depth into the clay seabed, with a transition between shallow and deep failure mechanisms.

In the SCR–seabed–water interaction modeling, in addition to undrained remoulding, the reduction of undrained shear strength due to other factors such as water entrainment is considered using "shear wetting". Cyclic degradation of penetration and uplift resistance, development of suction under the riser during uplift, and the formation of a trench are successfully simulated for a large number of cyclic motions near the seabed, where a significant shear strength reduction occurs, as reported from physical model tests.

The impact force on suspended offshore pipelines by submarine landsides is also simulated using both Abaqus CEL and ANSYS CFX. The development of forces on the pipe with its penetration into the soil block shows that the trapped water behind the pipe influences the failure mechanisms and magnitude of force. The suction in the trapped water and flow of free water through the channel formed behind the pipe is simulated using ANSYS CFX. Based on a comprehensive parametric study with calibration against a series of centrifuge test results, a set of empirical equations are proposed to calculate the impact force on suspended pipelines.

ACKNOWLEDGMENTS

First, I want to praise and express my sincerest thanks to the Almighty for giving me an opportunity to conduct the research presented in this thesis, which has been carried out under the supervision of Dr. Bipul Hawlader, Professor and Research Chair in Seafloor Mechanics, Memorial University of Newfoundland, Canada. I would like to thank Dr. Hawlader for his keen supervision, invaluable suggestions and encouragements throughout the PhD program. I would also like to thank my co-supervisor and supervisory committee member, Dr. Ryan Phillips at C-CORE and Dr. Michael Paulin at INTECSEA for their invaluable suggestions and comments.

I would like to thank C-CORE for providing an office space and what I believe is an excellent environment for doing research. The financial support of this research has been provided by NSERC, MITACS, C-CORE and the School of Graduate Studies of Memorial University of Newfoundland.

My sincere thanks go to Mr. John Barrett at C-CORE for his help during the initial stage of finite element model development. I would also like to thank Mr. Anup Fouzder for helping finite volume model development. Thanks to all my friends in St. John's that made my PhD life enjoyable.

Finally, I would like to thank my parents, daughter and sisters for their love and encouragements. I would not have been able to finish this research without the enduring love and support from my wife Mishu.

Table of Contents

ABSTRACT……...……. ii

ACKNOWLEDGMENTS……... iv

List of Figures……. xii

List of Tables…….. xviii

List of Symbols……... xix

CHAPTER ……..…..…... 1-1

Introduction…… 1-1

1.1 General……..... 1-1

1.2 Objectives…… 1-5

1.3 Outline of Thesis……. 1-6

1.4 Significant Contributions…… 1-7

CHAPTER 2……..……. 2-1

Literature Review…….. 2-1

2.1 Introduction……. 2-1

2.2 Surface Laid Pipeline: An Overview…….. 2-2

2.2.1 Partially Embedded Pipeline……... 2-2

2.2.1.1 Vertical Penetration……. 2-2

2.2.1.2 Pipe Lateral Resistance…… 2-4

2.2.2 Submarine Landslides Impact on Suspended Pipelines ……...…….. 2-6

2.3 Steel Catenary Riser: An Overview…… 2-9

2.3.1 Riser Vertical Penetration……... 2-9

2.3.2 Riser Cyclic Motion…… 2-16

2.4 Conclusion…….. 2-22

CHAPTER 3…..……. 3-1

Finite Element Modeling of Partially Embedded Pipelines in Clay Seabed Using Coupled Eulerian−Lagrangian Method……. 3-1

3.1 Abstract……... 3-1

3.2 Introduction……. 3-2

3.3 Previous FE Modeling……..... 3-4

3.4 Problem Statement……..... 3-5

3.5 Strain Rate and Softening Effects……... 3-6

3.6 Finite Element Model Development……..…… 3-7

3.7 FE Results: Vertical Penetration……. 3-10

3.7.1 Mesh Sensitivity and Softening and Rate Effects……... 3-10

3.7.2 Comparison with Previous Models……..... 3-13

3.7.3 Comparison with Centrifuge Test Results……... 3-13

3.7.4 Contact Width…….. 3-14

3.7.5 Strain Rate and Strain Softening……. 3-15

3.8 FE Results: Lateral Displacement……..…. 3-15

3.8.1 Comparison with Centrifuge Tests…….. 3-15

3.8.2 Pipe Invert Trajectories……... 3-17

3.8.3 Soil Velocity Field Around the Pipeline……. 3-17

3.8.4 Effects of Applied Vertical Load (P)…….. 3-18

3.8.5 Yield Envelope…… 3-19

3.8.6 Breakout and Residual Resistance…….. 3-20

3.9 Conclusions……. 3-22

CHAPTER 4……..……. 4-1

Penetration of Steel Catenary Riser in Soft Clay Seabed: Finite-Element and Finite-Volume Methods…… 4-1

4.1 Abstract……... 4-1

4.2 Introduction……. 4-2

4.3 Previous Studies…….. 4-4

4.4 Problem Definition……. 4-6

4.5 CFD Simulation…….. 4-6

4.5.1 CFD Model Setup…… 4-7

4.5.2 Modeling of Undrained Shear Strength in CFX……. 4-10

4.5.3 Penetration Resistance……. 4-11

4.6 Large Deformation FE Modeling……... 4-13

4.7 Comparison of CFX and CEL Results…… 4-14

4.8 Parametric Study……. 4-17

4.8.1 Uniform Strength, s_{u0}…….…. 4-17

4.8.2 Linearly Increasing Strength, s_{u0}……..…….. 4-19

4.9 Conclusions……. 4-21

CHAPTER 5……..……. 5-1

Numerical Modeling of a Steel Catenary Riser Section in the Touchdown Zone Under Cyclic Loading……. 5-1

5.1 Abstract……... 5-1

5.2 Introduction……. 5-2

5.3 Problem Statement…….. 5-6

5.4 CFD Model Development……...… 5-6

5.5 Shear Strength of Seabed Sediment…… 5-8

5.6 Numerical Implementation…….. 5-11

5.7 Results of Base Case Analysis…… 5-12

5.7.1 Penetration and Uplift Resistance…….. 5-12

5.7.2 Plastic Shear Strain…….. 5-14

5.7.3 Suction Under Riser during Uplift…….. 5-16

5.8 Parametric Study……. 5-17

5.8.1 Effects of Strain Rate Parameter, μ……..... 5-17

5.8.2 Effects of Soil Sensitivity, S_t……..……. 5-17

5.8.3 Effects of Accumulated Absolute Plastic Shear Strain for 95% of Undrained Shear Strength Degradation, ξ_{95}…….…….. 5-18

5.8.4 Effects of Accumulated Absolute Plastic Shear Strain during Shear Wetting, ξ_{ld}……...……... 5-18

5.8.5 Effects of Initial Embedment (w_{in})…….. 5-18

5.8.6 Effects of Amplitude (a)…….. 5-19

5.9 Conclusions……. 5-20

CHAPTER 6……...…… 6-1

Pipeline–Soil–Water Interaction Modeling for Submarine Landslide Impact on Suspended Offshore Pipelines……... 6-1

6.1 Abstract……... 6-1

6.2 Introduction……. 6-2

6.3 Previous Studies…….. 6-4

6.4 Problem Definition and Numerical Model formulation…….. 6-6

6.4.1 CFD Model Development……... 6-7

6.4.2 Shear Strength of Seabed Sediment ……... 6-8

6.4.3 Numerical Implementation……. 6-9

6.5 Results of Base Case Analysis……. 6-9

6.5.1 Force-Displacement Behaviour…….. 6-9

6.5.2 Comparison with FE Results…….. 6-11

6.6 Parametric Study……. 6-14

6.6.1 Depth of Pipe……..… 6-15

6.6.2 Attack Angle……. 6-15

6.6.3 Velocity of Clay Block……. 6-16

6.6.4 Undrained Shear Strength……... 6-16

6.6.5 Soil Failure Mechanisms……. 6-17

6.6.6 Proposed Simplified Equation……. 6-18

6.6.7 Comparison with Physical Model Tests…….. 6-21

6.7 Conclusions…… 6-21

CHAPTER 7…… 7-1

Conclusions and Recommendations for Future Research……..... 7-1

7.1 Conclusions……. 7-1

7.2 Recommendations for Future Research…….. 7-3

REFERENCES……... R-1

APPENDIX A……. A-1

Numerical Investigation of Dynamic Embedment of Offshore Pipelines…..... A-2

APPENDIX B……. B-1

A Comparative Study of Advanced Numerical Methods for Large Deformation Problems using Cylindrical Object Penetration into Seabed……..... B-2

APPENDIX C……. C-1

Vertical Penetration of Offshore Pipelines: A Comparative Study between Finite Element and Finite Volume Methods…….. C-2

APPENDIX D……... D-1

Numerical Investigation of Vertical Penetration of Steel Catenary Riser Near the Touch Down Zone……. D-2

APPENDIX E……. E-1

Numerical Modeling of Drag Force on Submarine Suspended Pipelines Using Finite Element and Finite Volume Methods…… E-2

List of Figures

Fig. 1.1. Applications of pipelines in deep water (Lee, 2007)……..…..… 1-2

Fig. 1.2. Mechanisms of pipe−soil interaction (Hill et al., 2012)…….…. 1-3

Fig. 1.3. Side-scan sonar image of pipe lateral displacement (Bruton et al., 2008)……... 1-4

Fig. 1.4 Schematic diagram and characteristics of submarine landslide (Boukpeti et al., 2012)……... 1-4

Fig. 1.5 Schematic diagram of Steel Catenary Riser (Bridge, 2005)……...…….. 1-5

Fig. 2.1. Proposed soil flow mechanisms around a pile (Vivatrat and Chen, 1985)……..... 2-7

Fig. 2.2. Extension of Randolph-Houlsby solution (Aubeny et al. 2005)…….…. 2-10

Fig. 2.3. Failure mechanism for riser vertical penetration (a) $0 < w \leq D$ (b) $w > D$ (Hu, 2010)……...……... 2-11

Fig. 2.4. Typical *P–y* curve (Aubeny and Biscontin, 2009) …….. 2-17

Fig. 2.5. Riser–seabed interaction model (Randolph and Quiggin, 2009) …… 2-17

Fig. 2.6. Variation of uplift resistance with number of cycles (Bridge, 2005)…….. 2-20

Fig. 2.7. Pipe−soil interaction during riser cyclic motion (Aubeny et al., 2008)…….. 2-20

Fig. 3.1. (a) Vertical penetration (b) Lateral displacement followed by vertical penetration 3-32

Fig. 3.2. Finite element model…… 3-33

Fig. 3.3. Penetration resistance in uniform soil for smooth pipe…….. 3-34

Fig. 3.4. Shear band formation mechanism…… 3-35

Fig. 3.5. Penetration resistance in non-uniform soil for smooth pipe……..….. 3-36

Fig. 3.6. Undrained shear strength s_u: (a) initial (left); (b) mobilized at w=0.45D (right)…. 3-37

Fig. 3.7. (a) Penetration resistance of smooth pipe in ideal soil (no softening or rate

effect)……... 3-38

Fig. 3.7. (b) Penetration resistance of rough pipe in ideal soil (no softening or rate effect)... 3-39

Fig. 3.8. Comparison of penetration resistance from FE analysis and centrifuge test……..... 3-40

Fig. 3.9. Comparison of pipe contact width……..... 3-41

Fig. 3.10. (a) Strain rate effects (b) Strain softening effects (Case-L1, smooth pipe)…… 3-42

Fig. 3.11. (a) Comparison of lateral resistance (case-D1)…….. 3-43

Fig. 3.11. (b) Comparison of lateral resistance (case-L2)……...…. 3-44

Fig. 3.11. (c) Comparison of lateral resistance (case-L4)…….…...…. 3-45

Fig. 3.12.Variation of pipe rear end surface area with travel direction at breakout event…. 3-46

Fig. 3.13. (a) Pipe trajectory during lateral displacement (case- D1)……. 3-47

Fig. 3.13. (b) Pipe trajectory during lateral displacement (case- L2)…….. 3-48

Fig. 3.13. (c) Pipe trajectory during lateral displacement (case- L4)…….…. 3-49

Fig. 3.14. (a) Predicted and observed velocity vectors at pipe lateral displacement of 0.04*D* (location A) and 0.1*D* (location B)……...…….…… 3-50

Fig. 3.14. (b) Predicted and observed velocity vectors at pipe lateral displacement of 0.15*D* (location C) and 0.53*D* (location D)…….....……..... 3-51

Fig. 3.15. (a) Lateral resistance for different applied load on pipe (smooth pipe/soil interface)……...……. 3-52

Fig. 3.15. (b) Pipe invert trajectory during lateral movement (smooth pipe/soil interface)… 3-53

Fig. 3.16. Soil velocity field around heavy pipes during lateral movement (*R*= 1.25)……... 3-54

Fig. 3.17. (a) Yield envelopes for w_{int}= 0.45*D*……..…. 3-55

Fig. 3.17. (b) Yield envelopes normalized by$V_{\max}$ for w_{int}= 0.45*D*…….…… 3-56

Fig. 3.18. Comparison of breakout resistance with pipe initial embedment…….. 3-57

Fig. 3.19.Comparison of residual resistance with pipe initial embedment……. 3-58

Fig. 3.20. Comparison of normalized lateral residual resistance…… 3-59

Fig. 4.1. Problem definition……..... 4-30

Fig. 4.2. CFX models …… 4-31

Fig. 4.3. Penetration resistance for three models (f_2 =1.0; s_{u0} = 3.7 kPa)…….. 4-32

Fig. 4.4. Finite element model using Abaqus CEL…… 4-33

Fig. 4.5. Comparison between Abaqus CEL and ANSYS CFX (f_2 =0.01; s_u= 3.7)…….. 4-34

Fig. 4.6. Suction at different pipe penetration depth (a) 2*D* (b) 3*D* (c) 4*D* (d)5*D*…….. 4-35

Fig. 4.7. Velocity vectors and trench formation at 2*D* and 3*D* pipe penetration depth……. 4-36

Fig.4.7. Velocity vectors and trench formation at 4*D* and 5*D* pipe penetration depth…….. 4-37

Fig. 4.8. Effects of f_2 on pipe penetration resistance for s_{u0}=3.7 kPa…… 4-38

Fig. 4.9. Effects of soil undrained hear strength on pipe penetration resistance for f_2 = 0.5. 4-39

Fig. 4.10. Contour of initial shear strength s_{u0}: (a) before penetration (b) at w= 5*D*in ANSYS CFX (c) At w=5*D* in Abaqus CEL……...…….. 4-40

Fig. 4.11. Comparison between CEL and CFX results for base case linearly increasing shear strength profile (s_{u0}= 2.3 + 2.0y' kPa with f_2 = 0.01)……..... 4-41

Fig. 4.12. Effects of $f_2$on penetration resistance for linearly increasing shear strength profile……. 4-42

Fig. 4.13. Effects of mudline shear strength on pipe penetration resistance (f_2 = 0.5; k = 2 kPa)…… 4-43

.

Fig. 4.14. Effects of shear strength gradient on penetration resistance (f_2 = 0.5; s_{um}= 2.3 kPa)…….. 4-44

Fig. 5.1. Problem statement ……... 5-31

Fig. 5.2. Finite volume model..…….. 5-32

Fig. 5.3. Shear strength degradation model…… 5-33

Fig. 5.4(a). Penetration and uplift resistance for shear wetting case ……. 5-34

Fig. 5.4(b). Penetration and uplift resistance for no shear wetting case……. 5-35

Fig. 5.5. Comparison normalized resistance with and without shear wetting. 5-36

Fig. 5.6. Degradation resistance with number of cycles……. 5-37

Fig. 5.7. Plastic shear strain and instantaneous velocity vectors: Left column without shear wetting (a) 5th cycle, (b) 10th cycle, (c) 15th cycle, (d) 20th cycle; Right column, with shear wetting (e) 5th cycle, (f) 10th cycle, (g) 15th cycle, (h) 20th cycle…….. 5-38

Fig. 5.7. Plastic shear strain and instantaneous velocity vectors during penetration: Left column without shear wetting (a) 5th cycle, (b) 10th cycle, (c) 15th cycle, (d) 20th cycle; Right column, with shear wetting (e) 5th cycle, (f) 10th cycle, (g) 15th cycle, (h) 20th cycle…….. 5-39

Fig. 5.8. Mobilization suction and instantaneous velocity vectors during uplift: Left column without shear wetting (a) 5th cycle, (b) 10th cycle, (c) 15th cycle, (d) 20th cycle; Right column, with shear wetting (e) 5th cycle, (f) 10th cycle, (g) 15th cycle, (h) 20th cycle…….. 5-40

Fig. 5.8. Mobilization suction and instantaneous velocity vectors during uplift: Left

column without shear wetting (a) 5th cycle, (b) 10th cycle, (c) 15th cycle, (d) 20th cycle; Right column, with shear wetting (e) 5th cycle, (f) 10th cycle, (g) 15th cycle, (h) 20th cycle……..... 5-41

Fig. 5.9. Effect of strain rate parameter μ on normalized resistance ratio R_n……. 5-42

Fig. 5.10. Effects of soil sensitivity on normalized resistance ratio R_n…….. 5-43

Fig. 5.11. Effects of strain softening parameter ξ_{95} on normalized resistance ratio R_n…….... 5-44

Fig. 5.12. Effects of strain softening parameter ξ_{ld} on normalized resistance ratio R_n…….... 5-45

Fig. 5.13. Effects initial embedment on normalized resistance ratio R_n……. 5-46

Fig. 5.14. Effects of cyclic amplitude on normalized resistance ratio R_n…… 5-47

Fig. 6.1. Model development for the base case……..... 6-30

Fig. 6.2. Normalized horizontal resistance with normalized displacement…… 6-31

Fig. 6.3. Normalized shear strain rate and suction around the pipe for $\widehat{w} = 3$ with lateral penetration: (a) 3*D* (b) 6*D* (c) 9*D* and (d) 15*D*……. 6-32

Fig. 6.4. Effect of depth of pipe on *N*……..... 6-33

Fig. 6.5. Normalized shear strain rate for $\widehat{w} = 1$ with lateral penetration: (a) 3*D* (b) 6*D* (c) 9*D* and (d) 15*D*. ……... 6-34

Fig. 6.6. Effect of attack angle……..... 6-35

Fig. 6.7. Effect of clay block velocity…… 6-36

Fig. 6.8(a). Effect of undrained shear strength on *N* for $\widehat{w}$ =1–3…… 6-37

Fig. 6.8(b). Effects of undrained shear strength on *N* for $\widehat{w}$ = 3–6…… 6-38

Fig. 6.9. Variation of soil failure mechanisms with depth of pipe……. 6-39

Fig. 6.10(a). Performance of combined approach for estimating N_m using empirical

equations ……..…… 6-40

Fig. 6.10(b). Performance of geotechnical approach for estimating N_m using empirical equations…… 6-41

.

List of Tables

Table 2.1. Summary of previous studies on pipeline/riser−seabed interactions……. 2-12

Table 3.1. Development of numerical modeling techniques…….. 3-60

Table 3.2. Geometry and soil properties used in finite element analysis…… 3-61

Table 3.3. FE simulation for mesh sensitivity, and softening and rate parameters effects….. 3-62

Table 3.4. Centrifuge test conditions (White and Dingle, 2011; Dingle et al., 2008)……. 3-63

Table 4.1. Geometry and parameters used in CFX analyses……... 4-45

Table 5.1. Geometry and model parameters for soil and water used in base case analysis… 5-48

Table 6.1. Parameters used in CFX modeling for base case…….. 6-42

Table 6.2. Maximum force N_m for varying pipe depths and soil properties ……. 6-43

List of Symbols

As the thesis is written in manuscript format, the symbols used in this study are listed at the end of each chapter (Chapters 3–6).

CHAPTER 1

Introduction

1.1 General

Safe and economic transportation of hydrocarbons are main concerns in offshore oil and gas development. While this is already challenging in shallow water, deepwater developments pose additional challenges as the seabed conditions and loading on offshore structures are different, and in many cases are not well-understood. Pipelines are often used to transport hydrocarbons (Fig. 1.1). In deepwater (water depth greater than 1000 m) (Randolph et al. 2011), pipelines are usually laid on the seabed (i.e. surface laid) where the sediments are mainly clay. Due to the installation process and weight of the pipeline and its contents, the surface laid pipeline might penetrate into the seabed a fraction of its diameter (D)—typically less than 1D. This type of pipeline is commonly known as a "partially embedded pipeline." Some sections of surface laid pipelines might be suspended when they pass through an uneven seabed, which is termed as a "suspended pipeline." In addition to surface laid pipelines, steel catenary risers (SCRs) are often used in deepwater to transport hydrocarbons from the seabed wellhead production systems to floating platforms. The design of these pipelines and risers is significantly influenced by soil–structure interaction under various loading conditions expected in deepwater offshore environments. The flow of water through the channel/trench that forms behind the pipe also plays a significant role in many cases.

During operation under high pressure and temperature, significant lateral displacement might occur in partially embedded pipelines to release the axial compressive force (Bruton et al.

2006). Field observations show that the lateral displacement could be 6–10 pipe diameters depending upon initial embedment and seabed conditions (Bruton et al., 2006) (Fig. 1.2). The lateral displacement could cause failure of the pipeline due to uncontrolled lateral buckling (Bruton et al., 2008). Snake-lay, vertical upset using sleepers and local weight reduction using buoyancy coating are the common industry practices to avoid lateral bucking related failure (Bruton et al. 2007). Therefore, for pipeline design where lateral buckling may be a concern, initial vertical penetration and lateral resistance need to be estimated properly. Note that the lateral displacement is influenced by axial movement of the pipe. Theoretical frameworks have been proposed on axial pipe–soil interaction that depend on a number of factors such as drainage of excess pore water pressure, pipe–soil interface behaviour, and strain rate and strain softening dependent soil shear strength (White et al., 2012; Hill et al., 2012; Randolph et al., 2012). However, axial behaviour is not examined in the present study.

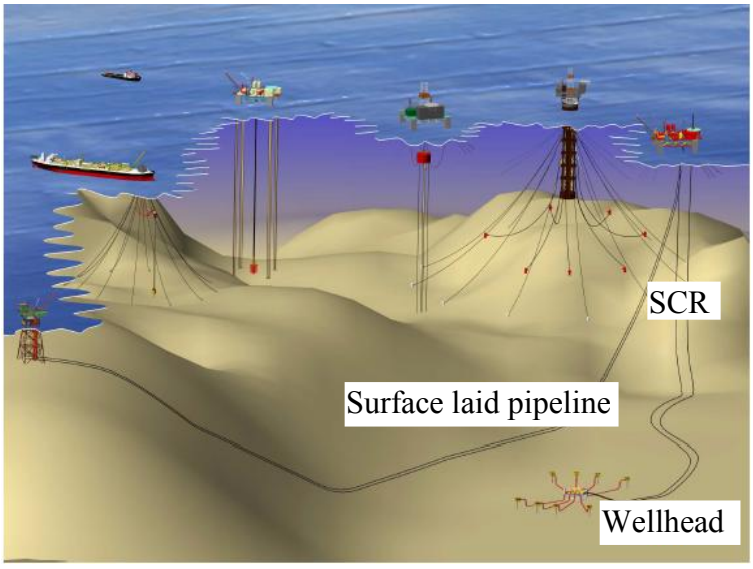

Fig. **1.1.** Applications of pipelines in deepwater (Lee, 2007)

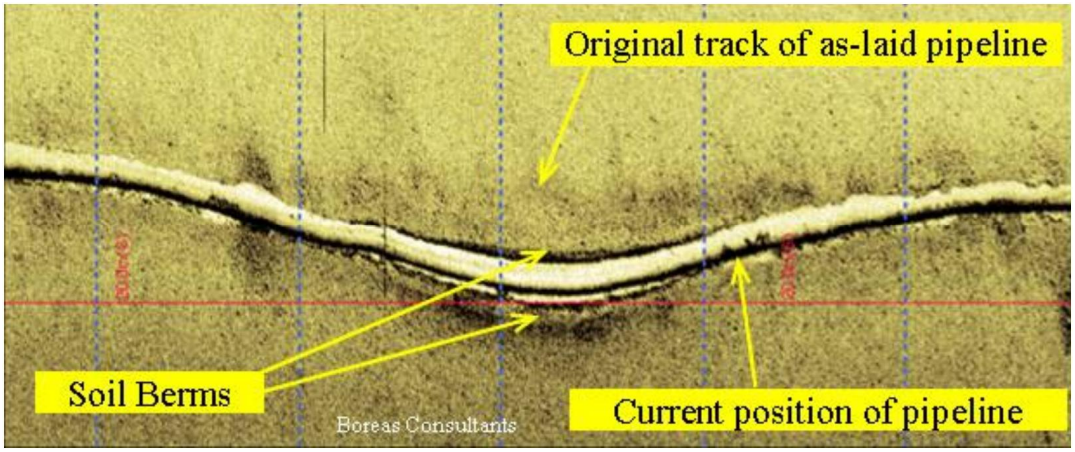

Fig. **1**.**2.** Side-scan sonar image of pipe lateral displacement (Bruton et al., 2008)

Small to large-scale landslides may occur in offshore environments. The failure could be triggered by earthquake, deposition, reduction of shear strength (e.g. gas hydrate dissociation) or human activities. The resulting soil blocks might travel hundreds of kilometers downslope on mildly sloped seabed (typically <10º, Hadj-Hamou and Kavazanjian, 1985). The velocity of the soil block increases with travel distance as shown in Fig. 1.3. At the same time, the strength of the soil reduces due to remoulding (Fig. 1.3). Depending upon the location of the suspended pipelines, an offshore pipeline might be impacted by the materials from submarine landslides in the form of a glide block, out-runner block or debris (definitions of these terms are provided in Chapter 2), at a speed of as high as 70 km/h (De Blasio et al., 2004) and having a wide range of variation in width (0.5–50 km, (Thomas, 2004)). Therefore, potential drag force due to submarine landslide impact is one of the key considerations in deepwater offshore pipeline design.

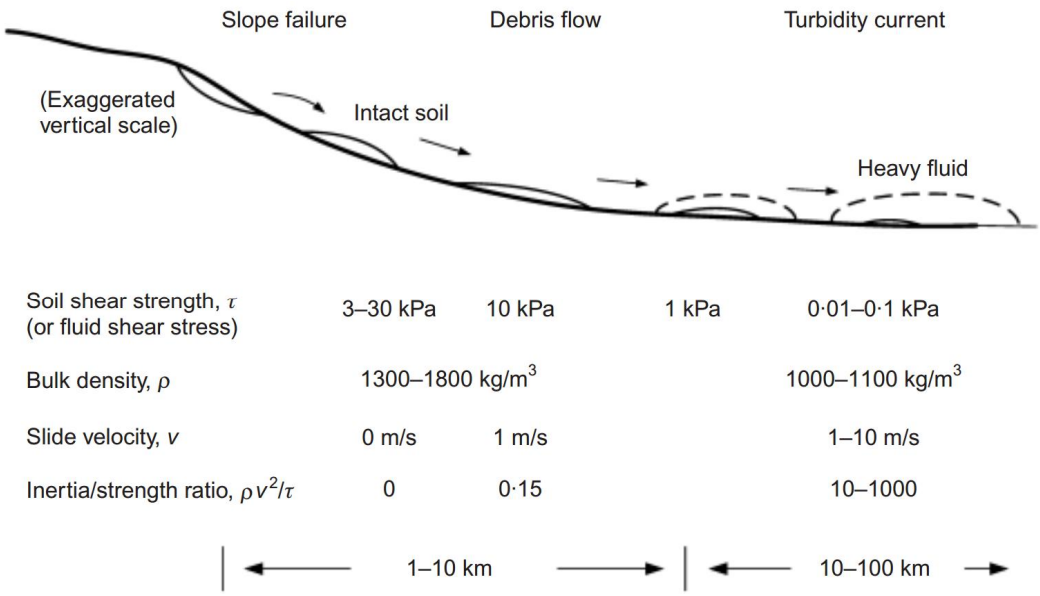

Fig. **1**.**3** Schematic diagram and characteristics of submarine landslides (Boukpeti et al., 2012)

The third type of pipe used for hydrocarbon transportation considered in this study is the steel catenary riser (SCR). In deepwater, SCRs might penetrate several pipe diameters into the seabed in the touchdown zone (Fig. 1.4). Environmental loading (e.g. wave and current) causes cyclic motion not only in the catenary part but also in the touchdown zone where riser movement causes significant displacement and remoulding of surrounding soil and water. Field observation shows that a trench forms in the touchdown zone around the riser due to cyclic loading, which is influenced by remoulding of seabed sediments and its erosion (Bridge, 2005; Clukey, et al., 2008). The fatigue response of the riser at this critical region depends on riser–seabed–water interaction. Note that, because of uncertainties, a factor of safety as high as 10 is generally adopted for riser fatigue life calculations (DNV, 2010). The vertical penetration and uplift resistance during cyclic motion of the riser needs to be estimated properly for safe and economic design. In the current design practice, the seabed is modeled either as a rigid surface or flexible

surface with lateral and axial friction coefficients (Hu, 2010). More complex seabed modeling includes a set of springs connected to the riser where the load−displacement behaviour of the spring is defined using empirical equations, proposed from the trend of two-dimensional experimental results (e.g. Hodder, 2009). It has been also recognized from model tests and numerical investigations that the load−displacement response under cyclic loading, especially near the seabed, is complex and therefore needs to be studied further (Clukey, et al., 2008; Hodder et al. 2008).

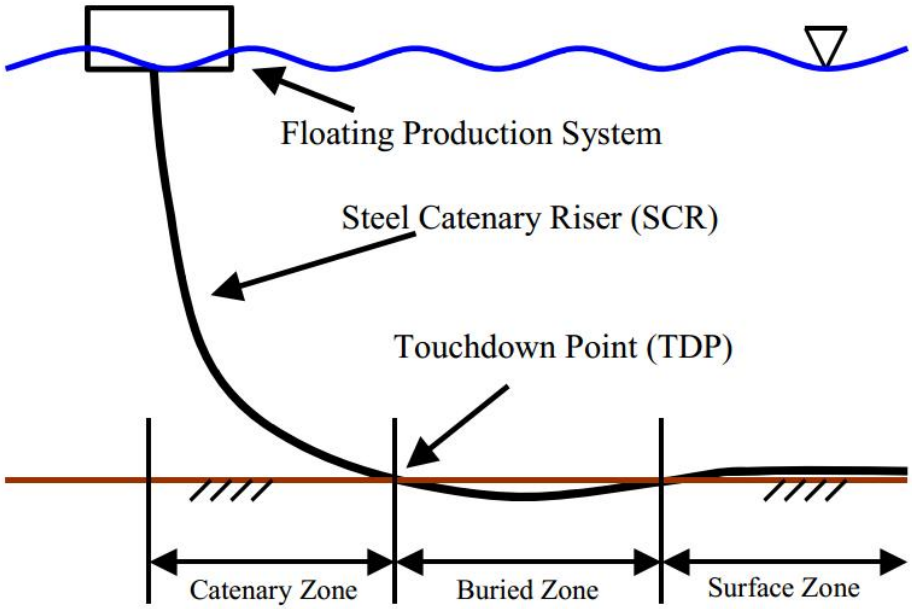

Fig. **1**.**4** Schematic diagram of Steel Catenary Riser (Bridge, 2005)

1.2 Objectives

In the design of surface laid pipelines and SCRs in deepwater, the response of a pipe section due to vertical penetration/extraction and lateral displacement under monotonic and cyclic loading needs to be properly understood. These problems involve significantly large

deformation of the pipe and surrounding soil. The strength degradation due to remoulding, shear wetting, shearing rate effects and formation of berms and trenches further complicated the problem. Finally, the effects of water in the trench might change the behaviour of soil and resistance to the pipe.

Traditional numerical modeling techniques (e.g. Lagrangian-based finite element (FE) modeling) cannot simulate this complex process properly. As the seabed sediment is very soft, these problems could be analyzed in a geotechnical framework (i.e. model the soil using geotechnical parameters) or a fluid mechanics framework (i.e. model the soil as a non-Newtonian fluid). Advanced numerical techniques are developed in this study to simulate the response of deepwater offshore pipelines and SCRs under various loading conditions.

The main objectives of this research are to:

1) Develop large-deformation finite element (FE) models for partially embedded pipelines to analyze vertical penetration due to monotonic and dynamic loading, and subsequent lateral displacements.

2) Develop numerical models using a computational fluid dynamics (CFD) approach to analyze penetration behaviour of a pipe section. Identify the advantages of CFD for modeling the effects of water flow in the channel behind the pipe during penetration.

3) Conduct FE and CFD analyses for submarine landslide impact on suspended pipelines in deepwater for estimation of drag force.

4) Conduct CFD analysis of a steel catenary riser near the touchdown zone under cyclic loading to examine penetration/extraction behaviour, which influences the fatigue life of a riser.

1.3 Outline of Thesis

This thesis is prepared in manuscript format. The outcome of the study is presented in seven chapters and five appendices. This first chapter demonstrates the background, objectives and contributions of the study.

Chapter 2 presents a short literature review. As the thesis is prepared in manuscript format, the problem specific literature reviews are provided in Chapters 3–6 and Appendices A–E.

Chapter 3 presents large-deformation finite element analysis of penetration and subsequent lateral displacements of a partially embedded pipeline. This chapter has been published as a technical paper in the Canadian Geotechnical Journal, which was selected as an Editor's Choice paper. Numerical modeling of dynamic embedment of a pipeline is also performed, which has been published as a technical paper in the 18th International Conference on Soil Mechanics and Geotechnical Engineering, Paris, France, 2013 (Appendix-A).

Chapter 4 presents a comparative study of vertical penetration of a pipeline/riser into a soft clay seabed using ANSYS CFX and Abaqus CEL software. This chapter has been published as a technical article in the ASCE International Journal of Geomechanics. The performance of different numerical techniques for modeling large-deformation behaviour during pipeline penetration is also compared. The outcome of that research has been published as two conference papers; one in the 69th Canadian Geotechnical Conference, GeoVancouver 2016 (Appendix-B), and the other one in the 34th International Conference on Ocean, Offshore and Arctic Engineering, St. John's, Canada, 2015 (Appendix-C).

Chapter 5 presents numerical modeling of a steel catenary riser in the touchdown zone under cyclic loading. This chapter has been submitted to a journal as technical paper for review. A part of this study has been published in the 11th International Pipeline Conference, IPC2016

(Appendix-D). The author of this thesis also co-authored another journal paper relevant to the work presented in this chapter (Hawlader, B. Fouzder, A and Dutta, S. 2015).

Chapter 6 presents modeling of submarine landslide impact on suspended pipelines. This chapter was prepared as a manuscript for a journal paper. A preliminary study on this topic has been published in the 25th International Ocean and Polar Engineering Conference, 2016 (Appendix-E).

Chapter 7 presents an overall summary of the thesis and recommendations for future studies.

As the thesis is prepared in manuscript format, the problem specific conclusions and references are provided at the end of Chapters 3–6 and Appendixes A–E. The references cited in Chapters 1 and 2 are listed in the Reference chapter at the end of the thesis.

1.4 Significant Contributions

The following technical papers have been produced from the research presented in this thesis.

Journal

1. **Dutta**, S., Hawlader, B. and Phillips, R. (2017). Numerical modeling of a steel catenary riser section in the touchdown zone under cyclic loading. Under review.

2. **Dutta**, S. and Hawlader, B. (2017). Pipeline–soil–water interaction modeling for submarine landslide impact on suspended offshore pipelines. Under review.

3. **Dutta**, S., Hawlader, B. and Phillips, R. (2015). Finite element modeling of partially embedded pipelines in clay seabed using Coupled Eulerian–Lagrangian method. Canadian Geotechnical Journal, 52(1):58–72. (Editor's Choice).

4. Hawlader, B., **Dutta**, S., Fouzder, A. and Zakeri, A. (2015). Penetration of steel catenary riser in soft clay seabed – finite element and finite volume methods. ASCE International Journal of Geomechanics, DOI: 10.1061/(ASCE)GM.1943-5622.0000474

5. Hawlader, B., Fouzder, A. and **Dutta**, S. (2015). Numerical modeling of suction and trench formation at the touchdown zone of steel catenary riser. ASCE International Journal of Geomechanics, DOI: 10.1061/(ASCE)GM.1943-5622.0000497

Conference

1. **Dutta**, S., Hawlader, B., Phillips, R. and Paulin, M. (2016). Numerical investigation of vertical penetration of steel catenary riser near the touch down zone. Proc. 11th International Pipeline Conference, IPC2016, Canada, Sept. 26–30, Paper No. 2016-64608, 9p.

2. **Dutta**, **S**., and Hawlader, B. (2016). Comparison of the Implicit and Explicit Finite Element Methods in Abaqus based on Penetration of Cylindrical Objects into Seabed. Proc. 69th Canadian Geotechnical Conference, GeoVancouver, Vancouver, BC, Canada, Oct. 2−5, Paper No.004011.

3. **Dutta**, S., Hawlader, B. and Phillips, R. (2015). Vertical penetration of offshore pipelines: a comparative study between finite element and finite volume methods. OMAE2015. Proc. ASME 2015 34th International Conference on Ocean, Offshore and Arctic Engineering, St. John's, Canada, May 31–June 5, Paper No. OMAE2015-42076.

4. **Dutta**, S. and Hawlader, B. (2015). Numerical modeling of drag force on submarine suspended pipelines using finite element and finite volume methods. Proc. 25th International Ocean and Polar Engineering Conference, Hawaii, United States, June 21–26, Paper No. 2015-TPC-1486.

5. **Dutta**, S., Hawlader, B. and Phillips, R. (2013). Numerical investigation on dynamic embedment of offshore pipelines. Proc. 18th International Conference on Soil Mechanics and Geotechnical Engineering, Paris, France, September 2–5, 2013. Paper No. 2347-2350

Co-Authorship: Most of the research presented in journal papers 1–3 and conference papers 1–5 have been conducted by the thesis author. He also prepared the draft manuscripts. The other authors supervised the research and reviewed the manuscripts. For journal paper 4, Dutta conducted most of the numerical analyses, prepared figures, and draft manuscript under close supervision of the first author. For journal paper 5, not included in this thesis, Dutta was involved in numerical modeling and manuscript preparation.

CHAPTER 2

Literature Review

2.1 Introduction

Offshore pipelines and Steel Catenary Risers (SCR) are widely used in deepwater environments for transportation of hydrocarbons. While there are differences, a section of pipeline or riser can be simply viewed as a cylindrical object. Theoretical, physical and numerical studies are available in the literature on modeling of interaction between cylindrical objects and seabed sediments and also water in some cases. This chapter is divided into two sections: (i) surface laid pipeline (partially embedded or suspended), and (ii) steel catenary riser. The literature review presented in the following sections focuses mainly on clay sediments, because in deepwater environments, the seabed sediments are mainly clay.

As the thesis is written in manuscript format, the problem specific literature reviews are presented in Chapters 3–6 and Appendices-A–E. The primary purpose of adding this chapter is to present additional critical review of available studies relevant to the present research. Where needed, a number of tables and figures are prepared for a better comparison and to provide further information about previous studies, which could not be included in the manuscript because of space limitation.

2.2 Surface Laid Pipeline: An Overview

2.2.1 *Partially Embedded Pipeline*

A short summary of vertical penetration and lateral displacement of partially embedded pipelines (i.e. embedment less than one pipe diameter, D) is presented in this section. A detailed review of available studies can be found in Dutta (2012) and in Chapter 3.

2.2.1.1 *Vertical Penetration*

Theoretical Approaches

Small et al. (1971) proposed a method to calculate pipeline embedment into a soft clay seabed of uniform undrained shear strength (s_u). They used the concept of bearing capacity of a shallow foundation in which the effects of berm formation were neglected. Murff et al. (1989) estimated the penetration resistance using the upper- and lower-bound theorem based on the failure mechanisms proposed by Randolph and Houlsby (1984). Later, Randolph and White (2008) proposed a yield envelope using Martin's mechanism (Martin and Randolph, 2006) for both uniform and linearly varying s_u profiles. In these studies, the reduction of s_u due to remolding has not been considered.

Physical Modelling

A number of small- to large-scale laboratory tests were conducted for modelling vertical penetration of offshore pipelines for several projects (e.g. PIPESTAB: Pipeline Stability Design 1986; AGA/PRC: American Gas Association/Pipeline Research Committee 1992−1993). Verley and Lund (1995) compiled available data and proposed an empirical equation for vertical penetration resistance. Cheuk et al. (2007) conducted a series of full-scale tests for pipe penetration into a kaolin clay bed. Dingle et al. (2008) performed centrifuge tests to get further

insight into the soil flow mechanisms during pipe penetration into the seabed profiles of linearly varying s_u.

Numerical Modelling

Pipeline penetration into the seabed has been modelled numerically for both wished-in-place (e.g. Aubeny et al., 2005; Bransby et al., 2008; Merifield et al., 2008; Morrow and Bransby, 2010) and pushed-in-place configurations (e.g. Barbosa-Cruz and Randolph, 2005; Bransby et al., 2008; Merifield et al., 2009; Wang et al., 2010; Tho et al., 2012), where the main focus was the movement of a section of pipe in a vertical plane. However, it is to be noted here that axial resistance also plays a major role on pipeline buckling. The wished-in-place configuration represents a pre-embedded pipe with horizontal seabed without consideration of berm due to penetration, while the pushed-in-place configuration represents the condition when a pipe is embedded by pushing from above the seabed (the real case) (Bransby et al., 2008; Merifield et al., 2009). Aubeny et al. (2005) compared FE results with an extended Randolph and Houlsby (1984) model and proposed generalized equations for penetration resistance. Bransby et al. (2008) showed the importance of the soil berm from FE analysis. Merifield et al. (2008) presented a comparison between FE and upper-bound theorem (using Martin's mechanism) and proposed analytical solutions. Barbosa-Cruz and Randolph (2005) showed the effects of soil berm and s_u on penetration behavior. Later, Merifield et al. (2009) compared FE results with theoretical investigations and proposed analytical solutions. Wang et al. (2010) and Chatterjee et al. (2012a) incorporated strain-softening and strain-rate effects on s_u to estimate the penetration resistance from large deformation FE analysis. Tho et al. (2012) showed that the Coupled Eulerian-Lagrangian (CEL) technique can also simulate large-deformation phenomenon of

vertical penetration of pipeline; however, the effects of strain-softening and strain-rate on s_u were not considered.

2.2.1.2 *Pipe Lateral Resistance*

After vertical penetration, partially embedded pipelines can move laterally on the seabed or can penetrate further into the seabed depending upon seabed sediment properties and the weight of pipeline and its contents. Two key stages values of lateral resistance are often considered in the pipeline design: (i) breakout resistance at small displacement, and (ii) residual resistance at large displacement (typically 3.0–4.0*D*). The following approaches have been used for estimation of lateral resistance.

Theoretical Approaches

Using the concept of wedge indenter and energy equilibrium principle, Karal (1977) calculated pipe breakout resistance, which is only for small pipe displacements. Cheuk et al. (2007) proposed an upper-bound solution assuming a circular slip surface. Using Martin's mechanism, a theoretical yield envelope was proposed by Merifield et al. (2008) for soil having uniform s_u. Randolph and White (2008) developed a theoretical yield envelope for a linearly varying s_u profile of the seabed. Limited number of studies are available in the literature for estimation of residual resistance. Cheuk et al. (2007) proposed an equation for residual resistance using the upper-bound theorem.

Physical Modeling

Small- to large-scale tests (Lyons, 1973; SINTEF 1986a,b; Cheuk et al., 2007) and centrifuge modeling (Dingle et al., 2008; White and Dingle, 2011) were conducted for estimation of pipe lateral resistance. Lyons (1973) showed that Coulomb's friction law—the lateral

resistance is the product of effective submerged vertical force and a soil friction coefficient—cannot be used to estimate the lateral breakout resistance for clay because the friction coefficient is not constant. Wagner et al. (1989) modified Coulomb's frictional model based on data from 200 tests and proposed an analytical model. Verley and Lund (1995) proposed an empirical equation for lateral resistance based on a large number of test data collected from different sources (SINTEF 1986a,b, 1987; Morris et al., 1988). Later, the SAFEBUCK JIP (2002–2012) was initiated to get further insight into pipeline–seabed interaction mechanisms and a generalized design guideline has been proposed (Bruton and Carr, 2011). This JIP included several small- to large-scale physical tests, FE analysis and comparison with field data. Cheuk et al. (2007) conducted a number of large-scale tests by cyclic lateral sweeping of pipes embedded at different depths. Dingle et al. (2008) performed centrifuge tests to quantify the lateral resistance of a light pipe. White and Dingle (2011) conducted additional centrifuge tests and proposed a design guideline. Based on field data, Westgate and White (2015) presented a probabilistic approach for lateral breakout resistance. Bruton et al. (2006) developed an equation for residual resistance using the data from different projects. Cardoso et al. (2010) proposed an equation for residual resistance from laboratory model test results.

Numerical Modeling

Lyons et al. (1973) conducted FE analysis to estimate the breakout resistance using nonlinear stress–strain behavior of soil. Merifield et al. (2008) developed a FE model to investigate breakout resistance; however, in their analysis strain-softening and strain-rate effects on s_u were not considered. Using Arbitrary Lagrangian-Eulerian (ALE) approach, Merifield et al. (2009) conducted FE analyses to calculate the horizontal breakout resistance. Wang et al. (2010) and Chatterjee et al. (2012b) conducted large-deformation FE analysis and proposed empirical

equations for breakout and residual resistances. They found that the residual resistance mobilizes after 2.5D of lateral displacement.

2.2.2 *Submarine Landslide Impact on Suspended Pipelines*

Theoretical Approaches

Demars (1978) presented an analytical approach to calculate the tension in an offshore pipeline resulting from submarine landslide impact. Swanson and Jones (1982) proposed a mathematical approach to estimate stresses in offshore pipelines impacted by a submarine landslide. Summers and Nyman (1985) developed an analytical approach using the principal of virtual work to calculate stresses and strains in pipelines during landslide–pipeline interaction events.

Studies on estimation of lateral limiting pressure on pile foundations—soil flows around a cylindrical object—might be extended to interpret soil–pipeline interaction (Aubeny et al., 2005, Zakeri et al., 2009). Randolph and Houslby (1984) used the lower- and upper-bound theorem to understand soil flow mechanisms around the pile and showed that the normalized resistances are 9.14 and 11.94 for smooth and rough pile, respectively. Vivatrat and Chen (1985) performed theoretical investigations of drag force on pile foundations considering strain rate effects on s_u using a power law model. An empirical equation was proposed to estimate pile lateral drag force. Three soil deformation patterns have been identified (Fig. 2.1); among them the teardrop condition gives a good agreement with previous theoretical solutions.

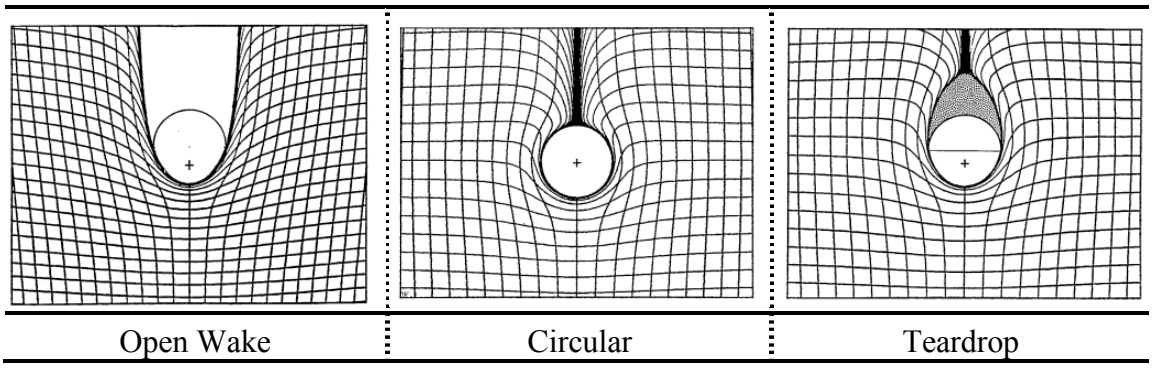

Fig. 2.1. Proposed soil flow mechanisms around the pile (Vivatrat and Chen, 1985)

Physical Modeling: Pipe–Soil Interaction

Brookes and Whitmore (1968) performed physical experiments from which a normalized drag force of 16.7, with a standard deviation of 0.75, was obtained. A detailed review of available studies on drag force and their limitations are summarized in Zakeri (2009a). Zakeri et al. (2008) performed flume tests to understand the impact of debris flow on pipelines, in which the debris were created from a mixture of kaolin clay, silica sand, water and black diamond coal slag of different compositions. From experimental results, the values of rheological model parameters have been estimated. Zakeri et al. (2012) also performed a number of centrifuge tests to understand the interaction between glide block (a block of detached soil that still carries the original soil strength after submarine landslide) and pipeline, and proposed a power law model to estimate drag force.

Physical Modeling: Pile–Soil Interaction

Similar to pipelines, physical modeling was also conducted in the past to estimate the drag force on piles. Schapery and Dunlap (1978) conducted several experiments where a model pile was inserted into a large simple shear device and walls of the simple shear device were cyclically displaced to create load on the pile. Towhata and Al-Hussaini (1988) performed several

experiments in which a model pile was moved laterally in a soft clay bed using a pulley-rail system. An average normalized force of 16 has been reported from their experimental study. Georgiadis (1991) summarized available studies and showed that the normalized force increases with relative velocity between pile and soil. A number of shear box tests were also performed at different shearing speed to estimate rate-dependent s_u. A power law equation has been proposed to estimate the drag force, which shows a good agreement with model test results (Schapery and Dunlap, 1978; Vivarat and Chen, 1985; Towhata and Al-Hussaini, 1988).

Numerical Analysis

Based on a fluid mechanics approach, Zakeri (2009b) developed numerical models in ANSYS CFX to calculate normal and longitudinal drag forces. Besides fluid mechanics approach, a combined approach (combination of geotechnical and fluid mechanics) has been also proposed by Zhu and Randolph (2011) and implemented in large-deformation FE analysis. Randolph and White (2012) reanalyzed Zakeri (2009b) data and validated the combined approach of geotechnical and fluid mechanics for estimation of drag force. Sahdi et al. (2014) conducted centrifuge tests and showed that the combined approach of Randolph and White (2012) can reasonably estimate the drag force on pipelines. Zakeri and Hawlader (2013) conducted finite volume analysis and showed that ANSYS CFX can reasonably simulate the centrifuge results of Zakeri et al. (2012). Liu et al (2015) also performed numerical analysis using ANSYS CFX for landslide–pipeline interaction and proposed a new yield envelope for lateral and axial resistances.

2.3 Steel Catenary Riser: An Overview

Heave (vertical), surge and sway motions of SCRs are equally important in modeling riser–seabed–water interaction near the touchdown zone; however, the latter two motions are outside the scope of the present study. Previous studies on the behavior of SCR near the touchdown zone for vertical penetration and uplift are discussed in the following sections.

2.3.1 *Riser Vertical Penetration*

The penetration of a riser into the seabed can vary from fractions of its diameter to several diameters (4–5*D*) (Bridge, 2005). As the penetration of a pipe section to shallow depths (<1*D*) has already been discussed in Section 2.2, the discussion in the following sections is mainly focused on intermediate depths (4–5*D*).

Theoretical Modeling

Aubeny et al. (2005) extended the Randolph and Houlsby (1984) mechanisms (Fig. 2.2) to calculate vertical penetration resistance up to 5*D* assuming that soil flows around the riser after penetration of 1.0*D* and 1.5*D* for smooth and for rough pipe, respectively. Hodder and Cassidy (2010) proposed an empirical relationship for estimation of vertical penetration resistance based on large-deformation FE analyses conducted by Barbosa–Cruz and Randolph (2005). The estimated bearing capacity factor ($N_p=V/s_uD$, where V is the vertical resistance) was compared with Aubeny et al. (2005) and a considerable difference was found for higher penetration depths (>0.5*D*). One of the potential reasons behind this discrepancy is that Aubeny et al. (2005) modeled riser penetration assuming an open trench. Hu (2010) estimated riser vertical penetration resistance using the upper-bound plasticity theorem where two types of soil flow mechanisms were considered depending upon vertical penetration depths ($w\leq D$ and $w>D$) (Fig.

2.3). The failure mechanisms were explained using a number of isosceles triangles, where the upper two additional triangles in Fig. 2.3(b) were considered to capture the flow around mechanisms for higher penetration depths. Compared with centrifuge test results; the upper-bound solution gives higher resistance than physical experiments.

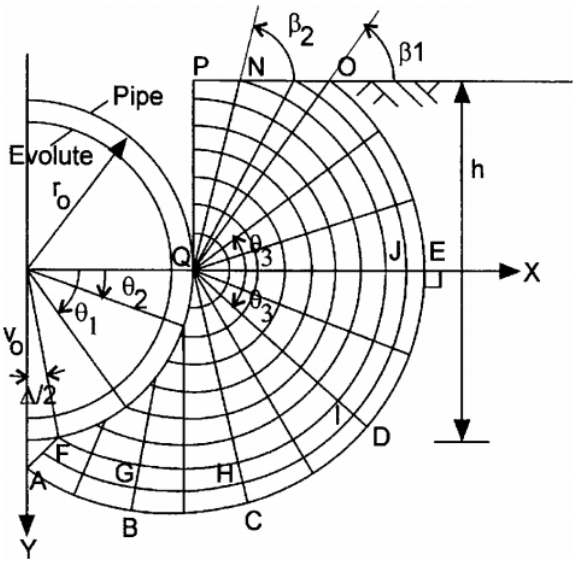

Fig. 2.2. Extension of Randolph–Houlsby solution (Aubeny et al. 2005)

Physical Modeling

Limited studies are available for intermediate vertical penetration depths as compared to shallow penetration depths discussed in Section 2.2. Other than riser vertical penetration tests, cylindrical objects such as T-bar penetration tests were conducted for estimation of s_u at varying depths (Dingle et al., 2008; Hodder and Cassidy, 2010; Cheuk and White, 2011). Clukey et al. (2008b) and Aubeny et al. (2008) performed several tests for estimation of riser penetration resistance of several pipe diameters (up to 4.3D) in uniform and linearly increasing s_u with depth (Table 2.1). Puech et al. (2010) conducted several T-bar tests to investigate soil failure mechanisms from shallow to deep penetration depths. The penetration resistance is almost constant after a vertical penetration of 6D. Hodder et al. (2009) also conducted several tests for

riser penetration of several diameters into the seabed in a linearly varying s_u profile. Hu (2010) conducted centrifuge modeling for riser penetration of 3–5D into the seabed having a linearly increasing s_u profile.

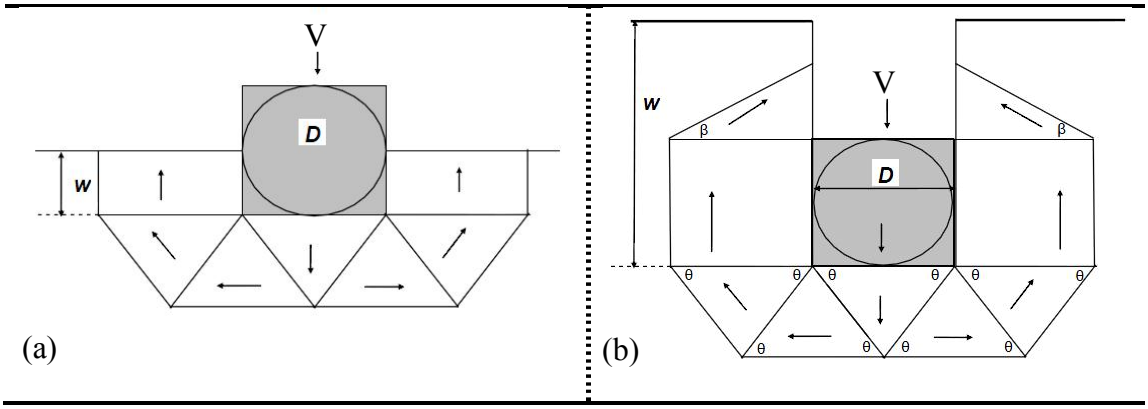

Fig. 2.3. Failure mechanism for riser vertical penetration (a) $0 < w \leq D$ (b) $w > D$ (Hu, 2010)

Numerical Modeling

Aubeny et al. (2005) performed FE analysis for wished-in-place (WIP) pipeline at different burial depths and proposed an empirical equation for riser vertical penetration resistance. White et al. (2010) performed large-deformation FE analyses using the RITSS technique where the riser was penetrated vertically up to 8D. It showed that the full-flow soil failure mechanisms occur early for low $s_u/\gamma' D$. Tho et al. (2012) performed extensive FE analyses with different soil parameters for penetrations depth up to 10D using the Coupled Eulerian-Lagrangian (CEL) technique in Abaqus FE software. Based on numerical results, a generalized equation was proposed for riser vertical penetration resistance. Hu et al. (2010) also conducted large deformation FE analysis using Abaqus CEL incorporating the strain-softening effect using the equation proposed by Einav and Randolph (2005).

Table 2.1. Summary of previous studies on pipeline/riser−seabed interaction

Reference	Test No	Virgin Penetration	Amplitude	Episodes	Remarks
Dunlap et al. (1990)	1	0.05–0.6*D*	–	1	*D*=0.152 m; *L*=1.5 m; s_u =1–1.5 kPa; five displacement controlled tests, *N*=1.
	2	0.02–0.5*D*	–	1	Sixteen load controlled tests; mean load=45–135 kg; final embedment=0.1–0.6*D*
	3	0.06–0.1*D*	–	1	Six displacement controlled tests; *N*=1–3 thousands; final embedment=0.2–0.3*D*
Bostrøm et al. (1998)	1	0.14*D*	0.14*D*	1	*D*=0.5 m; *L*=1.6 m; s_u=2.5+7.5*z*; *N*=1, no consolidation and with consolidation period of 18 hrs.
STRIDE JIP 1998	1	0.5*D*	–	–	*D*=0.168 m and 0.048 m; *L*=0.95 m; s_u=33*z* kPa/m; pipe was pulled at different velocities (6–17 mm/s) from a pre-prepared trench after consolidation period of 5 min–72 hrs.
CARISIMA-I JIP	1	0.5*D*	0.5*D*	1	*D*=0.1016 m and 0.22 m; *L*=0.4064 m; s_u=1.5+12.5*z*; load controlled; consolidation time=12 hrs; *N*=100; effects of venting, remolding and velocity were investigated.
CARISIMA-II JIP	1	0.5*D*	0.5*D*	1	*D*=0.1016 m; *L*=0.4064 m; $s_{u\_0.5D}$=3 kPa; consolidation time=2 hrs; penetrated into the soil and then uplifted at velocity=10 mm/s; results were compared with STRIDE JIP.

Reference	Test No	Virgin Penetration	Amplitude	Episodes	Remarks
Clukey et al. (2005)	1	0.28 – 0.50*D*	–	1	*D*=0.152 m; overnight consolidation.
			1±1 to 12 ± 13 mm; 200 ± 300 to 400 ± 600 N	2	*N*=1000; overnight consolidation at 0.28–0.50*D* after 1000 cycles; displacement amplitude for displacement controlled tests and load amplitude for load controlled tests. *Note*: Several tests were performed. Relevant tests are described here.
			–	3	Initial penetration depth 0.5*D*; overnight consolidation; *N*=75 to 1000; load and displacement controlled tests.
Clukey et al. (2008a)	1	3.5*D*	±0.3*D*	1	*D*=0.025 m; *L*=0.15 m; pushed the pipe to 4.3*D* and cycled 1000 times; consolidation for one day.
			±0.1*D*	2	*N*=100.
	2	4.3*D*	±0.3*D*	1	One day consolidation and push the pipe to 7.9*D;* one day consolidation and push the pipe to 8.6*D;* and cycled 1000 times.
			±0.05*D*	2	*N*=7540.
Aubeny et al. (2008)	1	0.8*D*	–	1	*D*=0.025 m; *L*=0.125 m; s_u=3.7 kPa; after uplift, penetrated to 2.8*D* at velocity 0.1 mm/s. Finally, penetrated to 6*D* and uplift to the mudline.
	2	2*D*	–	1	*v*=0.1 mm/s.

Reference	Test No	Virgin Penetration	Amplitude	Episodes	Remarks
		–	6.4; 12.8 & 19 kPa	2	10 cycles for each amplitude and 100 cycles for the last amplitude; load controlled tests.
	3	2*D*	–	1	*v*=0.1 mm/s; after penetration, uplifted to 1*D* and re-penetrated; *N*=30.
		5.7*D*	–	2	After penetration, the pipe was uplifted.
Langford and Aubeny (2008)	1	0.3*D*	–	–	*D*=0.174 m; *L*=1.3 m; s_u=2+13*z* kPa; *v*=0.05 mm/s; uplifting started when the pipe penetration resistance reached 9.5 kPa and each cycle pipe was moved to the seabed; *N*=7.
	2	0.3*D*	2000 ± 200 N	1	*v*=0.05 mm/s; load control tests; *N*=30; consolidation time 72 hrs.
	3	0.3*D*	0.02*D*	–	*v*=0.05 mm/s; displacement control tests; *N* =100 and after each episode, 1–4 hr consolidation time, total 500 cycles.
	4	0.3*D*	–	–	*v*=0.5 mm/s; uplifting started when pipe penetration resistance reached 11 kPa and each cycle pipe was moved to the seabed; *N*=4.
Hodder et al. (2009)	1	0.5*D*	0.5*D*	1–3	*D*=1 m; *L*=6 m; s_u=1+1.2z; *N* =20 with three episodes and consolidation time 1 year in between the episodes; centrifuge modeling.

Reference	Test No	Virgin Penetration	Amplitude	Episodes	Remarks
	2	1*D*	1*D*	1–3	*N* =20 with three episodes and consolidation time of one year in between the episodes.
	3	1*D*	0.5*D*	1–3	*N* =20 with three episodes and consolidation time of one year in between the episodes.
Hu (2010)	1 – 11	3.5–5 *D*	0.5 – 3*D*	1	*D*=0.6 m &1 m; *L*=6 m; s_u=1.39 & 5.19z; *N* =12–90; *v*=0.5–6 mm/s.
Hodder and Cassidy (2010)	1	–	–	–	*D*=0.5 m; *L*=2.5 m s_u=3.5+0.7*z*; unload-reload loops started at 1*D*, 3*D*, 5*D*, 7*D* and 2*D*, 4*D* and 6*D*. A number of inclined penetration tests were also performed.
Langford and Meyer (2010)	1	0.5*D*	0.5*D*	1	*D*=0.174 m; *L*=1.3 m; s_u=5+0.1*z*; *N* =20; displacement controlled; reconsolidation between cyclic phases=0.1–18 days.
Elliot et al. (2013a, b; 2014)	1	–	–	–	*D*=0.5 m; *L*=108m; s_u=4+1.6*z*; centrifuge tests for global riser analysis with heave, sway and surge motions.

Note: *D*=diameter of the pipe; *L*=Length of the pipe section; *z*=depth from seabed, *N*=number of cycle

2.3.2 *Riser Cyclic Motion*

Theoretical Modeling

Aubeny and Biscontin (2009) developed an analytical framework for cyclic riser–seabed interaction modeling. The seabed was modeled using springs and their stiffnesses were described by a set of equations to produce the force–displacement curve shown in Fig. 2.4. The performance of the proposed empirical model was verified against the physical test results of Dunlap et al. (1990) and a reasonable agreement was found. However, in the model, the effects of strain-rate and strain-softening on s_u were not considered. The Aubeny and Biscontin model was extended by Randolph and Quiggin (2009) to incorporate strain-softening effects (Fig. 2.5). The proposed model was compared with the centrifuge test results of Aubeny et al. (2008) and a reasonable agreement was found. However, suction mobilization and trench formation mechanisms during riser cyclic motions were not clearly explained. Hodder and Cassidy (2010) proposed an empirical model for uplift resistance based on the centrifuge test results. However, the role of water and trench formation mechanisms were not discussed. Hu (2010) predicted uplift resistance using the upper-bound theorem. The soil flow mechanisms are the same as penetration (Fig. 2.3); however, flow direction is reversed. Calculated uplift resistance based on these mechanisms gives higher values than centrifuge test results. Aubeny et al. (2015) extended the model of Aubeny and Biscontin (2009) incorporating the effects of strain-softening.

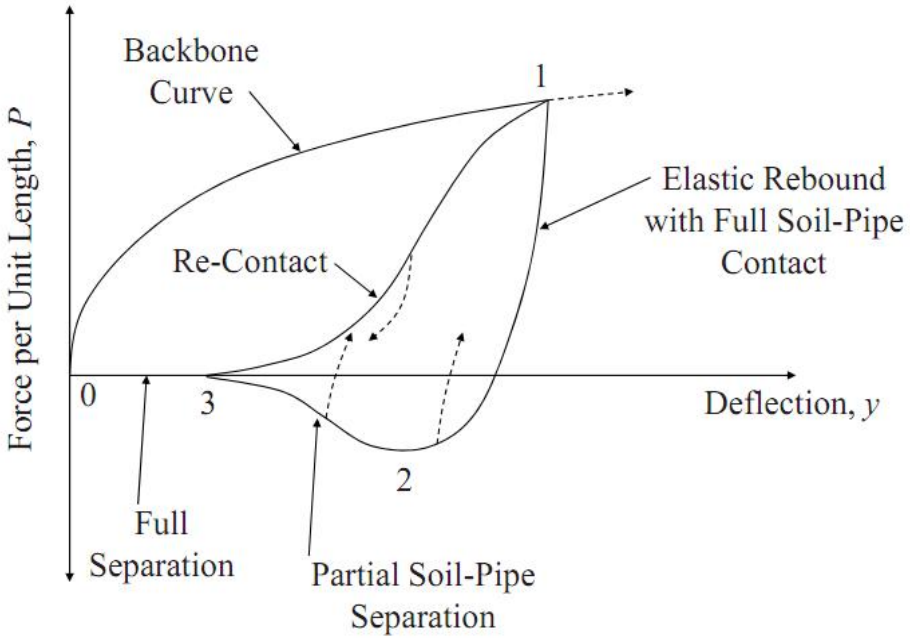

Fig. 2.4. Typical *P–y* curve (Aubeny and Biscontin, 2009)

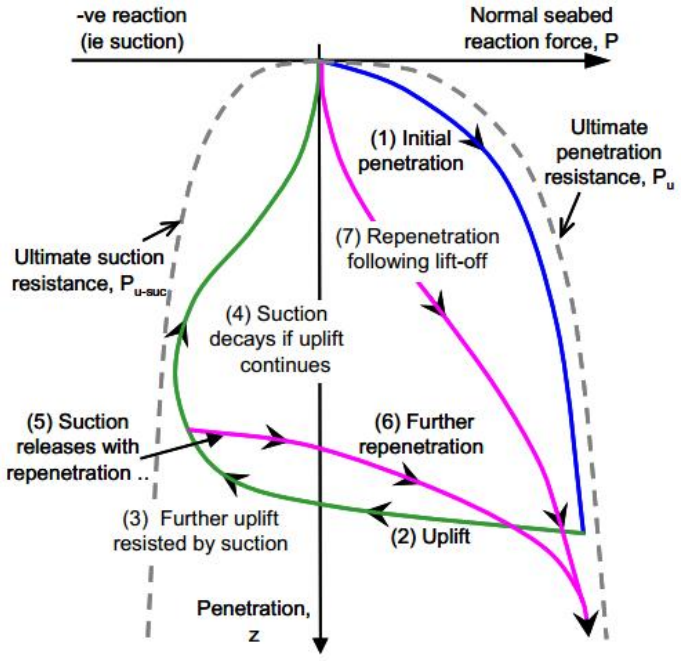

Fig. 2.5. Riser–seabed interaction model (Randolph and Quiggin, 2009)

Physical Modeling

Physical modeling of riser cyclic motions is summarized in Table 2.1. Here, the "virgin penetration" means the penetration into the seabed during its first cyclic motion and "episodes" means the stage change within the tests after some cyclic motions (e.g. rest period for consolidation or difference in riser travel distance (i.e. amplitude) etc.). Suction might play a vital role in uplift resistance during cyclic motions. Suction also plays a considerable role in other submerged objects in offshore environments (Muga, 1967; Vesić, 1969; Byrne and Finn, 1978; Foda, 1983). From physical experiments, Dunlap et al. (1990) showed that suction might occur during riser uplift motion. Bostrøm et al. (1998) observed that suction increases if the pipe is uplifted after a certain period of consolidation in between loading cycles. Later, STRIDE JIP (1998–2002) was initiated to model riser–soft clay–water interaction. This large JIP consisted of four components: (i) field investigation of trenches around the riser, (ii) full-scale tests, (iii) 2-D vertical pipe–soil interaction tests, and (iv) lateral pipe–soil interaction tests. Full-scale tests were conducted in the Watchet Harbor, UK, having soil properties similar to Gulf of Mexico clay. Tests were conducted using a 110 m long and 0.1683 m diameter riser under vertical and lateral cyclic motions. It was concluded that suction might significantly influence the fatigue stress near the TDZ. In 2-D pipe–soil interaction modeling, a pipe section was moved vertically into the seabed and then uplifted. The main objectives were to investigate the effects of pullout velocity, consolidation time on penetration and uplift resistance. It was observed that the maximum uplift resistance and breakout displacement increase with uplift velocity, and the maximum uplift resistance depends on riser-soil contact area.

In the CARISIMA-I JIP, several 2-D small-scale riser–soil interaction tests were conducted on Onsøy clay (Giertsen et al., 2004; Marintek, 2000). The effects of penetration rate,

consolidation time and vent around the trench were examined. It was found that suction varies with test conditions. In the CARISIMA-II JIP, cyclic tests were conducted using the Watchet Harbour clay. It was observed that the soil stiffness reduces with number of cycles (Fig. 2.6). Based on experimental results of STRIDE and CARISIMA JIPs, empirical relationships have been proposed to calculate the maximum uplift resistance and breakout displacement. Uplift resistance decreases significantly after the first pullout and it decreases further with subsequent loading cycles (Fig. 2.6). From a number of physical model test results, Clukey et al. (2005) showed that the decrease of uplift resistance with number of cycles depends on riser travel distance during pullout. When the riser was pulled up above the seabed, the uplift resistance after several cyclic motions is much lower than the cases where the riser was not pulled above the seabed. The authors mentioned that jetting and scouring might have occurred during re-penetration and uplift. Clukey et al. (2008a) also conducted several experiments at larger penetration depths and showed that the secant stiffness ratio stabilizes after a large number of cyclic motions (>100). Aubeny et al. (2008) conducted model tests on a kaolin clay bed having a uniform s_u where the cyclic displacements were applied at different penetration depths (Fig. 2.7). The uplift resistance increases with penetration depth.

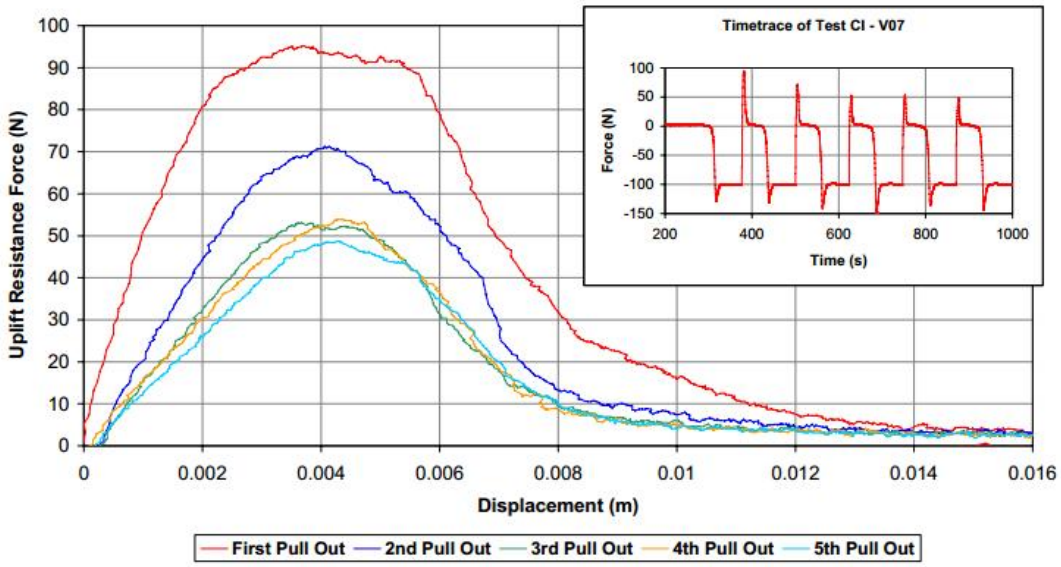

Fig. 2.6. Variation of uplift resistance with number of cycles (Bridge, 2005)

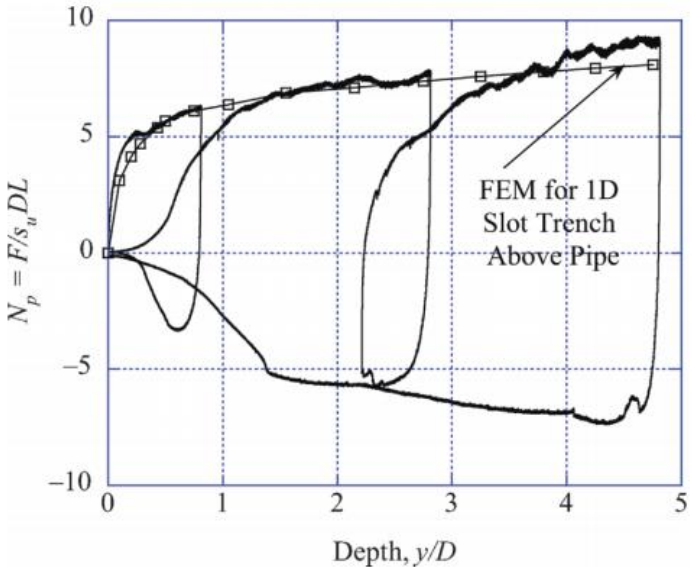

Fig. 2.7. Pipe−soil interaction during riser cyclic motion (Aubeny et al., 2008)

Hodder et al. (2009) conducted several tests where the riser was pulled out of the seabed in some tests during cyclic motions. The unloading stiffness of the soil stabilizes after 10 cycles

when the riser was moved above the seabed during uplift. However, the number of cycles required for stiffness stabilization is higher when the riser was not moved above the seabed. Hodder and Cassidy (2010) conducted a number of tests for vertical, lateral and oblique cyclic motions at different penetration depths and compared the results with plasticity solutions. Hu (2010) conducted centrifuge tests to study the effects of s_u profile, riser diameter, loading rate, riser separation from seabed, riser displacement during cyclic motions (amplitude) and frequency on penetration and uplift response. The penetration resistance reduces with the number of cycles. A quick reduction of resistance occurs when the riser was pulled above the seabed during uplift. Pore pressure transducers around the invert of the risers shows the development of suction during uplift. Langford and Meyer (2010) also conducted several cyclic tests at shallow penetration depths and showed that the depth of the trench is not significantly influenced by the number of cycles. Westgate et al. (2013) conducted a number of centrifuge tests to understand cyclic pipe–soil interaction for inclined displacement of the riser from initial penetration depth of 0.3D. Elliot et al. (2013a, b; 2014) performed full length riser–soil–water interaction modeling using an innovative test setup using the C-CORE geotechnical centrifuge. It was found that a trench of different sizes can be formed along the touchdown zone due to cyclic motions. The test results explain trench formation mechanisms and their effects on riser fatigue stresses. However, the mechanisms of water/soil mixing and erosion around the riser could not be explained properly. The erodibility of soil might depend on undrained shear strength, plasticity, clay minerology and grain size, and no simple correlation is currently available to model this complex process (Briaud, 2007). Yuan et al. (2016) conducted physical model tests where a section of riser was cycled vertically and laterally at different amplitudes.

Numerical Modeling

Modeling the soil as nonlinear springs both for penetration and uplift, Bridge (2005) performed FE analysis to investigate the response of riser motions around the touchdown zone. Using FLEXCOM software, Grealish et al. (2007) performed FE analysis to investigate the effects of suction on bending moment of the riser where the seabed was modeled as nonlinear springs. Clukey et al. (2007) presented the effects of trench formation on fatigue damage by conducting FE analysis in which the seabed has been modeled using the hyperbolic model proposed by Bridge (2005). Using LS-DYNA FE software, Clukey et al. (2008b) also investigated the effects of cyclic motions for two idealized riser–seabed interface conditions: (i) compression only and (ii) tension at interface. During uplift, no suction force develops for the compression only interface condition; however, suction develops for tension at interface condition. The effects of strain rate and softening on undrained shear strength was not considered in this study, although the authors recognized the importance of these factors in riser–seabed interaction modeling. Fouzder (2015) modeled riser−seabed−water interaction using a computational fluid dynamic approach to explain suction mobilization during uplift implementing a simplified strain softening model for seabed sediment. Barrett et al. (2015) incorporated the riser–seabed interaction model proposed by Aubeny and Biscontin (2009) in Abaqus FE software using user subroutines.

2.4 Conclusions

A comprehensive literature review is presented in this chapter on seabed interactions of two popular hydrocarbon transportation systems used in deepwater environments, namely surface laid pipelines (partially embedded and suspended) and steel catenary riser. One of the

critical parameters in the design of a partially embedded pipeline is the estimation of pipe lateral resistance, because the pipeline might be displaced laterally several pipe diameters during operation, which could cause lateral buckling. Based on seabed topography, the suspended sections of an as-laid pipeline might be impacted by the failed soil blocks resulting from submarine landslides. The estimation of drag force is one of the key design parameters for these conditions. Besides, a Steel Catenary Riser (SCR) interacts with the seabed near the touchdown zone because of its cyclic motion due to environmental loading, which has a significant influence on fatigue life of the riser. In all of these cases, a cylindrical section of pipe interacts with soft clay seabed and displaces a large distance during installation and operating conditions. Theoretical study, numerical analyses and physical model tests were performed to understand pipeline–seabed interaction. Numerical modeling of these large-deformation problems is challenging. In addition, the effects of strain-rate and strain-softening on undrained shear strength of clay, cyclic loading and soil erosion make the process further complex. Moreover, the water in the trench/cavity behind the pipe plays a considerable role in penetration and uplift behaviour. Another key question that needs to be answered is whether numerical analysis should be performed modeling soft seabed sediment in geotechnical framework or should it be modeled as a non-Newtonian fluid. Some of these issues are investigated in the present study.

CHAPTER 3

Finite Element Modelling of Partially Embedded Pipelines in Clay Seabed Using Coupled Eulerian−Lagrangian Method

Co-Authorship: This chapter has been published in the Canadian Geotechnical Journal as: Dutta, S., Hawlader, B. and Phillips, R. (2015) "Finite Element Modelling of Partially Embedded Pipelines in Clay Seabed Using Coupled Eulerian–Lagrangian Method." Most of the research presented in this chapter has been conducted by the first author. He also prepared the draft manuscript. The other authors mainly supervised the research and reviewed the manuscript.

3.1 Abstract

Vertical seabed penetration and lateral movement of deep water offshore pipelines are simulated using the Coupled−Eulerian Lagrangian (CEL) approach in Abaqus Finite Element (FE) software. Abaqus CEL has been used in some previous studies to simulate large-deformation behavior of offshore pipelines; however, the effects of strain rate and strain softening on undrained shear strength (s_u) have not been considered. In this study, the effects of these factors are critically examined. The available built-in models in Abaqus CEL cannot account for these factors directly, especially the strain rate; therefore the development of user subroutines is required. In the present study, a simple but realistic soil constitutive model (published by Zhou and Randolph, 2007) that considers the effects of strain rate and strain softening on s_u is implemented in Abaqus CEL. The effects of FE mesh size and shear band

formation on penetration resistance are discussed based on a comprehensive FE simulation. Lateral analyses are performed for 'light' and 'heavy' pipes in clay seabed having linearly increasing undrained shear strength profile for smooth and rough pipe/soil interface conditions. The FE results are compared with previous theoretical, numerical and centrifuge test results. Based on the present FE analyses, it is shown that, similar to the remeshing and interpolation technique with small strain (RITSS) technique developed at the University of Western Australia, the Abaqus CEL can successfully simulate the response of partially embedded pipelines in deep water clay seabed provided strain rate and softening dependent clay models are implemented. A methodology to implement such a model using Abaqus user subroutine is also presented.

Keywords: partially embedded pipelines; deep water; soft clay sediment; Coupled Eulerian−Lagrangian (CEL) method; finite element analysis.

3.2 Introduction

Pipelines are a key component in offshore oil and gas development. Pipelines in deep water are often laid on the seabed. However, because of other actions such as laying effects, hydrodynamic force and weight of the pipe and its contents, the pipelines often penetrate a fraction of its diameter into the seabed. Offshore oil pipelines are operated under high internal pressure and temperature. The axial force generated by thermal expansion of the pipe combined with high internal pressure might cause lateral buckling of the pipeline if sufficient resistance to prevent the movement of the pipeline is not available. The vertical embedment of pipeline and formation of berm during penetration have a significant effect on the pipeline lateral resistance.

Previous research on modeling of vertical penetration of pipelines can be broadly categorized into three groups: (i) theoretical, (ii) physical, and (iii) numerical modeling. Theoretical modeling includes the models based on bearing capacity equations, upper- and lower-bound plasticity models and slip-line field theory (e.g. Small et al., 1972; Murff et al., 1989; Aubeny et al., 2005; Zhao et al., 2009). The physical modeling includes small- and large-scale modeling (SINTEF 1986a, 1986b, 1987; Dunlap et al., 1990; AGA/PRC, 1992; Cheuk et al., 2007; Cardoso and Silveira 2010) and centrifuge modeling (e.g. Dingle et al., 2008; Hu et al., 2009; White and Dingle, 2011). Some empirical models have also been proposed based on laboratory tests and field data (Verley and Lund, 1995). The numerical analyses have been performed using small-strain finite element (FE) modeling techniques in Lagrangian framework (Aubeny et al., 2005; Bransby et al., 2008; Zhao et al., 2010; Martin and White, 2012), finite difference approach (Morrow and Bransby, 2010), and also recently introduced large-strain FE modeling techniques (Barbosa-Cruz and Randolph, 2005; Merifield et al., 2009; Wang et al., 2010; Shi et al., 2011; Tho et al., 2012; Chatterjee et al., 2012a).

The lateral resistance has also been modeled by previous researchers in theoretical framework using frictional law, plasticity theorem or upper-bound theorem and energy equilibrium principle (e.g. Karal, 1977; Cheuk et al., 2007; White and Cheuk 2008). Small- to large-scale physical tests (Lyons, 1973; SINTEF 1986a, 1986b, 1987; Cheuk et al., 2007) and centrifuge model tests (Dingle et al., 2008; White and Dingle, 2011) were conducted to understand this interaction mechanism. Moreover, FE analyses have been performed for lateral movement of pipelines in various soil conditions (e.g. Merifield et al., 2008; Wang et al., 2010; Chatterjee et al., 2012b).

The objective of this study is to present FE modeling of embedment and lateral displacement of pipelines in clay seabed. The Coupled Eulerian Lagrangian (CEL) approach in Abaqus FE software is used for numerical analysis. The effects of strain rate and strain-softening on s_u are incorporated in the present FE analyses, which were not investigated in previous studies using Abaqus CEL. A method to implement a soil constitutive model in Abaqus CEL using a user subroutine is presented.

3.3 Previous FE Modeling

As-laid pipelines in deep water might penetrate $0.25D-0.75D$ into the clay seabed (Westgate et al., 2009). These partially embedded pipelines might move laterally up to $10D-20D$ due to high temperature and pressure during its operation (Bruton et al., 2006). Therefore, vertical penetration and lateral displacement of partially embedded pipelines are fundamentally large-deformation problems. In general, the FE programs in Lagrangian framework cannot handle large deformation because of excessive mesh distortion and convergence issues (Woodworth-Lynes et al., 1996). Therefore, to calculate penetration resistance some researchers (e.g. Aubeny et al., 2005; Bransby et al., 2008; Merifield et al., 2008) have performed FE analysis of pre-embedded "wished in place" (WIP) pipes, where the pipe is initially placed at the desired embedment depth and then displaced further. The FE modeling techniques have been advanced significantly over the last several decades. Some advanced FE techniques can simulate large deformation problems (Barbosa-Cruz and Randolph, 2005; Bransby et al., 2008; Merifield et al., 2009; Wang et al., 2010; Shi et al., 2011; Tho et al., 2012; Dutta et al., 2012 a & b) where the pre-embedment is not required and the pipe could be displaced sufficiently without any numerical issues, which is known as "pushed in place" (PIP)

modeling condition. The development of numerical modeling of partially embedded pipelines is shown in Table 3.1. A summary of previous research on large strain FE modeling are discussed in the following text.

The Arbitrary Lagrangian−Eulerian (ALE) method has been used by some researchers for large-strain analysis (e.g. Merifield et al., 2009). A certain amount of mesh distortion is unavoidable in ALE, which grows with deformation. Mesh tangling-convergence issues could be overcome using "remeshing and interpolation techniques with small strain" (RITSS) as the one developed at the University of Western Australia (Hu and Randolph, 1998; Barbosa-Cruz and Randolph, 2005). The RITSS technique has been used by a number of researchers to calculate penetration and lateral resistances (e.g. Barbosa-Cruz and Randolph, 2005; Wang et al. 2010).

Finally, the CEL technique in Abaqus 6.10 EF1 FE software also has the capability of modeling large-deformation behavior (Pike et al., 2010; Tho et al., 2012, Dutta et al. 2012a). In Abaqus CEL, the mesh is fixed and Eulerian material flow through the mesh. While the Abaqus CEL has been used by some researchers for modeling partially embedded pipelines, none of them considered the effects of strain rate and softening on s_u. These two factors have significant effect on penetration and lateral resistances (e.g. Wang et al., 2010; Chatterjee et al., 2012a; Dutta et al., 2012b). In the present study, the analyses are performed using Abaqus CEL implementing a strain-softening and strain rate dependent soil shear strength model.

3.4 Problem Statement

Large-deformation FE analysis is performed to simulate the response of a pipeline during monotonic vertical penetration followed by lateral displacement. The authors presented dynamic penetration behavior elsewhere (Dutta et al., 2013). It is assumed that the vertical and lateral

displacements occur over a very long section of pipeline; hence, the simulation is performed only for a small section that represents the plane strain condition. At first, an offshore pipeline of diameter D is penetrated vertically downward at a constant velocity v_0 into the seabed as shown in Fig. 3.1(a). The soil is displaced during vertical penetration, and berms are formed by the displaced soil mass. After vertical penetration to the desired depth, the pipe is displaced laterally at a constant lateral velocity (v_h) under a constant vertical applied load (P) as shown in Fig. 3.1(b). In general, deep-water sediments are normally consolidated soft clay (Cheuk and White, 2011; Quiros et al., 2003). Based on previous geotechnical investigations (e.g. Fugro 1999), it is assumed that the in situ undrained shear strength (s_{u0} in kPa) increases linearly with depth as $s_{u0} = s_{um}+kz$, where s_{um} is the undrained shear strength of clay at the mudline in kPa, k is the strength gradient in kPa/m and z is the depth of the soil element below the seabed in metres. Tresca yield criterion is adopted in this study.

3.5 Strain Rate and Softening Effects

The undrained shear strength of clay depends on rate of shearing. Also upon loading, the soil around the pipeline experiences significant plastic strain that causes degradation of s_u. In this study, the following empirical model of s_u from Zhou and Randolph (2007) is used.

$$s_u = \underbrace{\left[1+\mu \log\left\{\frac{\max(|\dot{\gamma}_{\max}|,\dot{\gamma}_{ref})}{\dot{\gamma}_{ref}}\right\}\right]}_{f_1}\underbrace{\left[\delta_{rem}+(1-\delta_{rem})e^{-3\xi/\xi_{95}}\right]}_{f_2}s_{u0} = [f_1][f_2]s_{u0} \quad (1)$$

Here f_1 represents the strain rate effect and f_2 represents the strain-softening effect; s_{u0} is the in situ undrained shear strength at the reference shear strain rate ($\dot{\gamma}_{ref}$) and prior to any softening; μ is the rate of change of s_u per log cycle; δ_{rem} is the ratio of remoulded to in situ

shear strength, which is the inverse of remoulded sensitivity S_t; ξ is the accumulated absolute maximum plastic shear strain; and ξ_{95} is the value of ξ at which soil has undergone 95% reduction of s_{u0} due to remolding.

Equation (1) shows that three main parameters (μ, S_t and ξ_{95}) define the effects of strain-softening and strain rate. The value of μ typically varies between 0.05 and 0.2 (Einav and Randolph, 2005; Lehane et al., 2009). The remoulded sensitivity of seabed clay sediments typically varies between 2 to 5 (Kvalstad et al., 2001; Andersen and Jostad, 2004; Randolph, 2004). Finally, the value of ξ_{95} could be estimated from cyclic penetration test results. The range of ξ_{95} of 10−50 (1,000−5,000%) is suggested by previous researchers (Einav and Randolph, 2005; Zhou and Randolph, 2009). The parameters used in this study are listed in Table 3.2, which are obtained from careful review of previous studies (Dingle et al., 2008; Wang et al., 2010; White and Dingle, 2011). A comprehensive parametric study has been presented in Dutta et al. (2012b).

3.6 Finite Element Model Development

Abaqus 6.10 EF-1 is used to perform FE analyses. Figure 3.2 shows the FE model. The pipe is modeled as a rigid body in Lagrangian framework while the soil is modeled as Eulerian material using EC3D8R elements, which are 8-noded linear brick elements with reduced integration and hourglass control. As the Abaqus CEL analysis can generate only 3D geometries, the plane strain condition is simulated considering only one element in the axial direction of the pipe.

A void space is defined above the soil to accommodate the berms. Soil and voids for initial condition are created using the Eulerian volume fraction (EVF) tool in Abaqus (2010). For clay

EVF = 1, meaning that the elements are filled with Eulerian material (soil) while EVF = 0 for void space. When an element is filled 50% with soil, EVF = 0.5. Further information about EVF can be found in the Abaqus documentation files. Based on similar mesh sensitivity analysis presented in Dutta et al. (2012a) the FE mesh shown in Fig. 3.2 is used. Finer mesh is used in the top 3 m soil and 0.4 m of voids near the mudline because the soil displacement mainly occurs in these zones.

Zero velocity boundary conditions are applied normal to the bottom and all the vertical faces (Fig. 3.2) to make sure that Eulerain materials remain in the domain. However, at the seabed-void interface, no boundary condition is applied so that the soil can flow into the void space when needed. Displacement boundary conditions are applied at the reference point of the pipe to move it vertically and then laterally.

In the Abaqus CEL, the linear variation of s_{u0} with depth cannot be incorporated directly using the graphical user interface or from input file unless the soil layer is divided into a number of layers and assign different s_{u0} values. Moreover, Abaqus CEL does not have any direct option for modeling strain-rate dependent soil behaviour as shown in Eq. (1). Therefore, in this study, the soil model (Eq. 1) is implemented using the user subroutine VUSDFLD written in FORTRAN. The implementation of the soil constitutive model is briefly discussed in the following section.

The input file is first created using Abaqus/CAE. As the linear variation of s_{u0} cannot be defined, a linear variation of temperature with depth is defined in Abaqus/CAE. The temperature is used as a dummy variable. The temperature is called in the subroutine to define a linear variation of s_{u0} with temperature. Although the linear variation can be approximated using a number of layers, the implementation using temperature dummy variable is precise and efficient.

The strain components are called in the subroutine in each time increment, which are then transferred to the principal strain components and stored as state variables. The value of $\dot{\gamma}_{\max}$ in Eq. (1) is then calculated as $\dot{\gamma}_{\max} = (\Delta\varepsilon_1^p - \Delta\varepsilon_3^p)/\Delta t$, where $\Delta\varepsilon_1^p$ and $\Delta\varepsilon_3^p$ are the major and minor principal plastic strain components, respectively, and Δt is the time increment. The value of ξ is calculated as the sum of the accumulated plastic strain increments $\Delta\varepsilon_1^p - \Delta\varepsilon_3^p$ over the period of analysis. Using $\dot{\gamma}_{\max}$ and ξ, the value of f_1 and f_2 are calculated as Eq. (1). In the subroutine, s_{u0}, f_1 and f_2 are defined as three field variables. In the input file, s_u defined in tabular form as a function of these three field variables.

Each analysis is divided into three main steps. The first step is the geostatic step. In the second step, the pipe is moved vertically downward from the seabed to the desired depth of embedment at velocity v_0 of $0.015D$/s. In the third step, the pipe is moved laterally to the right to 3−4 diameters at velocity v_h of $0.05D$/s under a constant vertical load on the pipe. The conditions and input parameters are consistent with previous centrifuge tests (Dingle et al., 2008; White and Dingle, 2011).

The maximum shear resistance at the pipe/soil interface is generally expressed as $\tau_{max} = \alpha s_u$, where α is a constant ($0 \leq \alpha \leq 1.0$). Intermediate interface resistances cannot be defined in this version of Abaqus CEL. Two extreme cases "smooth" and "rough" are simulated. The smooth condition represents $\alpha = 0$; however, the rough condition represents the no-slip condition. Therefore, in rough condition the shear failure occurs through the soil near the pipe surface. Following the concept of Gui and Bolton (1998) and assuming that the failure is occurred at a distance of half of the element size from the outer surface of the pipe, the effective diameter (D_e) for rough condition can be calculated as 840 mm (=800 mm+[2(40)/2]) for 40 mm

element size. If D_e is used instead of D, the normalized penetration resistance will be reduced by 5%. However, in the following sections D is simply used to present the results.

3.7 FE Results: Vertical Penetration

3.7.1 *Mesh sensitivity and softening and rate effects*

Mesh sensitivity is one of the key concerns in the FE analysis, especially in the analyses with strain-dependent (strain rate and softening) soil constitutive models. A total of 32 FE simulations are performed first to show the effects strain rate and stain softening for four different sizes of mesh. Table 3.3 shows the conditions used in these simulations. Sixteen of them are for uniform initial s_{u0} while the other 16 are for linearly increasing s_{u0} as s_{u0} (kPa) = 2.3+3.6z (in metres). The penetration resistance is normalized by $s_{u0(i)}$, which is the value of s_{u0} at the invert of the pipe.

Figure 3.3 shows the penetration resistance with uniform s_{u0}. The penetration resistance is less in US0 series with softening than that of U00 series without any softening and rate. The four lines in the far right of this figure show the penetration resistances of U0R series where only the strain rate (no softening) is considered. It is clear that the strain rate significantly increases the penetration resistance. Both strain rate and softening are considered in the USR series of analyses. The combined effects of these two factors increase the penetration resistance compared to U00 series. In other words, the strain rate and softening effects increase the penetration resistance for the conditions analyzed in this study. It is to be noted here that for a slow penetration rate, the penetration curves will shift to the left. However, the present analysis is not applicable for a very slow rate because the loading must be undrained, which is possible if vd/c_v >20, where c_v is the coefficient of consolidation (House et al. 2001).

The effect of mesh size on penetration resistance is not significant in U00 and U0R series where softening is not considered. When only the softening is considered (US0), the shape of the curve with smaller mesh is slightly different from that of the larger mesh, although the penetration resistances are comparable for these four sizes of mesh. When both strain-rate and strain-softening are considered, the penetration resistance curves are similar for these four mesh sizes.

The FE simulation of slightly different shape of penetration curves with smaller mesh in US0 series is further explained here. Figures 3.4a−3.4c show the plastic shear strain in clay at different w with 20 mm×20 mm mesh. As shown in Fig. 3.4(a) that a new shear band (strain localization) is started to form at w=0.116D. Further penetration of the pipe from this position causes strain localization mainly along this band in which the shear strength is decreased as Eq. (1), and the length of the shear band increases as shown in Fig. 3.4(b) at w=0.168D. As the strength of soil along the band decreases, the penetration resistance does not increase significantly during penetration from w=0.116D to w=0.168D. Further penetration from w=0.168D will increase the stress and strain below this shear band, where the shear strength is higher than that in the band. Therefore, the penetration resistance increases with w until a new shear band is formed at w≈0.24D as shown in Fig. 3.4(c). This process is repeated during the penetration, and therefore penetration curves of cyclic nature are found with smaller mesh in US0 series. Penetration curves of cyclic nature are not obtained with larger meshes because the strain localization occurs in a larger area as shown in Figs. 3.4d−3.4f with 40mm×40mm mesh. When both strain rate and softening are considered in USR series, the penetration curves for all mesh sizes are almost similar. Both plastic strain and strain rate increase with a decrease in mesh

size. The reduction of s_u due to higher plastic strain is somehow compensated by higher strain rate; therefore, strain localization is not very significant in USR series compared to US0 series.

Sixteen analyses are performed for linearly increasing s_{u0} profile where s_{u0} (kPa) = 2.3+3.6z (in m). Table 3.3 shows the simulation conditions, and Fig. 3.5 shows the penetration resistance. The s_{u0} is assigned properly using a state variable available in Abaqus. Figure 3.6(a) shows the contour of s_{u0} at w=0.45D. As shown, the displaced soil elements carry the initial value of s_{u0}. For example, the soil elements, which were initially near the seabed were pushed under the pipe at point A or in the berm at point B still have the same value of s_{u0} although displaced to different locations. Using this value of s_{u0} (state variable in Abaqus), the mobilized s_u is calculated from Eq. (1) for each time increment during the FE simulation. The variation of s_u is shown in Fig. 3.6(b). The distribution of s_u near the pipe is different from s_{u0}, and in this case, s_u is higher than s_{u0} in the zone of shear band for the set of parameters used. Therefore, the penetration resistance in LSR series is higher than that of L00 series.

Figure 3.5 shows that the effects of strain-softening, strain rate, and mesh size on penetration resistance are similar to Fig. 3.3 with uniform s_{u0}. In the following sections, the FE analyses considering both strain rate and softening effects are presented. As the penetration resistance in USR and LSR series does not vary significantly with mesh size, 40 mm×40 mm×40 mm elements are used in the following analyses. The FE analysis with small mesh is computationally very expensive. For example, the FE simulation of vertical penetration and subsequent lateral movement with 20 mm×20 mm×20 mm elements takes >15 days with a 3.2 GHz Intel Core i5 processor and 8 GB RAM. Therefore, detailed parametric study of both vertical and subsequent lateral movement is not performed with such small mesh.

3.7.2 *Comparison with Previous Models*

The first set of analysis is performed for ideal soil (i.e. without softening or rate effects) with the shear strength increasing with depth as s_{u0} (kPa) = 2.3+3.6z (in m). Figures 3.7a and 3.7b show the penetration resistance with depth for smooth and rough interface conditions, respectively. To show the performance of the present FE model, the calculated vertical resistance is compared with four recent studies, namely Randolph and White (2008), Merifield et al. (2009), Wang et al. (2010) and Tho et al. (2012). Note that, Merifield et al. (2009) and Tho et al. (2012) used uniform s_u; therefore, a value of s_{u0} of 3.0 kPa (average s_u between mudline and w/D=0.45) is used to calculate the normalized resistance ($V/s_{u0(i)}D$) using their models. As shown in Fig. 3.7(a), the present FE results compares very well with the previous solutions except the upper-bound solution of Randolph and White (2008). The underestimate of penetration resistance from such upper-bound solutions is also shown by previous researchers (e.g. Wang et al., 2010). One of the reasons is that the upper-bound solutions are based on WIP pipe configuration where the effects of surface heave is not considered. Similar comparison is performed for rough interface condition (Fig. 3.7b), which shows that the present FE model calculates slightly higher penetration resistance. From this set of analysis it can be concluded that the present FE model can satisfactorily calculate the penetration resistance.

3.7.3 *Comparison with Centrifuge Test Results*

The performance of the present FE model is compared with the results of seven centrifuge tests (Dingle et al. 2008; White and Dingle 2011). The parameters used in the analyses are listed in Tables 3.2 and 3.4. These analyses include the influence of strain rate and softening. The s_{u0} profile and v_0 in tests D1 and L1 to L4 are the same; however, the initial depth of embedment

(w_{int}) is different. Therefore, only one simulation of vertical penetration to the maximum w_{int} (=0.52D) of these tests is shown in Fig. 3.8. The vertical penetration resistance from the centrifuge test D1 (Dingle et al., 2008) is also shown in this figure. The arrows on the right vertical axis show w_{int} from where lateral displacement is applied. The s_{u0} in L5 and L6 is higher than in other tests but w_{int} is very small (Table 3.4). Similar analyses of vertical penetration are performed for these tests but not shown in this paper. Figure 3.8 shows that the centrifuge test result is bounded by the calculated values using smooth and rough pipe-soil interface conditions. The influence of strain rate and softening on penetration resistance is shown in Fig. 3.5.

3.7.4 *Contact Width*

Figure 3.9 shows the contact width between soil and pipe (D') with depth of penetration. For comparison, the results of Merifield et al. (2009) and Dingle et al. (2008) are also plotted in this figure. The rough interface condition simulates lower D' than that with smooth condition. The contact width increases with increase in w/D and reaches to the maximum at $w/D \approx 0.4$ and then remains almost constant. The model proposed by Merifield et al. (2009) for ideal soil compares well with rough condition at low w/D but with smooth condition for w/D greater than 0.3. Although the overall trend is similar, the centrifuge tests give slightly higher value of D'/D than that of the present FE analysis with rough condition or Merifield et al. (2009). This might be due to higher reduction of shear strength near the pipe surface than the value used in the present study using Eq. (1).

3.7.5 *Strain Rate and Strain Softening*

The parameters f_1 and f_2 in eq. (1) represent the effects of strain rate and strain-softening, respectively. The variation of f_1 and f_2 around the pipe is shown in Fig. 3.10 for test L1 (Table 3.4) at w=0.52D. Figure 3.10(a) shows that high strain rate (i.e. high f_1) is developed in two narrow zones and in between these there is a zone of low shear strain rate. On the other hand the maximum strain softening occurs near the pipeline as shown in Fig. 3.10(b). Note that f_2 in Fig. 3.10(b) represents the effects of accumulated strain during the penetration while f_1 in Fig. 3.10(a) represents the strain rate in the current time increment. Significant plastic shear strain is developed near the pipe, which is decreased with distance from the pipe (Fig. 3.10b). The development of equivalent plastic shear strain around the pipe at different penetration depth is also presented in Dutta et al. (2012a & b). These figures clearly show how the strain rate and softening modify the mobilized shear strength as eq. (1).

3.8 FE Results: Lateral Displacement

3.8.1 *Comparison with Centrifuge Tests*

After initial vertical penetration, the lateral displacement is applied under a constant vertical load (P). For example, in Test L2 the pipe is penetrated vertically to w_{int}=0.46D, and then moved laterally under P=2.8 kN/m. Figure 3.11 shows the comparison between FE and centrifuge results for three tests (D1, L2 and L4). Note that all 7 tests are simulated using the present FE model and presented in Dutta (2012c). The developed lateral force per unit length of the pipe (H) is increased first with lateral displacement (u), reached to the peak and then decreased gradually almost to a constant value at large displacement. For a given lateral displacement, H is higher for rough pipe-soil interface condition. The peak lateral resistance is

termed as “breakout resistance”, and the approximately constant lateral resistance at large displacement is termed as “residual resistance” (Wang et al., 2010; White and Dingle, 2011). For light pipes, the breakout resistance is generally developed at 0.05−0.15D lateral displacement. The residual state is reached approximately at a lateral displacement of 3D. Note that, large plastic shear strain is developed in a thin zone near the bottom of the pipe during lateral movement, which has a significant influence on shear strength degradation and lateral resistance. Estimation of clay shear strength near the mudline is very difficult. Although T-bar is widely used to measure s_u, there are some uncertainties in s_u obtained from T-bar tests at shallow depths (White et al., 2010). Therefore, some discrepancies between centrifuge and FE results might be due to the selection of s_u values in shallow depths.

Figure 3.11 shows that the breakout resistance obtained from centrifuge tests is higher than that of FE results even with rough pipe-soil interface. One of the reasons might be the effects of suction at the rear end of the pipe. During vertical penetration, the soil around the pipe comes in contact with the pipe. In subsequent lateral movement, suction might be developed at the rear surface. The magnitude of lateral force from suction depends on contact area of the pipe with soil (Fig. 3.12). The higher the initial embedment the higher the rear surface contact area with soil, and thus higher suction force, if other conditions are same. The suction force also depends on the direction of pipe movement, which is related to P and w_{int} as shown schematically in Fig. 3.12. For a large w_{int} and small P the pipe moves in inclined upward direction as shown in Fig. 3.12a. The contact surface behind the pipe is shown by thick lines for three different directions of movement of the pipe. The contact surface is higher in Fig. 3.12a. The general contact algorithm available in Abaqus CEL cannot simulate the suction, which might be one of the causes of discrepancies between the measured and calculated breakout resistance. The discrepancy is

higher in tests D1 and L1-L3 as the pipe moves upward as in Fig. 3.12a, and the suction is expected to be higher than other tests.

3.8.2 *Pipe Invert Trajectory*

Figure 3.13 shows the trajectories of the invert of the pipe during lateral movement. As light pipes are considered, the pipes move up initially and then maintain approximately a constant depth of embedment at large displacement (i.e. residual state). The present FE results reasonably compare with the centrifuge test data. The higher the applied vertical load (P) the higher the depth of embedment at residual state (w_{res}). For example, in D1 and L2 the s_u profile and w_{int} is almost same but P is different; P = 3.4 kN/m in D1 and 2.8 kN/m in L2. The comparison between Figs. 3.13a and 3.13b shows a higher w_{res} in D1, which is because of higher value of P. The FE analyses also show lower depth of embedment of smooth pipe during lateral movement because the smooth pipe can climb up easily during lateral displacement. In L2 (Fig. 3.13b) the invert of the pipe for smooth interface condition moves to the mudline at u/D = 2.0. Although the pipe is at the mudline, there is a berm in front of the pipe which provides lateral resistance as shown in Fig. 3.11b. The very light pipe (e.g. L3 under P = 1.0 kN/m) even climbs up the initial berm formed by vertical penetration and then moves laterally on the seabed with a very small residual resistance (Dutta 2012). All the simulation results are presented in Dutta (2012).

3.8.3 *Soil Velocity Field around the Pipeline*

Figure 3.14 shows the soil velocity fields obtained from FE simulation of test D1 at four different locations (A, B, C, D) shown in Fig. 3.11a. Two of them (A and B) are near the lateral

breakout resistance and the other two (C and D) are in between the breakout and residual resistances. The arrows at the center of the pipe show the direction of movement of the pipe. The velocity fields obtained from FE simulation compare well with the centrifuge test results shown in the last column. Both FE and centrifuge test show that the direction of movement of soil and pipe varies with lateral displacement. At point D, the pipe and the soil in front of it move almost horizontally. A detailed discussion on FE simulation of soil flow mechanism, developed plastic shear strain, and breakout and residual resistance of all seven tests listed in Table 3.4 are presented in Dutta (2012c).

3.8.4 *Effects of Applied Vertical Load* (*P*)

A parametric study is performed for six different values of P. The soil shear strength is s_{u0} (kPa) = 2.3+3.6z (in m), and the initial embedment is 0.45D. Other parameters are shown in Table 3.2. Similar to Wang et al. (2010), the term "overpenetration ratio" (R), which is the ratio of the penetration resistance at w_{int} and vertical load P, is used. The lower the value of R the heavier the pipe. From centrifuge modeling, Dingle et al. (2008) show that the normalized vertical penetration resistance ($V/s_{u0(i)}D$) at w_{int} = 0.45D is 6.2. Thus, for six different overpenetration ratios (R = 1.25, 1.67, 2.0, 3.33, 5.26 and 10.0) the value of P is calculated and used for the parametric study. The FE analyses for smooth soil-pipe interface condition are shown in Fig. 3.15.

Figure 3.15(a) shows that the lateral resistance increases continuously with lateral displacement for lower overpenetration ratios ($R \leq 2$). However, for higher overpenetration ratios ($R > 2$) the lateral resistance is increased first to the peak and then gradually decreased with lateral displacement. That means higher applied vertical load causes higher lateral resistance and

vice versa. For higher vertical load, the pipe penetrates further (Fig. 3.15b) and plough more soil (Figs. 3.16c, 3.16d) during lateral displacements; and, therefore the lateral resistance is increased with lateral displacements. These results have close similarity with the numerical investigation conducted by Wang et al. (2010), although the value of α=0 in the present study while it is 0.5 in Wang et al. (2010). On the other hand, the light pipes of higher overpenetration ratio (R > 2) move up during lateral displacements as shown in Fig. 3.15b. The very light pipe (e.g. R = 10) the pipe moves even to the seabed. For R = 3.33, the lateral resistance is almost constant after a lateral displacement of 1.5D. Soil flow mechanism around a heavy pipe of R = 1.25 is shown in Fig. 3.16 for four different lateral displacements. As the heavy pipe started to move laterally, it tries to penetrate into the soil (Fig. 3.16a). The penetration continues with lateral displacements and the pipe ploughs more soil as shown in Figs. 3.16a−3.16d. After a lateral displacement of ~3.0D, the ploughed soil passed over the top of the pipe in this case.

3.8.5 *Yield Envelope*

The magnitude and direction of force at the breakout point can be illustrated better using the yield envelope shown in Fig. 3.17. Merifield et al. (2008) conducted FE analyses of WIP pipes in weightless clay of uniform s_u. Their FE yield envelopes compare well with the upper-bound plasticity solutions of Randolph and White (2008). Chatterjee et al. (2012b) conducted large-deformation FE analyses of PIP pipes using RITSS approach, incorporating the effects of strain rate and softening (eq.(1)). Figure 3.17a shows that the large-deformation FE analyses give larger yield envelope with higher vertical bearing capacity, V_{max} (the apex point of the yield envelope) than upper-bound solutions. The solid circles in Fig. 3.17a show the present FE results. The peak lateral resistance of the smoothed curve within u=0.15D is defined as the

breakout resistance (H_{brk}) of light pipes. No such distinct peak is observed in the simulation of heavy pipes. However, a significant reduction of the slope of H vs. u curves at u between $0.02D$ and $0.05D$ is found. The value of H at the displacement where this slope change occurred is defined as H_{brk} for heavy pipes. The present FE results compare well with Chatterjee et al. (2012b). The slight difference between the yield envelopes obtained from these two FE simulations might be the effect of interface condition (α=0.5 in Chatterjee et al. (2012b) while α=0.0 (smooth) in this study).

To investigate the shape of the yield envelopes further, the results have been plotted in Fig. 3.17b after normalizing V and H by V_{max}. All the FE results compare well with the upper-bound solutions for low values of V/V_{max} (light pipes). However, for heavy pipes the present study and Chatterjee et al. (2012b) calculate slightly higher H/V_{max} than the upper-bound solutions for a given V/V_{max}.

3.8.6 *Breakout and Residual Resistances*

Lateral resistance has two main components: (i) breakout resistance (H_{brk}) and (ii) residual resistance (H_{res}). Based on the experimental database, analytical models have been proposed by Bruton et al. (2006), Cardoso and Silveira (2010) and White and Dingle (2011) to calculate breakout and residual resistances. Figure 3.18 shows the comparison of breakout resistance obtained from the present FE analyses, analytical model (Bruton et al., 2006), and centrifuge tests (Table 3.4). The breakout resistance increases with w_{int}. The effect of P is also clear in this figure. For example in test L2 the applied load is 2.8 kN/m, which is higher than the applied load in test L3 (1 kN/m). The angle of movement of the pipe to the horizontal is higher in L3 than that in L2. Therefore, the possible contact area for suction in L3 is higher (Fig. 3.12), which could

cause higher suction that could not be modeled using Abaqus CEL. The discrepancy between FE results and centrifuge tests is then significant in test L3.

Bruton et al. (2006) underestimates the lateral breakout resistance observed in centrifuge tests. Note that, the analytical model by Bruton et al. (2006) is not only a function of $(w/D)_{int}$ but also depends on P and s_u. As these values are different in centrifuge tests (Table 3.4) the points obtained from this model do not show a general trend in Fig. 3.18 because they are plotted only with $(w/D)_{int}$. The present FE analyses give a reasonable comparison with centrifuge test results. Similarly, the residual resistances from the present FE model are compared with the analytical solutions and centrifuge test results in Fig. 3.19 and 3.20. In FE modelling, the average value of lateral resistance for the final $0.5D$ lateral displacement is defined as pipe residual resistance. Figure 3.19 shows the normalized residual resistance (H_{res}/P) with normalized w_{int} while Fig. 3.20 is with $(w_{int}/D)\ R^{-1/2}$, as White and Dingle (2011) showed that H_{res} is also a function of $R^{-1/2}$. Both plots show that the analytical solutions of Bruton et al. (2006) and Cardoso and Silveira (2010) give higher residual resistance than the values obtained from the present FE model and centrifuge tests. Again, in these two analytical models, the residual resistance is also a function of the applied vertical load and undrained shear strength of the soil, which are not constant in different centrifuge tests simulated in this study; and therefore the values calculated with these models are scattered in Figs. 3.19 and 3.20. The solid line in Fig. 3.20 shows the best fit line of centrifuge test results proposed by White and Dingle (2011). The values of residual resistance in centrifuge tests are slightly lower than that obtained in the present FE models with rough and higher than with smooth pipe-soil interface conditions.

3.9 Conclusions

The on-bottom stability, lateral buckling, and pipeline walking are some of the major issues in the design of deep-water partially embedded pipelines where the pipe-soil interaction and embedment play a key role. In the present study, this large-deformation problem is simulated using the CEL technique in Abaqus FE software. A strain-softening and rate dependent model for undrained shear strength of clay seabed is implemented. The performance of FE model is verified against a total of seven centrifuge test results and available empirical and numerical solutions. The Abaqus CEL with the implemented soil model can successfully simulate the vertical penetration and subsequent lateral displacement. The effects of three main parameters (initial vertical penetration depth, applied vertical load on the pipe, and undrained shear strength) on lateral resistances are investigated. For the conditions analyzed in this study, the direction of lateral movement changes from upward to downward for overpenetration ratio between 2.0 and 3.33. The downward movement of heavy pipe ploughs more soil and the resistance increases with lateral displacement. However, the lateral resistance at large displacement for a light pipe reduces to the residual resistance which could be very small for a very light pipe because the pipe moves to the seabed.

Although the present FE model shows a great success in modeling large deformation, the possible suction behind the pipe during initial lateral movement could not be simulated using the Abaqus CEL version 6.10 EF1, which might have significant effects on breakout resistance.

Acknowledgements

The work presented in this paper has been funded by C-CORE, MITACS, Petroleum Research Newfoundland & Labrador (PRNL) and a Natural Sciences and Engineering Research

Council of Canada (NSERC) discovery grant. Some valuable information from David White at the University of Western Australia on centrifuge modeling is gratefully acknowledged.

List of symbols

The following symbols are used in this paper:

c_v coefficient of consolidation

D pipe diameter

D' pipe contact width

D_e effective diameter of the pipe

d foundation diameter

E_u undrained modulus of elasticity

f_1 strain rate effect

f_2 strain-softening effect

H lateral resistance

H_{brk} breakout resistance

H_{res} residual resistance

k undrained strength gradient

P applied vertical load on pipe

R overpenetration ratio

S_t soil sensitivity

s_u undrained shear strength

s_{u0} intact undrained shear strength

$s_{u0(i)}$	s_{u0} at pipe invert
s_{um}	Undrained shear strength of clay at mudline
Δt	time increment
u	Pipe lateral displacement
V	pipe vertical penetration resistance
V_{max}	pipe penetration resistance at w_{int}
v	velocity
v_0	vertical penetration velocity
v_h	lateral displacement velocity
v_x	velocity of soil in the x direction
v_z	velocity of soil in the z direction
w	vertical displacement of pipe invert
w_{int}	w at the beginning of lateral displacement
w_{res}	w at residual state
$(w/D)_{int}$	Normalised embedment at beginning of lateral displacement
Z	depth of soil element
A	constant
γ'	submerged unit weight of soil
$\dot{\gamma}_{max}$	maximum shear strain rate
$\dot{\gamma}_{ref}$	reference shear strain rate
δ_{rem}	ratio of fully remoulded and intact shear strength
$\Delta\varepsilon_1^p$	major principle plastic shear strain component

$\Delta\varepsilon_3^p$ minor principle plastic shear strain component

μ rate of change of s_u per log cycle

ν_u Poison's ratio

ξ accumulated plastic shear strain

ξ_{95} ξ for 95% degradation of intact s_{u0}

τ_{max} maximum shear resistance

References

Abaqus, 2010. Analysis user manual. Abaqus 6.10-EF1. Simulia Inc., Dassault Systemes.

AGA/PRC. 1992. Weight Coating Design for Submarine Pipeline on-Bottom Stability. Final Report Comparing TAMU Test to SINTEF Model, American Gas Association, Report PR-178-918.

Andersen, K., and Jostad, H. 2004. Shear strength along inside of suction anchor skirt wall in clay. *In* Proceedings of the Offshore Technology Conference, Houston, TX. OTC 16844.

Aubeny, C. P., Shi, H., Murff, J. D. 2005. Collapse Loads for a cylinder embedded in trench in cohesive soil. International Journal of Geomechanics, **5**(4):320−325.

Barbosa-Cruz, E. R., and Randolph, M. F. 2005. Bearing capacity and large penetration of a cylindrical object at shallow embedment. *In* Proceedings of the 1st International Symposium on Frontiers in Offshore Geotechnics (ISFOG) 2005. pp. 615−621.

Bransby, M. F., Zajac, P., Amman, S. 2008. Finite element analysis of the vertical penetration of 'on-bottom' pipelines in clay. *In* Proceedings of the 18th International Offshore and Polar Engineering Conference, ISOPE 2008, 6−11 July 2008. International Society of Offshore and Polar Engineers. pp. 245−249.

Bruton, D. A. S., White, D. J., Cheuk, C. Y., Bolton, M. D., Carr, M. C. 2006. Pipe-soil interaction behaviour during lateral buckling, including large amplitude cyclic displacement tests by the safebuck JIP. *In* Proceedings of the Offshore Technology Conference, Houston, Tex. OTC 17944.

Cardoso, O. C., and Silveira, M. S. R. 2010. Pipe-soil interaction behaviour for pipelines under large displacements on clay soils−A model for lateral residual friction factor. *In* Proceedings of the Offshore Technology Conference, Houston, Tex. OTC 20767.

Chatterjee, S., Randolph, M. F., White, D. J. 2012a. The effects of penetration rate and strain softening on the vertical penetration resistance of seabed pipelines. Géotechnique, **62**(7): 573-582.

Chatterjee, S., White, D. J., Randolph, M. F. 2012b. Numerical simulation of pipe-soil interaction during lateral movements on clay. Géotechnique, **62**(8): 693-705.

Cheuk, C. Y., and White, D. J. 2011. Modelling the dynamic embedment of seabed pipelines. Géotechnique, **61**(1): 39-57.

Cheuk, C. Y., White, D. J., Bolton, M. D. 2007. Large-scale modelling of soil-pipe interaction during large amplitude cyclic movements of partially embedded pipelines. Canadian Geotechnical Journal, **44**(8): 977−996.

Dingle, H. R. C., White, D. J., Gaudin, C. 2008. Mechanisms of pipe embedment and lateral breakout on soft clay. Canadian Geotechnical Journal, **45**(5): 636−652.

Dunlap, W. A., Bhojanala, R. P., Morris, D. V. 1990. Burial of vertically loaded offshore pipelines in weak sediments. *In* Proceedings of the Offshore Technology Conference, Houston, TX. OTC 6375.

Dutta, S. 2012. Large deformation finite element analysis of partially embedded offshore pipelines for vertical and lateral motion at seabed. M.Eng. Thesis, Memorial University of Newfoundland, N.L.

Dutta, S., Hawlader, B., Phillips, R. 2012a. Finite element modeling of vertical penetration of offshore pipelines using Coupled Eulerian Lagrangian approach. *In* Proceedings of the 22nd International Offshore and Polar Engineering Conference, ISOPE 2012, Rhodes, Greece, pp. 343−348.

Dutta, S., Hawlader, B., Phillips, R. 2012b. Strain softening and rate effects on soil shear strength in modeling of vertical penetration of offshore pipelines. *In* Proceedings of the 9th International Pipeline Conference, IPC 2012, Calgary, AB, 24−28 September 2012. pp. 1−8.

Dutta, S., Hawlader, B., Phillips, R. 2013. Numerical investigation of dynamic embedment of offshore pipelines. *In* Proceedings of the 18th International Conference on Soil Mechanics and Geotechnical Engineering, Paris, France.

Einav, I., and Randolph, M. F. 2005. Combining upper bound and strain path methods for evaluating penetration resistance. International Journal for Numerical Methods in Engineering, **63**(14):1991−2016.

Fugro, L. 1999. STRIDE JIP – Touchdown point behaviour of steel catenary risers, Phase II – riser/soil response curve development study. Report no. 93819-1.

Gui, M.W., and Bolton, M.D. 1998. Geometry and scale effects in CPT and pile design. *In* Geotechnical site characterization. Edited by P.K. Robertson and P.W. Mayne, Balkema, Rotterdam, pp.1063−1068. ISBN 9054109394.

House, A.R., Oliveira, J.R.M.S., Randolph, M.F. 2001. Evaluating the coefficient of consolidation using penetration tests. International Journal of Physical Modelling in Geotechnics, **1**(3): 17−26.

Hu, J. E. H., Leung, C. F., Chow, Y. K., Palmer, C. A. 2009. Centrifuge model study of SCR motion in touch down zone. *In* Proceedings of the 28th International Conference on Ocean, Offshore and Arctic Engineering, OMAE2009, Honolulu, Hawaii, 31 May − 5 June 2009, pp. 221−229.

Hu, Y., and Randolph, M. F. 1998. Deep penetration of shallow foundations on non-homogeneous soil. Soils and Foundation, **38**(1): 241−246.

Karal, K. 1977. Lateral stability of submarine pipeline. *In* Proceedings of the Offshore Technology Conference, Houston, TX. OTC 2967, pp.71−75.

Kvalstad, T., Nadim, F., Arbitz, C. 2001. Deepwater geohazards: geotechnical concerns and solutions. *In* Proceedings of the Offshore Technology Conference, Houston, TX. OTC 12958.

Lehane, B., O'Loughlin, C., Gaudin, C., Randolph, M. 2009. Rate effects on penetrometer resistance in kaolin. Géotechnique, **59**(1): 41-52.

Lyons, C. G. 1973. Soil resistance to lateral sliding of marine pipelines. *In* Proceedings of the Offshore Technology Conference, Houston, TX. Pp. 479−482.OTC 1876.

Martin, C., and White, D. 2012. Limit analysis of the undrained bearing capacity of offshore pipelines. Géotechnique, **62**(9): 847−863.

Merifield, R., White, D. J., Randolph, M. F. 2008. The ultimate undrained resistance of partially embedded pipelines. Géotechnique, **58**(6): 461−470.

Merifield, R. S., White, D. J., Randolph, M. F. 2009. Effect of surface heave on response of partially embedded pipelines on clay. Journal of Geotechnical and Geoenvironmental Engineering, **135**(6): 819−829.

Morrow, D. R., and Bransby, M. F. 2010. Pipe-soil interaction on clay with a variable shear strength profile. *In* Proceedings of the 2nd International Symposium on Frontiers in Offshore Geotechnics, ISFOG 2010, 8−10 November 2010. Taylor & Francis, Balkema, pp. 821−826.

Murff, J. D., Wagner, D. A., Randolph, M. F. 1989. Pipe penetration in cohesive Soil. Géotechnique, **39**(2), pp. 213−229.

Pike, K., Duan, G., Sun, J., Jukes, P. 2010. Comprehensive FEA of thermal mitigation buoyancy module (TMBM)–Soil interaction using the coupled Eulerian–Lagrangian (CEL) method. *In* Proceedings of the 28th International Conference on Ocean, Offshore and Arctic Engineering, OMAE 2009, Honolulu, Hawaii, 31 May−5 June 2009. pp. 865−870.

Quiros, W. G., and Little, L. R. 2003. Deepwater soil properties and their impact on the geotechnical program. *In* Proceedings of the Offshore Technology Conference, Houston, TX. OTC 15262.

Randolph, M. 2004. Characterisation of soft sediments for offshore applications. *In* Proceedings of the 2nd International Conference on Site Characterisation, Porto, Portugal, pp. 209−231.

Randolph, M. F., and White, D. J. 2008. Upper-bound yield envelopes for pipelines at shallow embedment in clay. Géotechnique, **58**(4):297-301.

Shi, H., Sun, J., Hossain, K., Eltaher, A., Jukes, P. 2011. Offshore pipeline embedment in cohesive soil – a comparison between existing and CEL solutions. *In* Proceedings of the 30th International Conference on Ocean, Offshore and Arctic Engineering, OMAE2011, Rotterdam, the Netherlands, 19−24 June. pp. 1−6.

SINTEF. 1986a. Pipe-Soil Interaction Test, Soft Clay, STF60 F86023.

SINTEF. 1986b. Pipe-Soil Interaction Test, Stiff Clay, STF60 F86072.

SINTEF. 1987. Pipe-Soil Interaction Test on Sand and Soft Clay, STF60 F7018.

Small, S. W., Tamburello, R. D., Piaseckyj, P. J. 1972. Submarine pipeline support by marine sediments. Journal of Petroleum Technology, **24**: 317-322.

Tho, K. K., Leung, C. F., Chow, Y. K., Palmer, A. C. 2012. Deep cavity flow mechanism of pipe penetration in clay. Canadian Geotechnical Journal, **49**(1):59−69.

Verley, R., and Lund, K. M. 1995. Soil resistance model for pipelines placed on clay soils. *In* Proceedings of the 14th International Conference on Offshore Mechanics and Arctic Engineering, OMAE1995, Copenhagen, Denmark, 18−22 June 1995. ASME, pp. 225−232.

Wang, D., White, D. J., Randolph, M. F. 2010. Large-deformation finite element analysis of pipe penetration and large-amplitude lateral displacement. Canadian Geotechnical Journal, **47**(8): 842−856.

Westgate, Z., White, D., Randolph, M. 2009. Video observations of dynamic embedment during pipe laying in soft clay. *In* Proceedings of the 28th International Conference on Ocean, Offshore and Arctic Engineering, OMAE2009, 31 May – 5 June 2009, Honolulu, Hawaii. pp. 699−707.

White, D. J., and Cheuk, C. Y. 2008. Modelling the soil resistance on seabed pipelines during large cycles of lateral movement. Marine Structures, **21**(1): 59−79.

White, D. J., and Dingle, H. R. C. 2011. The mechanism of steady friction between seabed pipelines and clay soils. Géotechnique, **61**(12): 1035−1041.

White, D., Gaudin, C., Boylan, N., Zhou, H. 2010. Interpretation of T-bar penetrometer tests at shallow embedment and in very soft soils. Canadian Geotechnical Journal, **47**(2):218−229.

Woodworth-Lynes, C., Nixon, D., Phillips, R., Palmer, A. 1996. Subgouge deformations and the security of arctic marine pipelines. *In* Proceedings of the Offshore Technology Conference, Houston, TX. OTC 8222.

Zhao, B., Gao, F., Liu, J., Wu, Y. 2009. Vertical bearing capacity of a partially-embedded pipeline on Tresca soils. *In* Proceedings of the 19th International Offshore and Polar Engineering Conference, Osaka, Japan, 21−26 June 2009.

Zhao, B., Gao, F., Kang, R. 2010. Numerical investigation on bearing capacity of a pipeline on clayey soils. *In* Proceedings of the 29th International Conference on Ocean, Offshore and Arctic Engineering, OMAE2010, Shanghai, China, 6−11 June 2010. Pp.269−275.

Zhou, H., and Randolph, M. F. 2007. Computational techniques and shear band development for cylindrical and spherical penetrometers in strain-softening clay. International Journal of Geomechanics, **7**(4), 287-295.

Zhou, H., and Randolph, M. 2009. Numerical investigations into cycling of full-flow penetrometers in soft clay. Géotechnique, **59**(10):801−812.

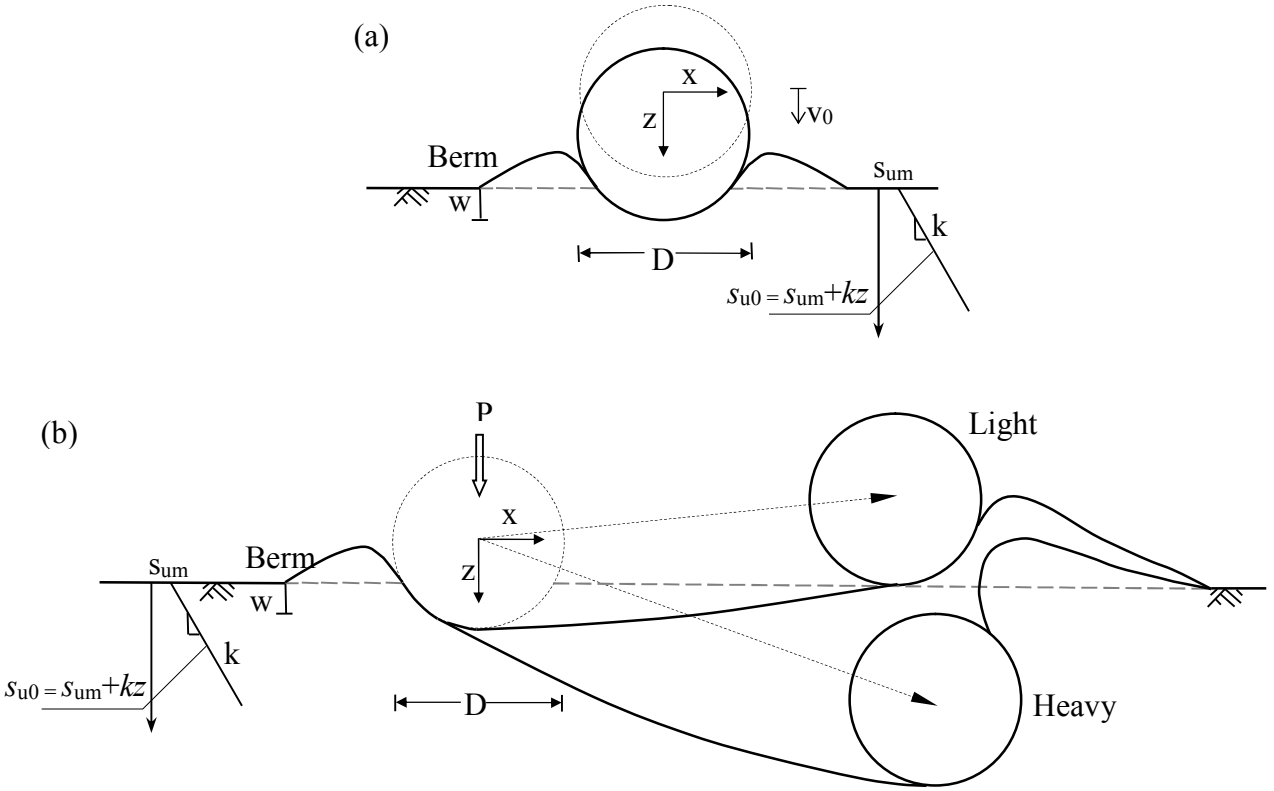

Fig. **3**.**1**. (a) Vertical penetration (b) Lateral displacement followed by vertical penetration

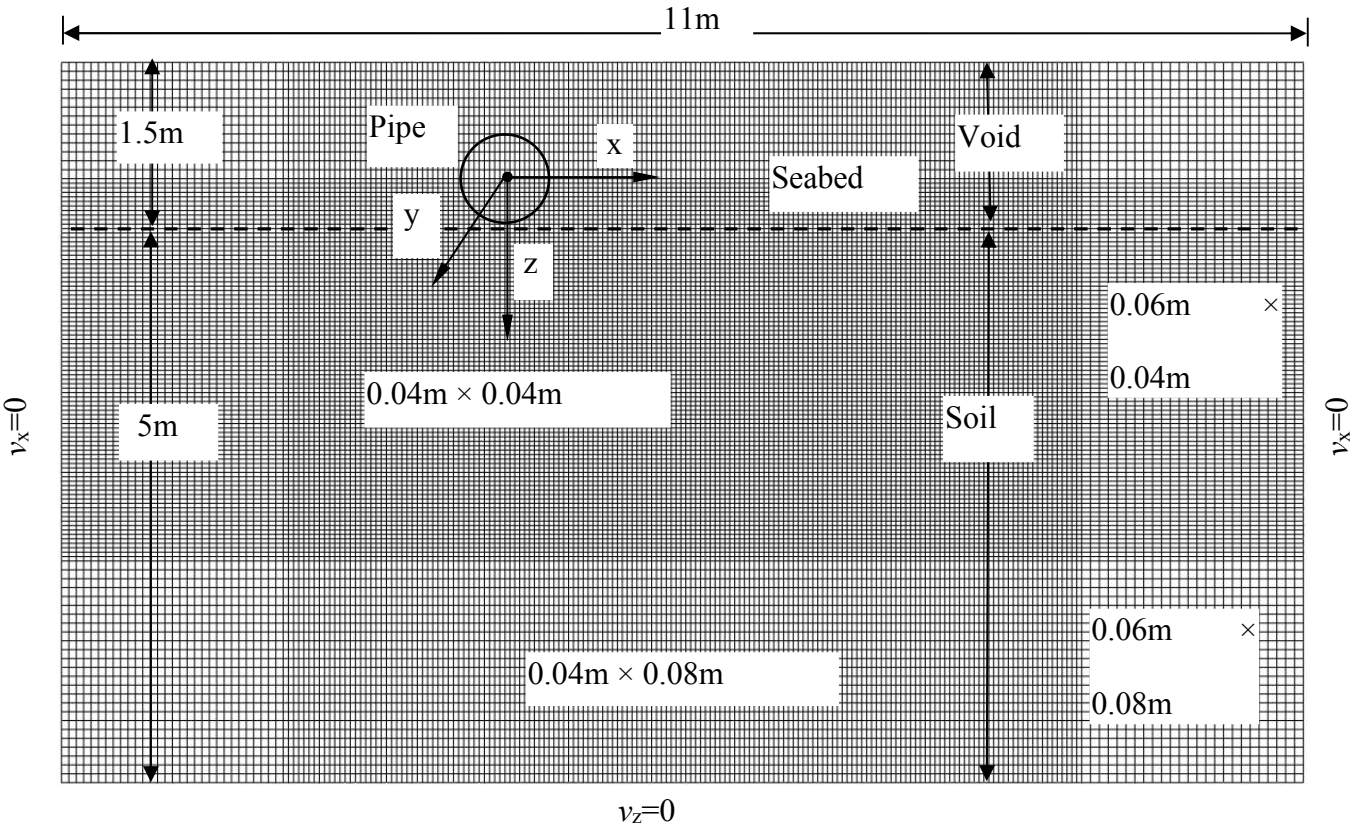

Fig. **3**.**2**. Finite element model

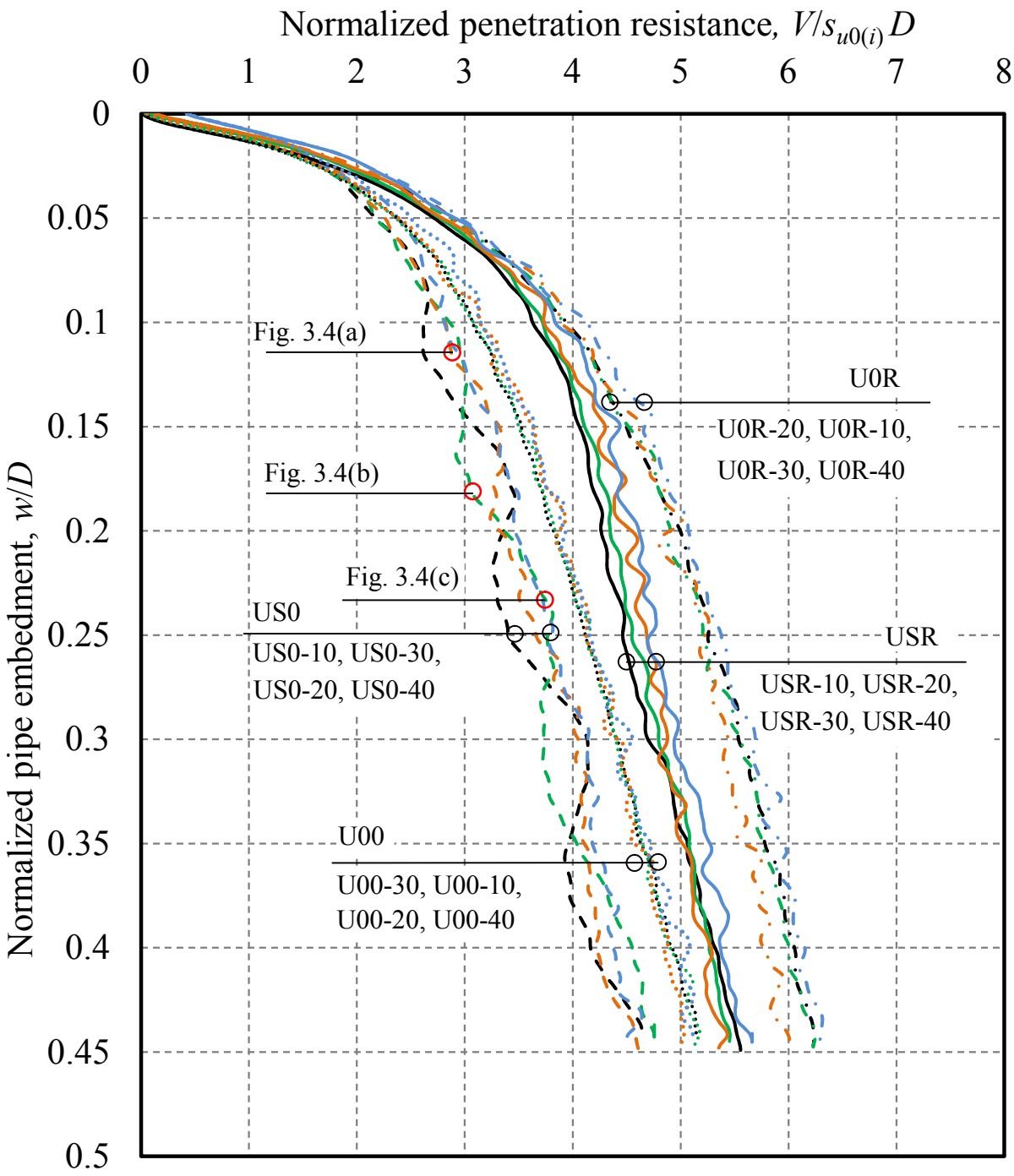

Fig. **3.3**. Penetration resistance in uniform soil for smooth pipe.

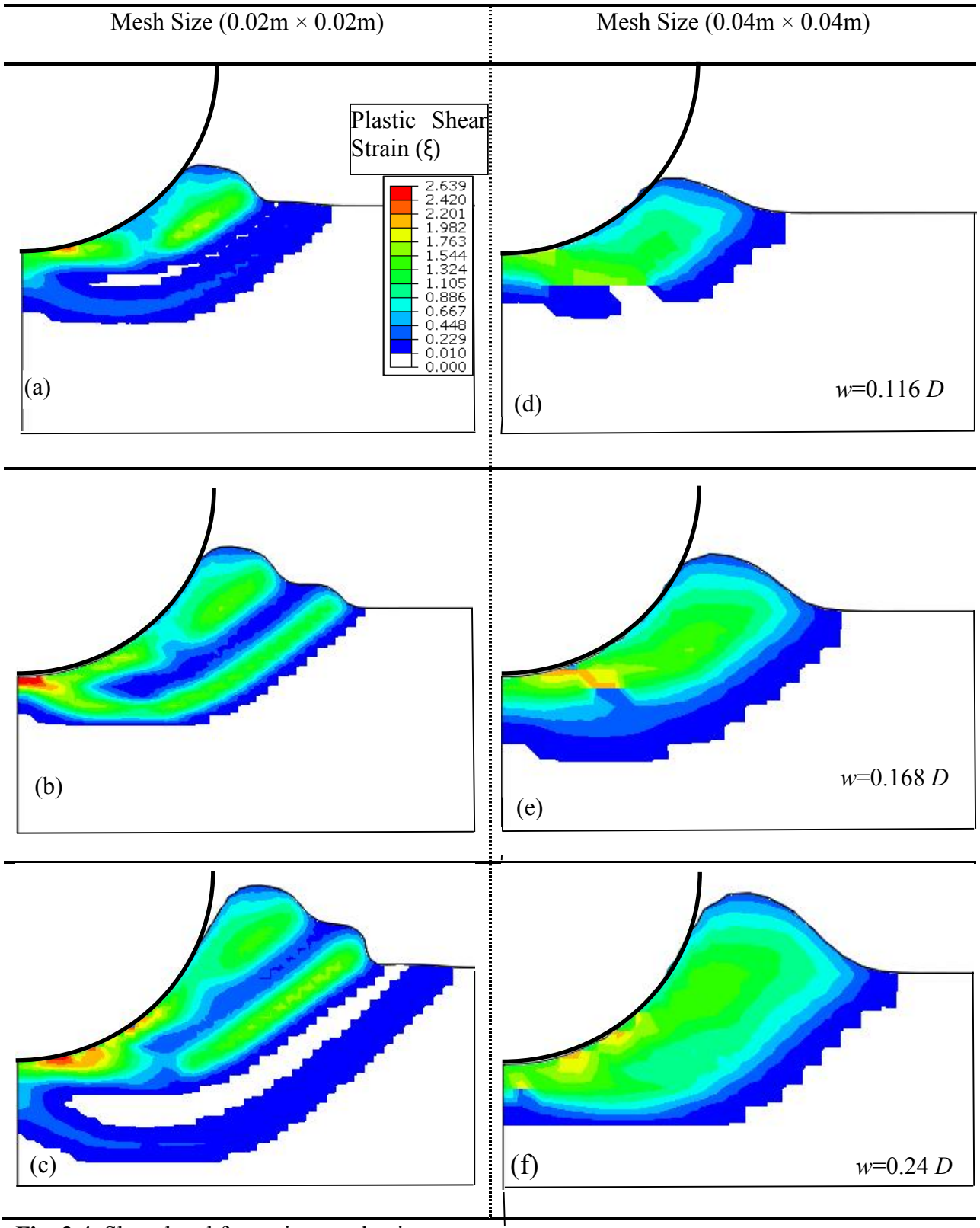

Fig. **3**.**4**. Shear band formation mechanism.

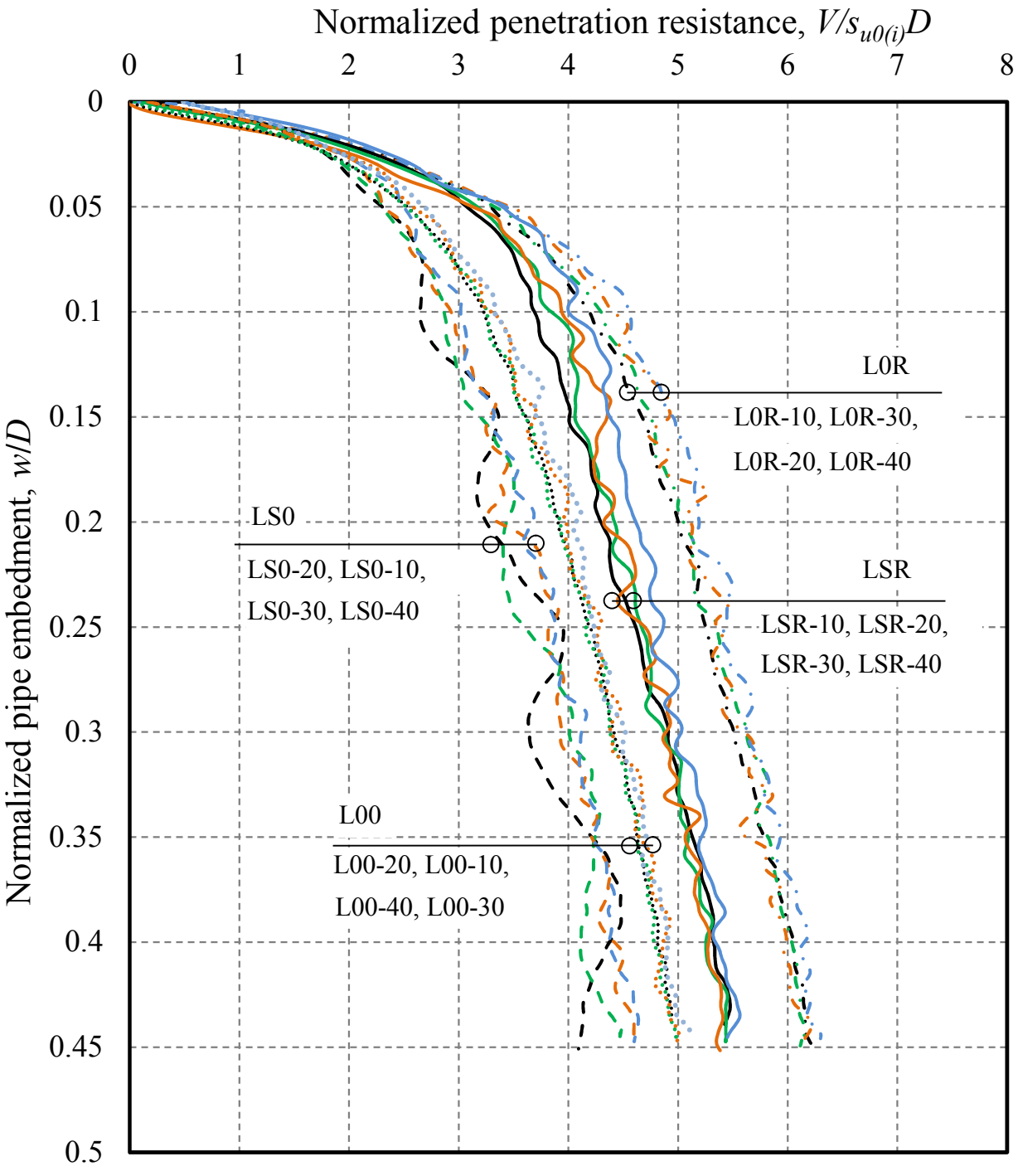

Fig. **3.5**. Penetration resistance in non-uniform soil for smooth pipe.

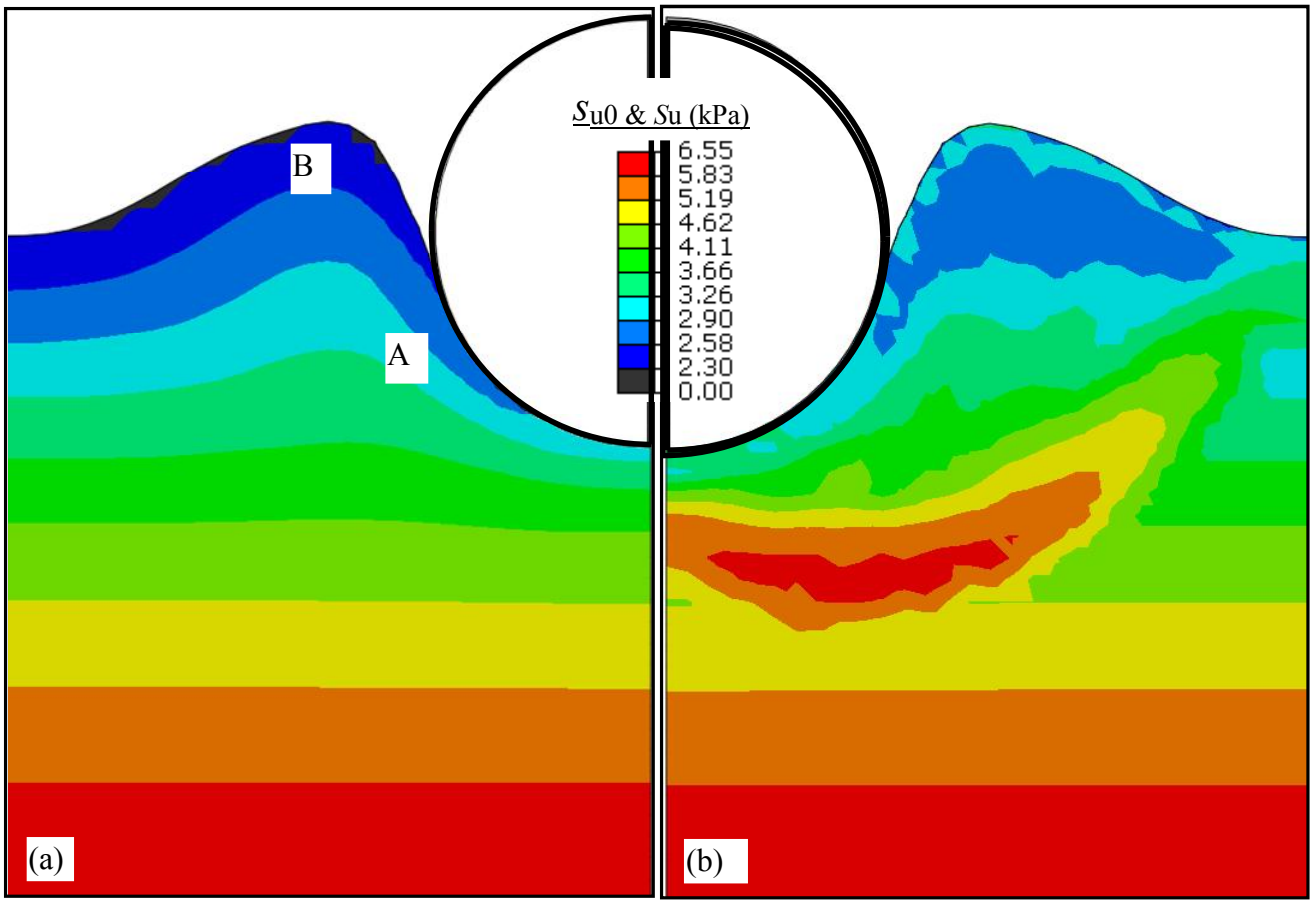

Fig. **3**.**6**. Undrained shear strength s_u: (a) initial (left); (b) mobilized at w=0.45D (right).

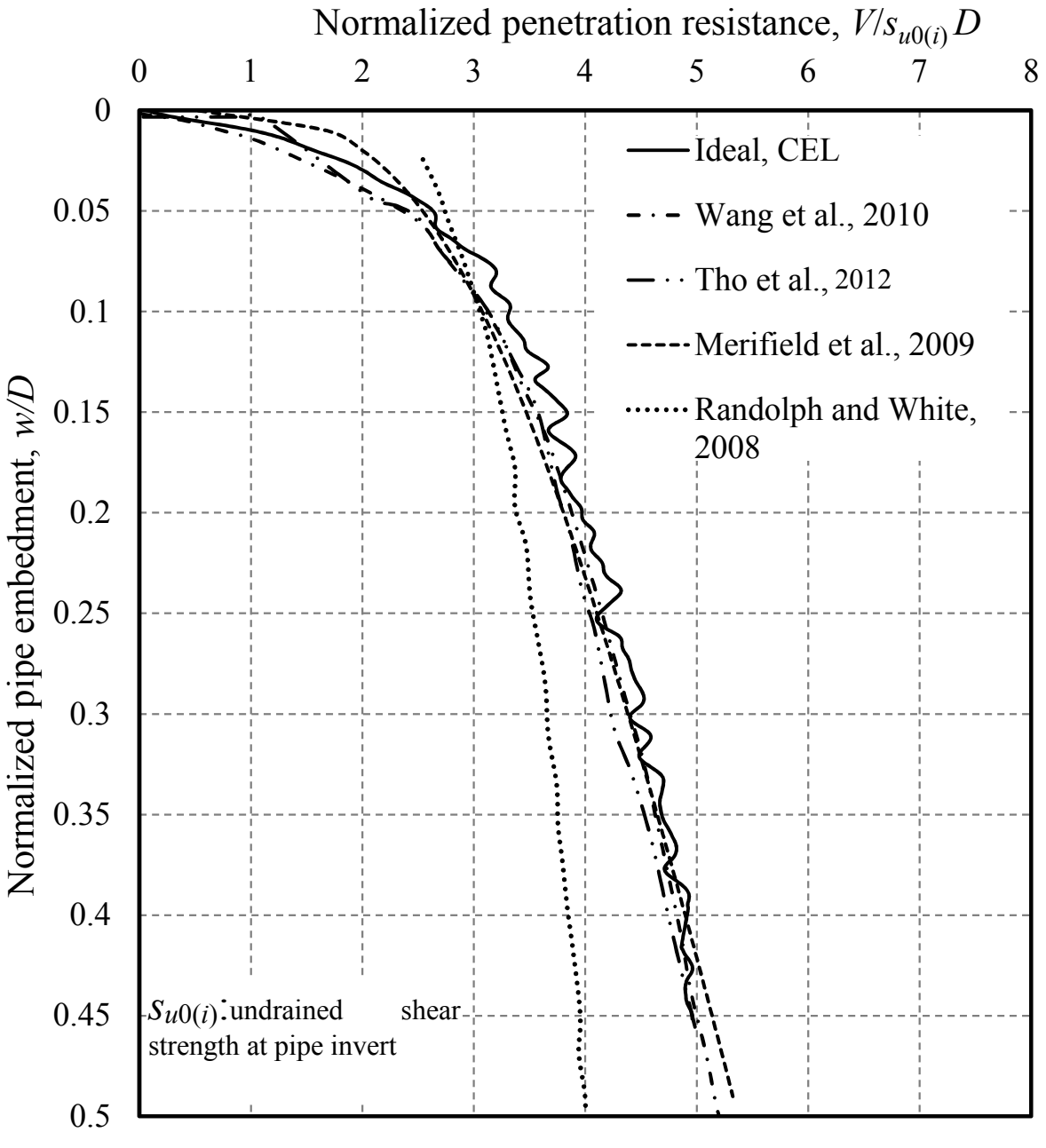

Fig. **3**.**7**. (a) Penetration resistance of smooth pipe in ideal soil (no softening or rate effect)

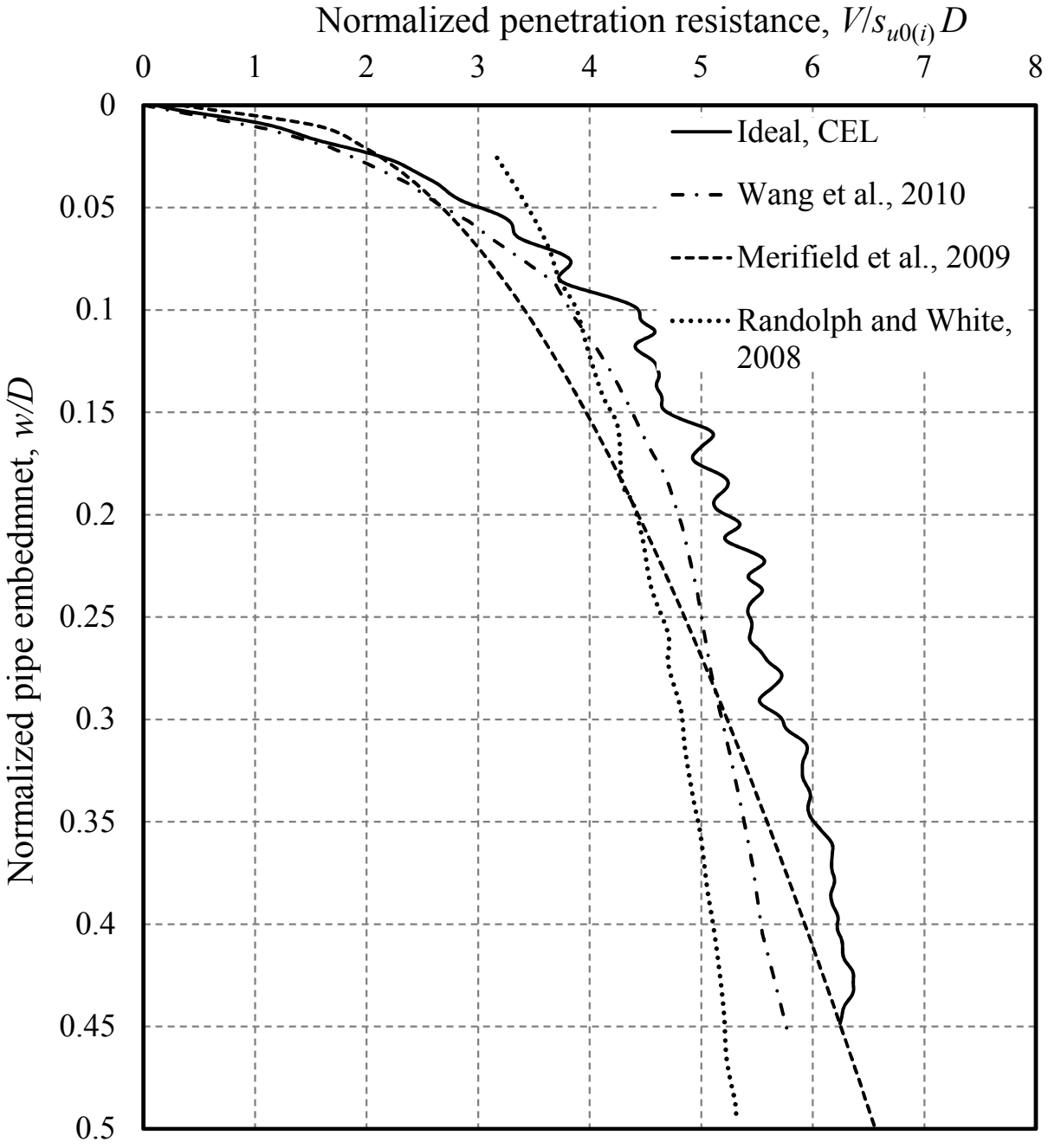

Fig. **3**.**7**. (**b**) Penetration resistance of rough pipe in ideal soil (no softening or rate effect)

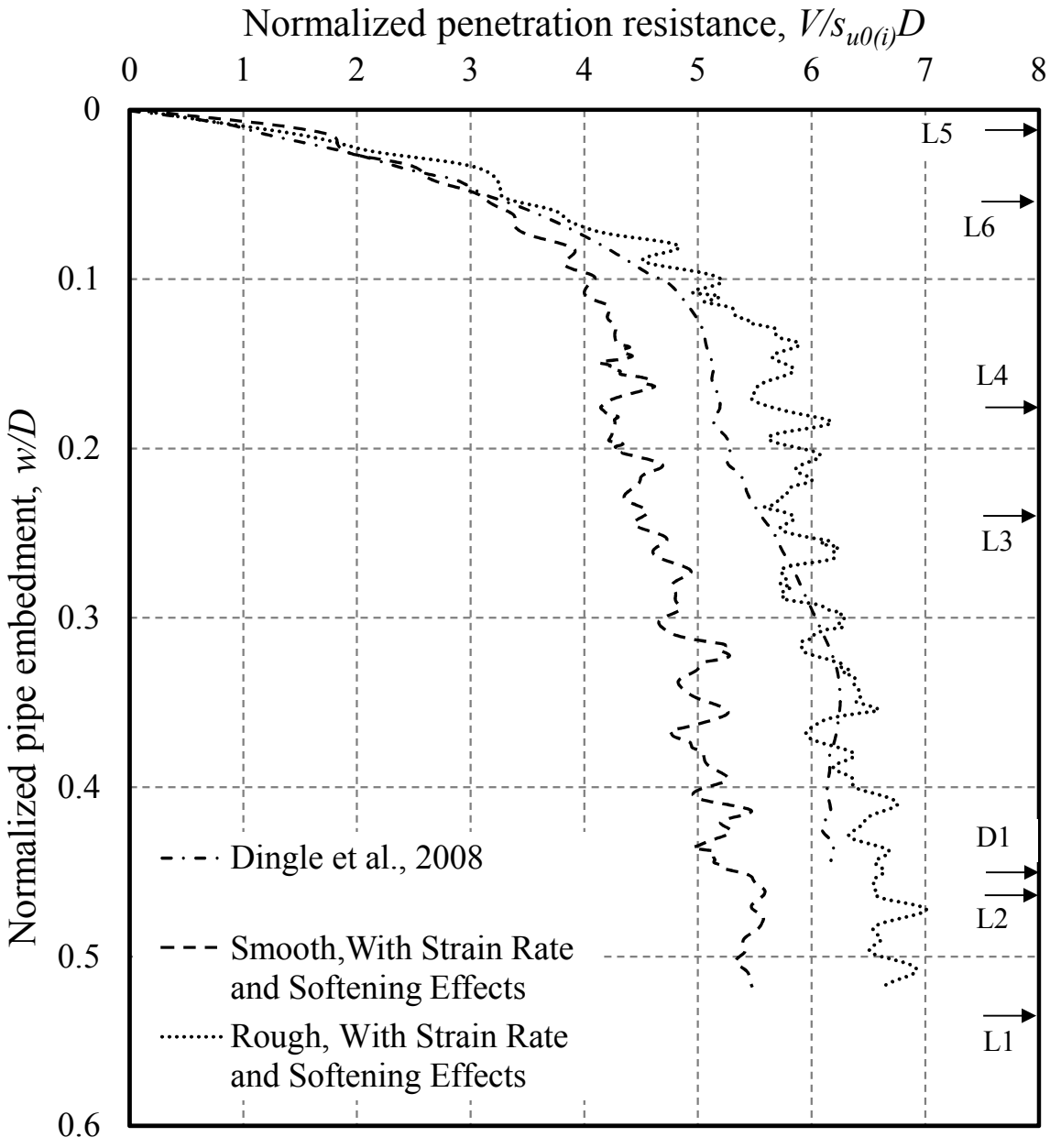

Fig. **3**.**8**. Comparison of penetration resistance from FE analysis and centrifuge test

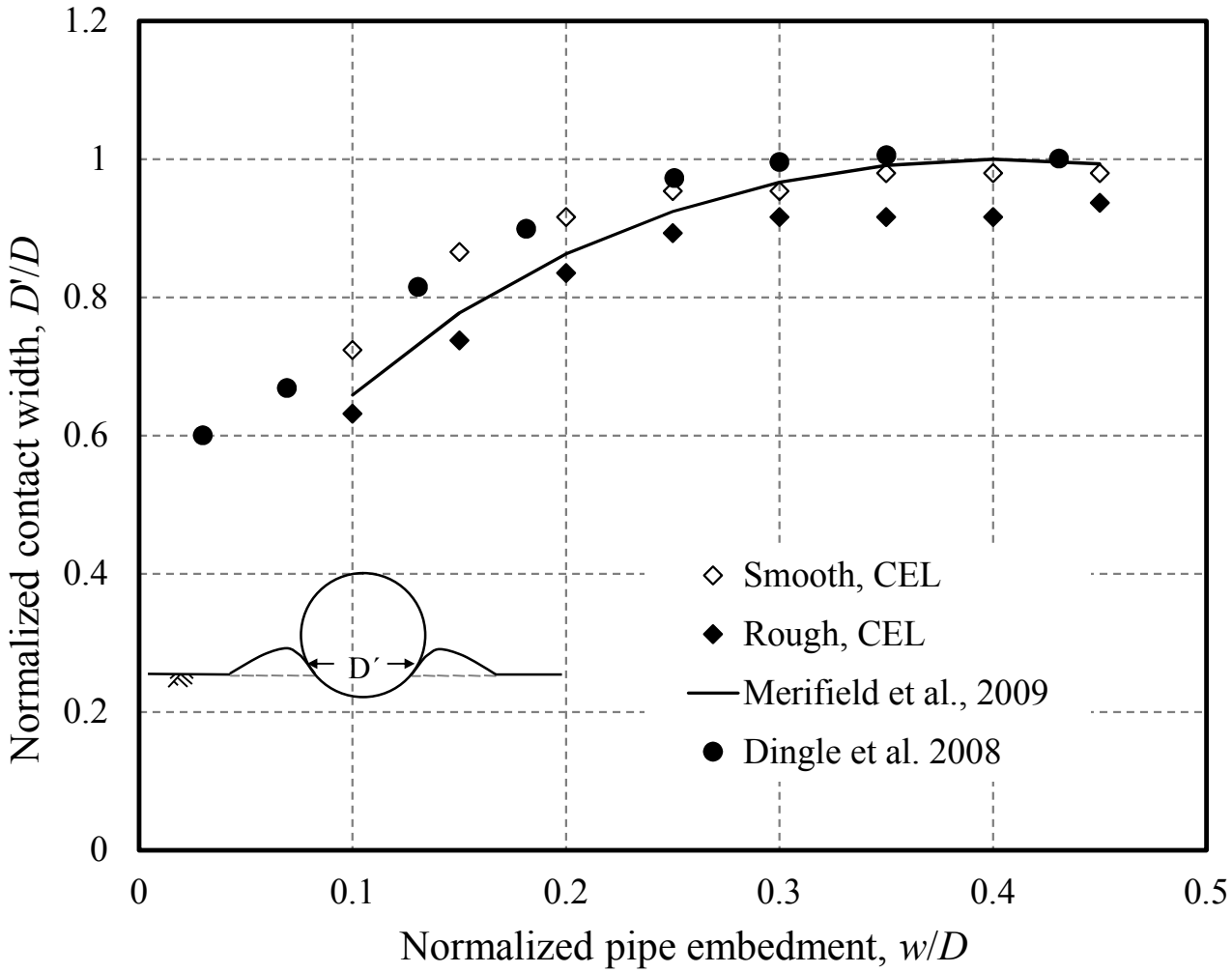

Fig. **3**.**9**. Comparison of pipe contact width

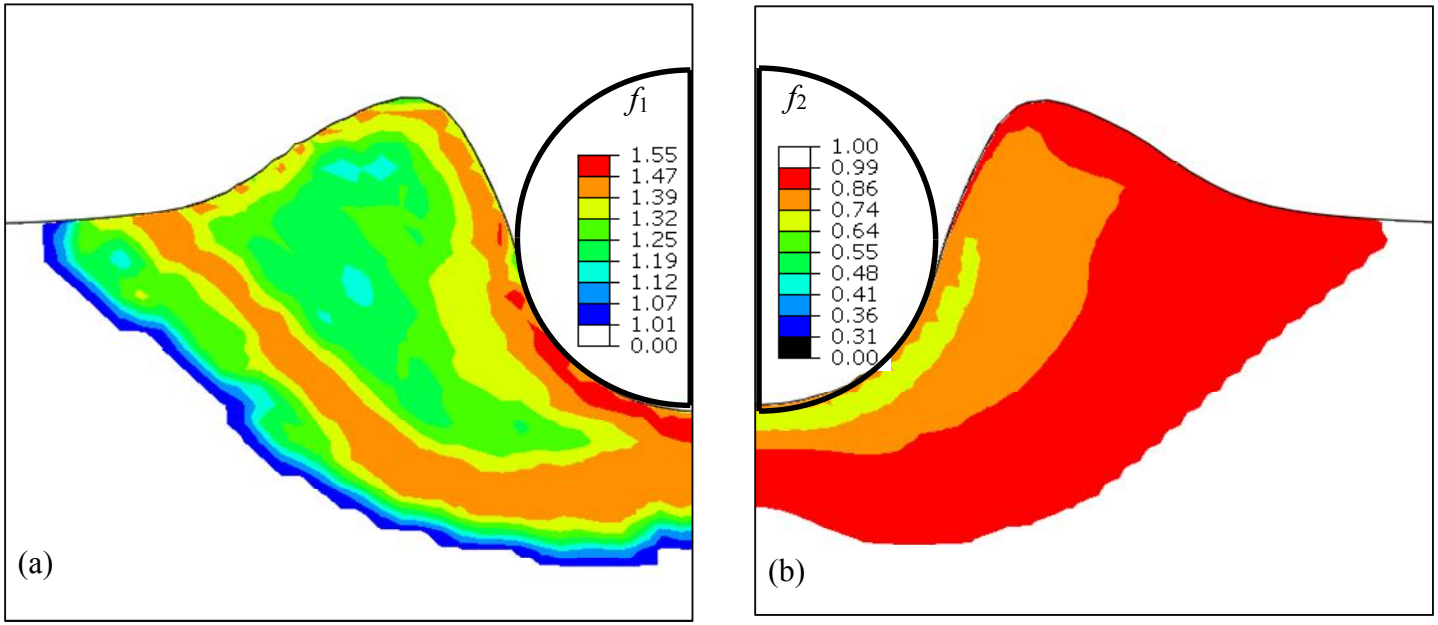

Fig. **3**.**10**. (a) Strain rate effects (b) Strain softening effects (Case-L1, smooth pipe).

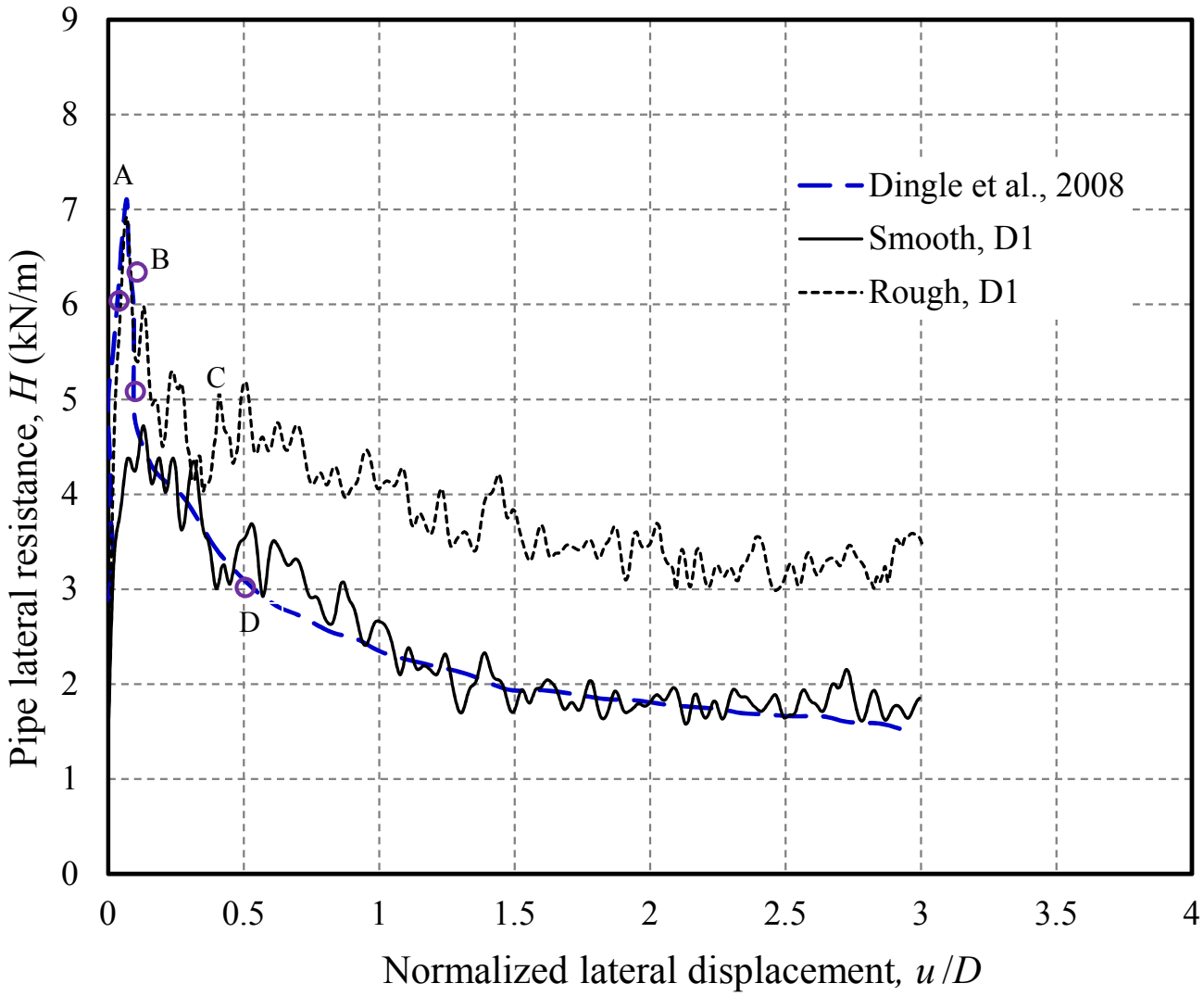

Fig. **3**.**11**. (a) Comparison of lateral resistance (case-D1)

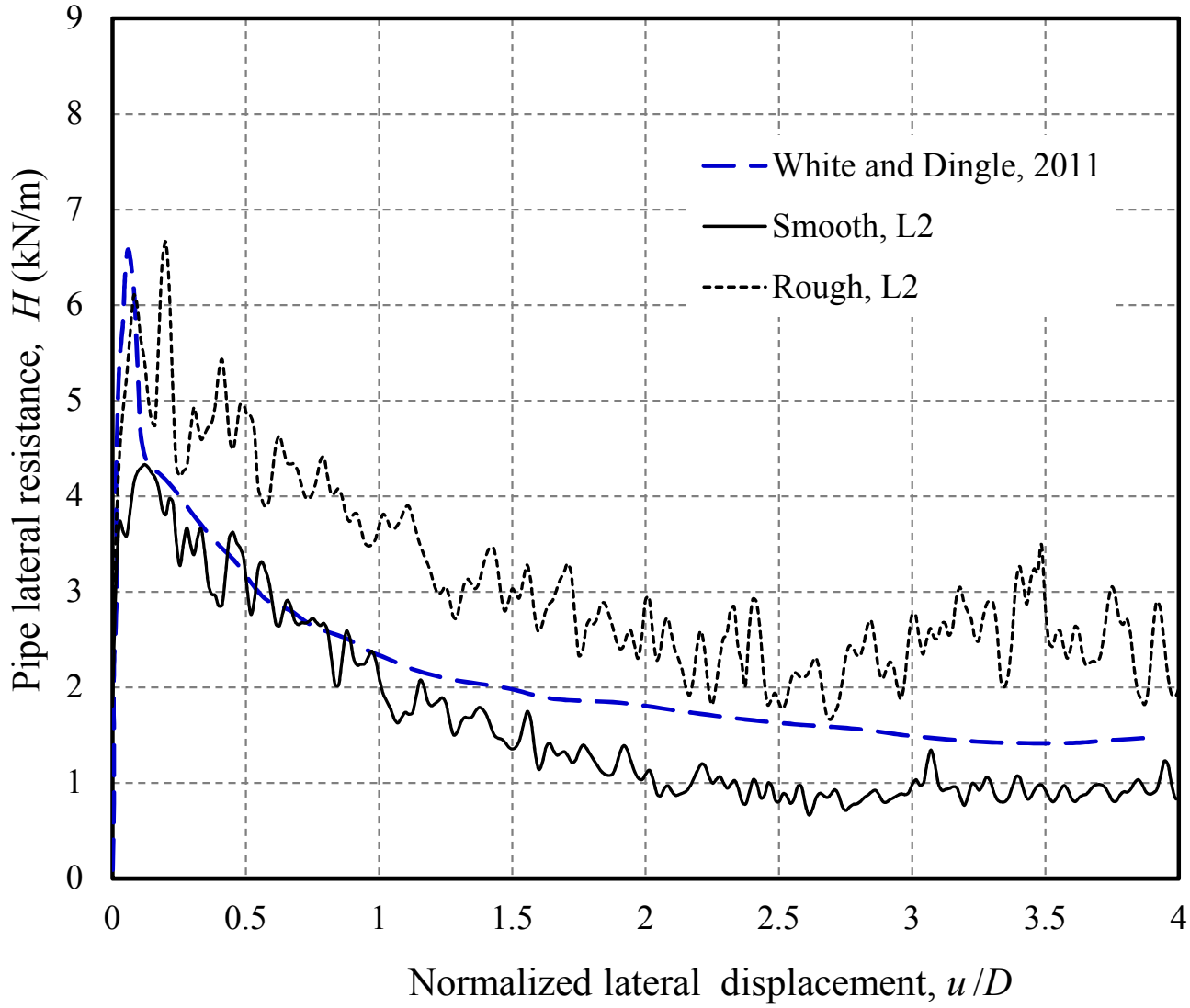

Fig. **3**.**11**. (b) Comparison of lateral resistance (case-L2)

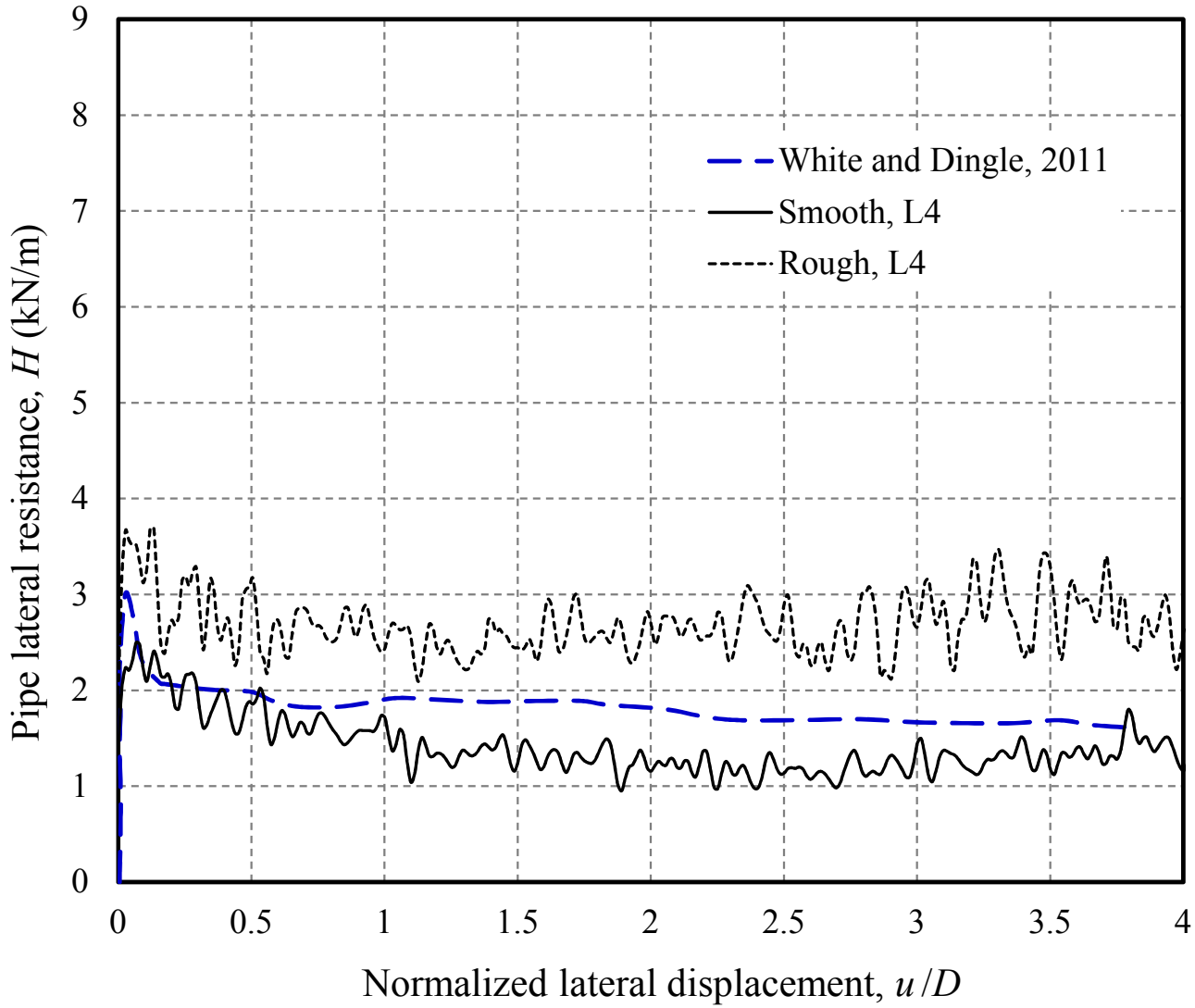

Fig. **3**.**11**. (c) Comparison of lateral resistance (case-L4)

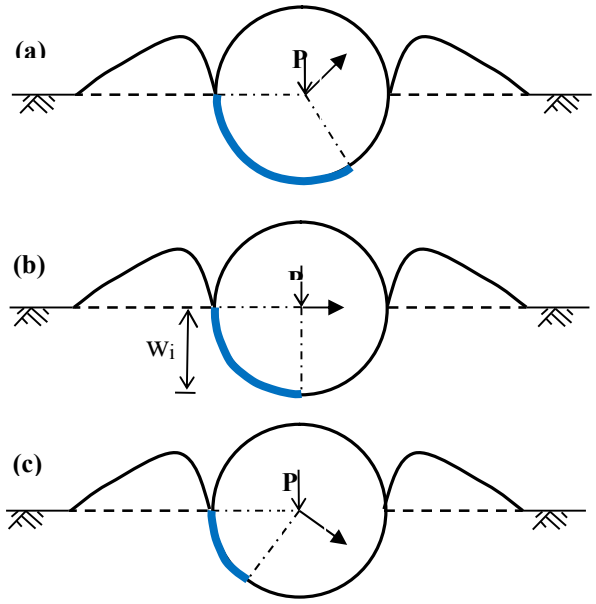

Fig. **3**.**12**.Variation of pipe rear end surface area with travel direction at breakout event (a) upward (b) horizontal (c) downward.

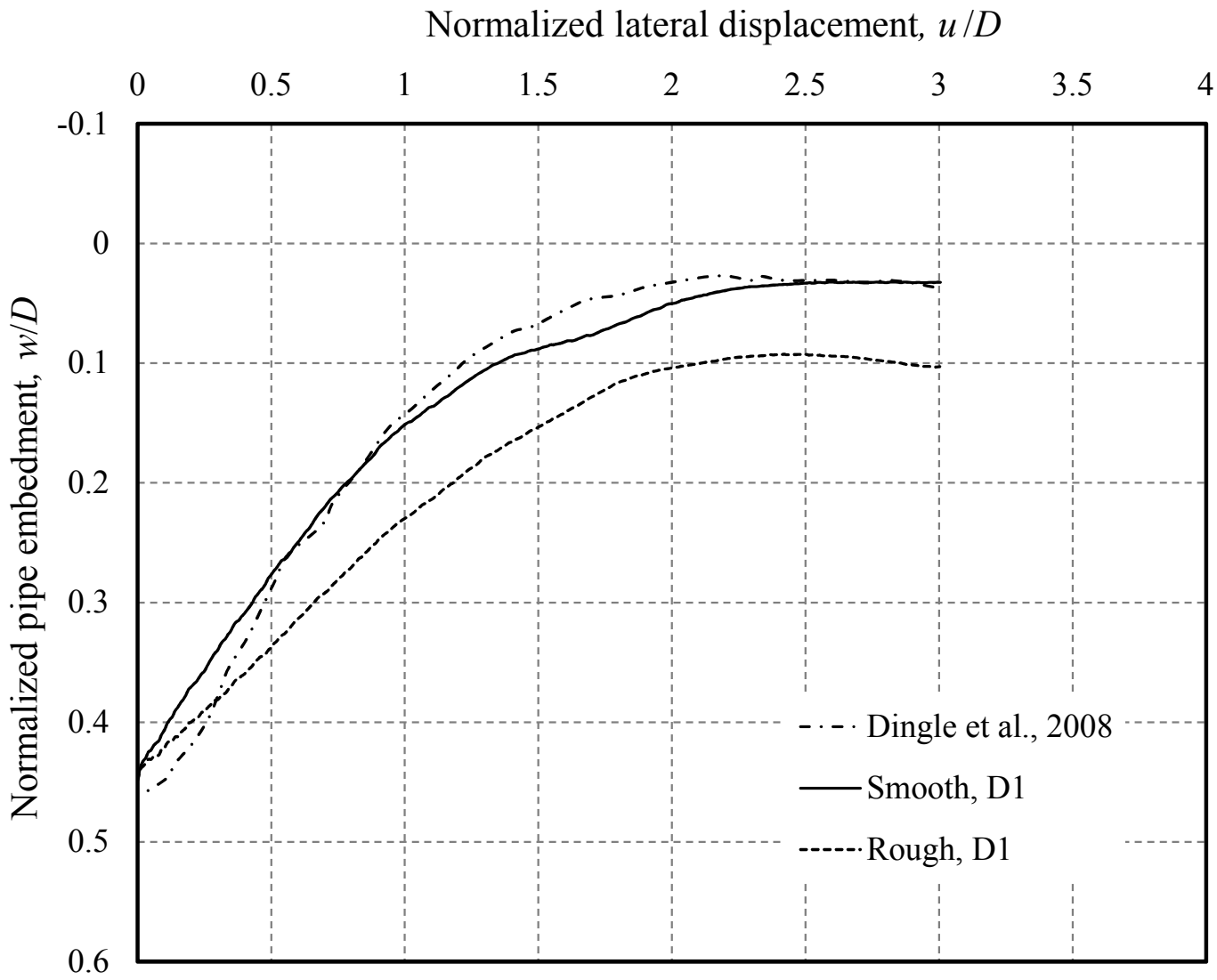

Fig. **3**.**13**. (**a**) Pipe trajectory during lateral displacement (case- D1)

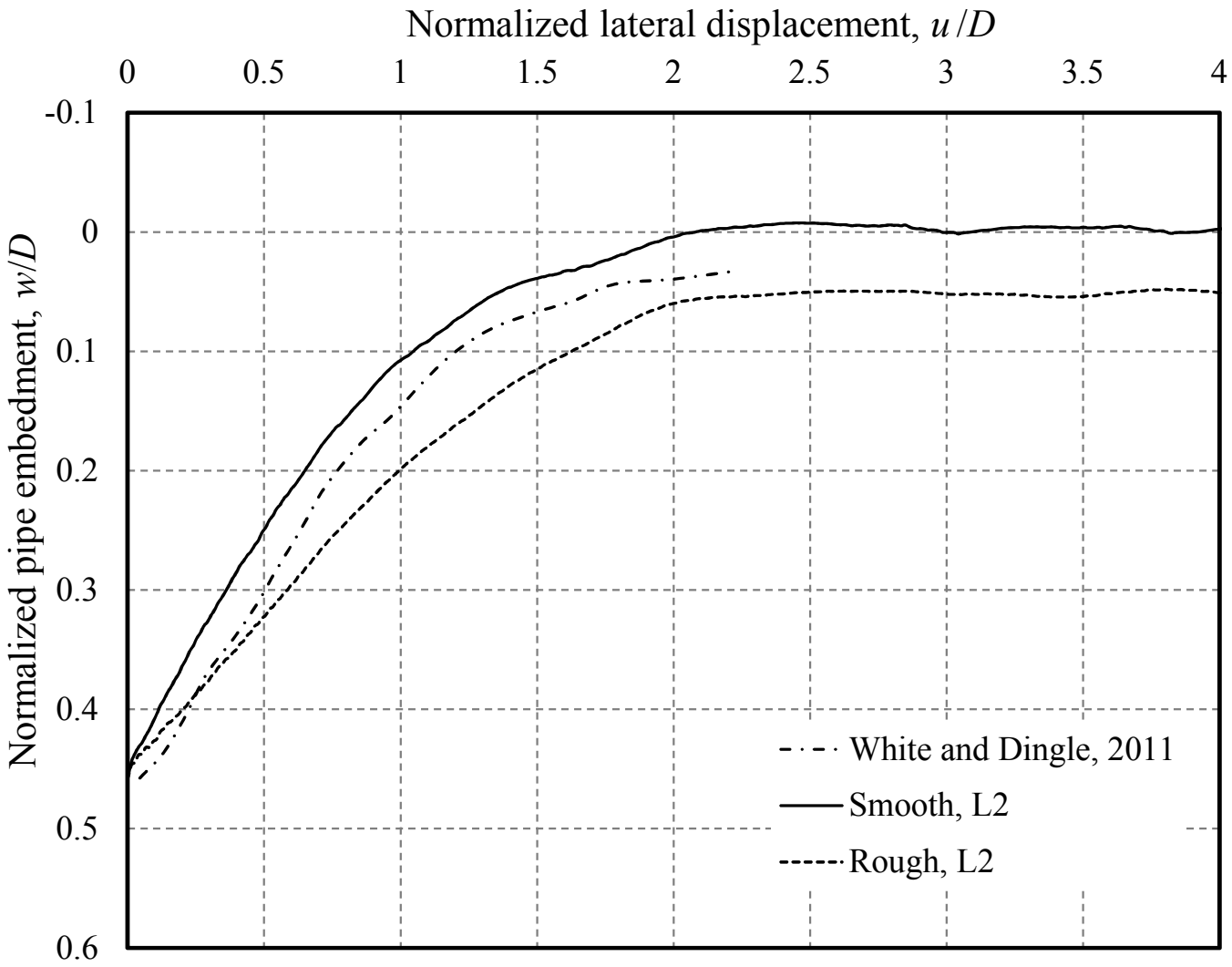

Fig. **3**.**13**. (**b**) Pipe trajectory during lateral displacement (case- L2)

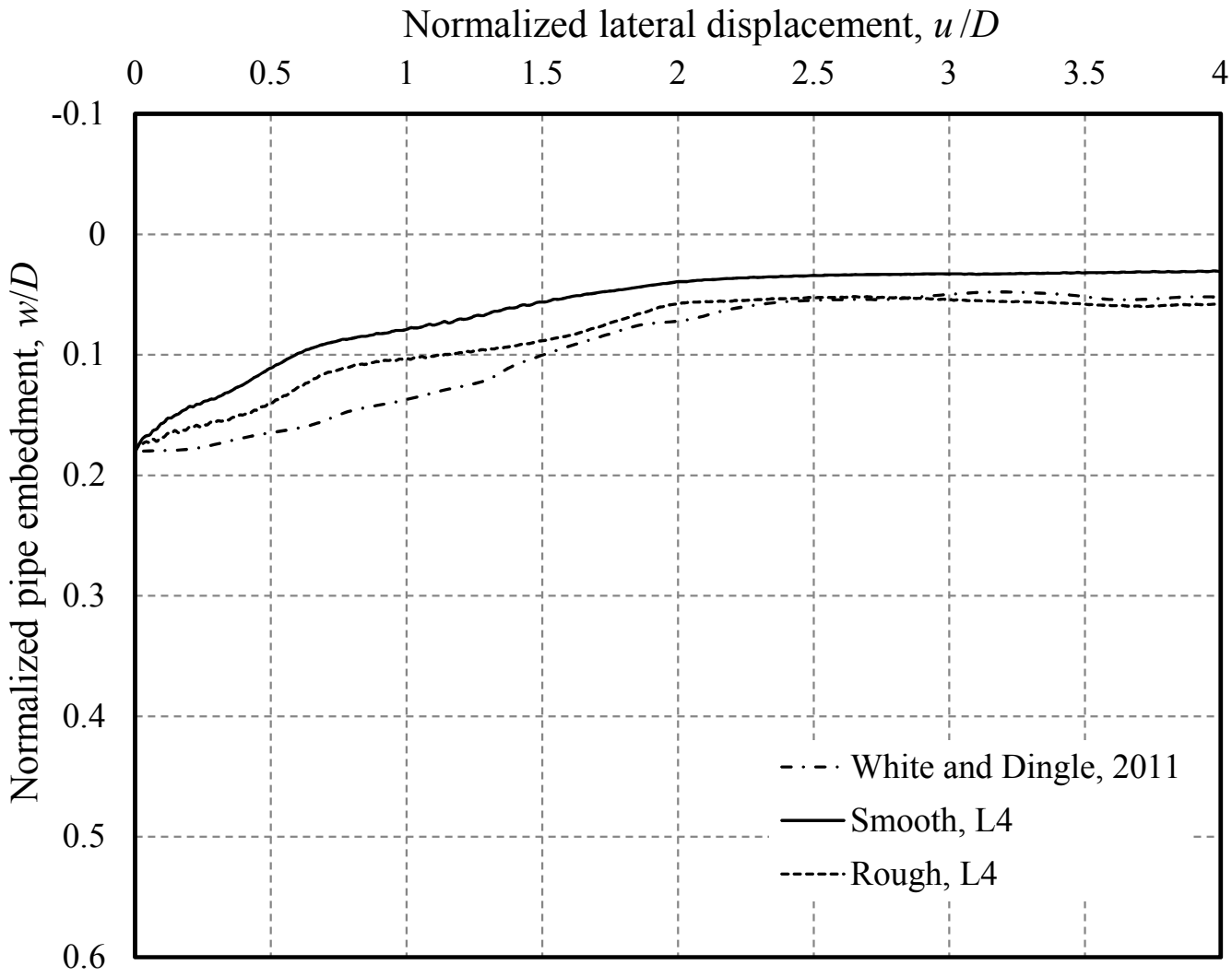

Fig. **3**.**13**. (**c**) Pipe trajectory during lateral displacement (case- L4)

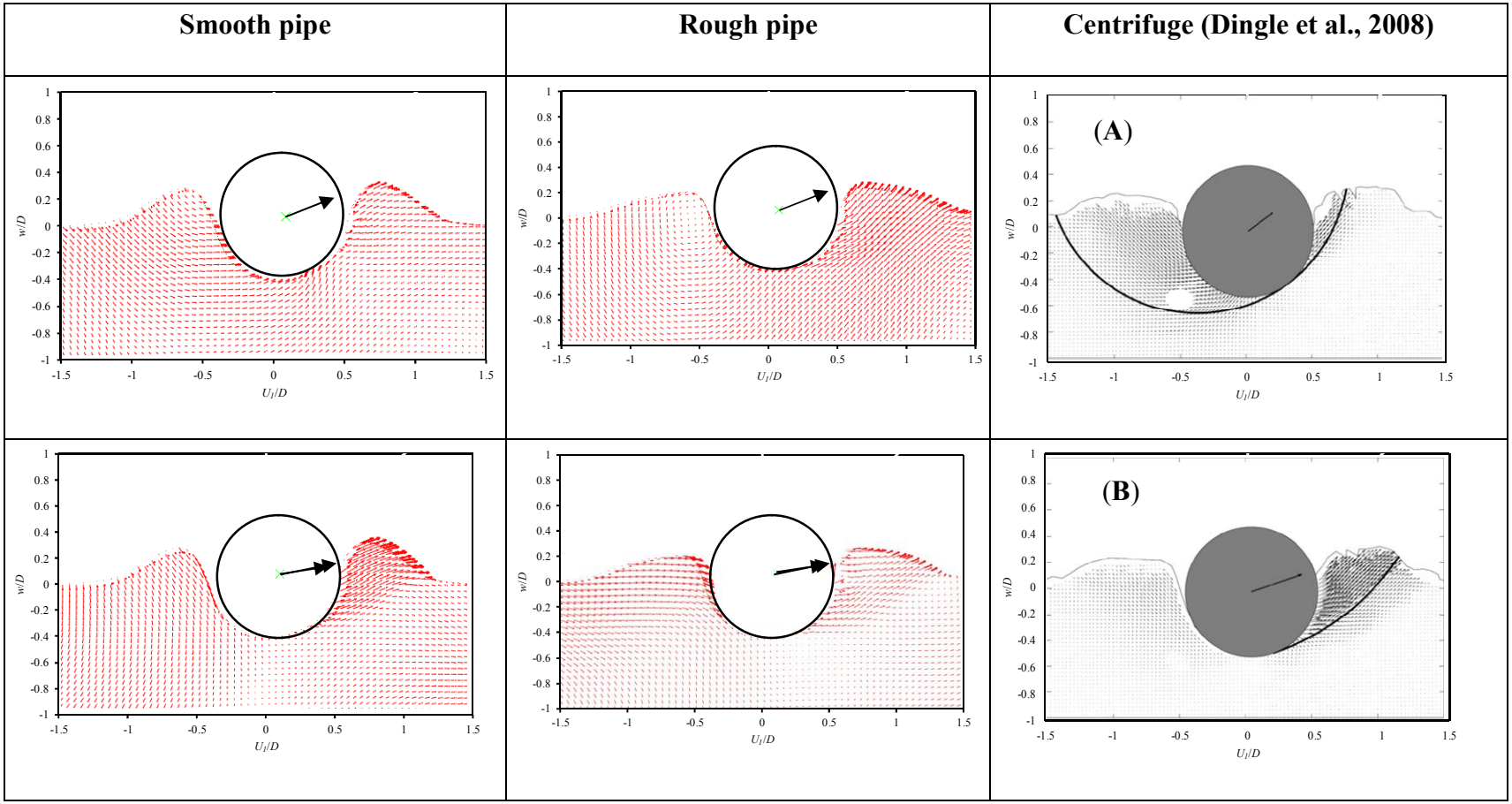

Fig. **3**.**14**. (a) Predicted and observed velocity vectors at pipe lateral displacement of 0.04*D* (location A) and 0.1*D* (location B)

Smooth pipe	Rough pipe	Centrifuge (Dingle et al., 2008)
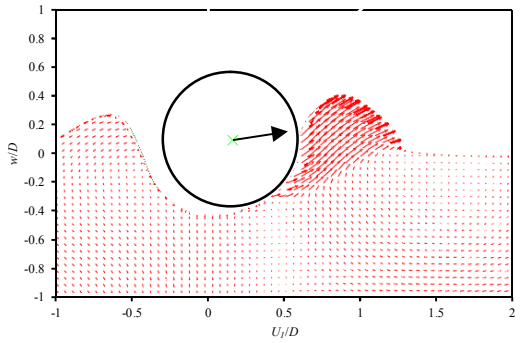	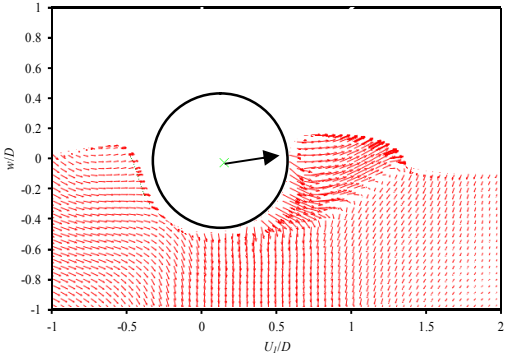	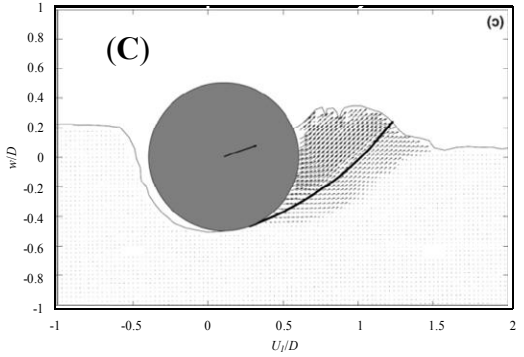
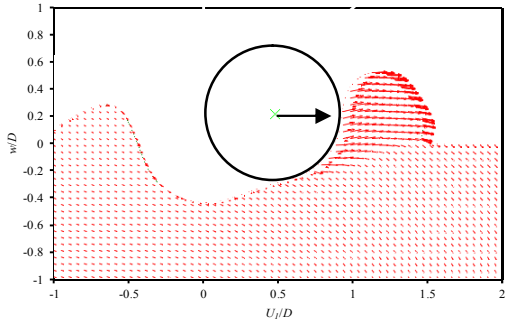	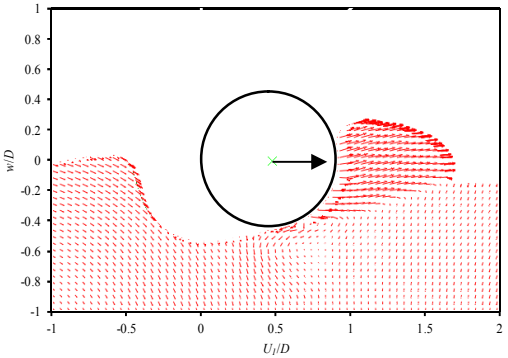	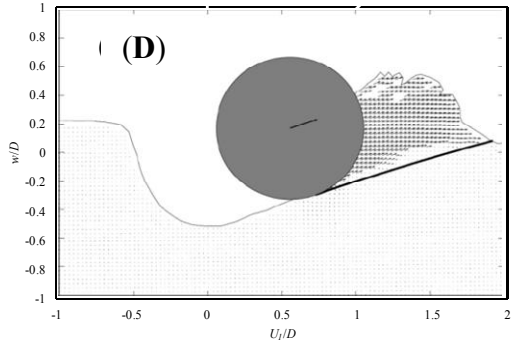

Fig. **3**.**14**. (**b**) Predicted and observed velocity vectors at pipe lateral displacement of 0.15*D* (location C) and 0.53*D* (location D)

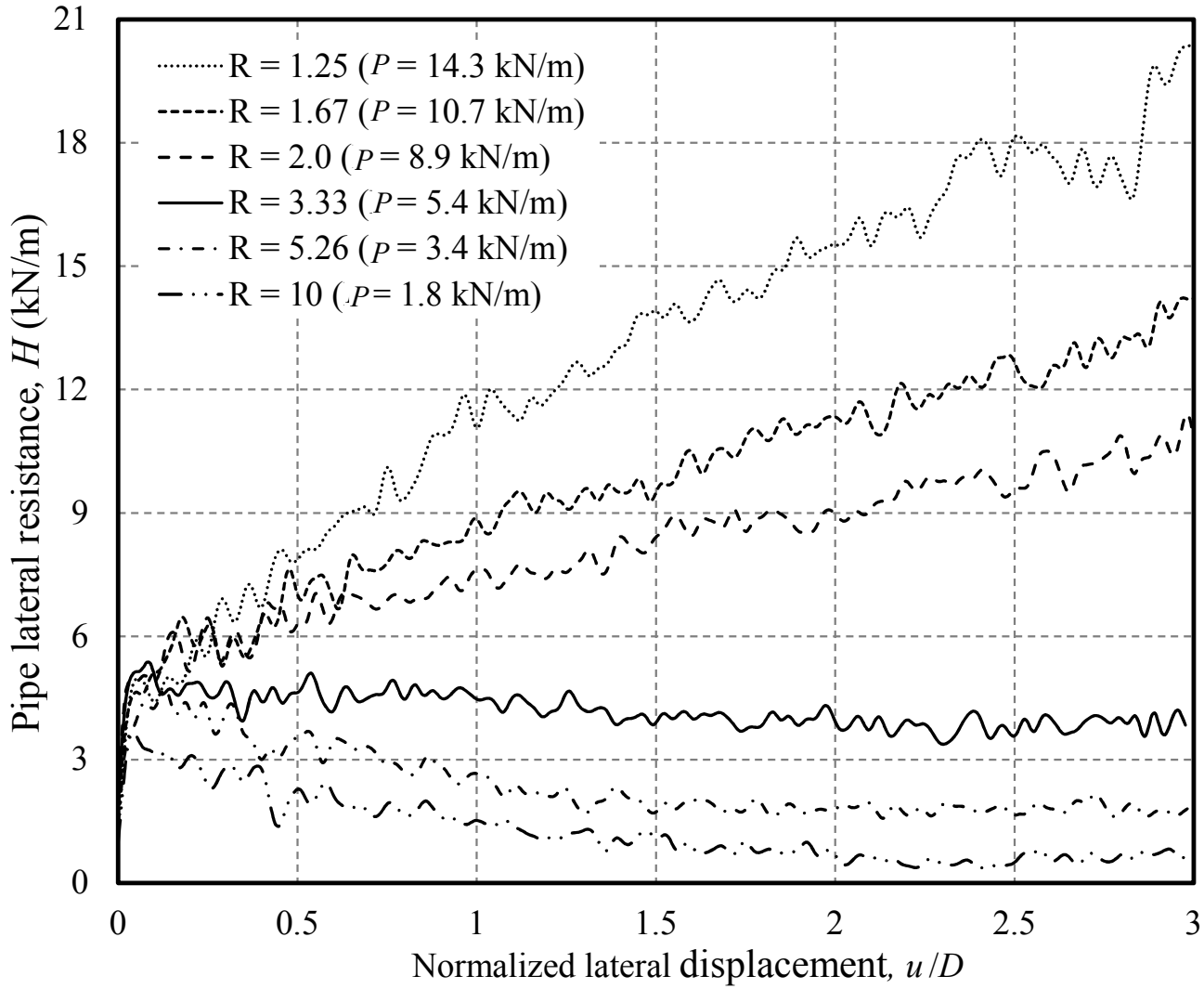

Fig. **3**.**15**. (a) Lateral resistance for different applied load on pipe (smooth pipe/soil interface)

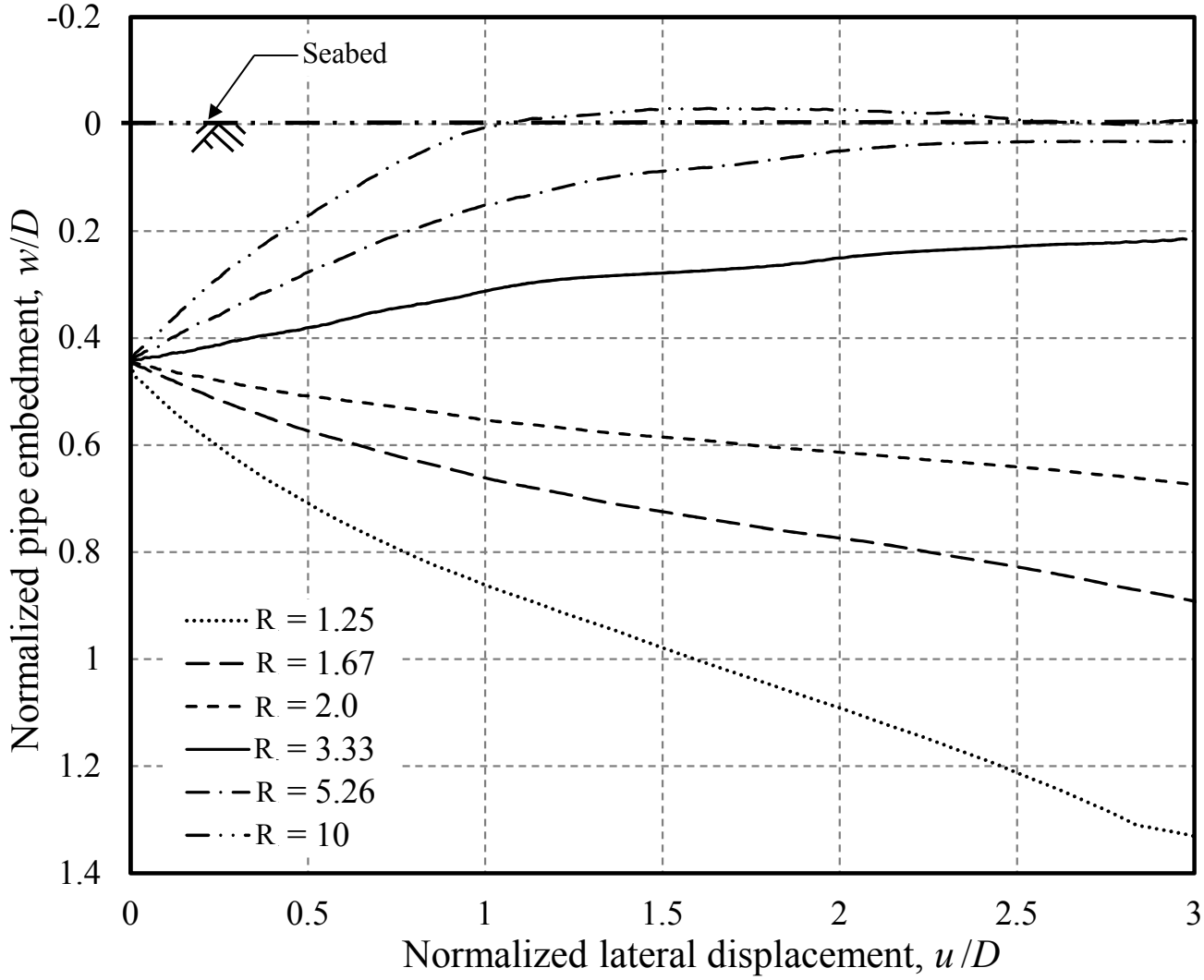

Fig. **3**.**15**. (**b**) Pipe invert trajectory during lateral movement (smooth pipe/soil interface)

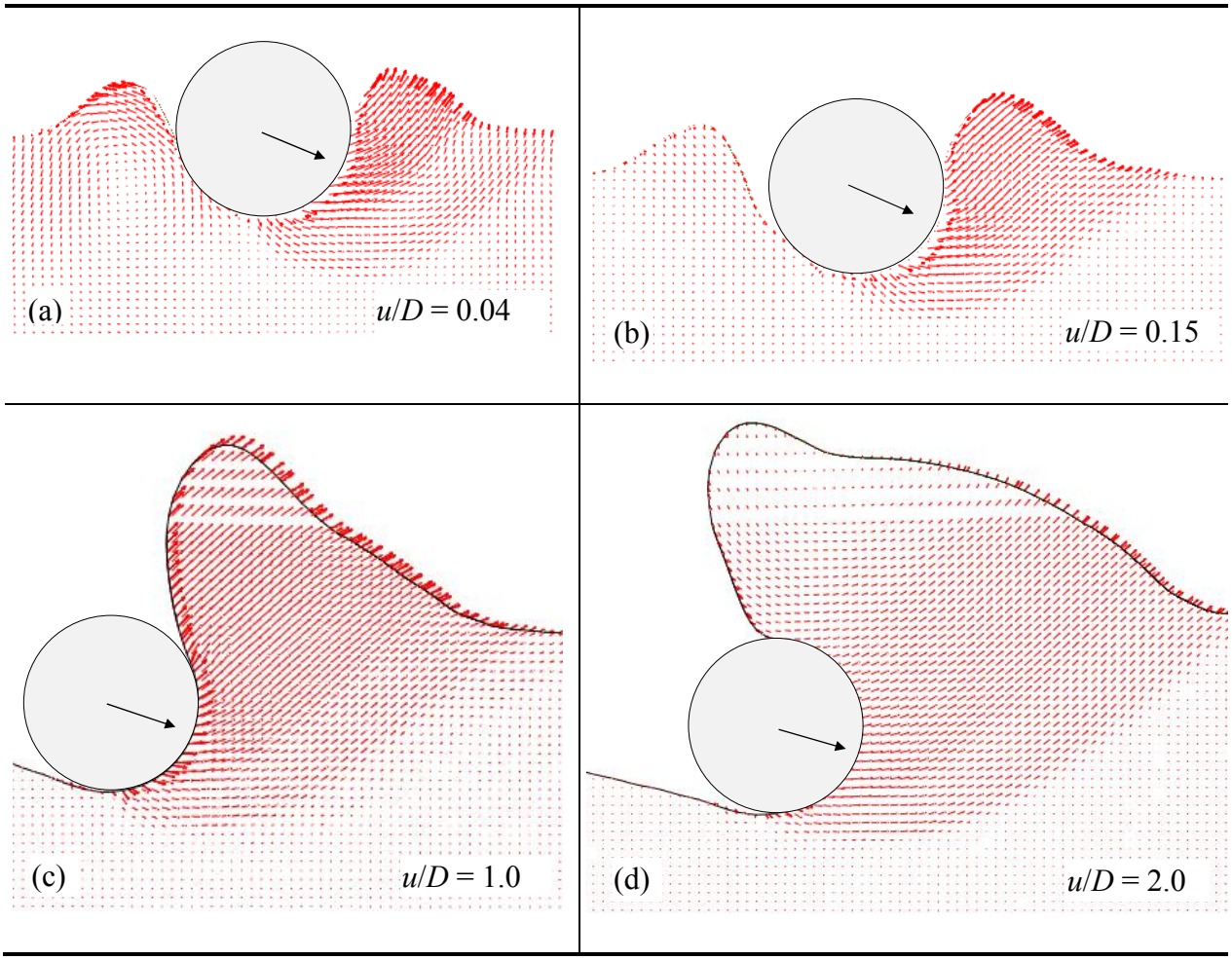

Fig. **3**.**16**. Soil velocity field around heavy pipes during lateral movement (*R*= 1.25).

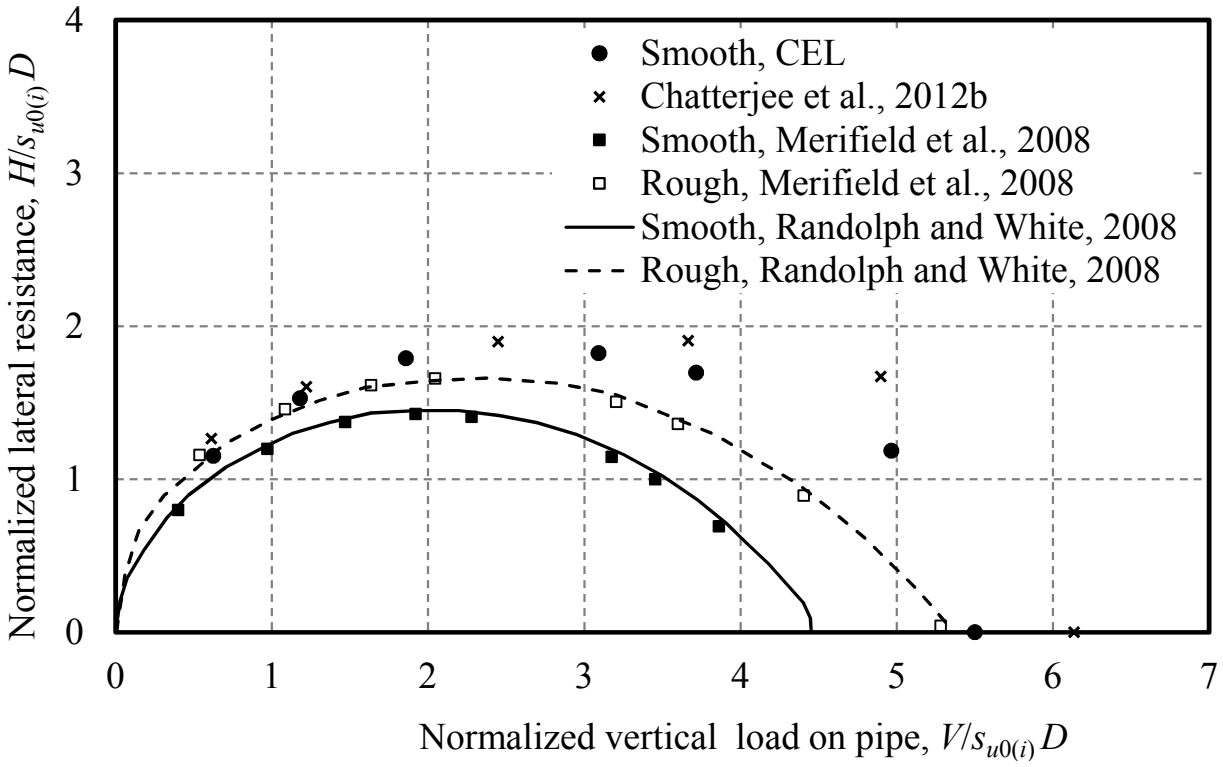

Fig. **3**.**17**. (a) Yield envelopes for w_{int}= 0.45D

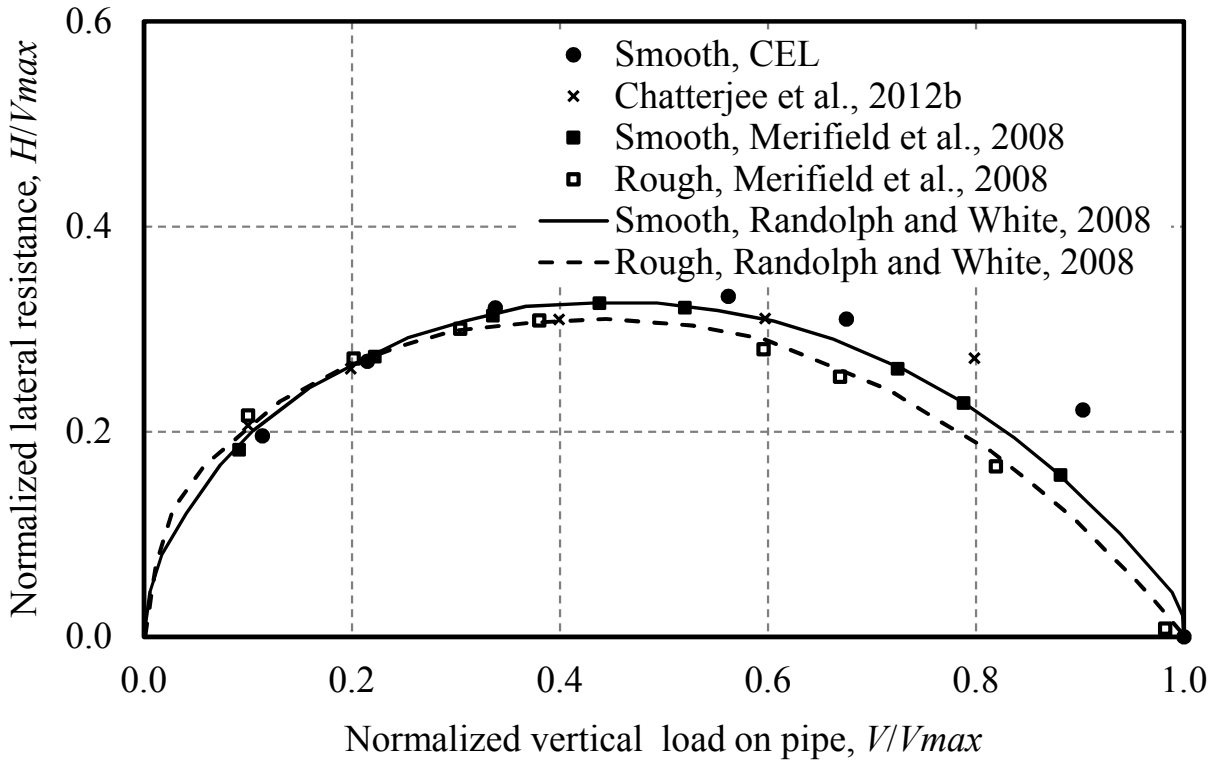

Fig. **3**.**17**. (b) Yield envelopes normalized by$V_{\max}$ for w_{int}= 0.45D

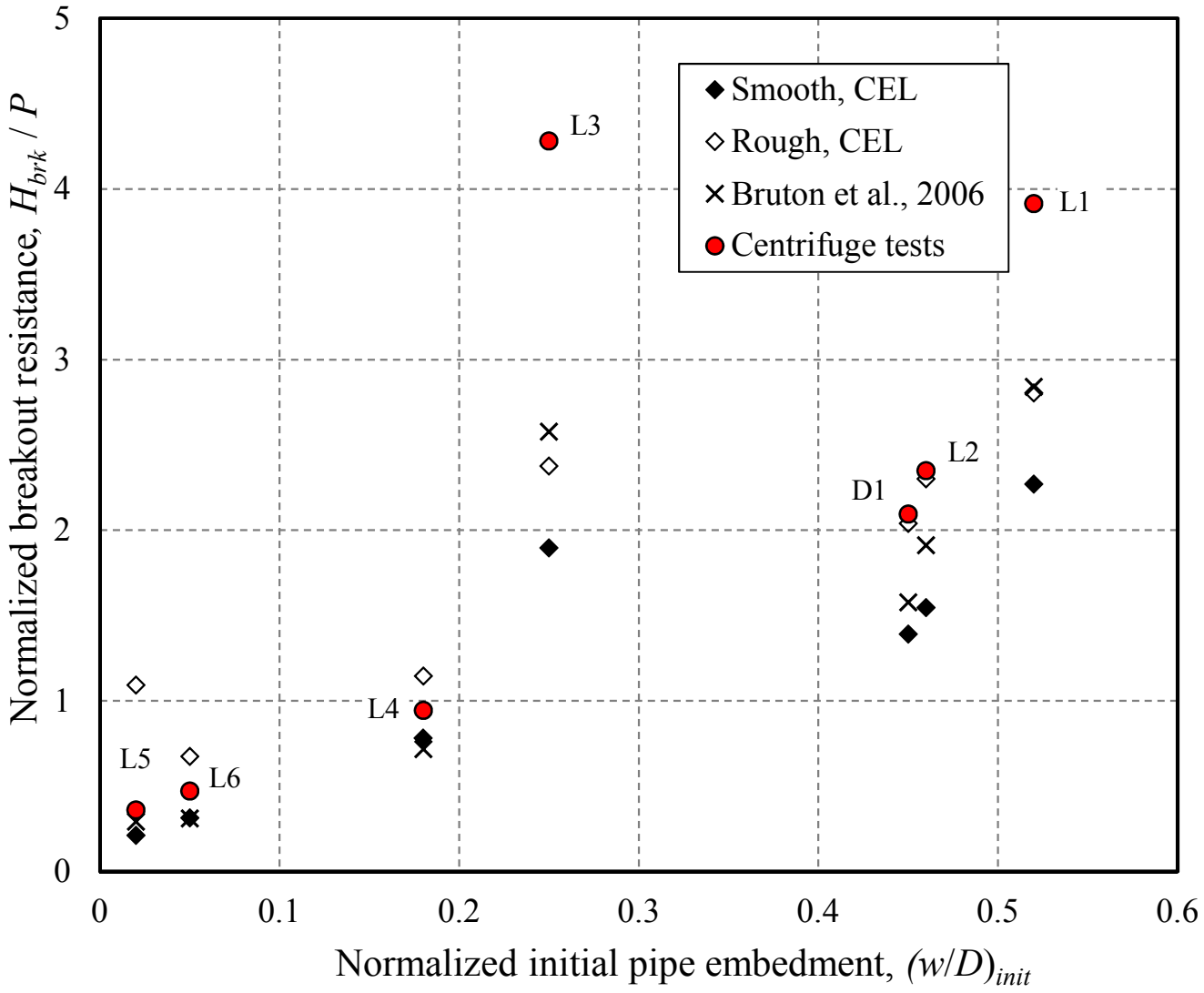

Fig. **3**.**18**. Comparison of breakout resistance with pipe initial embedment

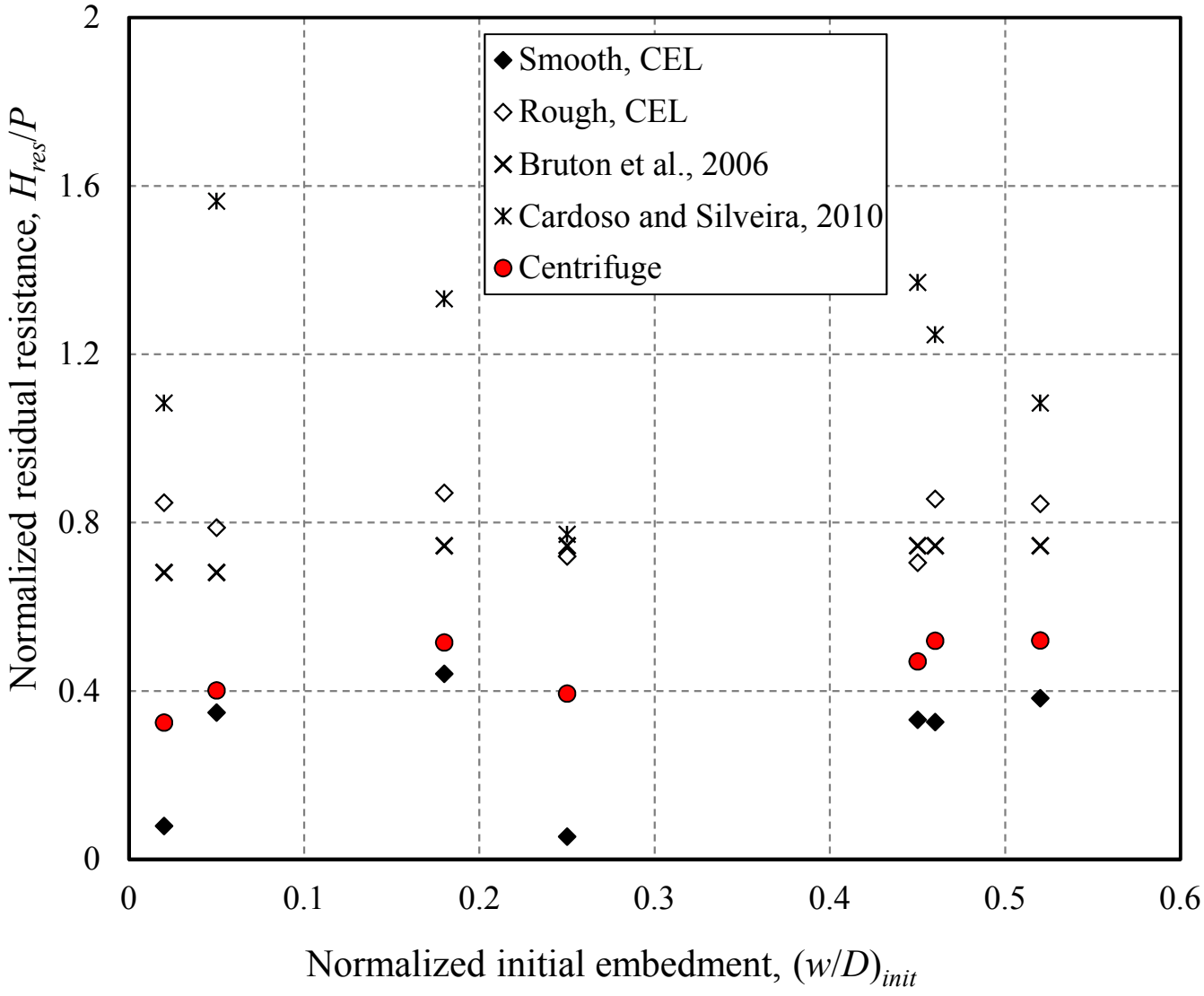

Fig. **3**.**19**.Comparison of residual resistance with pipe initial embedment

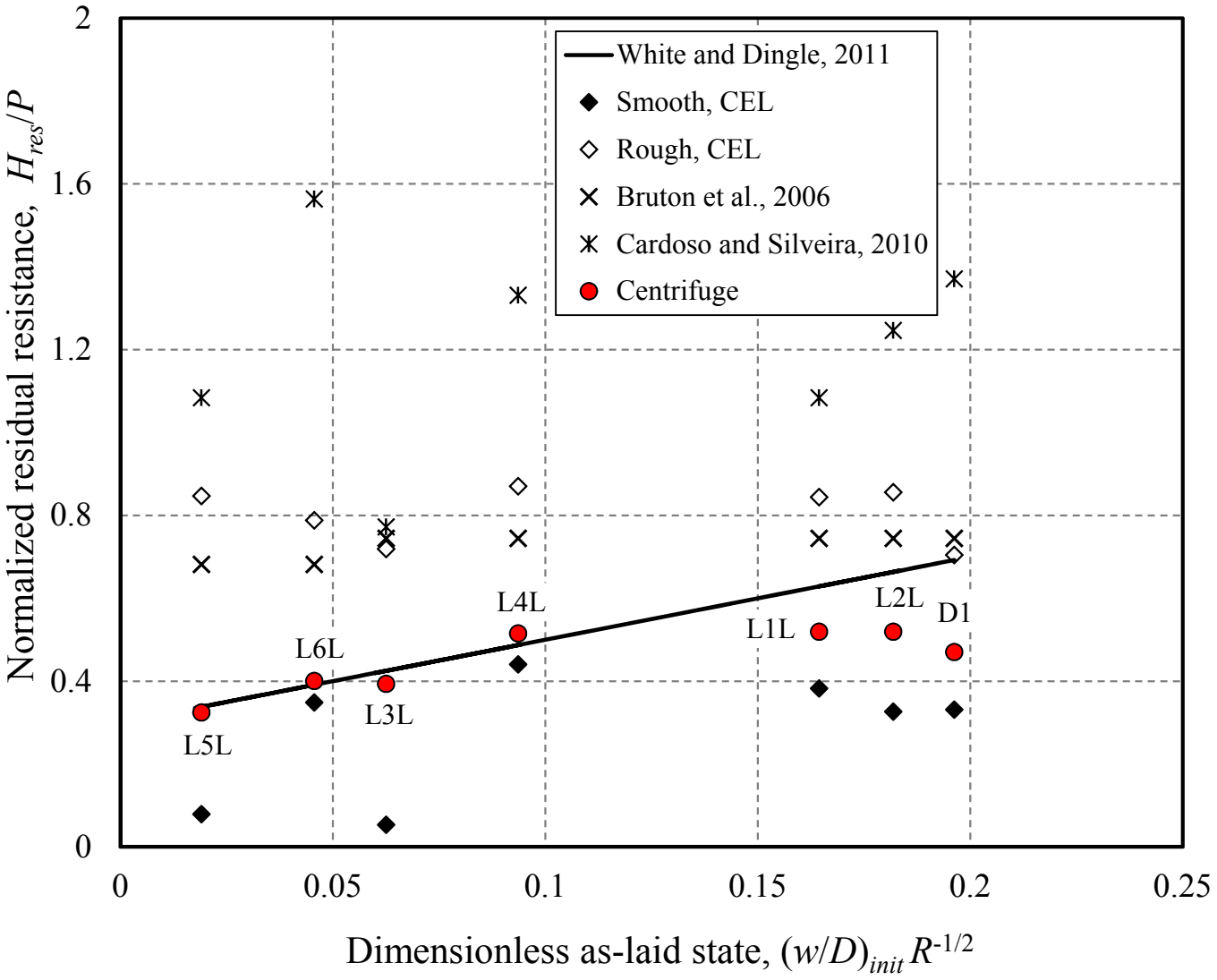

Fig. **3**.**20**. Comparison of normalized lateral residual resistance

Table 3.1. Development of numerical modeling techniques

Numerical Technique	Soil model (s_u)	References
Small strain FE analysis using ABAQUS	von-Mises, uniform , linearly increasing with depth	*,1Aubeny et al.(2005)
	Tresca, uniform	*,1Bransby et al.(2008); †,1Merifield et al.(2008)
	Linear Drucker- Prager (D-P) elasto-plasticity model, uniform	*,1 Zhao et al.(2010)
FE analysis using OxLim	Tresca, uniform, linearly increasing with depth	†,1 Martin and White (2012)
Finite difference technique using FLAC 6.0	Tresca, linearly increasing with depth	*,1 Morrow and Bransby (2010)
Large strain analysis using nonlinear geometry option in ABAQUS	Tresca, uniform	*,2Bransby et al.(2008)
Arbitrary Eulerian Lagrangian (ALE) using ABAQUS	Tresca, uniform	†,2Merifield et al.(2009)
Large deformation FE analysis using RITSS technique	Tresca, uniform , linearly increasing with depth	*,2Barbosa-Cruz and Randolph (2005)
	Tresca, linearly increasing with depth, strain softening and rate effects.	†,2Wang et al. (2010); *,2Chatterjee et al. (2012a); 2 Chatterjee et al. (2012b)
Coupled Eulerian Lagrangian technique using ABAQUS	Tresca, uniform	*,2Tho et al.(2012)
	von-Mises, linearly increasing with depth	*,2 Shi et al. (2011)
	von-Mises, linearly increasing with depth, strain softening and rate effects	*,2Dutta et al. (2012 a, b); †,2Dutta et al. (2012 c); Dutta (2013)

* Analyses performed only for vertical penetration
†Analyses performed for both vertical and lateral movement
1 Wished in place (WIP)
2 Pushed in place (PIP)

Table 3.2. Geometry and soil properties used in finite element analysis

Pipe	
Pipe diameter, D	800 mm
Soil (Clay)	
Undrained modulus of elasticity, E_u	$500s_u$
Poisson's ratio, ν_u	0.495
Submerged unit weight of soil, γ'	6.5 kN/m^3
Rate of shear strength increase, μ	0.1
Reference shear strain rate , $\dot{\gamma}_{ref}$	3×10^{-6} /s
Remoulded soil sensitivity, S_t	3.2
Accumulate absolute plastic shear strain for 95% degradation of soil strength, ξ_{95}	10

Table 3.3. FE simulation for mesh sensitivity, and softening and rate parameters effects

Soil strength	Series name	Simulation name	Softening f_2 (Eq. 1)	Rate f_1 (Eq. 1)
Uniform s_u	U00	U00-10, U00-20, U00-30, U00-40	No	No
	US0	US0-10, US0-20, US0-30, US0-40	Yes	No
	U0R	U0R-10, U0R-20, U0R-30, U0R-40	No	Yes
	USR	USR-10, USR-20, USR-30, USR-40	Yes	Yes
Linearly varying s_u	L00	L00-10, L00-20, L00-30, L00-40	No	No
	LS0	LS0-10, LS0-20, LS0-30, LS0-40	Yes	No
	L0R	L0R-10, L0R-20, L0R-30, L0R-40	No	Yes
	LSR	LSR-10, LSR-20, LSR-30, LSR-40	Yes	Yes

Example: In U0R-20 uniform s_u, no softening but rate effects are considered, and analysis is performed with 20 mm mesh.

Table 3.4. Centrifuge test conditions (White and Dingle, 2011; Dingle et al., 2008)

Test	Initial undrained shear strength of soil, kPa	Applied vertical load, kN/m	Initial embedment, $(w/D)_{int}$
D1	2.3+3.6×z	3.4	0.45
L1	2.3+3.6×z	2.1	0.52
L2	2.3+3.6×z	2.8	0.46
L3	2.3+3.6×z	1.0	0.25
L4	2.3+3.6×z	3.2	0.18
L5	3.0+5.0×z	2.1	0.02
L6	3.0+5.0×z	4.4	0.05

Note:

D1: Test conducted by Dingle et al., (2008)

L1 to L6: Tests conducted by White and Dingle (2011)

z: in metre

CHAPTER 4

Penetration of Steel Catenary Riser in Soft Clay Seabed: Finite-Element and Finite-Volume Methods

Co-Authorship: This chapter has been published in the ASCE International Journal of Geomechanics as: Hawlader, B., Dutta, S., Fouzder, A. and Zakeri, A. (2016) "Penetration of Steel Catenary Riser in Soft Clay Seabed: Finite Element and Finite Volume Methods." Most of the numerical investigations presented in this chapter have been conducted by the second author. He also prepared the draft figures and draft manuscript under close supervision of the first author. The other two authors have been involved in development of preliminary numerical models and review of the manuscript.

4.1 Abstract

The penetration of steel catenary riser and other cylindrical objects, such as offshore pipelines or T-bar penetrometers, in soft clay seabed is of practical importance in deepwater oil and gas development. Finite element (FE) analyses of these large-deformation problems are computationally very expensive. Water can also play a significant role through development of suction behind the riser. The main objective of the present study is to develop an advanced numerical modeling technique to simulate riser−seabed−water interaction near the touchdown zone (TDZ). Keeping in mind two critical issues, namely the computational cost and modeling of suction, two different numerical modeling techniques are developed. In the first one, the computational fluid dynamics (CFD) approach is used. The CFD modeling is performed using

ANSYS CFX 13.0 software. Among the three different types of CFX models developed in the present study, the subdomain modeling techniques is found to be more efficient. In the second numerical modeling technique, large-deformation FE analyses are performed using the Coupled Eulerian−Lagrangian (CEL) approach in *Abaqus* FE software. The comparison of results of CFX and CEL shows that CFX can successfully simulate the penetration of riser or pipeline in soft clay seabed. The main advantages of the present CFX modeling over CEL modeling are (1) the CFX can simulate suctions, and (2) the CFX modeling with a subdomain is computationally very efficient. The analyses compared in this study show that CFX simulations are computationally 10−15 times faster than CEL simulations.

Keywords: Finite-element method; Finite-volume method; Soft clay; Steel catenary riser; Penetration; Large deformation.

4.2 Introduction

Steel Catenary Risers (SCRs) are frequently used in offshore to connect floating production facilities to seabed well systems. Typically the diameter of SCR varies between 150 and 600 mm (Hu et al. 2011). The surface waves and current could cause vertical motion of the riser of several diameters near the touchdown point (TDP), which could be even higher in storm events. Proper modeling of cyclic motion of the riser near the TDP and its interaction with the seabed and water is very important in the design, because the region near the TDP is a fatigue hotspot. The fatigue life of a steel catenary riser depends on seabed properties at the touchdown zone (TDZ) as well as motion characteristics. In the current industry practice, the seabed response is idealized using linear/nonlinear soil springs or rigid surfaces. Empirical equations

have been proposed in the past to model the seabed taking into account of various complex mechanisms, including trench configuration, nonlinearity of soil stiffness, degradation of soil shear strength, and suction effects (Aubeny et al. 2005;Randolph and Quiggin, 2009). Although these methods attempt to capture the processes involved in riser−seabed−water interaction, significant uncertainties still remain in modeling of this intrinsically complex problem. Moreover, the uncertainties from other sources such as vortex-induced vibration could further complicate the process. Because of these uncertainties, the design codes (e.g. DNV 2010) recommend design fatigue factor of 6.0 and 10 for critical components. The design fatigue factor has no actual theoretical basis, but has been established from experience to maintain low risk of failure (Li and Low 2012).

The current research program, consists of both physical and numerical modeling, has an objective to investigate riser–seabed–water interaction mechanisms. The physical modeling was performed using the geotechnical centrifuge at C-CORE and the results have been published in previous papers (Elliott et al. 2013a&b, 2014).The main objective of the present study is to develop an advanced computationally efficient numerical tool to simulate the penetration behaviour of a section of riser. Similar to other researchers (e.g. Barbosa-Cruz and Randolph 2005), the authors' experience (Dutta et al. 2014, 2013, 2012a,b) is that the FE simulation of this large deformation problem is computationally very expensive. Also, it is recognized that water in the trench could have influence on the response of riser at the TDZ. In this study, the performance of two different numerical approaches is investigated: (1) the computational fluid dynamics (CFD) approach, and (2) a large-deformation FE approach. The paper is organized as follows. First, the three types of CFX modeling techniques developed in CFX-13 (ANSYS, 2010) are presented. In the second part, large deformation FE analyses using the coupled

Eulerian−Lagrangian (CEL) approach available in *Abaqus* 6.10 EF1 FE software are presented. The comparison of results obtained from CFX and CEL modeling is also presented. Finally, a parametric study is performed to show the effects of different input parameters on penetration resistance using the CFX models. The penetration behavior for shallow embedments (less than half a diameter) has been presented in Dutta et al. (2014). In this paper, the discussion is mainly focused on intermediate embedments (2−5 diameters) where transition might occur from shallow to deep failure mechanisms.

4.3 Previous Studies

Large-scale field tests and small-scale laboratory model tests have been performed in the past to understand the complex mechanism of riser−seabed−water interaction. In the Steel Risers in Deepwater Environments Joint Industry Project (STRIDE JIP), full-scale tests were conducted over a period of 3 months at a harbor location in the west of England (Bridge et al. 2003). Large-scale laboratory tests (e.g. Hodder and Byrne 2010; Wang et al. 2014) are also available in the literature. A series of small-scale laboratory tests were conducted under the Catenary Riser–Soil Interaction Model for Global Riser Analysis (CARISIMA) JIP using clay from a site in Onsøy, Norway. Similar tests were conducted in the STRIDE JIP, and it was shown that the results are consistent with CARISIMA test results (Bridge 2005). The STRIDE and CARISIMA test results provide some valuable insight into the riser−seabed−water interaction mechanisms, such as penetration resistance, suction mobilization during uplift, suction plateau, suction release and effect of soil consolidation (Bridge and Willis 2002; Willis and West 2001).

To understand load-displacement mechanisms, Dunlap et al. (1990) conducted a series of small-scale laboratory tests in soft sediment having undrained shear strength (s_{u0}) of 1.0−1.5 kPa

using a 1.52 m×152 mm (length×diameter) model pipe section. Aubeny et al. (2008) investigated the cyclic response by conducting tests in kaolin clay seabed of s_{u0}≈3.7 kPa using a 125 mm×25 mm model pipe section. Langford and Aubeny (2008) conducted tests in a high plastic clay of linearly increasing s_{u0} profile using a rough coated 1,300 mm×174 mm pipe section.

Besides 1-g laboratory tests, centrifuge tests have been conducted in the past. Hu (2010) presented centrifuge modeling of penetration and uplift behavior of riser sections in Malaysia kaolin clay of varying overconsolidation ratios of 1, 3, and 5, where the tests were conducted with 600- and 1,000-mm diameter (D) pipe sections in prototype scale. Whereas some other centrifuge tests (e.g. Dingle et al. 2008) provides penetration behavior of shallowly embedded pipelines, Hu (2010) shows the response for a wider range of embedments (3D). In the above centrifuge tests, only a section of the riser is modeled. However, in the current research program at C-CORE and Memorial University, centrifuge modeling of a full length riser (108 m in prototype) is performed using a novel experimental facility developed at C-CORE supported by offshore industry (Elliott et al. 2013a, b, 2014).

Currently, the riser−seabed interaction in the TDZ is modeled using the P−y curves, where P=force per unit length and y= vertical displacement. On the basis of model test results (e.g. Dunlap et al. 1990; Bridge 2005), Aubeny and Biscontin (2008, 2009) proposed a conceptual P–y curve model. The nonlinear mathematical model proposed by Randolph and Quiggin (2009) is in fact an improved version of Aubeny and Biscontin (2008) model with some additional features. One of the main components of these models is the backbone curve. Based on small strain FE modeling of pipes in "wished-in-place" configuration, Aubeny et al. (2005) proposed an empirical relation for penetration resistance, which has been further modified, incorporating the effects of initial width of the trench, in Aubeny and Biscontin (2009).

4.4 Problem Definition

In CFX modeling, a section of a riser of diameter D is placed in water above the mudline at a distance y_w as shown in Fig. 4.1. The riser is then displaced vertically downward at a velocity v. To eliminate buoyancy effect of water, the weight of the riser is assumed to be equal to the weight of the riser section filled with seawater. During the initial displacement through water, the resistance is simply governed by the flow of water around the riser. However, when the bottom of the riser is moved close to the mudline the response is govern by riser−seabed−water interaction. The penetration of the riser in the soft clay seabed is relatively fast and therefore undrained condition governs the behavior. Two types of variation of undrained shear strength (s_{u0}) are used in this paper: (1) uniform (s_{u0}), (2) linearly increasing s_{u0}, which is defined as $s_{u0}= s_{um} + ky'$, where s_{um} =undrained shear strength of clay at the mudline, k =strength gradient and y' =depth of the soil element from the mudline (Fig. 4.1).The depth of penetration (w) represents the depth of the invert of the riser from the mudline.

4.5 CFD Simulation

The general-purpose *ANSYS CFX* 13.0 software is used in this study for CFD simulation. Note that the CFD approach has been used in previous studies for modeling debris flows, glide blocks and out-runner blocks (e.g. De Blasio et al. 2004 a & b, 2005; Gauer et al. 2005 & 2006; Harbitz et al. 2003; Zakeri 2009; Zakeri et al. 2009a; Zakeri and Hawlader 2013). In *ANSYS CFX*, the domain is discretized into three-dimensional (3D) mesh. The governing equations are solved adopting a solution methodology based on finite volume and are constructed using the discretized mesh. The force−displacement behaviour is modeled using the Navier−Stokes equations, which has been developed applying Newton's Law ($F=ma$) to fluid elements. Here F

= force, m = mass and a = acceleration. The forcing term (F) = sum of gravitational force (F_{grv}), pressure force (F_{press}) and viscous force (F_{visc}). The gravitational force F_{grv} (=mg) is same as it is in solid mechanics, where g is the gravitational acceleration. The last two (F_{press} and F_{visc}) are the reaction forces to the motion, which are analogous to the normal and frictional resistance in solid mechanics. The parameters required in CFX to calculate F_{grv} and F_{press} are given by density of soil and water, and the boundary conditions including the displacement of the riser. The coefficient of dynamic viscosity (μ) is used to calculate F_{visc}. The definition of μ, as a function of undrained shear strength, is discussed in the following sections.

4.5.1 *CFX Model Setup*

Figure 4.2 shows the domains used in CFX simulation. The riser (D=350 mm) is modeled as an impermeable wall. The CFX allows only 3D modeling, and therefore the analyses are performed for one element of 10 mm in the out-of-plane direction. The following three CFX modeling techniques are first developed to identify an appropriate modeling approach.

Model I

In this case, the center of the riser is placed at 1D above the mudline in water and then displaced downward. As shown in Fig. 4.2(a), the upper 2.35 m (=6.7D) of the domain is water and the lower 4.65 m (=13.3D) is clay. The right vertical boundary is placed at 3 m (=8.6D) from the center of the riser. The boundaries are placed at sufficiently large distance from the riser and therefore no boundary effects are observed. Taking the advantage of symmetry, only the right half of the domain is modeled.

Clay and water are modeled using homogeneous multiphase Eulerian materials. The interface between clay and water that represents the mudline is defined by a step function through CFX Command Language (CCL), which is a declarative language in CFX for enhanced simulation without writing external FORTRAN routines. The clay and water in the domain are defined initially using the volume fraction tool. In the elements above the mudline, the volume fraction of the water is set to 1 and the volume fraction of the clay is 0. Conversely, in the elements below the mudline, the volume fraction of water is 0 and volume fraction of clay is 1.

The bottom and all the vertical faces are defined as walls, which are solid impermeable boundaries to fluid flow. A no-slip boundary condition is applied to the bottom wall and riser surface, and therefore the velocity of the Eulerian material (soil or water) next to these walls is zero. A free-slip boundary condition is applied on the right vertical wall. On the other three vertical faces, symmetry plane boundary conditions are applied, which implies that the flow of Eulerian materials (soil or water) on one side of the plane is a mirror image of the flow on the opposite side. The "Unspecified mesh motion" option in CFX is used for the vertical walls. This setting allows the mesh node on these walls to move in the vertical direction, preserving the quality of mesh during the displacement of the riser. The top of the water is defined as an opening to allow water to flow in and out of the domain.

The mesh is formed using the options available in CFX. Very fine mesh is used near the riser and the size of the elements is increased with distance from the riser. The maximum dimension of the mesh just outside the riser surface is 10 mm. The riser is displaced vertically downward at a given velocity specifying the motion of the nodes on the riser wall.

Model II

In this case, the riser is kept at a fixed location as shown in Fig. 4.2(b) and the clay is moved upward. The bottom boundary is defined as an inlet while the other boundary conditions are same as in Model I. The clay is entered through the inlet at a constant velocity (v). As the clay is modeled in undrained condition (no volume change), the top surface of the clay (mudline) moves upward at constant velocity v until it touches the riser. When the riser obstructs the flow of soil, the flow pattern changes and a berm forms near the pipe. However, the velocity of top soil surface far from the riser, such as the points near the right wall, is still same as the flow velocity in the inlet. This means that the relative velocity between the riser and soil surface farthest from it is the same in Model II as in Model I.

Model III

This approach can be considered as a subdomain approach. The Model III is same as Model I, except for an inner subdomain shown by the shaded zone near the riser in Fig. 4.2(c). No mesh deformation is allowed in the subdomain, and therefore the shape and size of the mesh does not change with displacement of the riser. However, the Eulerian materials (clay and water) can flow through the mesh both in subdomain and outside the subdomain. The radial thickness of the subdomain of $1.5D$ is used because the velocity of soil elements outside this zone during penetration is not significant, as shown later. Because the modeling of the zone near the riser is very critical, the inclusion of the subdomain increases the robustness of simulation significantly, which is discussed further in the following sections. In this case, the riser and the subdomain are displaced vertically at a constant speed specifying the motion of the nodes using CCL expressions. No additional interface conditions, such as no-slip or free-slip conditions, are

applied to the interface between the subdomain and surrounding soil/water. This allows inward and outward flow of soil and water through this interface maintaining the same fluid flux in both side of the interface.

4.5.2 *Modeling of Undrained Shear Strength in CFX*

On the basis of the fluid mechanics approach, the dynamic viscosity (μ) of soft clay can be defined as, $\mu = \tau/\dot{\gamma}$ where τ =shear stress and $\dot{\gamma}$ =shear strain rate. Following geotechnical notations, the symbol τ is replaced by undrained shear strength s_{u0}. Comprehensive discussions on estimation of shear strength of soft clays in deepwater are available in Lunne and Andersen (2007) and Lunne et al. (2011). It is known that the undrained shear strength increases with strain rate; however, this is not considered in this study. The authors discussed the effects of strain rate on s_{u0} elsewhere (Dutta et al. 2014; Zakeri and Hawlader 2013). In CFX analyses, the value of for each element is obtained at every time step, and then μ is assigned using CCL expressions.

Generally in FE modeling, the maximum undrained shear resistance at the pipe−soil interface is defined as αs_{u0}, where α =coefficient that varies between 0 (smooth/frictionless) and 1 (rough). Because it depends on many factors, analyses have been performed in the past for different values of α. For example, Wang et al. (2010) used α=0.5 while some other researchers (e.g. Tho et al. 2012) modeled for smooth condition (α=0). In CFX, different values of α cannot be defined directly. Therefore, the shear strength of one row of clay elements just outside the riser (s_{u_int}) is defined as $s_{u\_int}=f_2 s_{u0}$ with $0 \le f_2 \le 1.0$. Note that, f_2=0 approximately represents the smooth condition, as the soil near the riser cannot sustain any shear stress.

4.5.3 *Penetration Resistance*

The geometry and soil parameters used in the analyses are listed in Table 4.1. The penetration resistance (N_p) is presented in normalized form as $N_p=F/s_{uN}D_eL$, where F = penetration resistance, s_{uN} = undrained shear strength used for normalization, D_e =effective diameter and L = length of riser section (=10 mm). The undrained shear strength depends on mode of shearing (e.g. triaxial or simple shear), depth (e.g. in linear s_{u0}), and strain rate. One should interpret N_p value carefully because s_{uN} at different conditions has been used in previous studies (e.g. Langford and Aubeny 2008; Zhu and Randolph 2011; Wang et al. 2010; Bridge 2005). In the present study, considering triaxial compression as the standard test of reference, s_{u0} at the invert of the riser ($s_{u0(i)}$) in triaxial compression condition is used for s_{uN}. Using Tresca hexagon in the deviatoric plane, it can be shown that $s_{uN}=\frac{2}{\sqrt{3}}s_{u0(i)}$ (Smith and Griffiths 2004; Sousa et al. 2011; Tho et al. 2013). For uniform s_{u0} profile $s_{u0(i)}=s_{u0}$ and for linearly increasing s_{u0} profile the value of $s_{u0(i)}$ increases with depth of penetration. It is to be noted here that some researchers (e.g. White et al. 2010; Tho et al. 2012) reported a corrected value of N_p by subtracting the influence of soil buoyancy on penetration resistance. However, the normalized penetration resistance presented in the following sections is without any correction of buoyancy.

Following the concept of Gui and Bolton (1998) and assuming that the failure is occurred at a distance of half of the element size from the outer surface of the riser, the value of D_e can be calculated as 360 mm (=350 mm+2×10 mm/2) for 10 mm element size just outside the riser. If D (=350 mm) is used instead of D_e, the normalized penetration resistance will be increased by only 2.8%. In this study, D_e is used. The depth of penetration is normalized as $\hat{w}=w/D_e$.

Figure 4.3 shows the N_p vs $\hat{w}$ curves obtained from three CFX models (I, II, and III in Fig. 4.2) for the following parameters: s_{u0}=3.7 kPa (uniform); γ_{sat} =16.31 kN/m3; f_2=1; and v=60 mm/s. The value of N_p is zero until the riser touches the mudline at $\hat{w} = 0$. In all three models (I−III), the penetration resistance increases with depth of penetration. The value of N_p at $\hat{w} = 5D$ is 10.45. If the buoyancy effect (approximately equal to $\gamma' A_s/s_{u0}D$) is subtracted, the value of N_p will reduce to 9.97. The plasticity limit analysis (Randolph and Houlsby 1984; Martin and Randolph 2006) shows that the value of N_p for deep embedments and rough pipe-soil interface condition is 11.94, which is higher than the calculated value because a fully deep failure mechanism is not developed at $\hat{w} = 5D$; rather, it is in the transition stage, as shown later.

For all three cases, very similar N_p vs $\hat{w}$ curves are obtained for these conditions. However, in Model I, significant mesh distortion occurs at large penetration. Although the analysis could be performed for this particular condition, numerical issues are encountered for other conditions presented in the following sections, and therefore the Model II and III are developed.

Unlike Model I, numerical errors due to mesh distortion are not encountered in Model II. However, one disadvantage with this model is that the presentation of the results, such as instantaneous velocity vectors of soil, is difficult because soil is moved instead of the riser. In addition, one of the main objectives of the present research program is to model the suction under the riser when it moves upward during cyclic motion, which could not be simulated using Model II.

Some mesh distortion occurs outside the subdomain in Model III; however, it does not have significant influence on simulation. In this case, nondeformable subdomain mesh moves with the riser at same velocity, and Eulerian materials flow through it. Numerical issues due to mesh distortion near the riser also could be avoided. Another advantage is that the value of f_2

could be precisely assigned to the first row of the soil elements near the riser surface because the size of the mesh does not change with riser displacement. Considering these advantages, the Model III is used in the following CFX analyses.

4.6 Large Deformation FE Modelling

Abaqus 6.10 EF-1 is used to perform large-deformation FE analysis of the same problem shown in Fig. 4.1. Note that, conventional FE technique in Lagrangian framework cannot simulate such a large-deformation problem properly due to mesh distortions issues. Therefore, the CEL technique available in *Abaqus* is used. In CEL, mesh is fixed and the Eulerian material (clay) flows through the mesh.

Given the authors' previous experience (Dutta et al. 2012a, 2014), the FE model shown in Fig. 4.4 has been developed. A fine mesh of 17.5mm×17.5mm (i.e. 0.05D×0.05D) is used in a zone of 2.5D×8D where significant soil deformation is expected during penetration. A relatively coarser mesh is used outside this zone to increase computational efficiency. The FE model consists of three parts: (1) riser; (2) soil; and (3) void space to accommodate displaced soil mass. The riser is modeled as a weightless rigid body in Lagrangian framework while the soil is modeled an Eulerian material using EC3D8R 8-noded brick elements (*Abaqus* 2011). Similar to CFX, the CEL can generate only 3D models. Therefore, the simulation is performed for only one element along the axial direction of the riser.

A void space is defined above the clay to accommodate the berms. Soil and voids for initial condition are created using the Eulerian Volume Fraction (EVF) tool available in *Abaqus*. For clay EVF=1 meaning that the elements are filled with Eulerian material (clay) while EVF=0 for void space. Zero velocity boundary conditions are applied normal to the bottom and all the

vertical faces of the domain. However, at the seabed−void interface, no boundary condition is applied so that soil can flow into the void space when needed. A displacement boundary condition is applied at the reference point of the riser to displace it vertically downward. The von Mises yield criterion is adopted, and the simulations are performed for smooth pipe−soil interface condition. The following parameters are used: D=350 mm; s_{u0}=3.7 kPa (uniform); γ'=6.5 kN/m^3; v=60 mm/s; Poisson's ratio ν=0.495 and undrained modulus of elasticity E_u=500s_{u0}. Similar to CFX modeling, N_p is calculated using the undrained shear strength in triaxial stress condition. Note that, CEL analyses are also performed adopting the Tresca yield criterion, and N_p is obtained normalizing by $s_{u0(i)}$ instead of $s_{u0(i)}$ in triaxial condition. Both yield criteria give almost same N_p. However, in order to be consistent with CFX analyses, the CEL analyses with the von Mises yield criteria is presented in this paper. Unlike CFX modeling, the diameter D of the riser is used to calculate N_p and $\hat{w}$ because the smooth interface condition is directly assigned in the present FE analyses. Further details of FE simulation using *Abaqus* CEL are available in Dutta et al. (2012a, b, 2013, 2014).

4.7 Comparison of CFX and CEL results

Figure 4.5 shows the comparison of penetration resistance. In CFX, a very small value of f_2 (=0.01) is used to simulate a condition similar to the frictionless contact between riser and soil used in CEL. The effects of f_2 are presented in the parametric study section. As shown in Fig. 4.5, the value of N_p obtained from CFX modeling compares very well with CEL modeling up to $\hat{w}$ =3.0. After that, N_p from CFX is higher than the value of N_p from CEL. This difference results from suction above the riser as discussed below. It is to be noted here that, comparing with

centrifuge test results and other numerical solutions, Dutta et al. (2014) showed that *Abaqus* CEL can simulate the penetration resistance of shallowly embedded pipelines.

Fig. 4.6 shows the negative pressure in the Eulerian materials (clay and water) calculated by CFX. Because the clay and water are modeled as homogeneous Eulerian materials some diffusion occurs at the interface between these two Eulerian materials, forming a thin finite thickness interface. The solid lines show the clay-water interface which has been drawn using the clay volume fraction of 0.5. For w=2.0D, the suction (absolute values of negative pressure) is developed in a small zone just above the springline of the riser. At this depth of penetration, there is a wide space above the riser between clay−water interface and symmetry plane. Water can flow easily through this space during penetration. With increase in penetration depth, the width of the trench above the riser becomes narrow as shown in Fig. 4.6 (c and d). For this penetration speed (60 mm/s), sufficient water cannot flow through this narrow space and therefore considerable suction develops above the riser as shown in Figs. 4.6(c and d) by the shaded zones. Because CEL cannot simulate this suction, N_p from CEL is less than the values obtained from CFX for $\hat{w}$ >3.0.

In a recent study, Tho et al. (2012) showed the influence of size and shape of the trench or soil cavity on penetration resistance. They also recognized the importance of the boundary conditions at the trench wall or cavity which are related to drainage of water through the trench. Two extreme idealized scenarios identified are (1) open drainage, where the water in the cavity can easily drain away; and (2) closed drainage, where the water in the cavity is hydraulically isolated. They performed FE analyses using *Abaqus* CEL for an open-drainage condition by modeling the trench as void and therefore the trench walls are stress-free.

Similar to Tho et al. (2012), the present CEL modeling simulates the penetration process in which trench walls are stress-free, and a void space represents the trench (Fig. 4.7). In contrast, the trench is filled with water in CFX modeling. The stress on the clay−water interface is not always zero. The CFX calculates the stress that depends mainly on trench shape and penetration speed. For example, Fig. 4.6(a) shows that at w=2D the stress on the clay−water interface of the trench is negligible. However, at w=5D, a considerable stress acts on trench wall due to suction in water above the crown. Comparing CEL and CFX analyses it can be concluded that CFX can simulate the stress condition on the trench wall which could not be done using CEL.

The suction above the riser also has some effects on trench formation and instantaneous velocities of clay. Figure 4.7(a) shows that at shallow depths (e.g. $\hat{w}$ =2) the shape of the trench and instantaneous velocity vectors obtained from CEL and CFX are very similar. At a large $\hat{w}$ (e.g. $\hat{w}$ =3 or 5) the suction in water pulls the clay particles towards the crown of the riser, which enhances formation of circular shaped instantaneous velocity vectors in CFX. On the other hand, in CEL the clay velocity vectors at these depths pointed upwards and towards the symmetry plane. One of the possible reasons is that there is no suction in CEL models. In CFX simulation, the suction above the crown could also promote the backflow mechanism and speed up the closure of trench walls. The CFX simulation of clay velocity vectors even at large $\hat{w}$ is consistent with centrifuge test results of Hu (2010).

The CEL analysis is computationally very expensive. For example, the FE simulation shown in Fig. 4.5 takes approximately 23 h with a 3.2 GHz Intel Core i5 processor and 8 GB RAM. On the other hand, the CFX analysis shown in Fig. 4.5 takes only 104 min on the same computer (i.e. 13 times faster than CEL). One of the main advantages of the CFX Model-III is that the finer mesh near the riser moves at same velocity as the riser. However, in CEL the mesh

is fixed and therefore finer mesh has to be created in a 2.5D×8D zone. Moreover, to maintain the aspect ratio of rectangular elements outside this zone in acceptable range, the FE mesh shown in Fig. 4.4 is created. Therefore, the number of elements in CEL is higher than that in CFX, although finer mesh is used near the riser in CFX. The difference between solution techniques of these two numerical programs is also the cause of significant variation in computational time. It is to be noted here that Remeshing and Interpolation Technique with Small Strain (RITSS) (Hu and Randolph 1998) is also computationally intensive and takes several days to analyze this type of problem (Barbosa-Cruz and Randolph 2005). In summary, the present CFX modeling is computationally very efficient compared with other FE analyses.

4.8 Parametric Study

As shown in the previous sections, CFX can successfully simulate penetration resistance. Moreover, the proposed CFX Model III is computationally very efficient. This model is used for a parametric study.

4.8.1 *Uniform* s_{u0}

In the parametric study for uniform s_{u0}, the following parameters are kept constant: D=350 mm; γ_{sat} =16.31 kN/m3; and v=60 mm/s; while the value of f_2 and s_{u0} are varied.

Effects of f_2 - uniform s_{u0}

Figure 4.8 shows the variation of N_p with $\hat{w}$ for four different values of f_2 (0.01, 0.2, 0.5 and 1.0) and s_{u0}=3.7 kPa. The penetration resistance increases with f_2. At shallow depths, these results are comparable with previous studies (e.g. Wang et al. 2010, ideal soil without rate and

softening effects). At $\hat{w}$ =5, N_p=9.33 and 10.45 for f_2=0.01 and 1.0, respectively. Note that, at this $\hat{w}$ the suction in the cavity above the riser increases the magnitude of N_p. The comparison with CEL for f_2=0.01 is shown in Fig. 4.5.

Effects of s_{u0}

Figure 4.9 shows the variation of N_p for three different values of uniform s_{u0}. The magnitude of N_p increases with decrease in s_{u0}. Martin and White (2012) conducted FE analyses of pipes in wished-in-place configuration and showed that N_p increases with a normalized parameter $\gamma' D/s_{u0}$. The values of $\gamma' D/s_{u0}$ for the analysis presented in Fig. 4.9 are 1.0 and 0.46 for s_{u0}= 2.3 and 5 kPa, respectively. At $\hat{w}$ =5, N_p=10.94 and 9.69 for s_{u0}= 2.3 and 5 kPa, respectively. Although the analyses of Martin and White (2012) are for some idealized conditions (full tension/no tension and smooth/rough), the calculated N_p in their study are comparable with the present study.

The insets of Fig. 4.9 show the shape of the trench for two penetration depths and s_{u0}. As shown in inset (a), that for a low s_{u0}=2.3 kPa the wall of the trench touches the symmetry plane at $\hat{w}$ =4, almost resulting in a closed-drainage condition for the water in the cavity just above the crown. Further penetration results in suction in this cavity and increases N_p. On the other hand, for s_{u0}=5 kPa there is still a wide space between the trench wall and symmetry plane even at $\hat{w}$ =5 [inset (b) in Fig. 4.9]. In other words, the shape of the trench at the intermediate depths also influences N_p.

4.8.2 *Linearly Increasing* s_{u0}

The analyses presented in the previous sections are for uniform s_{u0}. In deepwater, the linear increase of s_{u0} with depth has been reported by many researchers (e.g. Puech et al. 2010; Jeanjean 2002; Dingle et al. 2008). The linearly increasing s_{u0} profile is defined as $s_{u0} = s_{um} + ky'$ (Fig. 4.1). The parameters used in the base case analyses for linearly increasing shear strength profile are: D=350 mm, v=60 mm/s, s_{um}=2.3 kPa, k=2.0 kPa/m, f_2=0.01 and γ'=6.5 kN/m^3. In the parametric study, only one parameter is varied, and the other parameters are same as above unless otherwise mentioned.

In this study, the authors developed a special technique in CFX such that the soil elements carry the initial value of s_{u0} although they move through the mesh. The parallel contours in Fig. 4.10(a) show that s_{u0} increases linearly with depth before penetration of the riser in the seabed. Figure 4.10(b) shows the s_{u0} contours at w=5D, which are no longer parallel lines. The displaced soil elements carry the initial value of s_{u0}. For example, the soil elements just below the riser is pushed down from a higher location but still carry s_{u0} at original locations. Similarly, another technique was developed for carrying initial s_{u0} in *Abaqus* CEL, which is discussed elsewhere (Dutta et al. 2014). For comparison, the contours of s_{u0} obtained from CEL at w=5D are shown in Fig. 4.10(c). In summary, s_{u0} is properly carried by the displaced clay elements during the progress of analysis both in CEL and CFX.

Figure 4.11 shows the comparison of N_p from CEL and CFX simulations for the base case of linearly increasing s_{u0} profile. Similar to Fig. 4.5 with uniform s_{u0}, the CFX and CEL calculated N_p values compare very well at shallow embedments. However, at $\hat{w}$ >2.5 the CFX gives higher N_p than CEL. In the inset of Fig. 4.11, the zone of suction (negative pressure) is shown for three different w (2.5D, 4D and 5D) obtained from CFX analysis. Considerable

suction is developed above the riser at large embedments (e.g. w=4D−5D), which increases the penetration resistance. The effects of suction on N_p are discussed in detail in the previous sections for uniform s_{u0}.

Effects of f_2 for linear s_{u0}

The effects of f_2 on N_p for linearly increasing s_{u0} profile are shown in Fig. 4.12. The normalized penetration resistance increases with increase in f_2. At $\hat{w}$ =5, N_p=8.5 and 9.4 for f_2=0.01 and 1.0, respectively.

Effects of s_{um}

The mudline shear strength might vary from zero to several kPa (e.g. s_{um}=2.0 kPa in Langford and Aubeny 2008; s_{um}=3.7 kPa in Aubeny et al. 2008; s_{um}=0 in Hu 2010; s_{um}=4.3 kPa in Clukey et al. 2011). Figure 4.13 shows the variation of N_p for three different values of s_{um} (=1.0 2.3, 3.7 kPa) with f_2=0.5. As shown in this figure that with increase in s_{um}, the normalized penetration resistance decreases. The insets of this figure show the shape of the trench. When s_{um}=3.7 kPa, the trench is open, even at $\hat{w}$ =5 [see inset (b)]. However, the face of the trench touches the symmetry plane for a low s_{um}=1.0 kPa at $\hat{w}$ =3 as shown in the inset (a). The water in the cavity above the crown is hydraulically isolated and therefore suction will develop during further penetration, which also contributes to the higher N_p for s_{um}=1.0 kPa.

Effects of shear strength gradient, k

The shear strength gradient (k) could vary widely in deepwater offshore clays (e.g. Fugro 1999; Jeanjean 2002). Model tests have also been conducted in the past for a wide range of k. For

example, Aubeny et al. (2008) conducted model tests in kaolin clay of uniform s_{u0} (k=0) of 3.7 kPa, while Langford and Aubeny (2008) conducted a series of model tests using a high plastic marine clay from the Gulf of Guinea with k=13 kPa/m and s_{um}=2.0 kPa (i.e. s_{u0}=2.0+13y' in kPa). Similarly, Hu (2010) conducted centrifuge modeling varying k between 1.39 and 5.19.

Figure 4.14 shows the variation of N_p for four different values of k. The other soil parameters used in these analyses are s_{um}=2.3 kPa/m and f_2=0.5.Very small variation in N_p is obtained up to $\hat{w}$ =0.75. This is consistent the small strain FE analyses of Aubeny et al. (2005), who showed that at shallow embedments ($\hat{w} \leq 0.5$) the normalized penetration resistances fall into a very narrow range for uniform and linearly increasing s_{u0}. For $\hat{w} \geq 0.75$, the higher the value of k the lower the N_p. This trend is also similar to previous studies (Morrow and Bransby 2010; Martin and White 2012), although their analyses are for different soil properties and riser−soil interface conditions.

4.9 Conclusions

The penetration of riser, pipeline or T-bar penetrometer in soft clay seabed is fundamentally a large-deformation problem. In addition to physical modeling, various numerical modeling techniques have been developed in the past to simulate this. Among them the RITSS and *Abaqus* CEL are the two FE approaches used by a number of researchers. Both of these techniques are computationally very expensive and cannot simulate the suction properly. In this study, two different numerical approaches are used to simulate the load-penetration response of a cylindrical body. The numerical simulations cover a wide range of embedments (up to 5D).The failure mechanisms in the 'transition zone' where they change from shallow to deep failure mechanisms are critically examined. The following conclusions can be drawn from this study:

1) The *Abaqus* CEL and *ANSYS* CFX give the same load-penetration response up to a certain depth of embedment. For the cases analyzed in this study, it is $2.5D-3.0D$. After this depth, CFX gives higher penetration resistance.

2) The depth of the transition zone and shape of the trench depend on the magnitude and variation of the undrained shear strength of clay with depth. A cavity is formed above the crown when the two faces of the trench touch each other. The negative pressure in the hydraulically isolated cavity increases the penetration resistance and it could enhance the initiation of deep failure mechanisms. These processes can be simulated by CFX modeling.

3) The proposed CFX Model III is computationally very efficient as compared with *Abaqus* CEL.

4) The present CFX model can successfully simulate the influence of water on penetration behavior which could not be done using the FE models.

Although an excellent performance of CFX modeling is shown, one of the limitations of this study is that strain softening and strain rate effects on undrained shear strength are not considered in the numerical simulations.

Acknowledgements

The work presented in this paper was funded by C-CORE, MITACS, and Natural Sciences and Engineering Research Council of Canada (NSERC) Discovery grants.

References

Abaqus. (2011). User Manual, version 6.10-EF1, Dassault Systems, Waltham, MA.

ANSYS CFX. (2013). CFX program (version 13.0) physical modelling documentation. ANSYS, Canonsburg, PA.

Aubeny, C., and Biscontin, G. (2008). "Interaction model for steel compliant riser on soft seabed." *Offshore Technology Conf. OTC 19493*, Houston, 8.

Aubeny, C. P., and Biscontin, G. (2009). "Seafloor–riser interaction model." *Int. J. Geomech.*, 9(3), 133−141.

Aubeny, C., Gaudin, C., and Randolph, M. (2008). "Cyclic tests of model pipe in kaolin." *Soc. Petrol. Eng. J.*, 3(4). 1−6.

Aubeny, C. P., Shi, H. and Murff, J. D. (2005). "Collapse loads for a cylinder embedded in trench in cohesive soil." *Int. J. Geomech.*, 5(4), 320-325.

Barbosa-Cruz, E. R., and Randolph, M. F. (2005). "Bearing capacity and large penetration of a cylindrical object at shallow embedment." *Proc., 1st Int. Sym. on Frontiers in Offshore Geotechnics* (*ISFOG 2005*), M. Cassidy and S. Gourvenec, eds., Taylor & Francis, Perth, WA,615−621.

Bridge, C. (2005). "Effects of Seabed Interaction on Steel Catenary Risers." PhD. Thesis, Univ. of Surrey, U.K.

Bridge, C., Howells, H., Toy, N., Parke, G., and Woods, R. (2003). "Full scale model test of steel catenary riser." *Int. Conf. on Fluid Structure Interaction*, Cadiz, Spain, 1−10.

Bridge, C., and Wills, N. (2002). "Steel Catenary Risers – Results and conclusions from large scale simulations of seabed interaction." *Proc., Int. Conf. on Deep Offshore Technology, DOT02*, PennWell, New Orleans. 15p.

Clukey, E. C., Tognarelli, M. A., Li, G., Ghosh, R., Phillips, R., Zakeri, A., Elliot, B. J., and Bhattacharyya, A. (2011). "Simulation of SCR behaviour at touch down zone- Part-II: Testing

of a sectional SCR model in a geotechnical centrifuge." *Offshore Technology Conf*., *OTC* 22569, Rio de Janerio, Brazil, 1−14.

De Blasio, F. V., Elverhi, A., Issler, D., Harbitz, C. B., Bryn, P., and Lien, R. (2004a). "Flow models of natural debris flows originating from overconsolidated clay materials." *Mar*. *Geol*., 213(1−4), 439−455.

De Blasio, F. V., Elverhi, A., Issler, D., Harbitz, C. B., Bryn, P., and Lien, R. (2005). "On the dynamics of subaqueous clay rich gravity mass flows—the giant Storegga slide, Norway." *Mar*. *Pet*. *Geol*., 22(1-2), 179−186.

De Blasio, F. V., Engvik, L., Harbitz, C. B., and Elverhoi, A. (2004b). "Hydroplaning and submarine debris flows." *J*. *Geophys*. *Res*., 109(C1), 1978−2012.

Dingle, H. R. C., White, D. J., and Gaudin, C. (2008). "Mechanisms of pipe embedment and lateral breakout on soft clay." *Can*. *Geotech*. *J*., 45(5), 636−652.

DNV (Det Norske Veritas). (2010). "Riser fatigue", *DNV-RP-F204*, Oslo, Norway.

Dunlap, W. A., Bhojanala, R. P., Morris, D. V. (1990). "Burial of vertically loaded offshore pipelines in weak sediments." *Proc., Offshore Technology Conf.*, *OTC 6375*, Houston, TX, USA,.

Dutta, S., Hawlader, B., and Phillips, R. (2012a). "Finite element modeling of vertical penetration of offshore pipelines using Coupled Eulerian Lagrangian approach." *Proc., 22nd Int. Offshore and Polar Engineering Conf*., Rhodes, Greece, 343−348.

Dutta, S., Hawlader, B., and Phillips, R. (2012b). "Strain softening and rate effects on soil shear strength in modeling of vertical penetration of offshore pipelines." *Proc.*, *2012 9th Int. Pipeline Conf.*, The American Society of Mechanical Engineers, Calgary, AB, Canada, 13−20.

Dutta, S., Hawlader, B., and Phillips, R. (2013). "Numerical investigation of dynamic embedment of offshore pipelines." *Proc*., *of the 18th Int. Conf. on Soil Mechanics and Geotechnical Engineering*, Paris, France, 2347−2350.

Dutta, S., Hawlader, B., and Phillips, R. (2014). "Finite element modelling of partially embedded pipelines in clay seabed using coupled Eulerian Lagrangian Method" *Can*. *Geotech*. *J*., 52(1), 58−72.

Elliott, B., Phillips, R., Macneill, A., and Piercey, G. (2014). "Physical modelling of SCR in the touchdown zone under three axis motions." *Proc*., *8th Int*. *Conf*. on *Physical Modelling in Geotechnics*, Taylor & Francis, Perth, Australia, 265−270.

Elliott, B. J., Zakeri, A., Barrett, J., Hawlader, B., Li, G., and Clukey, E. C. (2013a). "Centrifuge modeling of steel catenary risers at touchdown zone part II: Assessment of centrifuge test results using kaolin clay." *Ocean Eng*., 60(1), 208−218.

Elliott, B. J., Zakeri, A., Macneill, A., Phillips, R., Clukey, E. C., and Li, G. (2013b). "Centrifuge modeling of steel catenary risers at touchdown zone part I: Development of novel centrifuge experimental apparatus." *Ocean Eng*., 60(1), 200−207.

Fugro, L. (1999). "STRIDE JIP – touchdown point behaviour of steel catenary risers, phase II – Riser/soil response curve development study." *Rep*. *No*. 93819-1, Fugro, Hemel Hempstead, U.K.

Gauer, P., Elverhoi, A., Issler, D., and DeBlasio, F. V. (2006). "On numerical simulations of subaqueous slides: Back calculations of laboratory experiments of clay-rich slides." *Norw*. *J*. *Geol*., 86(3), 295-300.

Gauer, P., Kvalstad, T. J., Forsberg, C. F., Bryn, P., and Berg, K. (2005). "The last phase of the Storegga slide: Simulation of retrogressive slide dynamics and comparison with slide-scar morphology." *Mar. Pet. Geol.*, 22(1−2), 171−178.

Gui, M. W., and Bolton, M. D. (1998). "Geometry and scale effects in CPT and pile design." *Geotech. Site Char.*, 1, 1063−1068.

Harbitz, C. B., Parker, G., Elverhøi, A., Marr, J. G., Mohrig, D., and Harff, P. A. (2003). "Hydroplaning of subaqueous debris flows and glide blocks: Analytical solutions and discussion." *J. Geophys. Res.*, 108(B7), 2349.

Hodder, M. S., and Byrne, B. W. (2010). "3D experiments investigating the interaction of a model SCR with the seabed." *Appl. Ocean Res.*, 32(1), 146−157.

Hu, H. J. E. (2010). "Pipeline/riser soil interaction analysis." PhD. Thesis, National University of Singapore (NUS), Singapore.

Hu, H. J. E., Leung, C. F., Chow, Y. K., and Palmer, A. C. (2011). "Centrifuge modelling of SCR vertical motion at touchdown zone." *Ocean Eng.*, 38(7), 888−899.

Hu, Y., and Randolph, M. F. (1998). "Deep penetration of shallow foundations on non-homogenous soil." *Soils Found.*, 38(1), 241−246.

Jeanjean, P. (2002). "Innovative design method for deepwater surface casing." *SPE* 77357.

Langford, T., and Aubeny, C. (2008). "Model tests for steel catenary riser in marine clay." *Offshore Technology Conf.*, *OTC 19495*, Houston, TX, USA, 1−7.

Li, F. Z., and Low, Y. M. (2012). "Fatigue reliability analysis of a steel catenary riser at the touchdown point incorporating soil model uncertainties." *Appl. Ocean Res.*, 38, 100−110.

Lunne, T. and Andersen, K. H. (2007). "Soft clay shear strength parameters for deepwater geotechnical design." *Proc., 6th Int. Offshore Site Investigation and Geotechnics*, Confronting

New Challenges and sharing Knowledge, Society of Underwater Technology, London, 151−176.

Lunne, T., Andersen, K. H., Low, H. E., Randolph, M. F. and Sjursen, M. (2011). "Guidelines for offshore in situ testing and interpretation in deepwater soft clays." *Can. Geotech. J.*, 48, 543−556.

Martin, C. M., and Randolph, M. F. (2006). "Upper-bound analysis of lateral pile capacity in cohesive soil." *Géotechnique*, 56(2), 141−145.

Martin, C., and White, D. (2012). "Limit analysis of the undrained bearing capacity of offshore pipelines." *Géotechnique*, 62(9), 847−863.

Morrow, D. R., and Bransby, M. F. (2010). "Pipe-soil interaction on clay with a variable shear strength profile." *Proc.*, *2nd Int. Symp. on Frontiers in Offshore Geotechnics*, Taylor & Francis, Australia,, 821-826.

Puech, A., Orozco-Calderon, M., and Foray, P. (2010). "Mini T-bar testing at shallow penetration." *Proc.*, *2nd Int. Symp. on Frontiers in Offshore Geotechnics*, Taylor & Francis, Australia, 305−310.

Randolph, M. F., and Houlsby, G. T. (1984). "Limiting pressure on a circular pile loaded laterally in cohesive soil." *Géotechnique*, 34(4), 613−623.

Randolph, M., and Quiggin, P. (2009). "Non-linear hysteretic seabed model for catenary pipeline contact." *Proc.*, *28th Int. Conf. Ocean*, *Offshore and Arctic Engineering*, American Society of Mechanical Engineers, Honolulu, Hawaii, 145−154.

Smith, I.M. and Griffiths, D.V. (2004). *Programming the finite element method*.4th Ed., Wiley, West Sussex, U.K.

Sousa, J. R.M., Porto, E.C., Foppa, D., Aguiar, C. S., Ellwanger, G. B. and Medeiros, C.J. Jr. (2011). "Undrained load capacity of torpedo anchors embedded in cohesive soils." *J. Offshore Mech. Arct. Eng.*, 133(2), 1−12

Tho, K. K., Leung, C. F., Chow, Y. K., and Palmer, A. C. (2012). "Deep cavity flow mechanism of pipe penetration in clay." *Can. Geotech. J.*, 49(1), 59−69.

Tho, K. K., Leung, C. F., Chow, Y. K., and Swaddiwudhipong, S. (2013). "Eulerian finite element simulation of spudcan-pile interaction." *Can. Geotech. J.*, 50(6), 595−608.

Wang, D., White, D. J., and Randolph, M. F. (2010). "Large-deformation finite element analysis of pipe penetration and large-amplitude lateral displacement." *Can. Geotech. J.*, 47(8), 842−856.

Wang, L, Zhang, J., Yuan, F. and Li, K. (2014). "Interaction between catenary riser and soft seabed: Large-scale indoor tests." *Appl. Ocean Res.*, 45, 10−21.

White, D. J., Gaudin, C., Boylan, N., and Zhou, H. (2010). "Interpretation of T-bar penetrometer tests at shallow embedment and in very soft soils." *Can. Geotech. J.*, 47(2), 218−229.

Wills, N., and West, P. T. J. (2001). "Interaction between deepwater catenary risers and a soft seabed: Large scale sea trials." *Offshore Technology Conference*, *OTC-13113-MS*, Houston, TX, USA.

Zakeri, A. (2009). "Submarine debris flow impact on suspended (free-span) pipelines: Normal and longitudinal drag forces." *Ocean Eng.*, 36(6−7), 489−499.

Zakeri, A., and Hawlader, B. (2013). "Drag forces caused by submarine glide block or out-runner block impact on suspended (free-span) pipelines - Numerical analysis." *Ocean Eng.*, 67, 89−99.

Zakeri, A., Høeg, K., and Nadim, F. (2009). "Submarine debris flow impact on pipelines—Part II: Numerical analysis." *Coastal Eng.*, 56(1), 1−10.

Zhu, H., and Randolph, M. F. (2011). "Numerical analysis of a cylinder moving through rate-dependent undrained soil." *Ocean Eng.*, 38(7), 943–953.

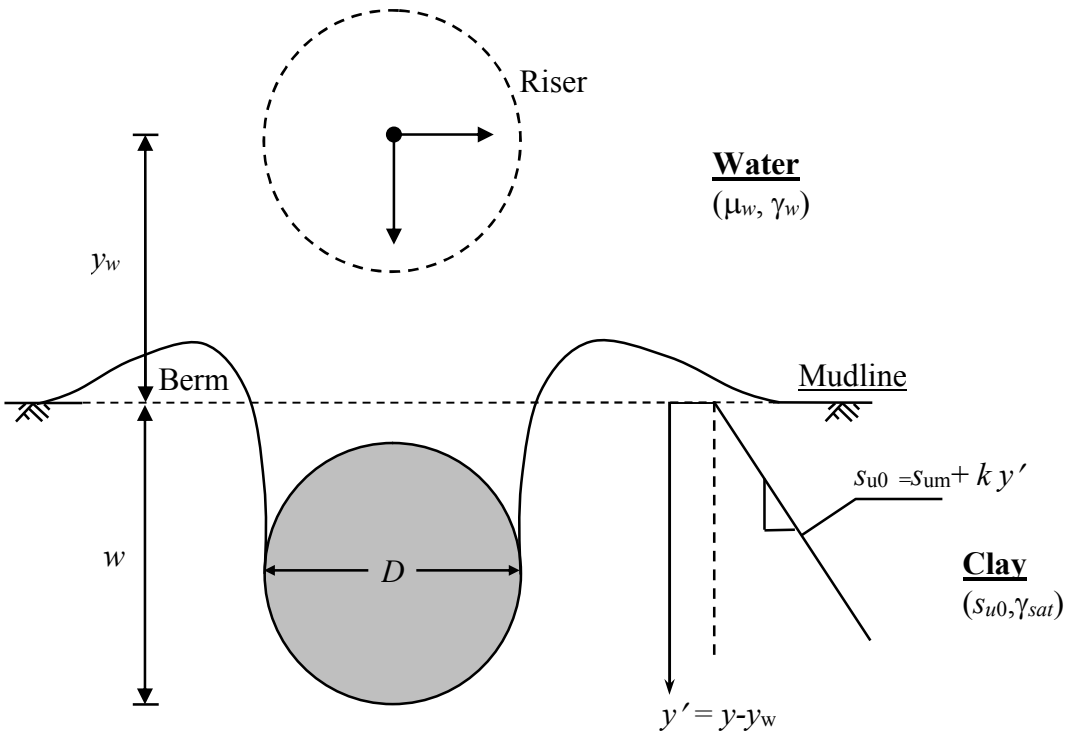

Fig. 4.1. Problem definition

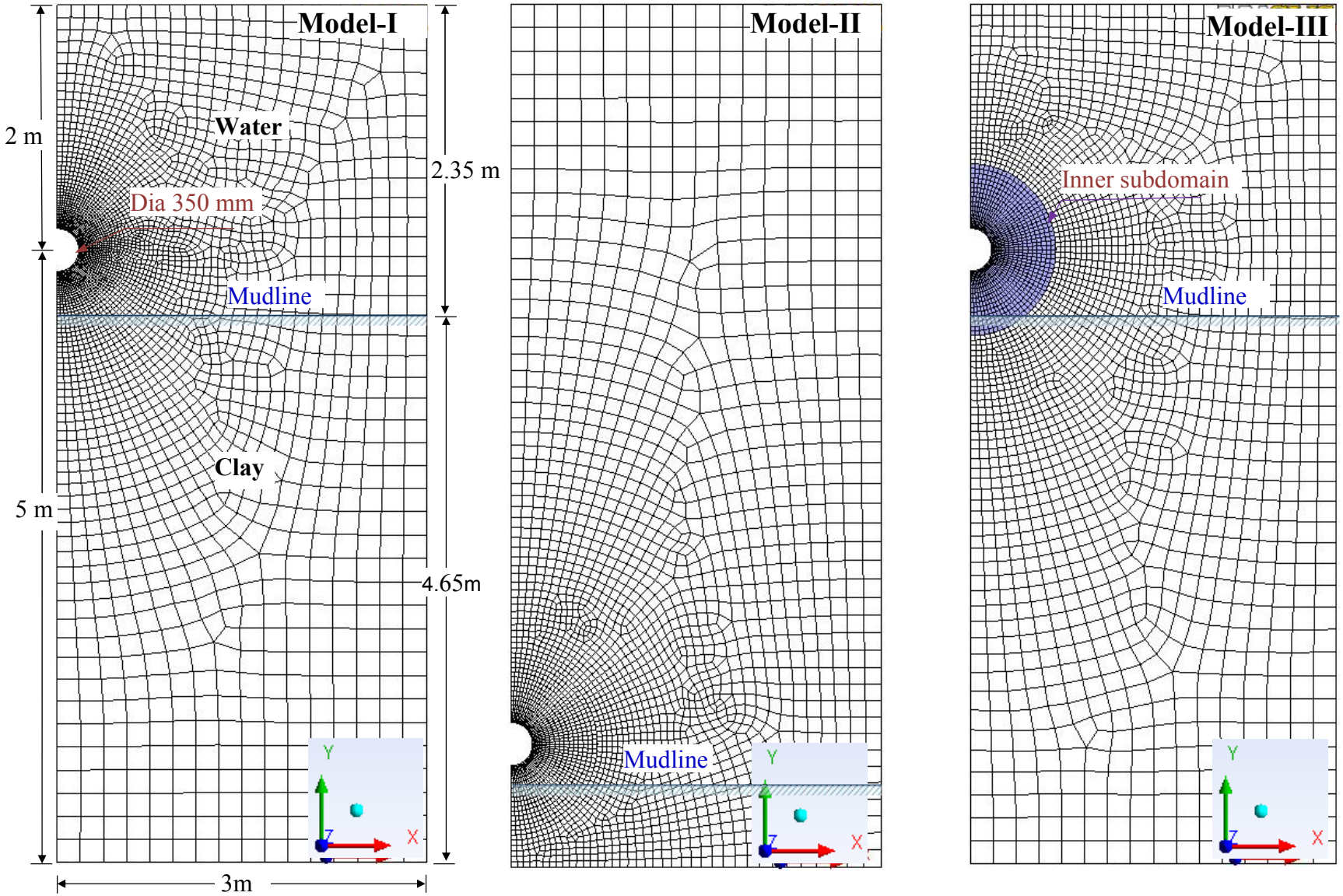

Fig. 4.2. CFX models

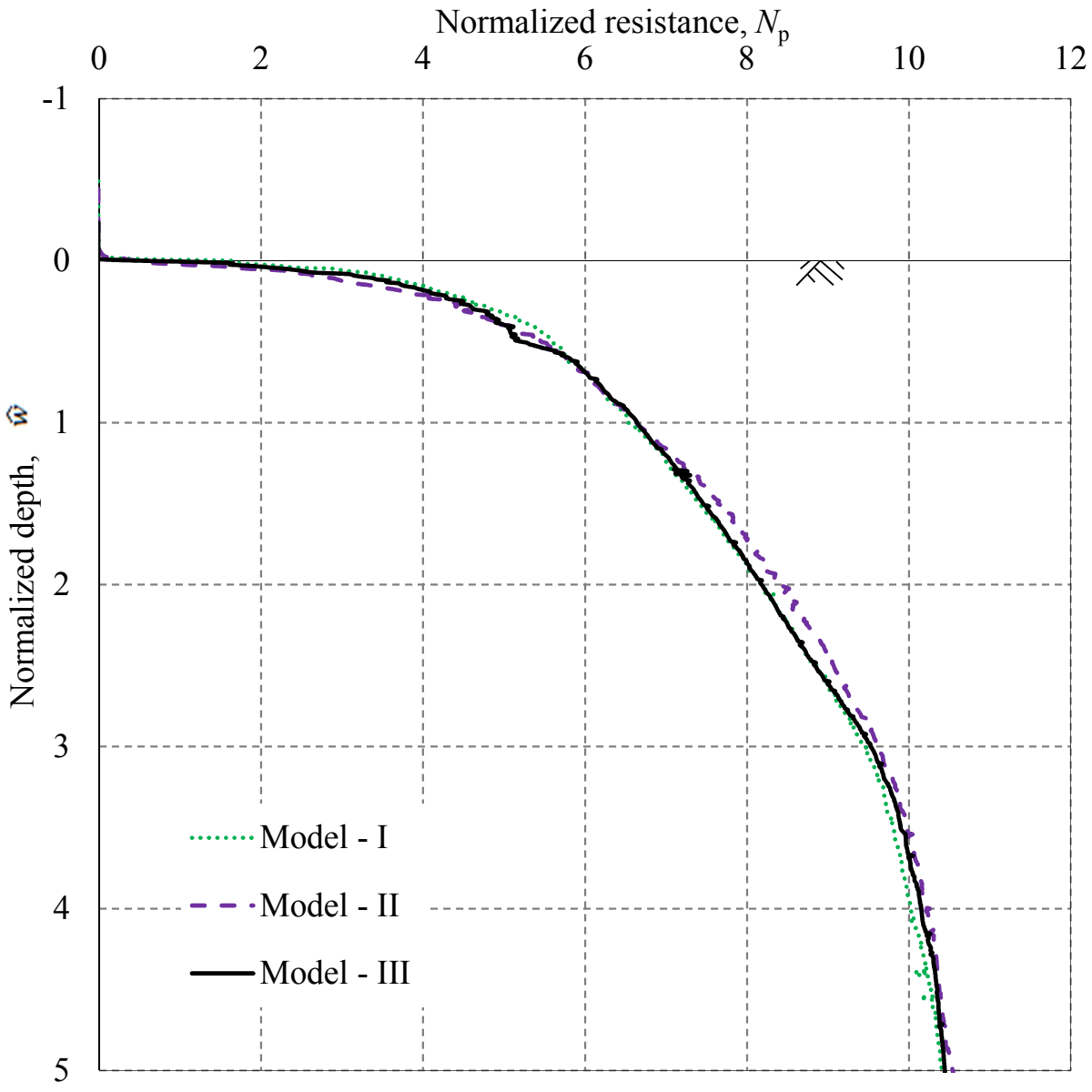

Fig. 4.3. Penetration resistance for three models (f_2 =1.0; s_{u0} = 3.7 kPa).

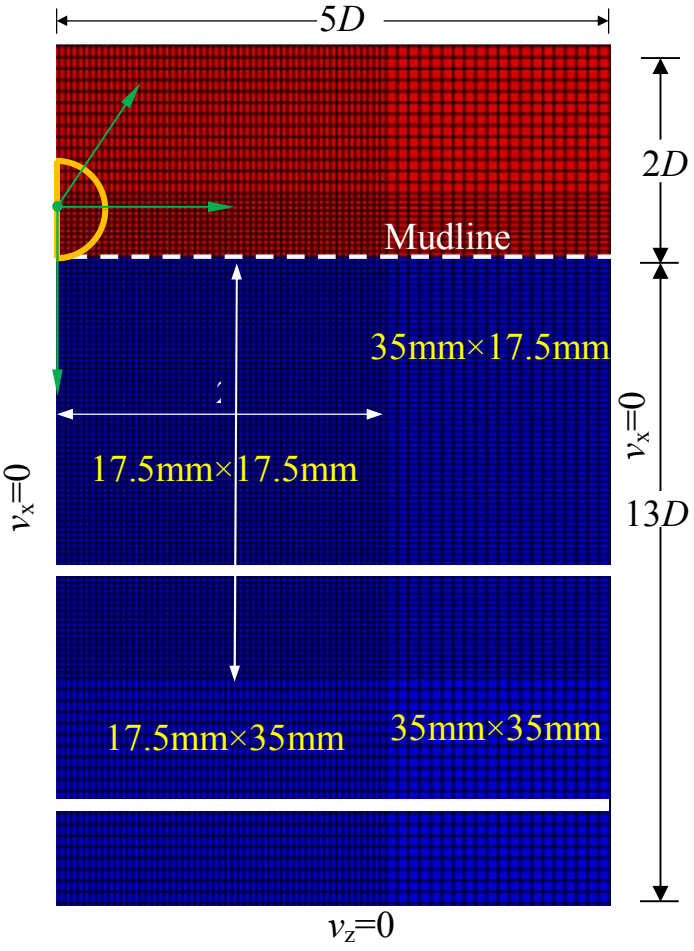

Fig. 4.4. FE model using Abaqus CEL

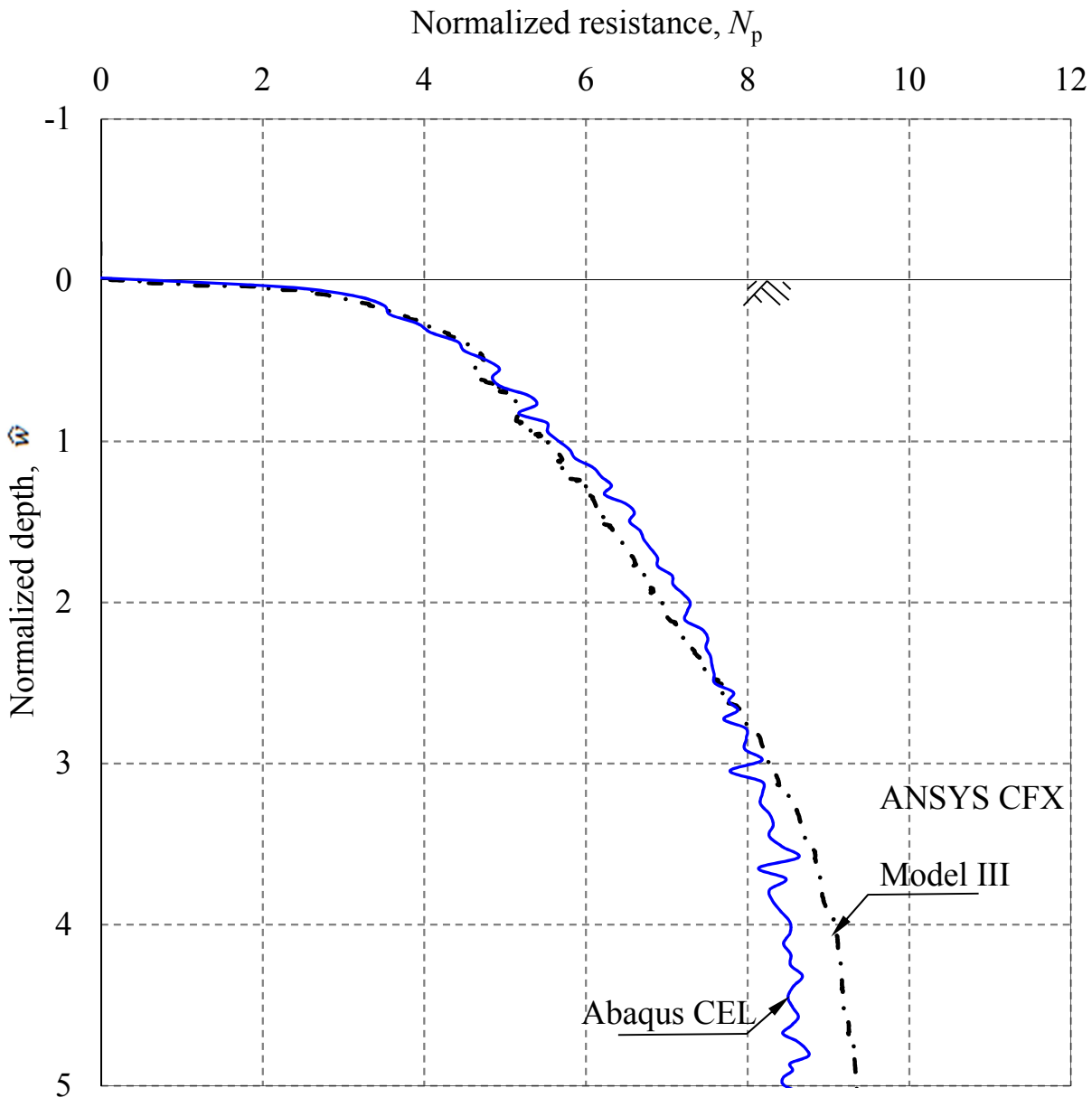

Fig. 4.5. Comparison between Abaqus CEL and ANSYS CFX (f_2 =0.01; s_u= 3.7).

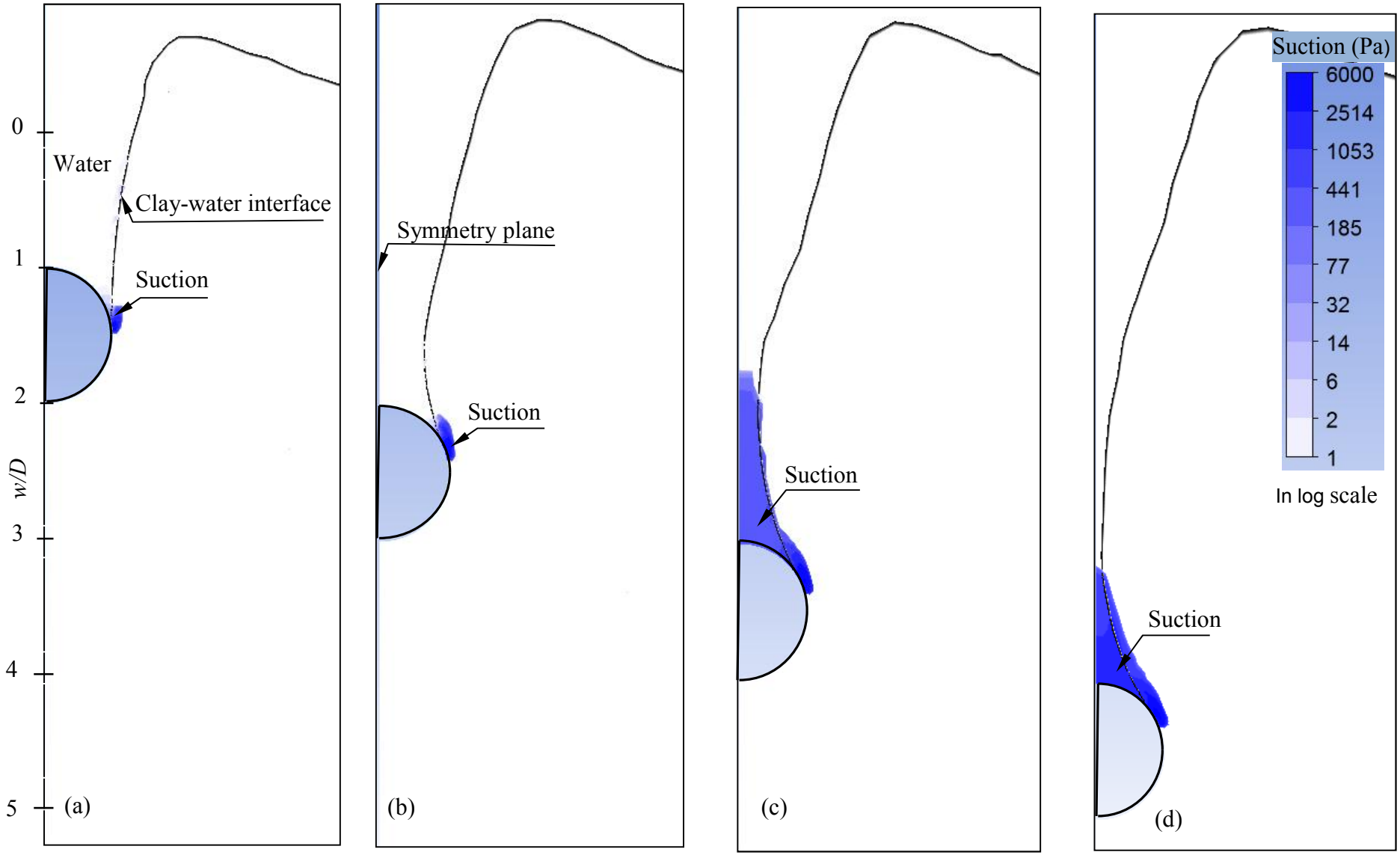

Fig. 4.6. Suction at different pipe penetration depth (a) 2*D* (b) 3*D* (c) 4*D* (d) 5*D*.

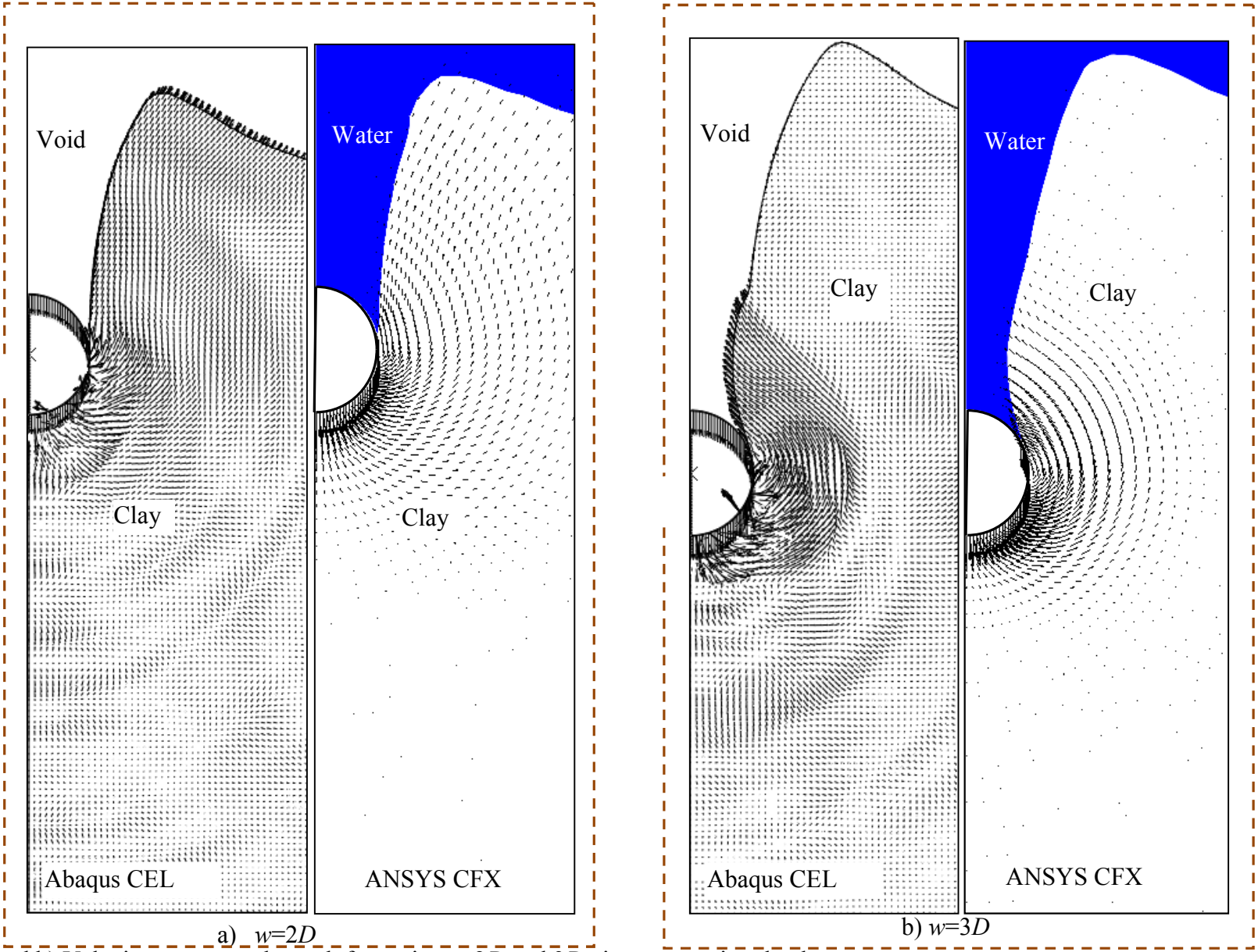

Fig. 4.7. (a and b) Velocity vectors and trench formation at 2*D* and 3*D* pipe penetration depth.

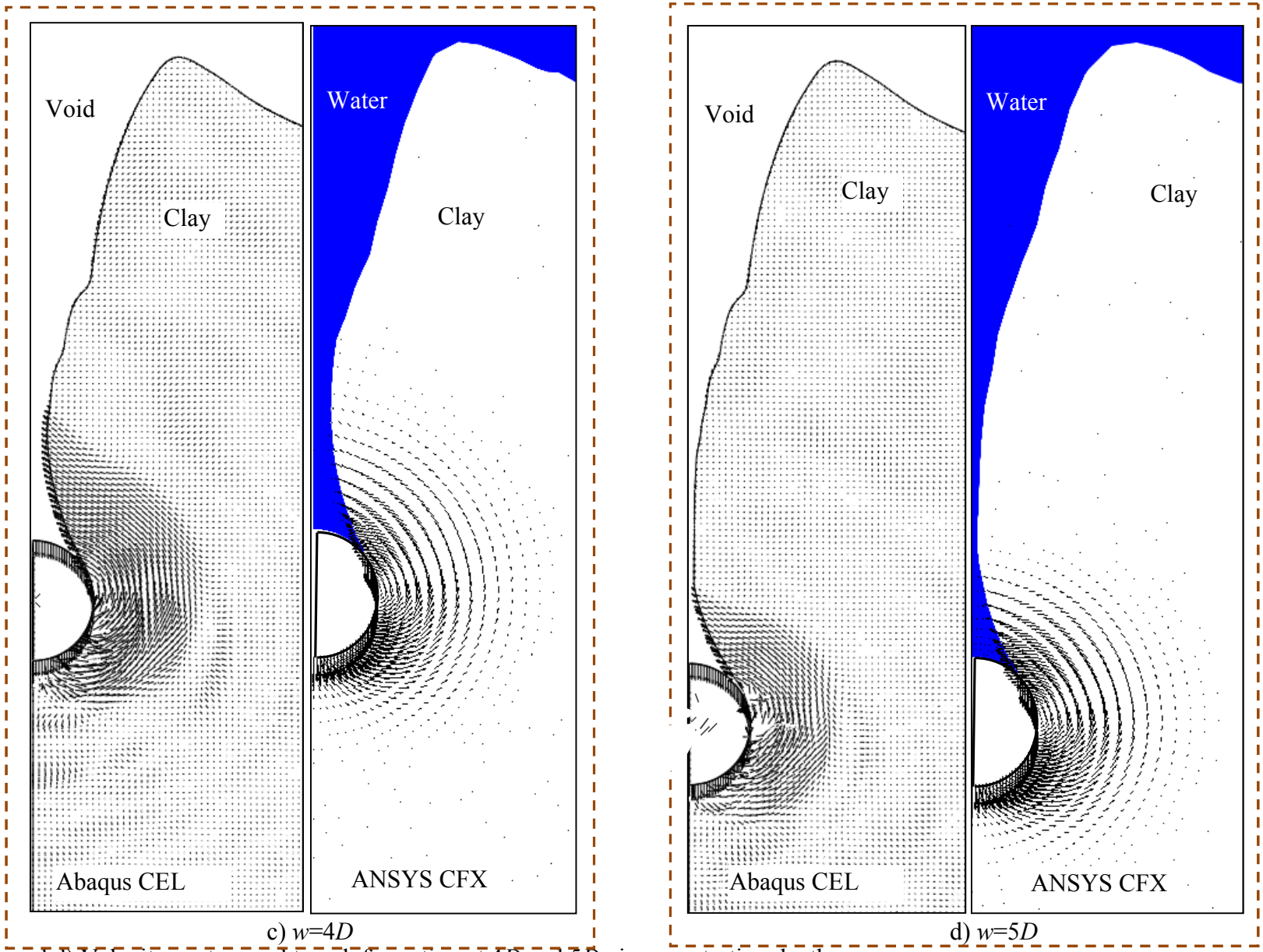

Fig. 4.7. (c and d) Velocity vectors and trench formation at 4*D* and 5*D* pipe penetration depth.

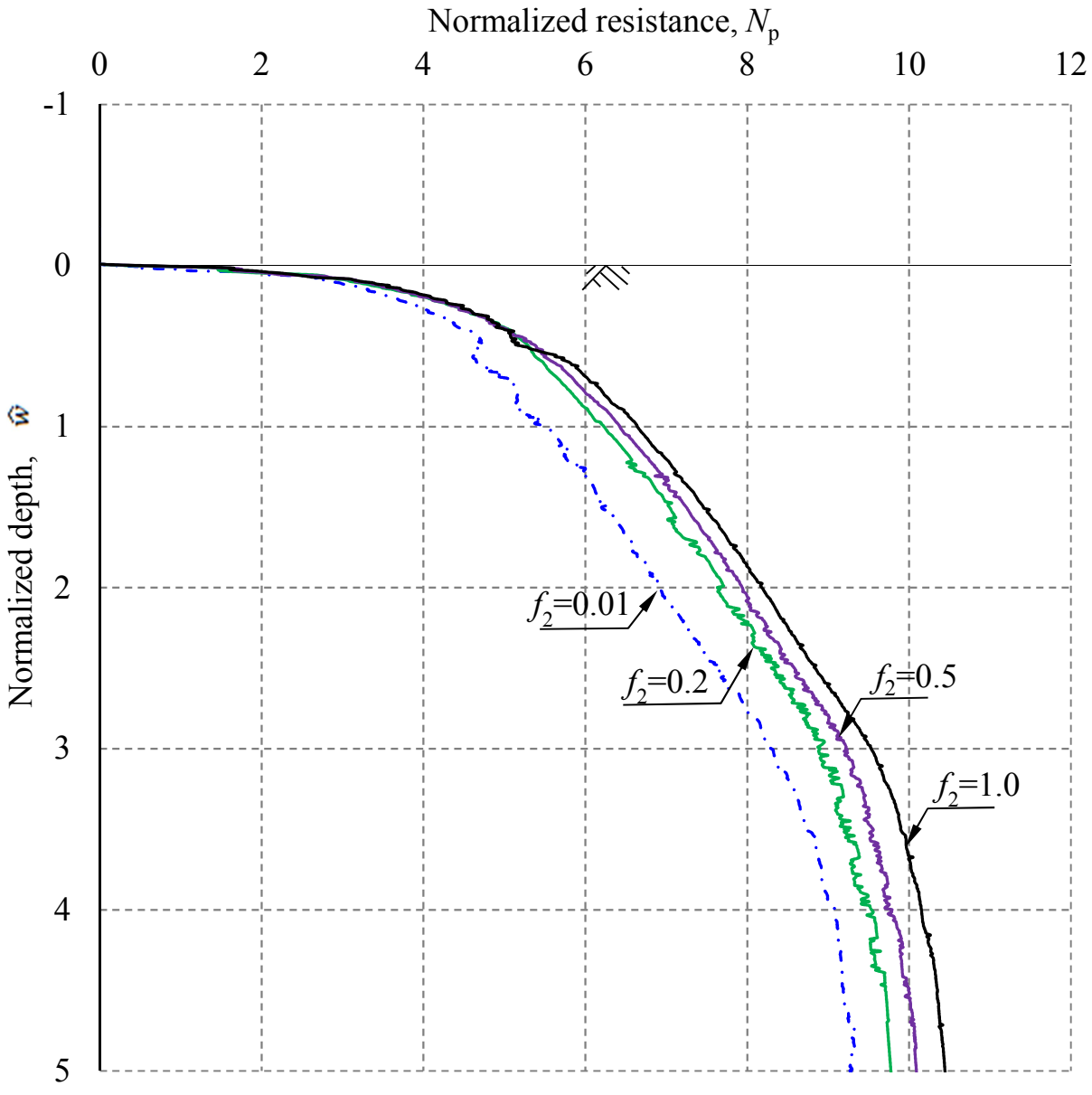

Fig. 4.8 .Effects of f_2 on pipe penetration resistance for s_{u0}=3.7 kPa

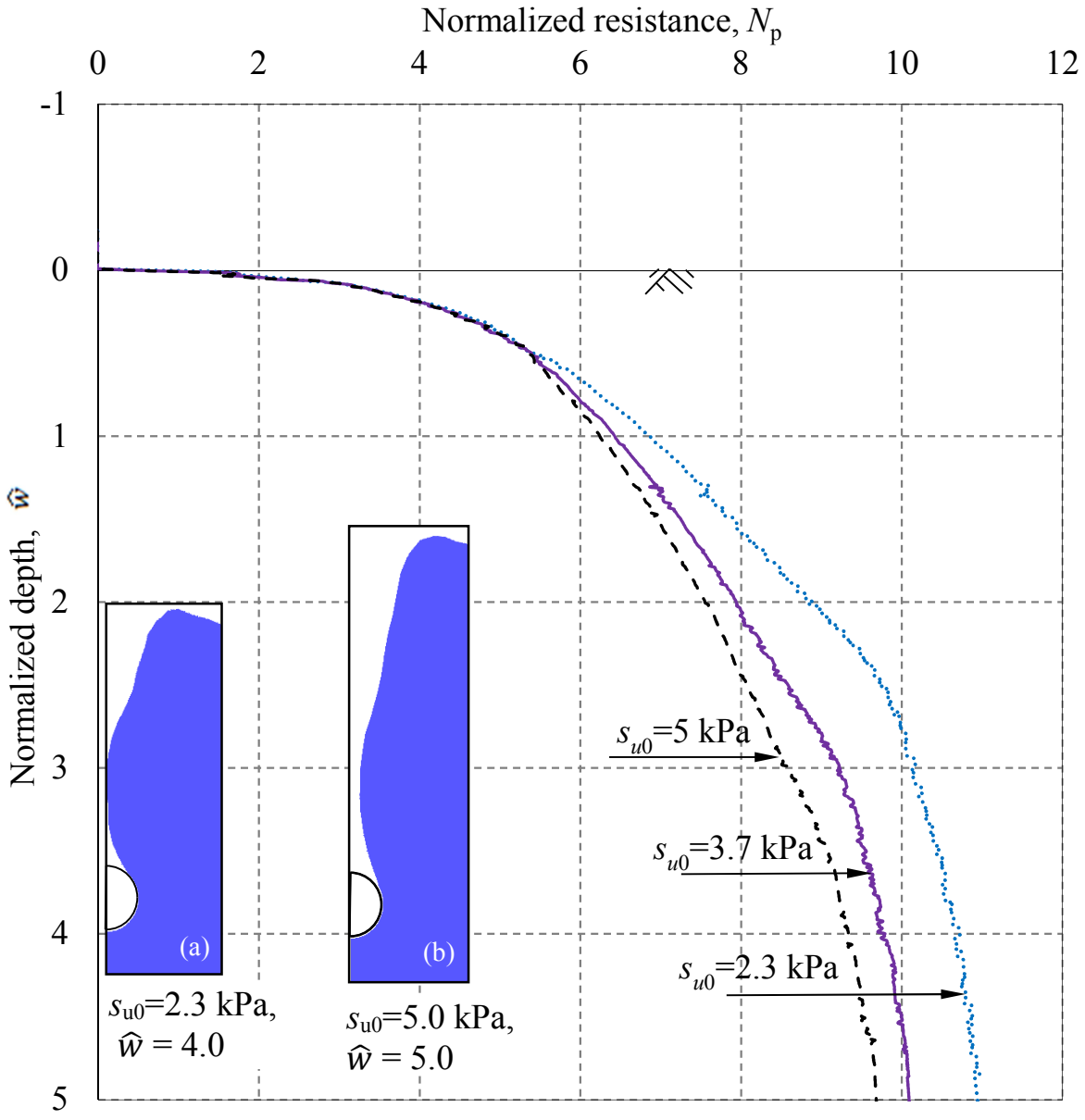

Fig. 4.9. Effects of soil undrained shear strength on pipe penetration resistance for f_2 = 0.5.

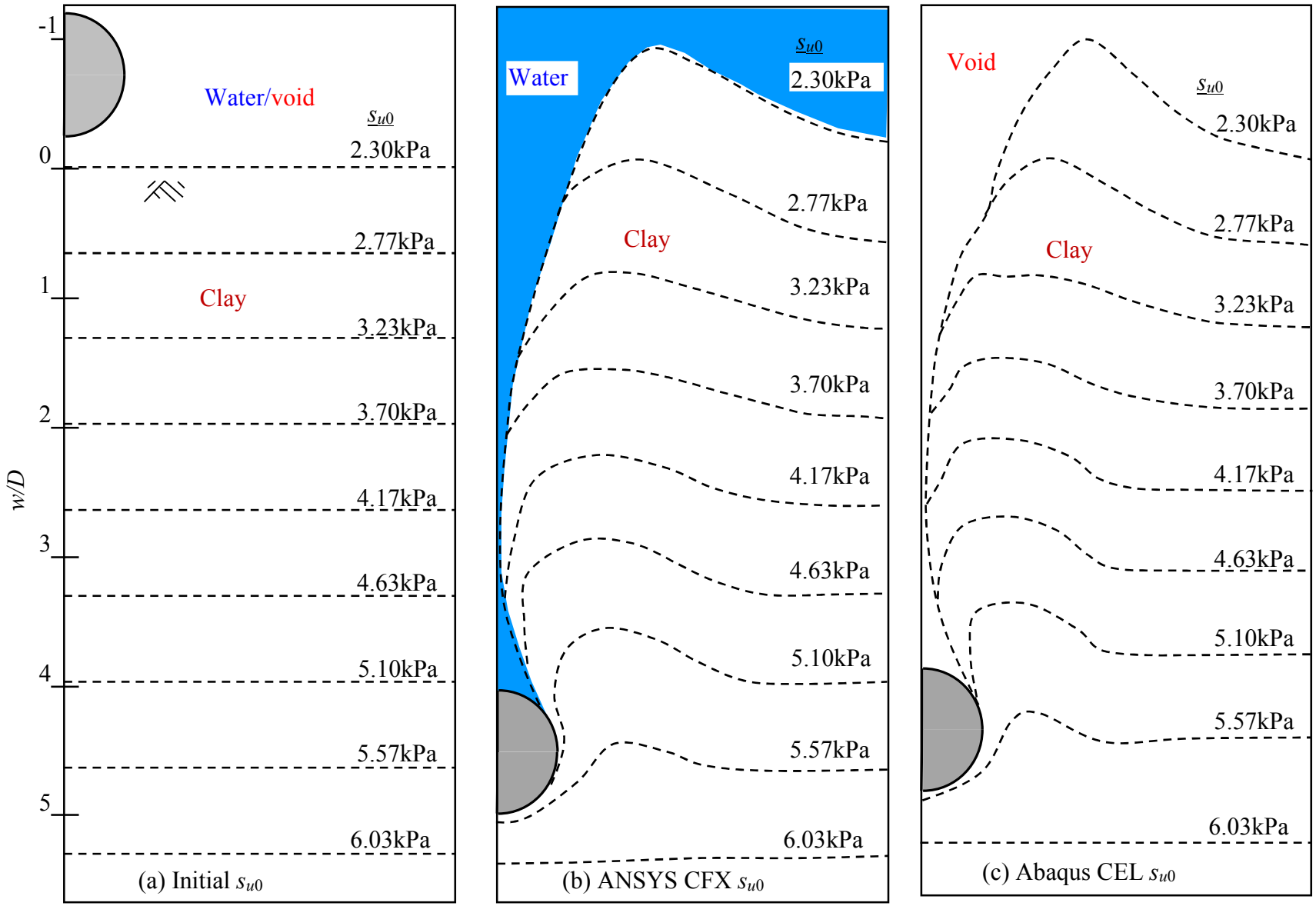

Fig. 4.10.Contour of initial shear strength s_{u0}: (a) before penetration; (b) at w= 5Din ANSYS CFX; (c) At w=5D in *Abaqus* CEL

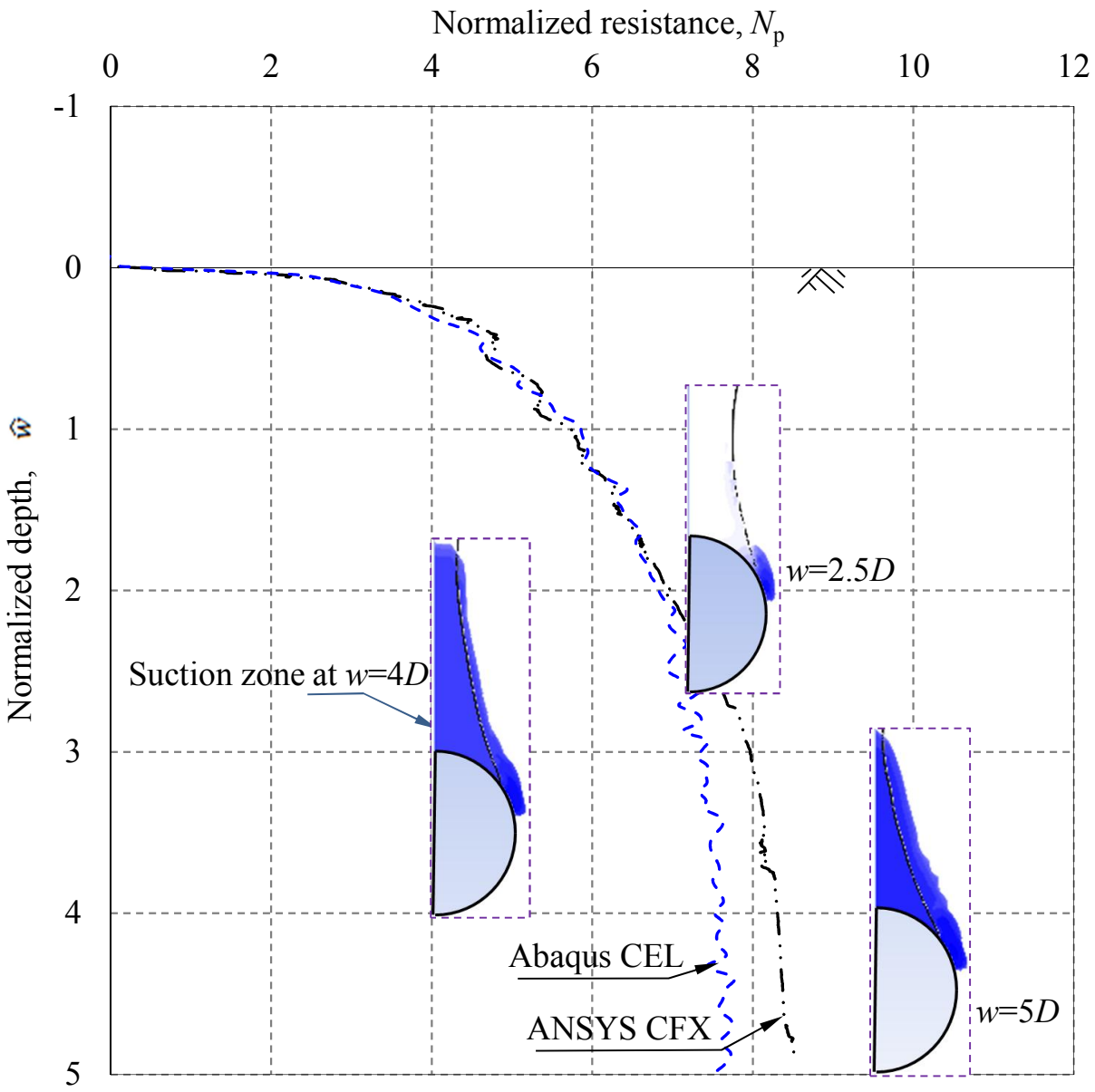

Fig. 4.11.Comparison between CEL and CFX results for base-case linearly increasing shear strength profile (s_{u0}= 2.3 + 2.0y' kPa with f_2 = 0.01)

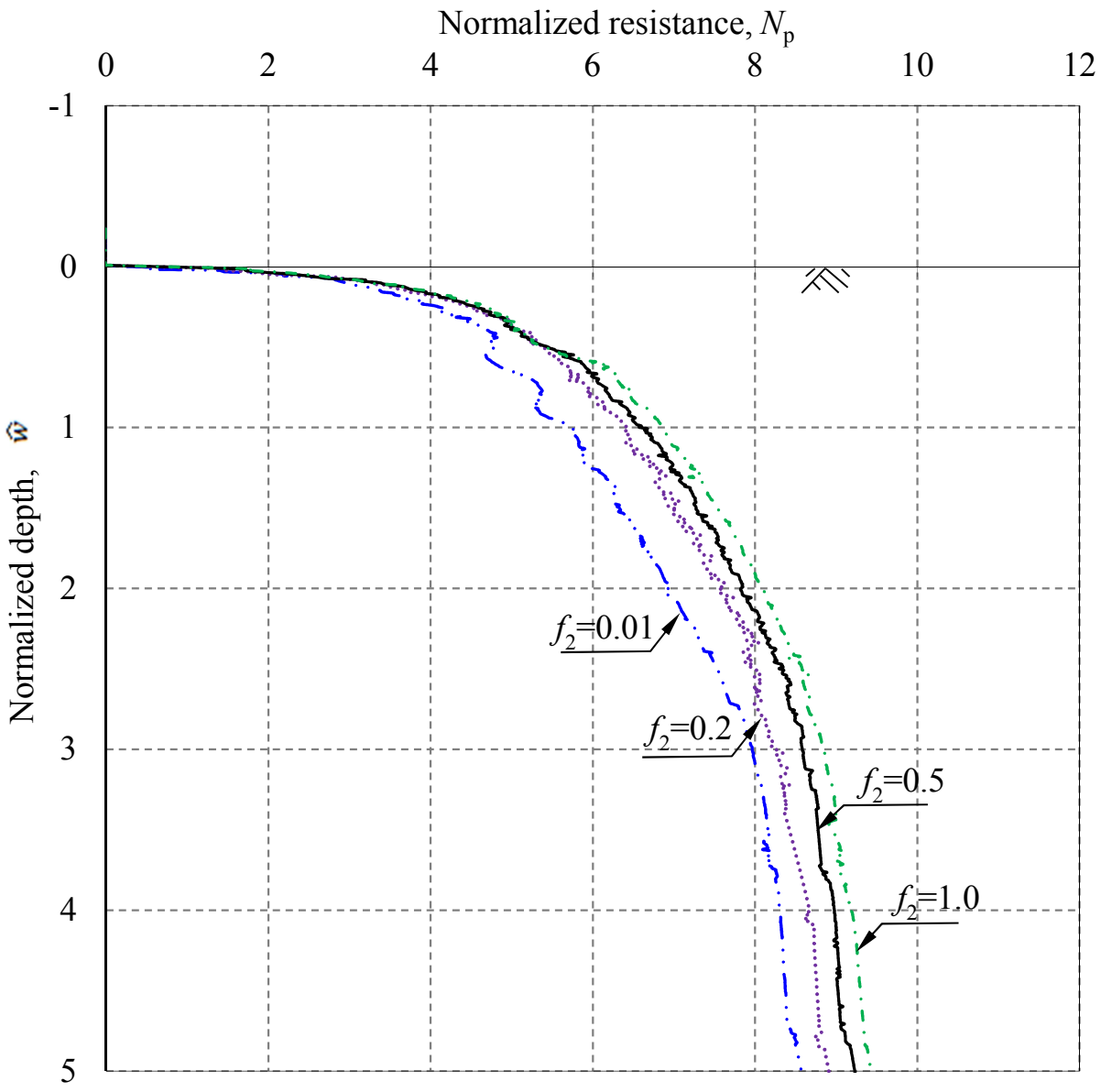

Fig. 4.12. Effects of f_2 on penetration resistance for linearly increasing shear strength profile

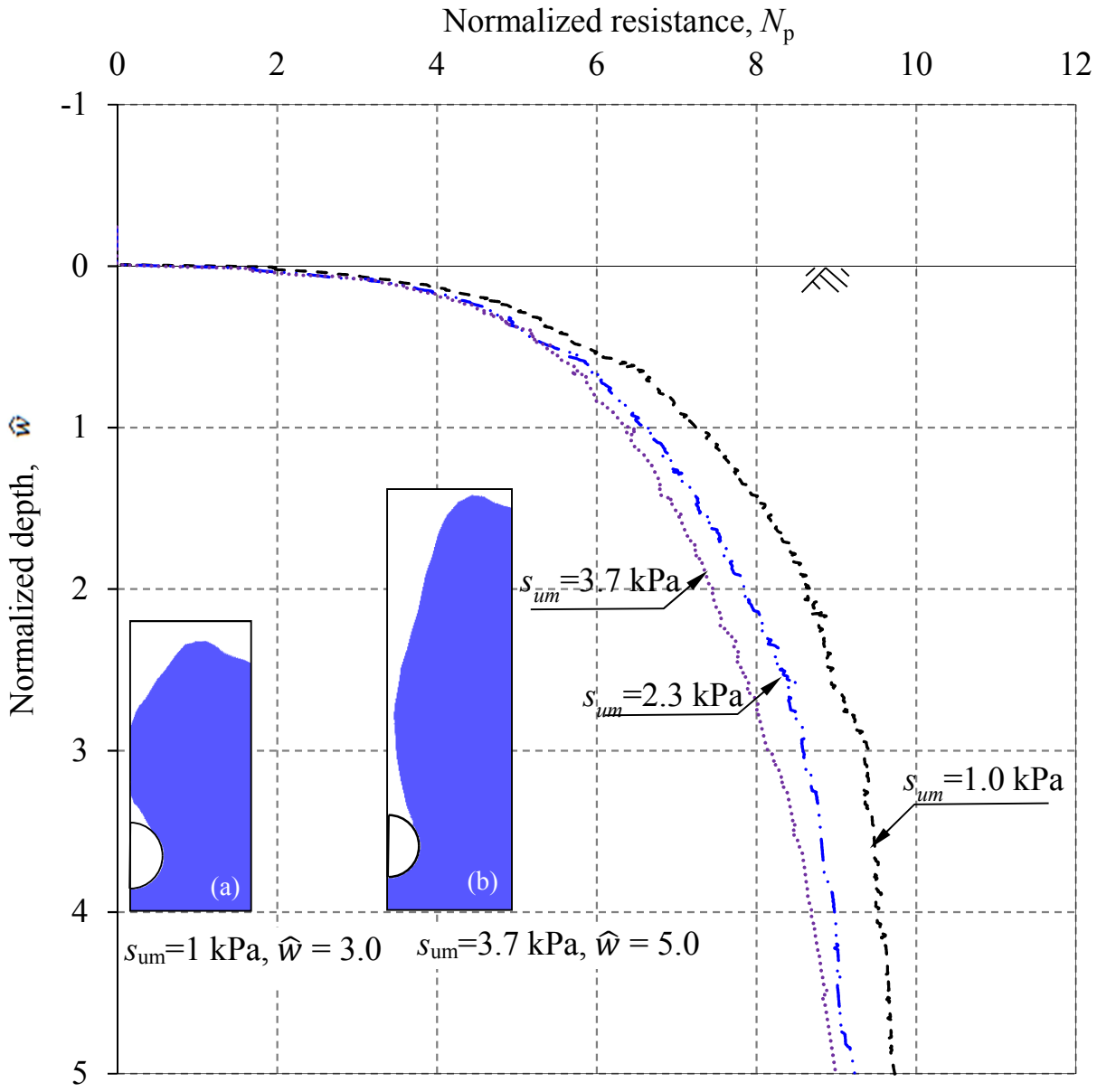

Fig. 4.13. Effects of mudline shear strength on pipe penetration resistance (f_2 = 0.5;k = 2 kPa)

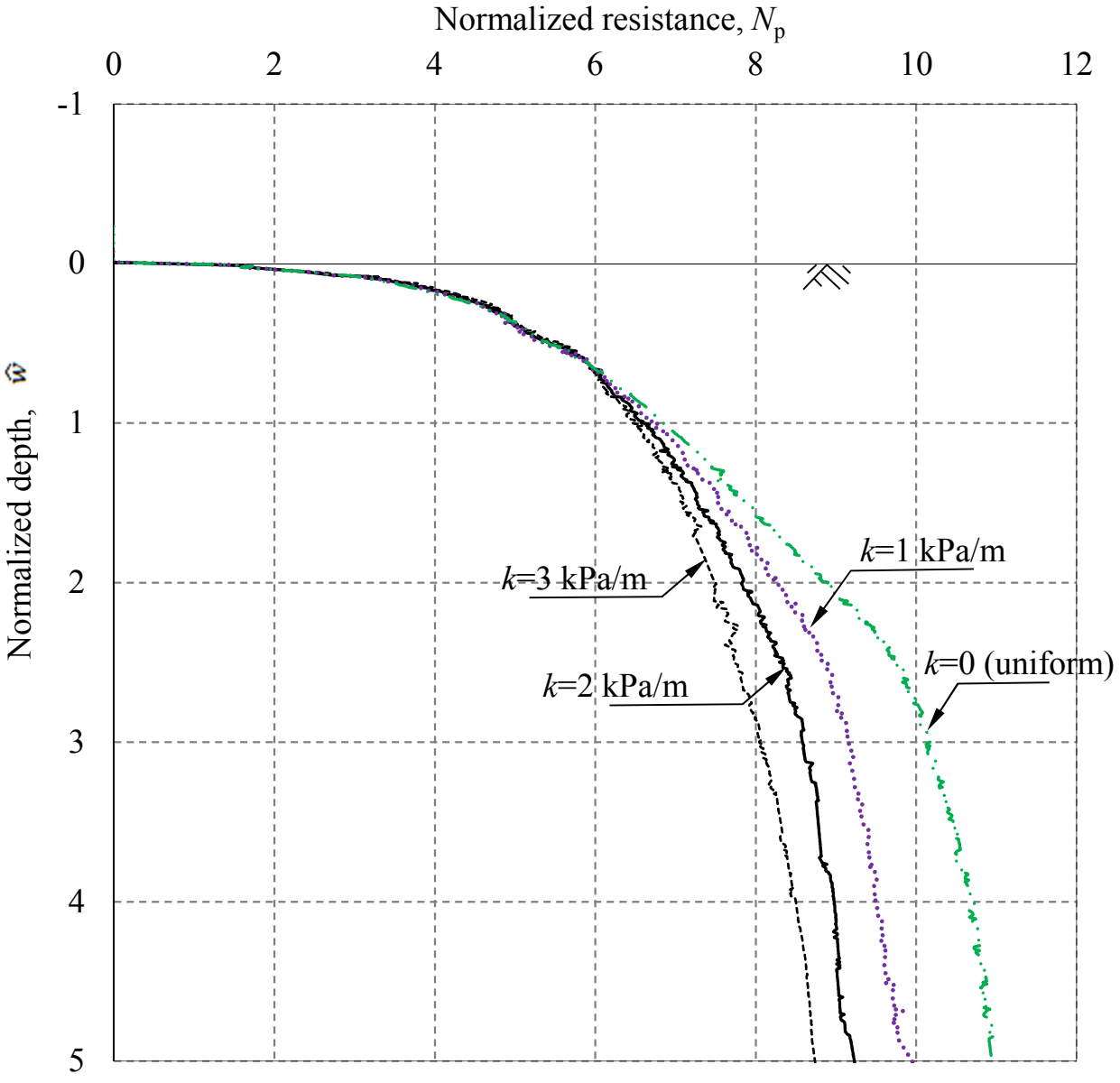

Fig. 4.14.Effects of shear strength gradient on penetration resistance (f_2 = 0.5; s_{um}= 2.3 kPa)

Table 4.1: Geometry and Parameters Used in CFX Analyses

Parameters	Values
Diameter of riser, D (mm)	350
Length of riser section, L (mm)	10
Saturated unit weight, γ_{sat} (kN/m^3)	16.31
Uniform soil shear strength, s_{u0}	
Undrained shear strength, s_{u0} (kPa)	3.7 (2.3,5)
Coefficient, f_2	1.0 (0.01,0.2,0.5)
Linearly increasing soil shear strength, $s_{u0} = s_{um} + ky'$	
Mudline shear strength, s_{um} (kPa)	2.3 (1.0,3.7)
Shear strength gradient, k (kPa/m)	2.0 (0,1,3)
Coefficient, f_2	0.01(0.2,0.5,1.0)

Note: Numbers in parenthesis in right column show the values used in the parametric study

CHAPTER 5

Numerical modelling of a steel catenary riser section in the touchdown zone under cyclic loading

Co-Authorship: This chapter has been submitted to a journal as a technical paper for review as: Dutta, S., Hawlader, B., and Phillips, R. (2017) "Numerical Modelling of a Steel Catenary Riser Section in the Touchdown Zone under Cyclic Loading." Most of the research presented in this chapter has been conducted by the first author. He has prepared the draft manuscript. The other two authors mainly supervised the research and reviewed the manuscript.

5.1 Abstract

The fatigue life of steel catenary risers is significantly influenced by cyclic riser–seabed–water interaction in the touchdown zone. In this study, the penetration and extraction behaviour of a shallowly embedded riser section subjected to cyclic vertical loading is simulated using a computational fluid dynamics approach with ANSYS CFX. A strength degradation model is proposed to capture the processes of undrained remoulding and clay–water interaction in the highly sheared interface termed as 'shear wetting.' The combined effect of strain rate and strength degradation on undrained shear strength of deep water offshore clay is implemented in CFX. A sufficiently large number of loading cycles is simulated using the present computationally efficient numerical technique to achieve a stable response. Significantly high reduction of penetration and extraction resistance of shallowly embedded pipe due to cyclic

loading, as observed in laboratory experiments, is obtained using the proposed strength degradation model with shear wetting, which cannot be explained simply by undrained remoulding.

Keywords: steel catenary riser; finite volume method; soft clay; cyclic loading; strength degradation; suction.

5.2 Introduction

Steel catenary risers (SCRs) — long flexible pipes of 150–600 mm typically diameter — are widely used in deepwater to transport hydrocarbon from seabed well systems to floating platforms or surface vessels. Environmental loading, such as surface wave or current, causes cyclic motion of the riser. One of the key concerns in the design is the fatigue response of risers near the touchdown point (TDP), the point where the riser first touches the seabed. The fatigue response is significantly influenced by riser–seabed–water interaction in the touchdown zone (TDZ), the zone where cyclic riser–soil interaction exists. In the current industry practice, the fatigue performance is mainly evaluated modelling seabed as linear/nonlinear spring or rigid surface. Large-scale field and laboratory tests (e.g., Bridge et al., 2003; Hodder and Byrne, 2010; Wang et al., 2014) and reduced-scale centrifuge tests (e.g., Hu, 2010; Elliott et al., 2013a, b, 2014) were conducted to understand the response of riser under cyclic loading. Still this complex behaviour is not well understood.

Environmental loading could cause six degrees of motion; however, the vertical motion of the riser is the most critical because the penetration near the TDP could increase the curvature and bending moment (Clukey et al., 2005). Moreover, suction under the riser during uplift also increases fatigue damage (Clukey et al., 2007; Ting et al., 2010). Therefore, the focus of the

present study is to investigate the response of SCR subjected to cyclic vertical motion only; although it is understood that the response might be influenced by the motions in the other directions in several ways such as altering trench shape/size and water flow mechanisms.

The riser separates from the seabed around the TDP when lifted upward during cyclic motion. The degree of separation is high during storm events because of the large amplitude vertical motion. Further away from the TDP in the buried zone, the amplitude of motion reduces and therefore the maximum vertical displacement may not be sufficient to cause separation of the riser from the seabed. As compared to large amplitude motion during storm events, risers generally experience much more frequent day-to-day small to medium amplitude cyclic motions over a long period that governs the fatigue design (Bridge, 2005; Clukey et al., 2005, 2007).

Model tests have been conducted to understand riser–seabed–water interaction under cyclic loading. In these tests, the invert of a model pipe section of diameter D is first penetrated into the seabed to the desired depth (w_{in}) and then cyclic vertical displacement of amplitude a is applied. Tests were conducted under submerged condition in order to investigate the effect of water. The depth of embedment (w) represents the vertical distance between the invert of the pipe and mudline (Fig. 5.1). For brevity, the symbols $\hat{w}=w/D$, $\hat{w}_{in}=w_{in}/D$ and $\hat{a}=a/D$ are used in the following sections. In most of the tests, cyclic loading started from a shallow initial embedment ($\hat{w}_{in}\leq 1.2$) (Bridge, 2005; Clukey et al., 2005; Aubeny et al., 2008; Langford and Aubeny, 2008a & b; Langford and Meyer, 2010) while some tests were performed from larger $\hat{w}_{in}$ (Clukey et al., 2008b; Hu et al., 2010 and Yuan et al., 2016). When the pipe is not fully covered by soil during cyclic loading, 'free water' available in the trench could interact with seabed sediment at the interface between water and clay.

The following are the key observations in these experimental programs when free water was available: (i) Pipe separates from the seabed during extraction in the large amplitude cyclic motions, and the degradation of resistance is high (Hodder et al., 2008 & 2009; Langford and Meyer, 2010; Yuan et al., 2016). (ii) Large number of small or intermediate amplitude cyclic motions also reduce the soil resistance significantly (Clukey et al., 2005, 2008b). (iii) Soil and free water mixing near the interface exacerbate the strength degradation process, and (iv) The degradation of soil resistance is much higher than T-bar tests when the cyclic motion is applied under fully embedded condition.

Recognizing the complex nature of riser–seabed–water interaction, mathematical models in the form of *P*-*y* curve, where *P* is the vertical reaction per unit length of riser and *y* is the vertical displacement, have been proposed for practical engineering purpose (Bridge et al., 2004; Aubeny and Biscontin, 2009; Randolph and Quiggin, 2009). A number of empirical model parameters are required in these models and the authors proposed the ranges for these parameters based on two-dimensional model test results (Dunlap et al., 1990; Bridge, 2005, Aubeny et al., 2008). The degradation of shear strength due to cyclic loading is not considered in these models. These models have been also used to investigate fatigue response of risers (e.g., Shiri and Randolph 2010; Ting et al. 2010; Li and Low 2011). Nakhaee and Zhang (2010) incorporated the degradation of soil resistance due to plastic deformation during cyclic loading in the *P*–*y* curve; however, they neglected the effects of water entrainment and erosion and thixotropy of seabed sediment. Aubeny et al. (2015) proposed a revised *P*-*y* curve where the effects of amplitude and number of loading cycles have been incorporated using a set of empirical equations.

Numerical modelling could provide further insights into the mechanisms and can explain some of these experimental observation. Finite element (FE) analysis of cyclic penetration and

extraction process in fully embedded (deep) condition is available in the literature (Zhou and Randolph, 2009). Similarly, FE modelling of penetration of shallowly embedded pipeline has been presented by a number of researchers (Wang et al., 2010; Chatterjee et al., 2012; Dutta et al., 2014). However, numerical modelling of extraction behavior at shallow depths is very limited. Clukey et al. (2008a) demonstrated some advantages of Eulerian simulation of riser–seabed–water interaction in the presence of free water. They suggested that soil and free water mixing might be incorporated in the strength degradation model, although it was not considered in that study. Moreover, simulations have been performed only for one loading cycle (one penetration followed by an extraction phase) instead of simulating a sufficiently large number of cycles. Using a finite element limit analysis program, Martin and White (2012) calculated the lower- and upper-bound limit loads of 'wished in place' pipes for rough/smooth and fully-bonded/unbonded cases. The soil has been modeled as rigid-plastic material without softening. Again, cyclic loading was not simulated in that study. The authors of the present study used the Eulerian solution technique in ANSYS CFX to model penetration of a pipe into a soft clay seabed (Hawlader et al., 2015a). They also implemented a simplified strength degradation model as a function of distance from the riser in CFX and simulated only one loading cycle (Hawlader et al., 2015b). Comparing with model test and FE results, it was shown that CFX can simulate both penetration and uplift behaviour.

In summary, when subjected to cyclic loading, the response of shallowly embedded SCR is very different from the response of a fully embedded T-bar. Numerical modelling of a SCR subjected to cyclic displacements near the seabed, where free water could play a major role, is not available. In the present study, numerical simulations in an Eulerian framework are performed using ANSYS CFX software which can accommodate both geotechnical and

hydrodynamic aspects of the problem. A strength degradation model is proposed and implemented in CFX to simulate the reduction of soil resistance under cyclic loading for a range of model parameters and loading conditions. Using this computationally efficient technique, simulation is continued over a sufficiently large number of cycles until considerable reduction in soil resistance is found.

5.3 Problem Statement

A section of pipe located at a distance y_w above the seabed is displaced downward to $w=w_{in}$ and then a sinusoidal cyclic displacement of amplitude a is applied maintaining an average velocity v_0 during penetration and extraction (Fig. 5.1). The simulation is performed for an undrained loading condition.

5.4 CFD Model Development

The general purpose ANSYS CFX 14.0 software is used for numerical modelling (ANSYS CFX, 2012). The computational fluid dynamics (CFD) approach has been used in the past not only for modelling fluid but also for the problems involved in soft seabed sediments including debris flows, glide blocks and out runner blocks modelling (De Blasio et al., 2004a, b, 2005; Gauer et al., 2005, 2006; Harbitz et al., 2003; Zakeri, 2009; Zakeri et al., 2009; Zakeri and Hawlader, 2013). The basic principle of CFD modelling, the similarity and differences between solid mechanics which is the basis of FE formulations and the advantages of CFD over FE methods to simulate riser–seabed–water interaction have been discussed in Hawlader et al. (2015 a, b).

Figure 5.2 shows the CFX model used in the present study. As CFX allows only three-dimensional modelling, the analysis is performed only for one element of 10 mm thickness in the out of plane direction. A riser section of D=350 mm and L=10 mm is placed in water above the seabed at y_w=1.0D. The soil and water domains are discretized into a three-dimensional mesh. Previous FE analyses and model tests for shallowly embedded conditions show that the soil elements outside 1.5D from the pipe surface does not experience significant deformation during vertical displacement (Dutta et al., 2014). A subdomain of 1.5D thickness, the shaded zone in Fig. 5.2, is created where mesh deformation is not allowed and therefore the size and shape of the mesh in the subdomain does not change with loading. However, mesh distortion is allowed outside the subdomain. Soil and water, modeled as Eulerian material, can flow through the mesh both inside and outside the subdomain and also through the outer boundary of the subdomain. Numerical issues related to mesh distortion are avoided using the subdomain. Further details are available in Hawlader et al. (2015, a,b).

All the boundaries are placed at sufficiently large distance from the riser to avoid boundary effects. The bottom and all the vertical boundaries are defined as impermeable surfaces. No-slip boundary condition is applied to the bottom, which represents zero velocity of soil elements next to this boundary. Free-slip boundary condition is applied to the right vertical face. Symmetry plane boundary condition is applied to the other three vertical faces, which implies that the flow of Eulerian materials (soil/water) on one side of the plane is a mirror image of the flow on the opposite side. The unspecified mesh motion option in CFX is used for the vertical walls. This setting allows the mesh node on these faces to move in the vertical direction, preserving the quality of mesh during the displacement of the riser. The top of the water is defined as an opening to allow water to flow in and out of the domain. Compared with typical FE modelling,

the above boundary conditions represent rollers in vertical faces and hinges at the bottom. The mudline is defined by the volume fraction tool in CFX. The volume fraction of water is 1.0 and clay is 0 above the mudline, while it is reverse in the elements below the mudline.

The riser is modeled as an impermeable wall with no-slip boundary condition. Following the concept of finite thickness interface element (Supachawarote et al., 2004; Jostad and Andresen, 2004), the shear strength of a thin zone of soil of 10 mm thickness around the riser is modeled as αs_u, where α=0 and α=1 represent the conditions similar to smooth and rough interface, respectively.

5.5 Shear Strength of Seabed Sediment

Experimental evidence shows that the undrained shear strength of clay (s_u) increases with shear strain rate ($\dot{\gamma}$) and decreases with accumulated plastic shear strain (ξ). Combining these two effects, Einav and Randolph (2005) proposed the following empirical equation.

$$s_u = f_1 f_2 s_{u0} \; s_u = f_1 f_2 s_{u0} \tag{1}$$

where f_1 and f_2 represent the strain rate and strain softening effects, respectively; s_{u0} is the value of s_u at the reference shear strain rate ($\dot{\gamma}_{ref}$) and prior to any softening. In this study, f_1 and f_2 are defined as (Einav and Randolph, 2005):

$$f_1 = 1 + \mu \log\left\{\frac{\max(\dot{\gamma}, \dot{\gamma}_{ref})}{\dot{\gamma}_{ref}}\right\} \tag{2}$$

$$f_2 = \frac{1}{S_t} + \left(1 - \frac{1}{S_t}\right) e^{-3\xi/\xi_{95}} \tag{3}$$

where μ is the rate of change of s_u per log cycle of $\dot{\gamma}$; remoulded sensitivity $S_t = s_{up}/s_{uR}$ in which s_{up} and s_{uR} are the peak and remoulded s_u, respectively, for a given ; and ξ_{95} is the value of ξ at which s_u is reduced by 95% of (s_{up}-s_{uR}) (Fig. 5.3).

Equation (3) successfully simulates the degradation of soil resistance during cyclic vertical movement of cylindrical objects if cycling occurs in fully embedded conditions such as T-bar tests (Zhou and Randolph, 2009). However, if the cycling occurs near the seabed, the reduction of reaction force on riser pipe is significantly high as compared to fully embedded condition (Clukey et al., 2005; Hodder et al., 2008; Langford and Meyer, 2010). For example, Hodder et al. (2008) showed a reduction of soil reaction on a riser section by a factor of 7.5 when cyclic loading was applied at w_{in}=0.5D, while S_t is only 2.4 when a T-bar was cycled under a fully embedded condition. Free water near the riser section and re-penetration of riser, which separates from the seabed during unloading, through the water filled trench attributed to a dramatic increase of the remolding process and additional s_u degradation. Experimental results also show that small amplitude cyclic motion could also cause a significant reduction of resistance which is again due to complex interaction behaviour between free water and soil, which cannot be explained simply using the remoulded strength of the soil (Clukey et al., 2005). However, the number of cycles required for a degree of remoulding is high for small amplitudes as compared to large amplitude cyclic motion where the riser separates from the seabed.

These experimental results clearly show additional strength reduction in the presence of free water. However, the modelling of free water effects on s_u degradation is very difficult. A number of factors might be involved in this process including water entrainment, soil-water mixing near interface, increase in pore water pressure and moisture content, high plastic shear strain accumulation, microchannel formation and erosion of disturbed soil. Clukey et al. (2008a)

noted that free water effect might be implicitly encompassed in an empirical s_u degradation function, although they did not propose any model or explicitly consider it in numerical modelling. Note that challenges in soil–water interface modelling have been encountered not only in this problem but also in other fields such as river bed erosion and hydroplaning in submarine debris flow.

Following the water entrainment concept of De Blasio and his co-workers for modelling runout of submarine landslides, the strength degradation process is divided into two components (De Blasio et al., 2005; Elverhøi et al., 2005). The first component is due to breakage of bond, fabric change and particle alignment that result from plastic shear strain accumulation (strain softening). This type of undrained remoulding occurs without significant change in moisture content (e.g. cyclic T-bar tests in fully embedded condition). The second component of s_u degradation occurs due to water entrainment in the highly sheared zone near the soil-water interface where free water is available. This process has been termed as 'shear wetting' (De Blasio, 2005; Elverhøi et al., 2005). Although it is difficult to quantify accurately, De Blasio (2005) proposed an empirical model for s_u degradation due to shear wetting as a function of shear strain. Based on some simplifying assumptions, Kobayashi et al. (2015) made an attempt to incorporate water entrainment effects in a modified Cam Clay based model.

The solid line abcd in Fig. 5.3 shows the s_u degradation model used in the present study. The line abe represents strain softening (Eq. (1)) without strain rate effect (i.e. f_l=1). In order to incorporate shear wetting effects, su is linearly decreased from s_{u95} to $s_{u(ld)}$ and then maintained constant (line bcd). As shown later, large plastic shear strains accumulate mainly near the riser and clay-water interface where shear wetting is also possible. Therefore, the shear wetting effect (segment bcd) is primarily applicable to the highly sheared zones near the clay-water interface.

Note that De Blasio (2005) also used an exponential degradation function similar to Eq. (3); however, the strain softening and shear wetting effects have been combined by defining sensitivity as $s_{up}/s_{u(ld)}$. In the present study, these effects are modeled separately (i.e. undrained remoulding at $\xi \leq \xi_{95}$ and shear wetting at $\xi > \xi_{95}$) because the mechanisms of strength degradation are different as discussed before. It has also some other advantages. The soil elements far from free water having $0 < \xi \leq \xi_{95}$ will experience only undrained remoulding effect. If De Blasio (2005) type model is used, these elements will have also some effect of shear wetting, because s_u degradation curve has been defined by $s_{u(ld)}$, which is not realistic as free water is not available.

The geometry and soil parameters used in the 'base case' analysis are shown in Table 5.1. A uniform s_{u0} of 2.25 kPa is used, although it is understood that s_{u0} might increase with depth in many cases. Typical range S_t is 2–5 for offshore sediments (Kvalstad et al., 2001). A range of ξ_{95}=10–50 and μ=0.05–0.2 have been used in the past for successful modelling of undrained remoulding and strain rate effects, respectively (Randolph, 2004; Einav and Randolph, 2005). Although it is difficult to quantify, the shear wetting parameter ξ_{ld}=15–35 is used. The value of s_u after ξ_{ld} is assumed to be 0.1 kPa.

5.6 Numerical Implementation

Both clay and water are modeled as homogeneous multiphase Eulerian materials where the shear behaviour is defined using the dynamic viscosity (μ_d). For water, a constant value of dynamic viscosity is used (Table 5.1). Clay is modeled as rigid-plastic material with $\mu_d = s_u/\dot{\gamma}$, where s_u is defined by Fig. 5.3. Using the CFX Expression language—a declarative language in

CFX for enhanced simulation—the displacement of riser, material properties and desired output variables are defined.

The CFX does not have any direct option to define s_u as Fig. 5.3. Therefore, in each time increment, $\dot{\gamma}$ is called, which represents the second invariant of the deviatoric strain rate tensor (a scalar quantity). Multiplying $\dot{\gamma}$ by time increment (Δt), the shear strain increment $\Delta\xi$ is calculated. Summing up $\Delta\xi$ over the period of analysis, the accumulated strain ξ is calculated. The authors developed a special technique in CFX to calculate ξ. Using the value of $\dot{\gamma}$ and ξ, s_u is calculated for each element, which is then used to update μ_d.

5.7 Results of Base Case Analysis

5.7.1 *Penetration and Uplift Resistance*

Figure 5.4(a) shows the variation of normalized resistance ($N=F/s_{uN}D_eL$) with normalized depth ($\hat{w}= w/D_e$) for the base case. The undrained shear strength used for normalization (s_{uN}) is $2/\sqrt{3}\ s_{u0}$ (see Hawlader et al. (2015 a, b) for further discussion). As finite thickness interface elements together with no-slip riser–soil interface condition are used, the failure occurs through the soil instead of riser–soil interface. Therefore, following the concept of Gui and Bolton (1998) and assuming that the failure occurs at a distance of half of the element thickness from the outer surface of the riser, the value of effective diameter (D_e) is calculated as 360 mm (=350 mm + 2×10/2 mm) for 10-mm element size just outside the riser.

Figure 5.4(a) shows that both the penetration and uplift resistance decrease with number of cycle (n), although the reduction of N per cycle reduces with increase in n. Note that, if the extraction is continued instead of re-penetration at $\hat{w}$=0.25, the uplift resistance will decrease and

the riser pipe will be separated from the seabed leaving a trench in some cases as observed in model tests (Bridge, 2005) and simulated by the authors in Hawlader et al. (2015b).

The simulation shown in Fig. 5.4(a) takes only 2.5 hours with a 3.4 GHz Intel Core i7 processor and 12 GB RAM. To compare, large deformation FE analysis is performed using Abaqus CEL only for penetration from the seabed to $\hat{w}$=0.5 (see Dutta et al. 2014 for further details). The present CFX analysis is more than six times faster than Abaqus CEL analysis. The use of a subdomain of fine mesh that moves without any deformation during cyclic motion, together with different solution techniques in CFD, make CFX simulation computationally very efficient. Note that the extraction phase is not simulated using Abaqus CEL because the versions to date cannot model the interface tensile capacity (bonding) properly, which is a very important factor in uplift behaviour.

A similar analysis is performed without shear wetting (i.e. s_u degradation is modeled by the line abe instead of abcd in Fig. 5.3). Figure 5.4(b) shows that both penetration and uplift resistance decrease with n; however, after 6–8 cycles the resistance does not decrease further with cyclic loading. A comparison of Figs. 5.4(a) and 5.4(b) shows that penetration and uplift resistances are same in both figures for the first few loading cycles, because the initial part of s_u degradation curve (segment ab in Fig. 5.3) is the same in both simulations. However, when $\xi > \xi_{95}$, s_u degradation is more in the former case (Fig. 5.4a) with shear wetting (see the vertical distance between lines be and bcd in Fig. 5.3). Therefore, the degradation of resistance continues over a large number of cycles in Fig. 5.4(a) and provides low resistance compared to Fig. 5.4(b).

For a better comparison, the normalized resistance presented in Figs. 5.4(a) and 5.4(b) is plotted against n in Fig. 5.5. Following Randolph et al. (2007), the values of N at the halfway of riser travel during cyclic loading (i.e. at w=0.375D_e in Fig. 5.4) are obtained (solid circle and

triangle in Fig. 5.4a). The obtained penetration and uplift resistances at a given cycle (N_i) is then normalized by the penetration resistance at w=0.375D_e during initial penetration (point A in Fig. 5.4a) which is denoted as $N_{0.25}$ assuming that 25% of the average total strain that accumulates in the first cycle is developed at this stage (Zhou and Randolph 2009) and therefore it is considered as n=0.25. Similarly, n=0.75 at w=0.375D_e during first uplift (point C in Fig. 5.4a). The degradation of resistance with cyclic loading is then examined defining the ratio of normalized resistance as $R_n = N_i/N_{0.25}$. The ratio of extraction to penetration resistance for the first cycle ($N_{0.75}/N_{0.25}$) is 0.82, and therefore uplift curves in Fig. 5.6 started from R_n=0.82. This ratio depends on several factors such as soil properties and loading conditions, as presented in the parametric study. Physical model test results also show a wide variation of this ratio (Bridge et al., 2005).

A very close agreement between the simulations with and without shear wetting in the first 4 cycles indicates that overall ξ is less than ξ_{95}. However, the difference between these two simulations increases with cycle number. R_n is almost constant after 10 cycles in the simulation without shear wetting, which represents the undrained remolded condition as observe in cyclic T-bar tests in fully embedded condition. However, the degradation process continues in the shear wetting case, and after 29 cycles considerably low penetration and extraction resistances, compared to no shear wetting case, are obtained. Define the inverse of R_n (=$N_{0.25}/N_i$) at a large value of n (=30 in this case) as the sensitivity considering shear wetting as S_{t_swp} and S_{t_swu} for penetration and uplift, respectively. From Fig. 5.6, S_{t_swp}=7.7 and S_{t_swu}=17 can be obtained. Such a high level of resistance degradation has been reported in a number of previous studies from physical model tests when cycling occurred near the seabed having free water available (Hodder

et al., 2008, Clukey et al., 2005). In the present study, the consideration of shear wetting could explain this process.

In the following sections, the degradation of resistance with n is examined using R_{n-n} curves as presented in Fig. 5.6.

5.7.2 *Plastic Shear Strain*

Figure 5.7 shows the accumulated plastic shear strain during the 5th, 10th, 15th and 20th cycle just before the end of penetration to $\hat{w}$=0.5. The figures in the left column (Figs. 5.7a–d) show the results for no shear wetting case while the right column (Figs. 5.7e–h) is for shear wetting case. At the 5th cycles, ξ and instantaneous soil velocity vectors are very similar for both cases (Figs. 5.7a and 5.7e). The colored zone in these figures represents the area where shear wetting occurs (ξ>10, i.e. ξ>ξ_{95}). As the difference between s_u at these strains is not very significant (see Fig. 5.3), the velocity vectors and resistance are almost the same in both cases. At n=10, the zone of large ξ is slightly smaller in Fig. 5.7(f) than that in Fig. 5.7(b). At these strains considerable s_u reduction occurs due to shear wetting and therefore gives low resistance as compared to no shear wetting case (Fig. 5.5). With increase in n, high shear strains mainly localised near the riser in the shear wetting case, which reduces s_u significantly in that zone. Therefore, in this case, soil elements mainly displace in this narrow zone as shown by the instantaneous velocity vectors (Figs. 5.7g and 5.7h). However, for no shear wetting case, soil elements displace over a large area (Figs. 5.7c and 5.7d).

As s_u decreases significantly when shear wetting is considered, this weak soil can displace easily during re-penetration and therefore a higher berm near the riser can form as shown in Figs. 5.7g and 5.7h. However, the berm shape is different when shear wetting is not considered.

The highly s_u degraded soil around the riser might be eroded by flow of this weak soil along the length of the riser during cyclic motion and by current when it reaches the seabed. These factors, together with lateral movement, could enhance the shear wetting process and trench formation as observed in the field (Bridge, 2005). The effects of these factors need to be studied further.

5.7.3 *Suction under Riser during Uplift*

Figure 5.8 shows the suction (-ve pressure with respect to the initial) under the riser during the 5th, 10th, 15th and 20th cycle just before re-penetration at $\hat{w}$=0.25. The contour intervals of suction are shown in logarithmic scale for clarity. Note that, although cycle numbers are same as before, because of additional upward displacement of 0.25D, ξ at this stage is higher than the values shown in Fig. 5.7 but the pattern of ξ is very similar to Fig. 5.7 and therefore is not shown again. Instead, the development of suction is examined which is an important parameter for design. Comparison of figures in the left and right columns of Fig. 5.8 shows that suction reduces with number of cycles if shear wetting is considered. The suction pulls the soil elements down toward the invert of the riser. The extent of zone and magnitude of suction reduce with n in shear wetting case because of reduction of s_u with n. However, such reduction is not significant when shear wetting is not considered and therefore a very small change in uplift resistance is calculated after n=5 (Fig. 5.6). Langford and Meyer (2010) conducted model tests using 174 mm diameter riser section cycled in highly plastic West African clay where the pore pressure was measured at the invert of the riser. Although their test configuration was different from the present study (s_{u0}=5–7 kPa, cycled between $\hat{w}$=0 and $\hat{w}$=0.5), a negative pore pressure of

approximately 10 kPa at the first cycle and it subsequent reduction similar to Figs. 5.8e–h suggest that present numerical modelling can simulate the process.

One important observation is that, when shear wetting is considered, a trough above the clay–water interface forms in the remoulded soil (Figs. 5.8 f–h). The size of the trough increases with n. During extraction, water gushes toward the trough as shown by instantaneous velocity vectors of water above the clay–water interface. The bottom of the trough (e.g. point B in Fig. 5.8h) progresses deeper than the highest point clay sticks to the pipe surface (point A). Note that, based on experimental observation Clukey et al. (2008a) suggested that during uplift clay might adhere to the riser while failure might occur through the soil. Present simulation with shear wetting can explain that process. When shear wetting is not considered this type of trough does not form.

5.8 Parametric Study

The parametric study is performed for the shear wetting case varying only one parameter while other parameters are same as the base case (Table 5.1).

5.8.1 *Effect of μ*

The value of μ could vary between 0.05 and 0.2 (Einav and Randolph, 2005; Lehane et al., 2009). Figure 5.9 shows a very small difference between R_{n-n} curves with μ=0.05–0.2 for both penetration and extraction resistance. Note however that N_i and $N_{0.25}$ increases with μ although their ratio (R_n) is almost same for all 4 values of μ. For example, $N_{0.25}$ is 6.4 and 7.9 for μ=0.11 and μ=0.2, respectively. In summary, μ has a negligible effect on R_n and therefore R_n is a better parameter to describe cyclic degradation than N_i.

5.8.2 *Effect of S_t*

The remoulded sensitivity of offshore clays typically varies between 2 and 5 (Kvalstad et al., 2001; Andersen and Jostad, 2004; Randolph, 2004). As shown in Fig. 5.3 that with increase in S_t the point b shifts downward, meaning that s_u degrades quickly with ξ. As a result both penetration and extraction resistances decreases quickly for high S_t as shown in Fig. 5.10. However, R_n is almost same for all three values of S_t at large n. Because at this stage significantly high ξ generates around the riser (Fig. 5.7) and therefore s_u degrades to $s_{u(ld)}$, which is same for all three cases.

5.8.3 *Effect of ξ_{95}*

Figure 5.11 shows that R_n decreases quickly with decrease in ξ_{95}, because the lower value of ξ_{95} the faster the degradation of s_u (Fig. 5.3). Similar to Fig. 5.10, R_n is almost same at large n because s_u degrades to $s_{u(ld)}$ at this stage near the riser.

5.8.4 *Effect of ξ_{ld}*

While S_t and ξ_{95} primarily affect the shape of the initial part of the s_u degradation curve ($\xi \leq \xi_{95}$), ξ_{ld} mainly influence the later part at large ξ (Fig. 5.3). Figure 5.12 shows that ξ_{ld} does not have any influence on R_n up to 4 cycles of loading. However, with increase in n, the zone of large plastic shear strain ($\xi_{95} < \xi < \xi_{ld}$) around the riser increases where s_u degrades quickly for small ξ_{ld}. Therefore, at a given n (>4), Rn is smaller for smaller values of ξ_{ld}. Again, R_n will be same for all three ξ_{ld} if the analysis is continued for a large number of cycles, because s_u will degrade to $s_{u(ld)}$.

5.8.5 *Effect of Initial Embedment (w_{in})*

Depending upon location with respect to the TDP, installation and loading conditions, a section riser might have different initial depths of embedment and experience cyclic loading of different amplitudes.

Figure 5.13 shows that R_n decreases quickly with n for shallow initial penetration depths. This trend is similar to the first episode of 20 cycles of Hodder et al. (2009) where they showed that the slope of the load–displacement curve (stiffness) decreases rapidly for shallow initial embedments. At large n, the uplift resistance is almost same for this range of w_{in} because the localized shear strength of highly remoulded clay at high ξ mainly governs the extraction behaviour. However, for penetration, R_n at large n increases with w_{in} because, unlike extraction, the penetration behaviour is also influenced by the less remoulded clay outside the highly remoulded zone and the influence is more for the deeper conditions. This has been verified by examining clay velocity vectors at these stages.

5.8.6 *Effect of Cyclic Amplitude (a)*

Experimental evidences show that small- to large-amplitude riser motion could cause significant degradation of cyclic resistance (Clukey et al., 2008b; Hodder et al., 2009; Langford and Meyer, 2010). Figure 5.14 shows the variation of R_n with n for two amplitudes (a=0.1D and 0.25D). In both cases $\hat{w}_{in}$=0.5. Because of higher displacement of the riser in each cycle, R_n decreases quickly with n for a=0.25D and becomes almost constant after n=25. The reduction of R_n with n is slow for low amplitude motion of a=0.1D and the reduction continues even until 60 cycles. Similar trend of decreasing resistance for small amplitude motion has been reported from model tests (Clukey et al., 2005).

Very large amplitude motions near the TDP are expected during storm events, although it does not occur frequently. The effect of water flow in the trench along the riser is more significant near the TDP. This has not been simulated in this study.

5.9. Conclusions

Numerical modeling of penetration and extraction behaviour of a section of riser subjected to cyclic vertical motion at shallow depths is presented in this study. In order to capture the role of free water in the trench and suction under the riser during extraction, the numerical simulation is performed using a computational fluid dynamics approach in ANSYS CFX software. A strain rate and strain softening depended model for undrained shear strength of clay is used. In addition to undrained remoulding, the potential effect of water entrainment in the highly sheared zone is incorporated in the strength degradation model using the concept of shear wetting. The present CFX model successfully simulates the flow/large deformation of clay and water around the riser, together with the formation of trench and berm, during cyclic loading. The following conclusions are drawn from this study.

1) No significant reduction in penetration and extraction resistances is found after a number of cycles when the strength degradation of clay only due to undrained remoulding is considered. However, the analyses with shear wetting show continued reduction of resistances over a large number of cycles.

2) The additional reduction of resistance in shear wetting cases supports the experimental observation that the undrained remoulding alone cannot explain the complete degradation process during cyclic loading.

3) When the shear wetting is considered, after a large number of cycles, the extent of the soil failure mechanism around the riser reduces because of significant reduction of strength of soil that flows through this narrow zone, which also causes the reduction of suction under the riser during extraction.

4) The rate of reduction of normalized resistance ratio with number of cycle decreases with increase in initial depth of embedment and increases with cyclic amplitude.

5) The normalized resistance ratio is almost independent of strain rate, although the resistance itself increases with strain rate. The rate of reduction of normalized resistance ratio with number of cycle increases with the model parameters that accelerate the soil strength degradation process—high remoulded sensitivity, low ξ_{95} and low ξ_{ld}.

Finally, although the inclusion of shear wetting could explain better the reduction of resistance as observed in physical experiments, which cannot be explained using the remoulded sensitivity only, the complex process of water entrainment and its effects on undrained shear strength need to be studied further. Moreover, the effects of a number of factors, such as combined vertical–horizontal cyclic motion, erosion of remoulded soil and reconsolidation, should be investigated.

Acknowledgements

The works presented in this paper have been supported by the Natural Sciences and Engineering Research Council of Canada (NSERC), Mitacs, and Petroleum Research Newfoundland and Labrador (PRNL).

Notations

a cyclic amplitude

D riser diameter

D_e effective riser diameter

F resistance

f_1 strain rate effects

f_2 strain softening effects

L length of riser section in the out of plane direction

N_i normalized resistance at ith cycle

$N_{0.25}$ normalized resistance at 0.25 cycle

$N_{0.75}$ normalized resistance at 0.75 cycle

n number of cycle

R_n ratio of normalized resistance

s_u mobilized undrained shear strength

s_{u0} intact undrained shear strength

s_{up} peak undrained shear strength

s_{u95} s_u at ξ_{95}

$s_{u(ld)}$ s_u at ξ_{ld}

s_{uN} $(2/\sqrt{3})\, s_{u0}$

s_{uR} remoulded undrained shear strength

S_t remoulded sensitivity

S_{t_SWp} inverse of R_n for penetration at large n

S_{t_SWu} inverse of R_n for uplift at large n

v_0 riser velocity

w invert depth of riser from seabed

w_{in} initial w

y_w initial distance from the riser to mudline

α riser–soil interface factor

μ shear strain rate parameter

μ_d dynamic viscosity

γ' submerged soil unit weight

$\dot{\gamma}$ shear strain rate

$\dot{\gamma}_{ref}$ reference shear strain rate

ξ accumulated absolute plastic shear strain

References

Andersen, K. H. & Jostad, H. P. (2004). Shear strength along inside of suction anchor skirt wall in clay. *Proceedings of the offshore technology conference*, Houston, TX, USA. OTC 16844.

ANSYS CFX (2012). *CFX program* (*version 14.0*) *solver theory guide*, ANSYS, Canonsburg, PA, USA.

Aubeny, C. P., & Biscontin, G. (2009). Seafloor–riser interaction model. *ASCE Int. J. Geomech.* **9**, No. 3, 133–141.

Aubeny, C. P., Shi, H. & Murff, J. D. (2005). Collapse loads for a cylinder embedded in trench in cohesive soil. *ASCE Int. J. Geomech.* **5,** No. 4, 320–325.

Aubeny, C. P., Gaudin, C. & Randolph, M. (2008). Cyclic tests of model pipe in kaolin. *Soc. Petroleum Engs.* **3**, No. 4, 1–6. doi:10.2118/123131-PA.

Aubeny, C. P., White, T. A., Langford, T., Meyer, V. & Clukey, E. C. (2015). Seabed stiffness model for steel catenary risers. *Proceedings of the 3rd international symposium on frontiers in offshore geotechnics* (*ISFOG*), Oslo, Norway, pp. 351–356.

Bridge, C. (2005). *Effects of seabed interaction on steel catenary risers*. PhD Thesis, University of Surrey, UK.

Bridge, C., Howells, H., Toy, N., Parke, G. & Woods, R. (2003). Full scale model tests of a steel catenary riser. *Proceedings of the international conference of fluid structure interaction*, Cardiz, Spain, pp.107−116.

Bridge, C., Laver, K., Clukey, E., & Evans, T. (2004). Steel catenary riser touchdown point vertical interaction models. *Proceedings of the offshore technology conference*, Houston, TX, USA. OTC 16628.

Chatterjee, S., Randolph, M. F. & White, D. J. (2012). The effects of penetration rate and strain softening on the vertical penetration resistance of seabed pipelines. *Géotechnique* **62**, No. 7, 573–582.

Clukey, E. C., Haustermans, L. & Dyvik, R. (2005). Model tests to simulate riser–soil interaction in touchdown point region. *Proceedings of the 1st international symposium on frontiers in offshore geotechnics* (*ISFOG*), pp. 651–658.

Clukey, E., Ghosh, R., Mokarala, P. & Dixon, M. (2007). Steel catenary riser (SCR) design issues at touchdown area. *Proceedings of the 17th international offshore and polar engineering conference* (*ISOPE*), pp. 814–819.

Clukey, E., Jacob, P. & Sharma, P. (2008a). Investigation of riser seafloor interaction using explicit finite element methods. *Proceedings of the offshore technology conference*, Houston, TX, USA. OTC 19432.

Clukey, E., Young, A. G., Garmon, G. S., & Dobias, J. R. (2008b). Soil response and stiffness laboratory measurements of SCR pipe/soil interaction. *Proceedings of the offshore technology conference*, Houston, TX, USA. OTC 19303.

De Blasio, F., Elverhøi, A., Issler, D., Harbitz, C., Bryn, P. & Lien, R. (2004a). Flow models of natural debris flows originating from overconsolidated clay materials. *Marine Geo.* **213**, No. 1, 439–455.

De Blasio, F., Engvik, L., Harbitz, C. & Elverhøi, A. (2004b). Hydroplaning and submarine debris flows. *J. Geo. Res.* **109**, No. C011002, 1–15.

De Blasio, F., Elverhøi, A., Issler, D., Harbitz, C., Bryn, P. & Lien, R. (2005). On the dynamics of subaqueous clay rich gravity mass flows—the giant Storegga slide, Norway. *Mar. Petroleum Geo.* **22**, No. 1–2, 179–186.

Dunlap, W. A., Bhojanala, R. P., & Morris, D. V. (1990). Burial of vertically loaded offshore pipelines in weak sediments. *Proceedings of the Offshore Technology Conference*, Houston, TX, USA. OTC 6375.

Dutta, S., Hawlader, B. & Phillips, R. (2014). Finite element modeling of partially embedded pipelines in clay seabed using Coupled Eulerian–Lagrangian method. *Can. Geotech. J.* **52**, No. 1, 58–72.

Einav, I., & Randolph, M. F. (2005). Combining upper bound and strain path methods for evaluating penetration resistance. *Int. J. Numer. and Analy. Methods in Geotech. Eng.* **63**, No. 14, 1991–2016.

Elliott, B. J., Zakeri, A., Macneill, A., Phillips, R., Clukey, E. C. & Li, G. (2013a). Centrifuge modeling of steel catenary risers at touchdown zone part I: Development of novel centrifuge experimental apparatus. *Ocean Engng.* **60**, No. 1, 200–207.

Elliott, B. J., Zakeri, A., Barrett, J., Hawlader, B., Li, G. & Clukey, E. C. (2013b). Centrifuge modeling of steel catenary risers at touchdown zone part II: Assessment of centrifuge test results using kaolin clay. *Ocean Engng.* **60**, No. 1, 208–218.

Elliott, B., Phillips, R., Macneill, A. & Piercey, G. (2014). Physical modelling of SCR in the touchdown zone under three axis motions. *Proceedings of the 8th international conference on physical modelling in geotechnics* (*ICPMG*), Perth, Australia, pp. 265–270.

Elverhøi, A., Issler, D., De Blasio, F.V. and Ilstad, T., Harbitz, C.B. and Gauer, P. (2005). Emerging insights into the dynamics of submarine debris flows. *Nat. Haz. and Ear. Sys. Sci.* **5**, No. 5, 633–648.

Gauer, P., Kvalstad, T. J., Forsberg, C. F., Bryn, P. & Berg, K. (2005). The last phase of the Storegga Slide: Simulation of retrogressive slide dynamics and comparison with slide-scar morphology. *Mar. Petroleum Geol.* **22**, No. 1–2, 171–178.

Gauer, P., Elverhøi, A., Issler, D. & De Blasio, F.V. (2006). On numerical simulation of subaqueous slides: Back calculations of laboratory experiments of clay rich slides. *Nor. J. Geo*. **86**, No. 3, 295–300.

Gui, M. W. & Bolton, M. D. (1998). Geometry and scale effects in CPT and pile design. *Proceedings of the 1st international conference on geotechnical site characterization*, Atlanta, GA, USA, pp. 1063–1068.

Harbitz, C.B., Parker, G., ElverhØi, A., Marr, J.G., Mohrig, D. & Harff, P.A. (2003). Hydroplaning of subaqueous debris flow and glide blocks: Analytical solutions and discussions. *J. Geophy. Res*. **108**, No. B 7, 1–18.

Hawlader, B., Dutta, S., Fouzder, A. & Zakeri, A. (2015a). Penetration of steel catenary riser in soft clay seabed: Finite element and finite volume methods. *ASCE Int. J. Geomech.* **15**, No. 6, 1–12.

Hawlader, B., Fouzder, A. & Dutta, S. (2015b). Numerical modeling of suction and trench formation at the touchdown zone of steel catenary riser. *ASCE Int. J. Geomech* **16**, No. 1, 1–14.

Hodder, M.S., White, D.J. & Cassidy, M.J. (2008). Centrifuge modelling of riser–soil stiffness degradation in the touchdown zone of a steel catenary riser. *Proceedings of the 27th international conference on offshore mechanics and arctic engineering* (*OMAE*), Estoril, Portugal, pp. 1–9.

Hodder, M. S., White, D.J. & Cassidy, M. (2009). Effect of remolding and reconsolidation on the touchdown stiffness of a steel catenary riser: Observations from centrifuge modelling. *Proceedings of the offshore technology conference*, Houston, TX, USA. OTC 19871.

Hodder, M. S., & Byrne, B. W. (2010). 3D experiments investigating the interaction of a model SCR with the seabed. *Appl. Ocean Res.* **32**, No. 2, 146–157.

Hu, H. J. E. (2010). *Pipeline/riser soil interaction analysis*. PhD Thesis, National University of Singapore, Singapore.

Jostad, H.P. & Andresen, L. (2004). Modelling of shear band propagation in clays using interface elements with finite thickness. *Proceedings of the 9th international symposium on numerical models in Geomechanics - NUMOG IX*, Ottawa, ON, Canada, pp. 121–128.

Kobayashi, T., Soga, K. & Dimmock, P. (2015). Numerical analysis of submarine debris flows based on critical state soil mechanics. *Proceedings of the 3rd international symposium on frontiers in offshore geotechnics (ISFOG),* Oslo, Norway, pp. 975–980.

Kvalstad, T., Nadim, F. & Arbitz, C. (2001). Deepwater geohazards: Geotechnical concerns and solutions. *Proceedings of the offshore technology conference,* Houston, TX, USA. OTC 12958.

Langford, T. & Aubeny, C. (2008a). Model tests for steel catenary riser in marine clay. *Proceedings of the offshore technology conference*, Houston, TX, USA. OTC 19495.

Langford, T. & Aubeny, C. (2008b). Large scale soil–riser model testing on high plasticity clay. *Proceedings of the 18th international offshore and polar engineering conference (ISOPE)*, Vancouver, BC, Canada, pp. 80–86.

Langford, T.E. & Meyer, V.M. (2010). Vertical cyclic testing of model steel catenary riser at large scale. *Proceedings of the 2nd international symposium on frontiers in offshore geotechnics (ISFOG)*, Perth, Australia, pp. 803–808.

Lehane, B. M., O'Loughlin, C.D., Gaudin, C. & Randolph, M.F. (2009). Rate effects on penetrometer resistance in kaolin. *Géotechnique* **59**, No. 1, 41–52.

Li, F. Z. & Low, Y.M. (2011). Fatigue analysis of a steel catenary riser with uncertain seabed parameters. *Proceedings of the 30th international conference on ocean, offshore and arctic engineering* (*OMAE*), Rotterdam, Netherlands, pp. 1–9.

Martin, C. & White, D. (2012). Limit analysis of the undrained bearing capacity of offshore pipelines. *Géotechnique* **62**, No. 9, 847–863.

Nakhaee, A. & Zhang, J. (2010). Trenching effects on dynamic behavior of a steel catenary riser. *Ocean Engng.* **37**, No. 2–3, 277–288.

Randolph, M. F. (2004). Characterization of soft sediments for offshore applications. *Proceedings of the 2nd international conference on site characterization*, Porto, Portugal, pp. 209−232.

Randolph, M., Low, H. E. & Zhou, H. (2007). In situ testing for design of pipeline and anchoring systems. *Proceedings of the 6th international offshore site investigation and geotechnics conference: Confronting new challenges and sharing knowledge*, London, UK.

Randolph, M. & Quiggin, P. (2009). Non-linear hysteretic seabed model for catenary pipeline contact. *Proceedings of the 28th international conference on ocean, offshore and arctic engineering* (*OMAE*), Honolulu, HI, USA, pp. 145–154.

Shiri, H. & Randolph, M. (2010). The influence of seabed response on fatigue performance of steel catenary risers in touchdown zone. *Proceedings of the 29th international conference on ocean, offshore, and arctic engineering* (*OMAE*), Shanghai, China, pp. 1–10.

Supachawarote, C., Randolph, M. & Gourvenec, S. (2004). Inclined pull-out capacity of suction caissons. *Proceedings of the 14th international offshore and polar engineering conference* (*ISOPE*), Toulon, France, pp. 500–506

Ting, I. H. Y., Kimiaei, M. & Randolph, M. F. (2010). Advanced nonlinear hysteretic seabed model for dynamic fatigue analysis of steel catenary risers. *Proceedings of the 2nd international symposium on frontiers in offshore geotechnics*, Perth, Australia, pp. 833–838.

Wang, D., White, D. J. & Randolph, M. F. (2010). Large-deformation finite element analysis of pipe penetration and large-amplitude lateral displacement. *Can. Geotech. J.* **47**, No. 8, 842–856.

Wang, K., Xue, H., Tang, W. & Guo, J. (2013). Fatigue analysis of steel catenary riser at the touch-down point based on linear hysteretic riser-soil interaction model. *Ocean Engng.* **68**, 102–111.

Wang, L., Zhang, J., Yuan, F. & Li, K. (2014). Interaction between catenary riser and soft seabed: Large-scale indoor tests. *App. Ocean. Res*. **45**, 10−21.

Yuan, F., White, D. J. & O'Loughlin, C. D. (2016). The evolution of seabed stiffness during cyclic movement in a riser touchdown zone on soft clay. *Géotechnique* (*ahead of print*).

Zakeri, A. (2009). Submarine debris flow impact on suspended (free-span) pipelines: Normal and longitudinal drag forces. *Ocean Engng.* **36**, No. 6, 489–499.

Zakeri, A. & Hawlader, B. (2013). Drag forces caused by submarine glide block or out-runner block impact on suspended (free-span) pipelines—Numerical analysis. *Ocean Engng.* **67**, 89–99.

Zakeri, A., Høeg, K. & Nadim, F. (2009). Submarine debris flow impact on pipelines—Part II: Numerical analysis. *Coastal Engng.* **56**, No. 1, 1–10.

Zhou, H. & Randolph, M. (2009). Numerical investigations into cycling of full flow penetrometers in soft clay. *Géotechnique* **59**, No. 10, 801–812.

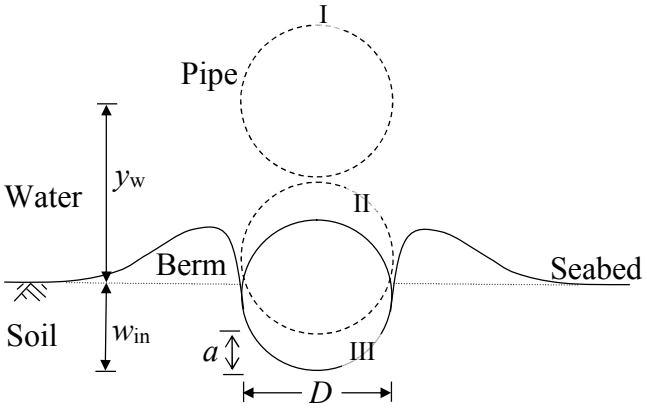

Fig. 5.1. Problem statement

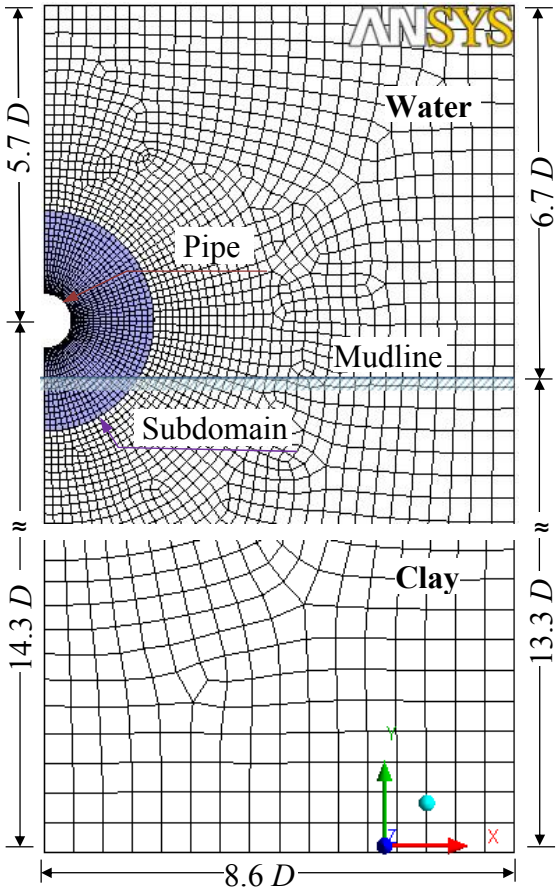

Fig. 5.2. Finite volume model

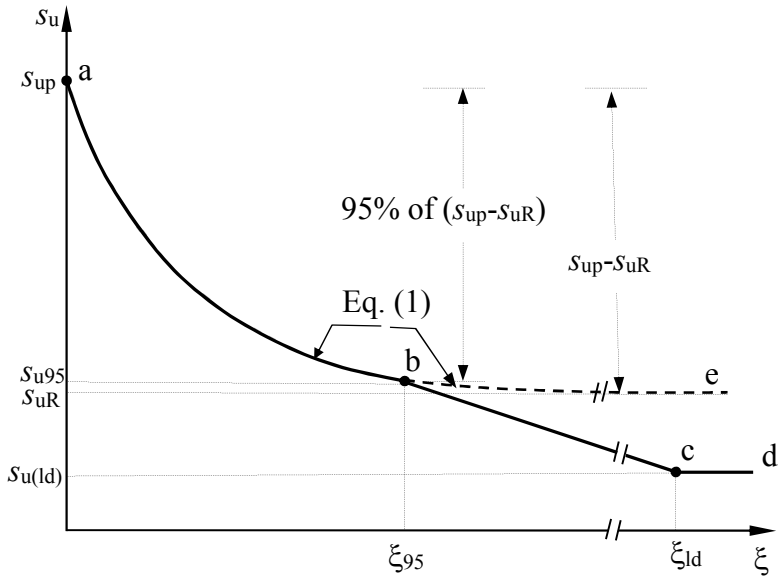

Fig. 5.3. Shear strength degradation model

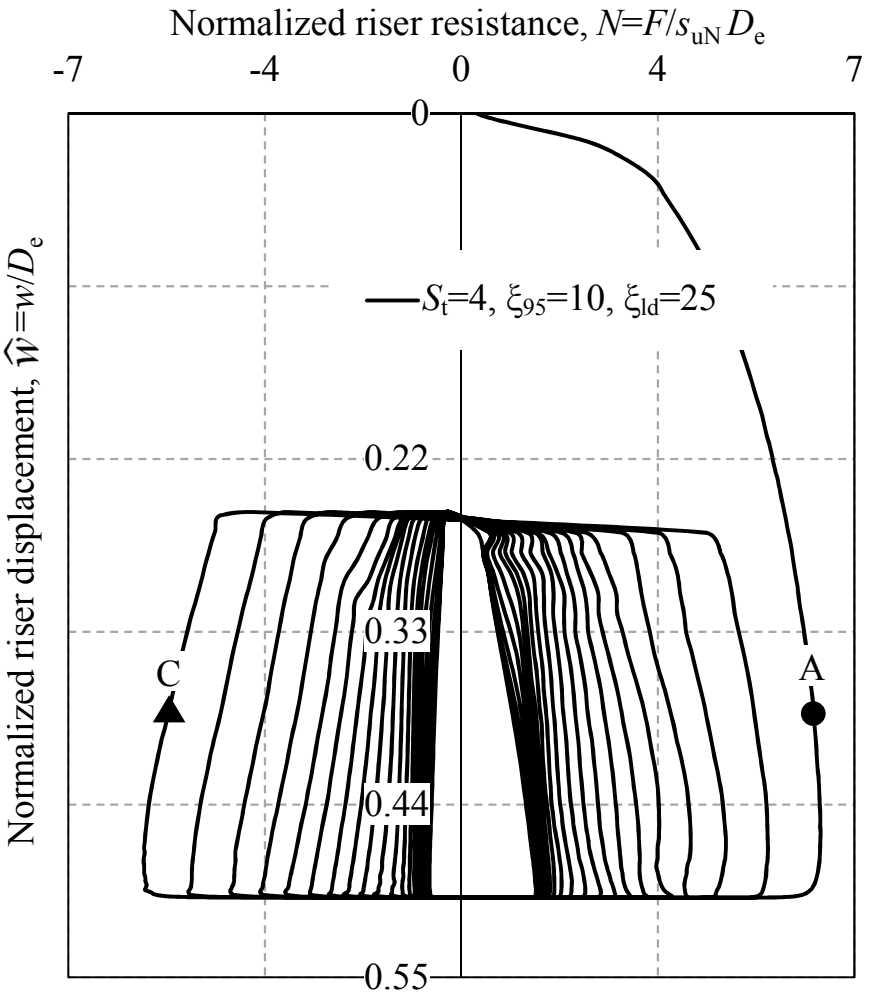

Fig. 5.4(a). Penetration and uplift resistance for shear wetting case

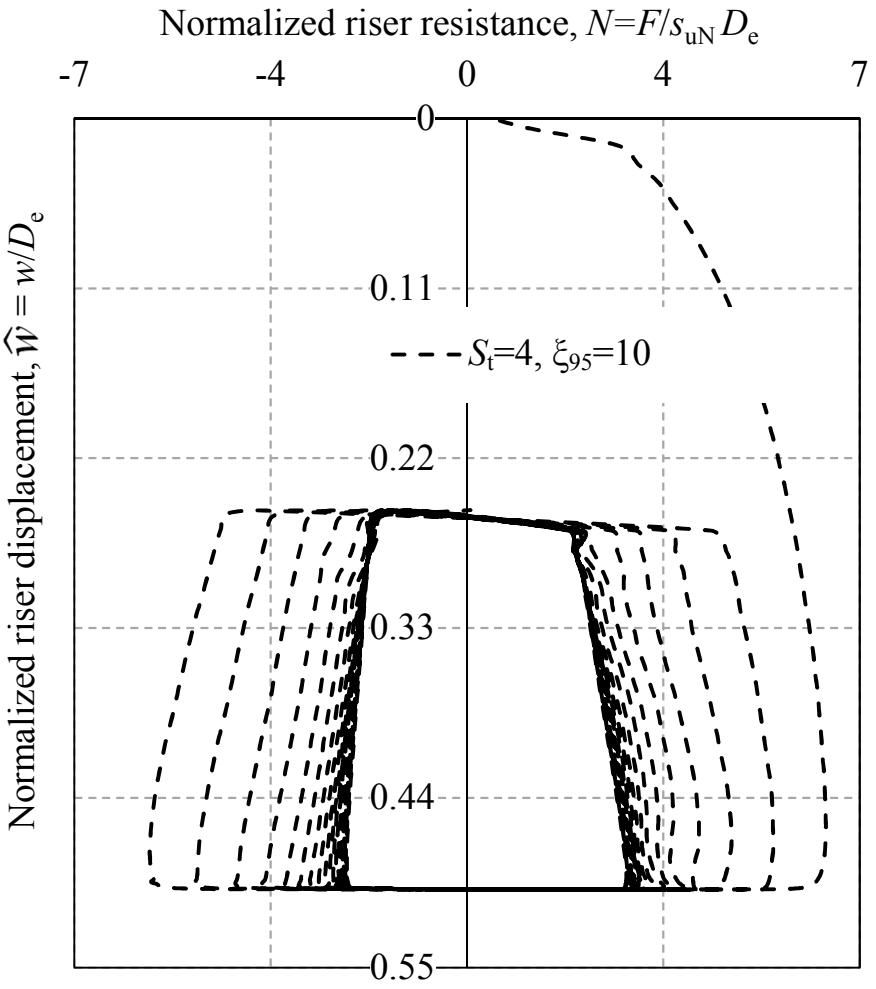

Fig. 5.4(b). Penetration and uplift resistance for no shear wetting case

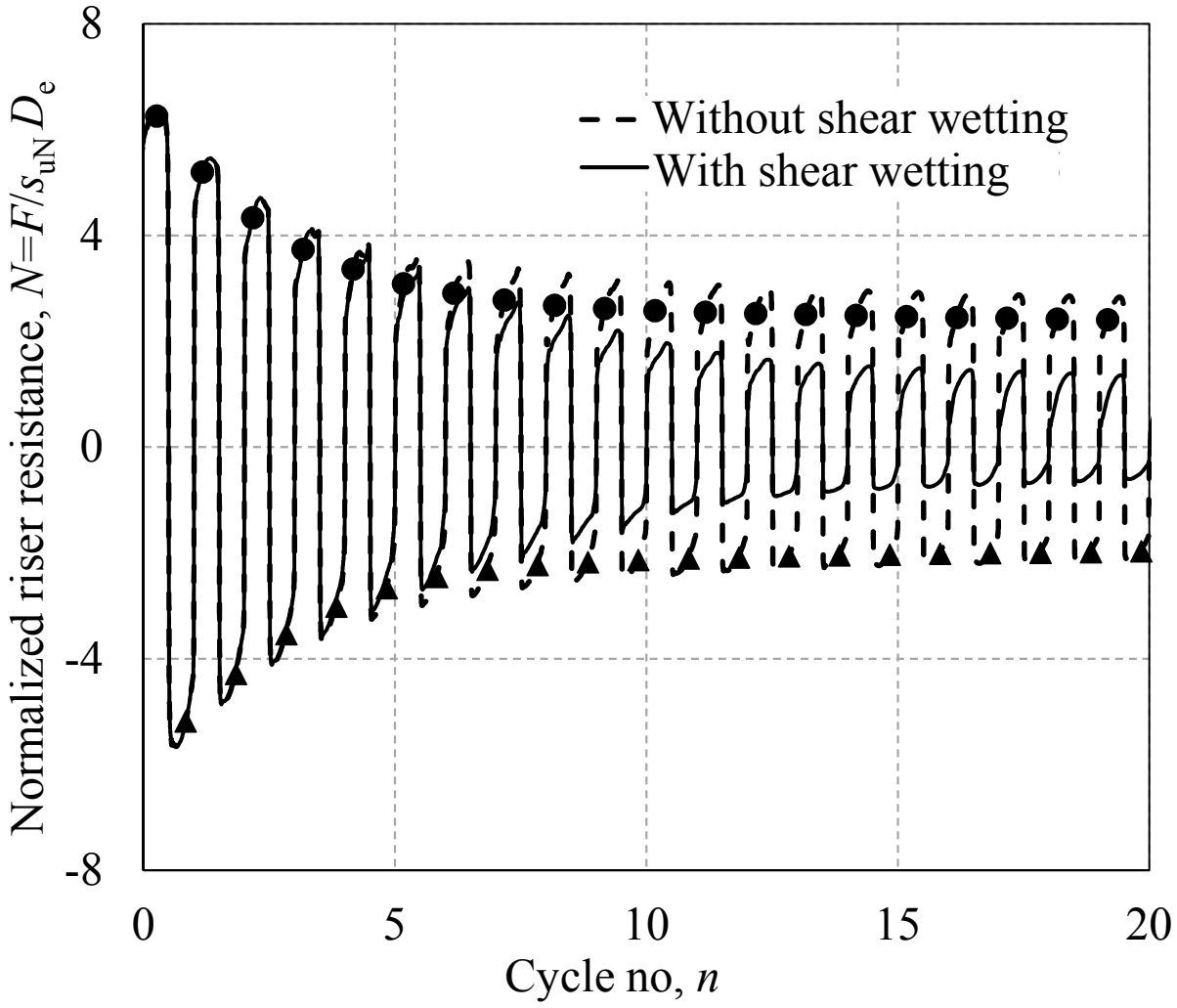

Fig. 5.5. Comparison normalized resistance with and without shear wetting

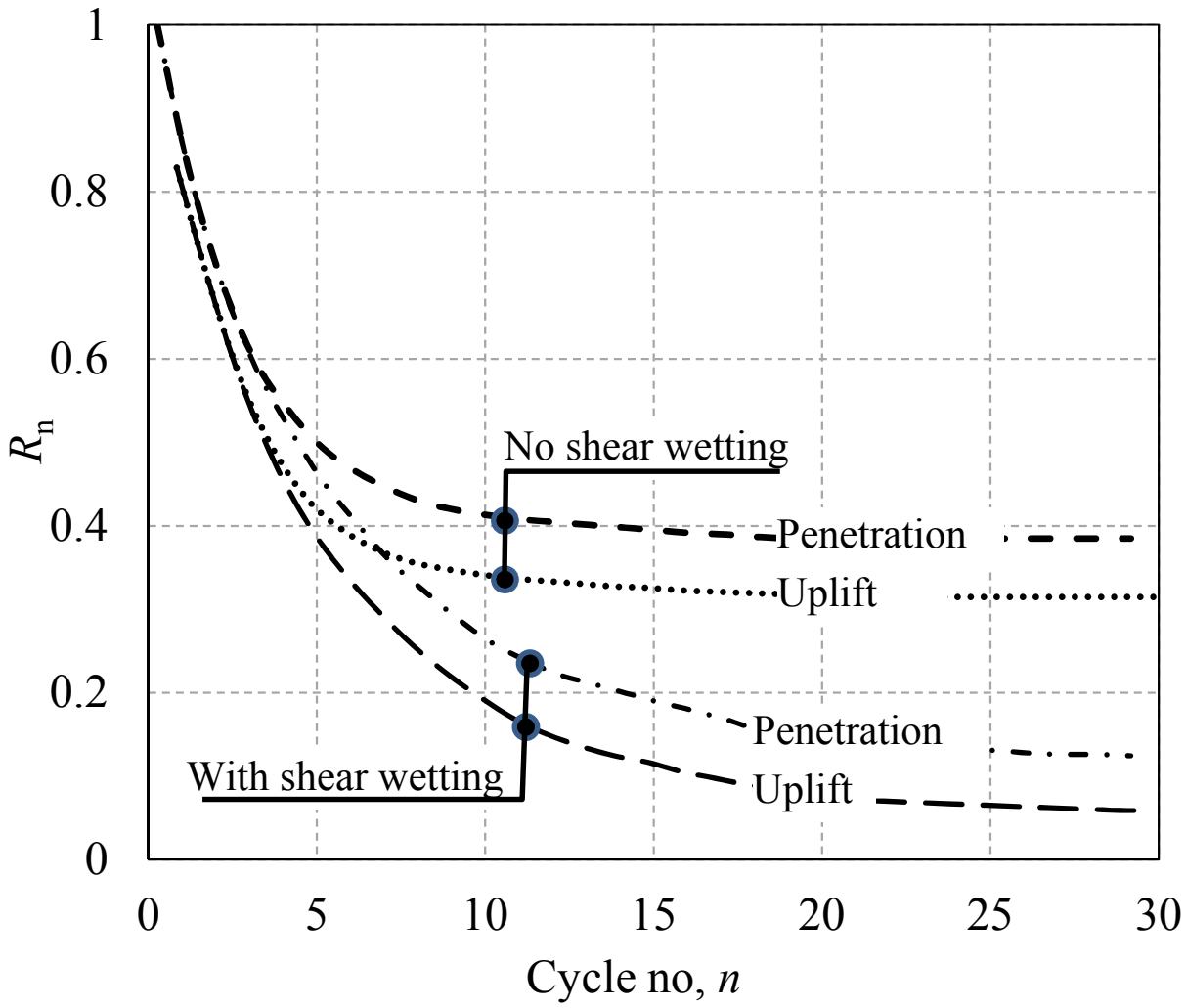

Fig. 5.6. Degradation resistance with number of cycles

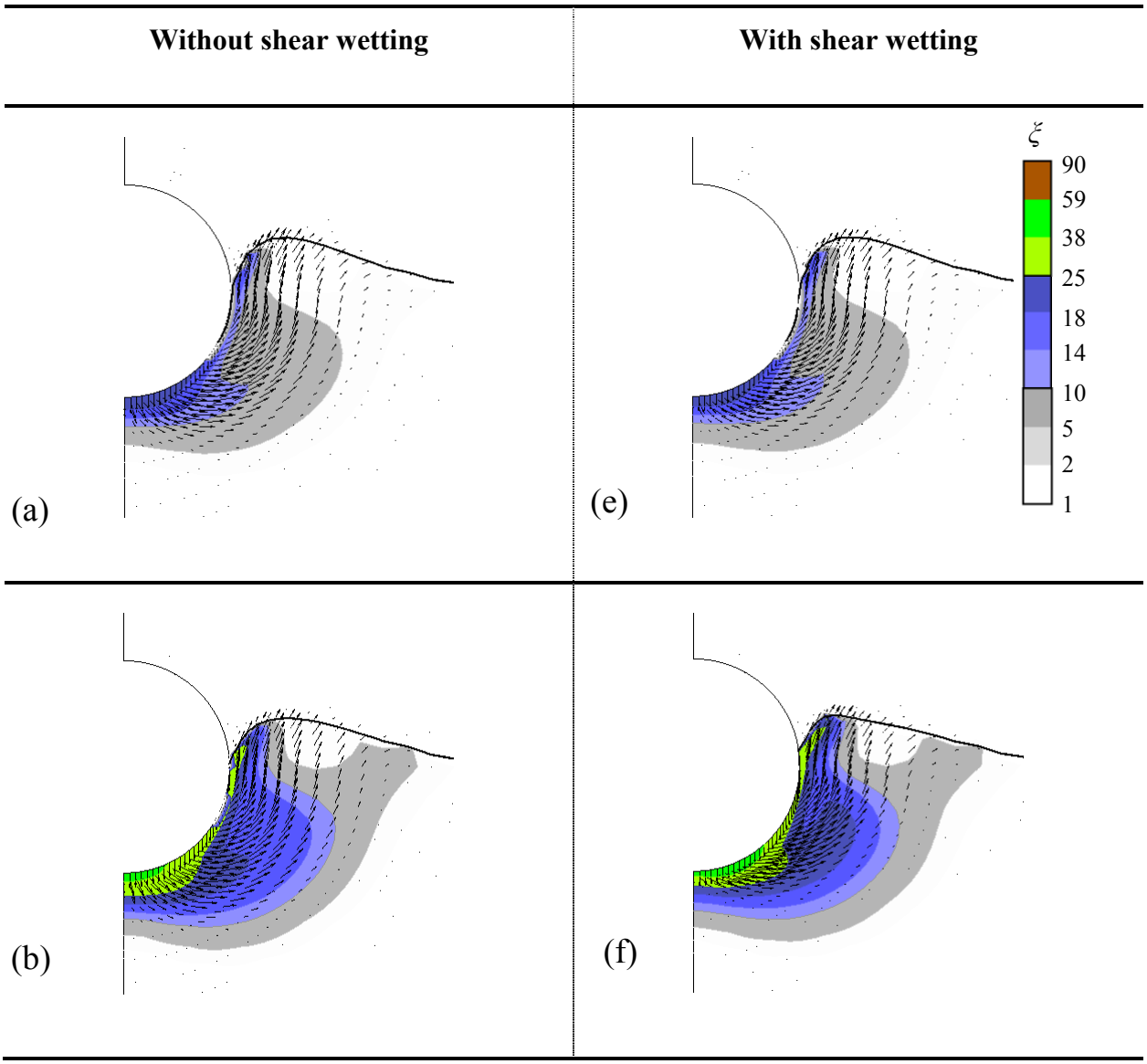

Fig. 5.7. Plastic shear strain and instantaneous velocity vectors: Left column without shear wetting (a) 5th cycle, (b) 10th cycle, (c) 15th cycle, (d) 20th cycle; Right column, with shear wetting (e) 5th cycle, (f) 10th cycle, (g) 15th cycle, (h) 20th cycle

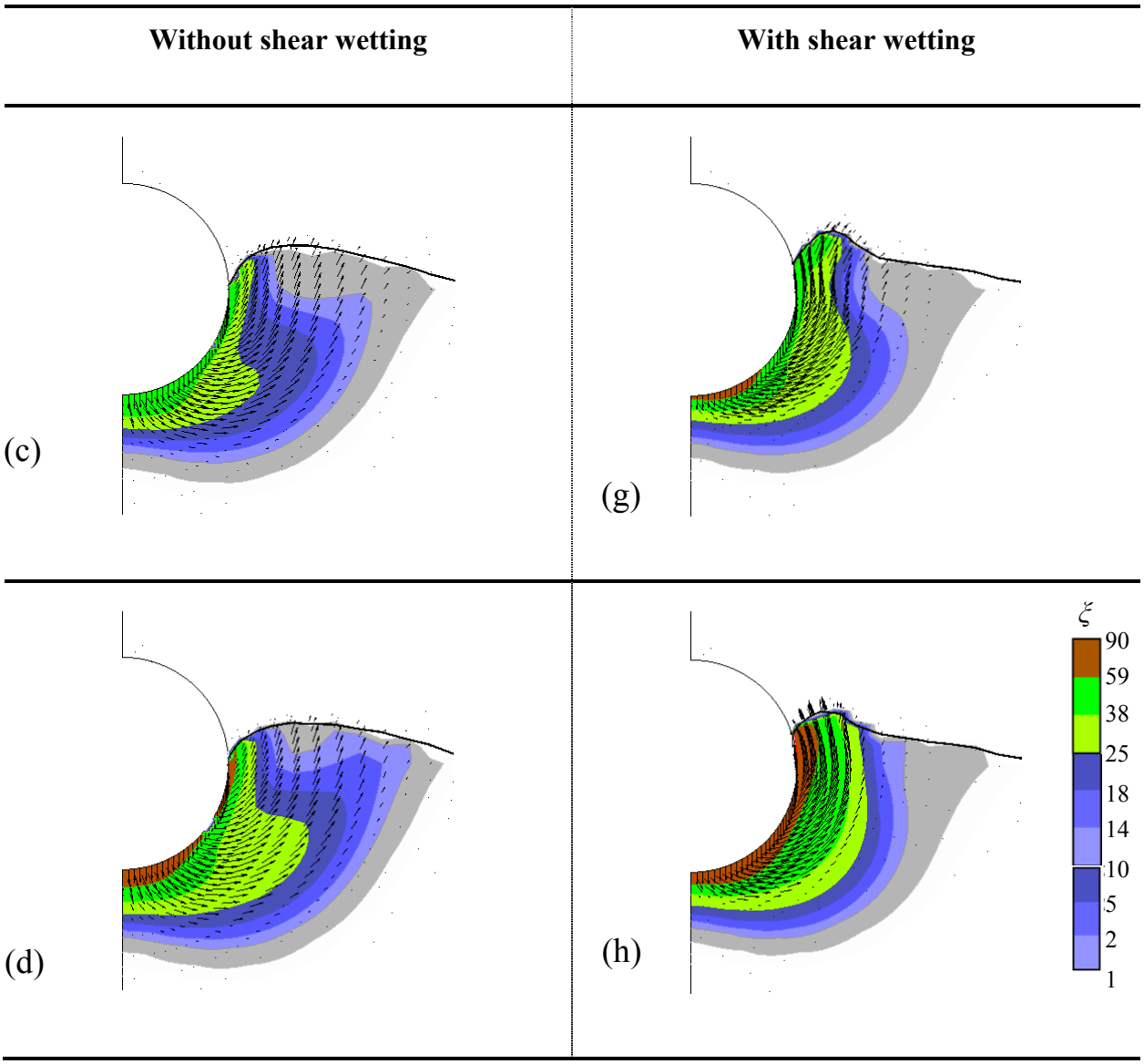

Fig. 5.7. Plastic shear strain and instantaneous velocity vectors during penetration: Left column without shear wetting (a) 5th cycle, (b) 10th cycle, (c) 15th cycle, (d) 20th cycle; Right column, with shear wetting (e) 5th cycle, (f) 10th cycle, (g) 15th cycle, (h) 20th cycle

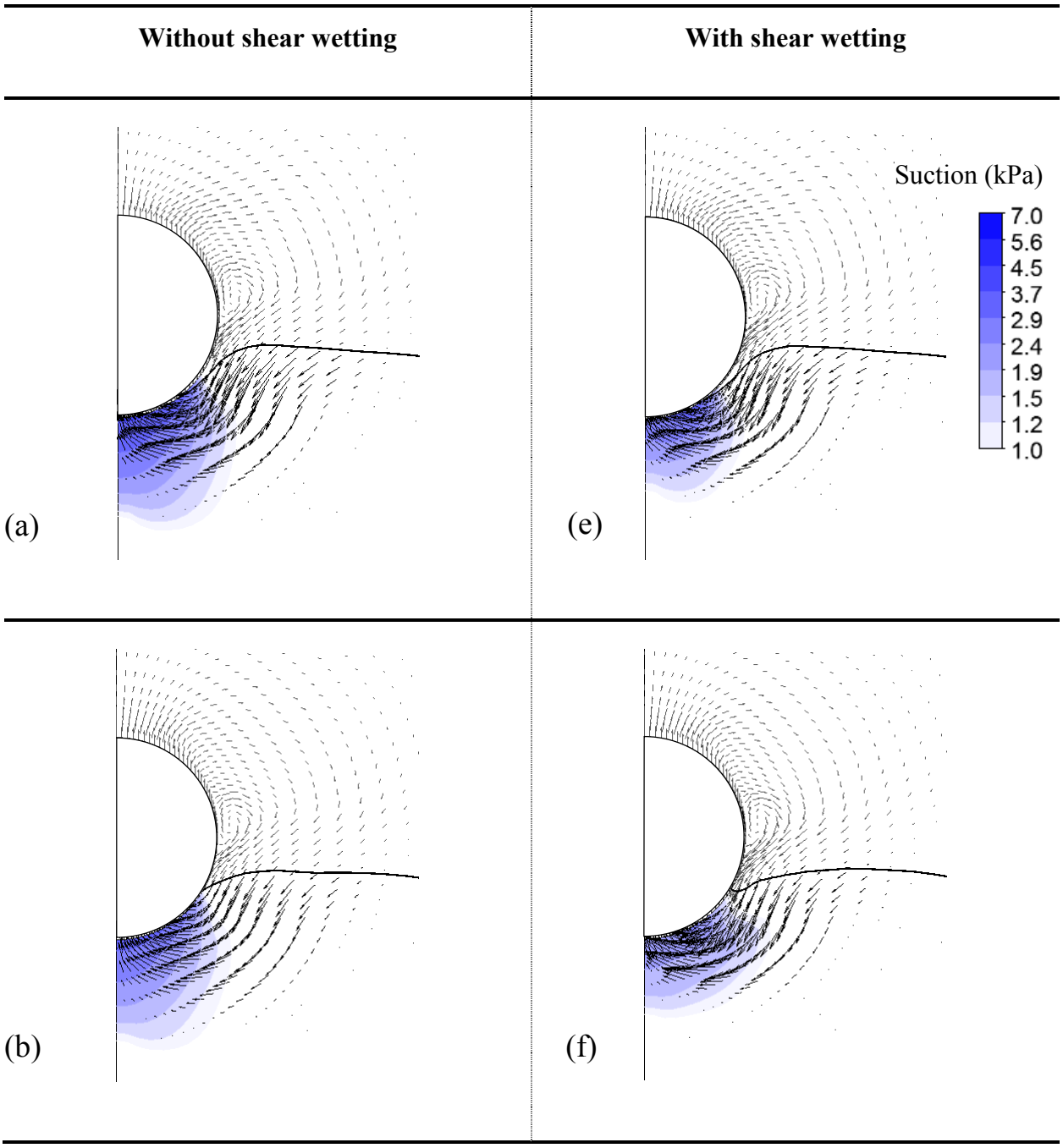

Fig. 5.8. Mobilization suction and instantaneous velocity vectors during uplift: Left column without shear wetting (a) 5th cycle, (b) 10th cycle, (c) 15th cycle, (d) 20th cycle; Right column, with shear wetting (e) 5th cycle, (f) 10th cycle, (g) 15th cycle, (h) 20th cycle

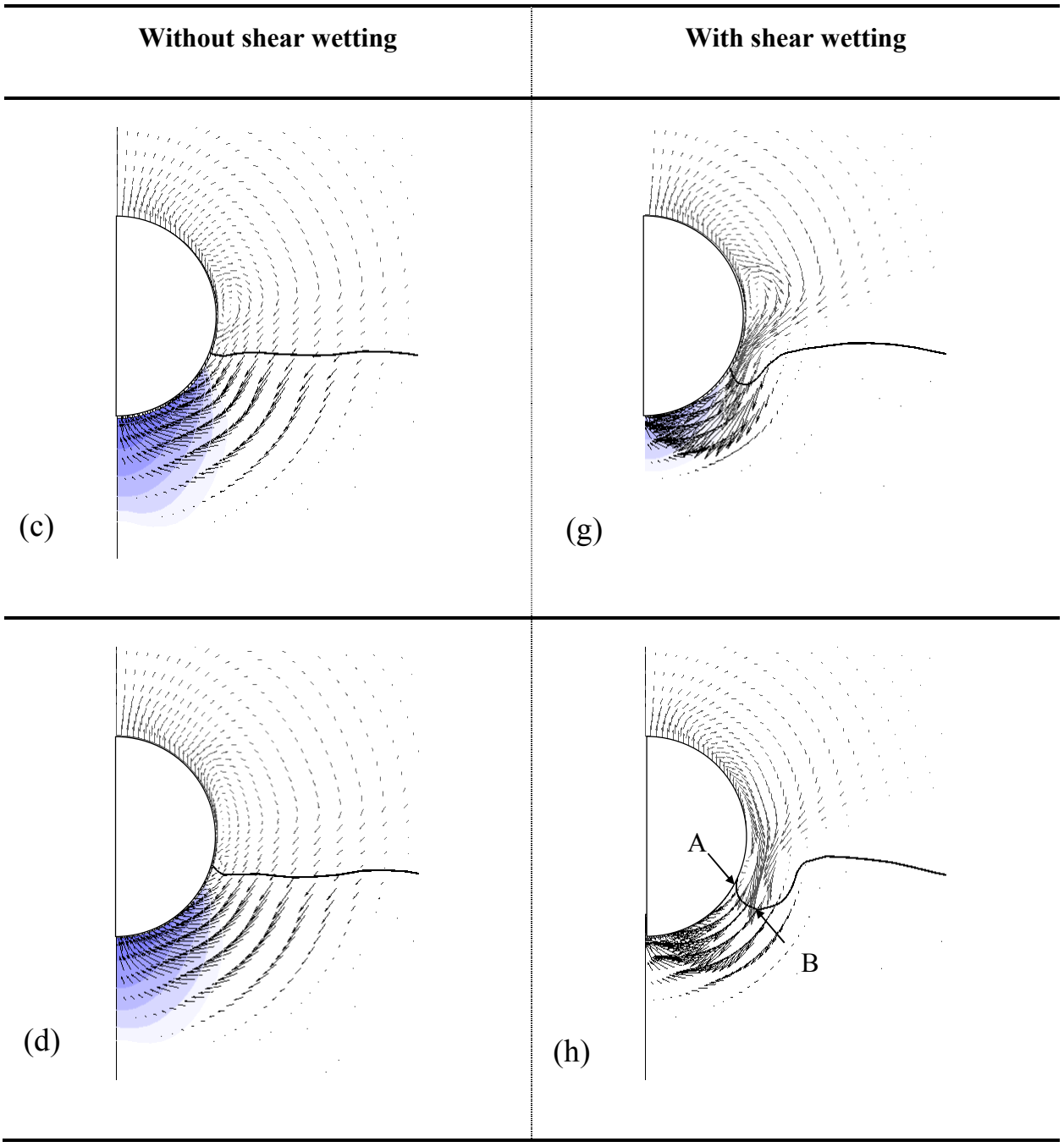

Fig. 5.8. Mobilization suction and instantaneous velocity vectors during uplift: Left column without shear wetting (a) 5th cycle, (b) 10th cycle, (c) 15th cycle, (d) 20th cycle; Right column, with shear wetting (e) 5th cycle, (f) 10th cycle, (g) 15th cycle, (h) 20th cycle

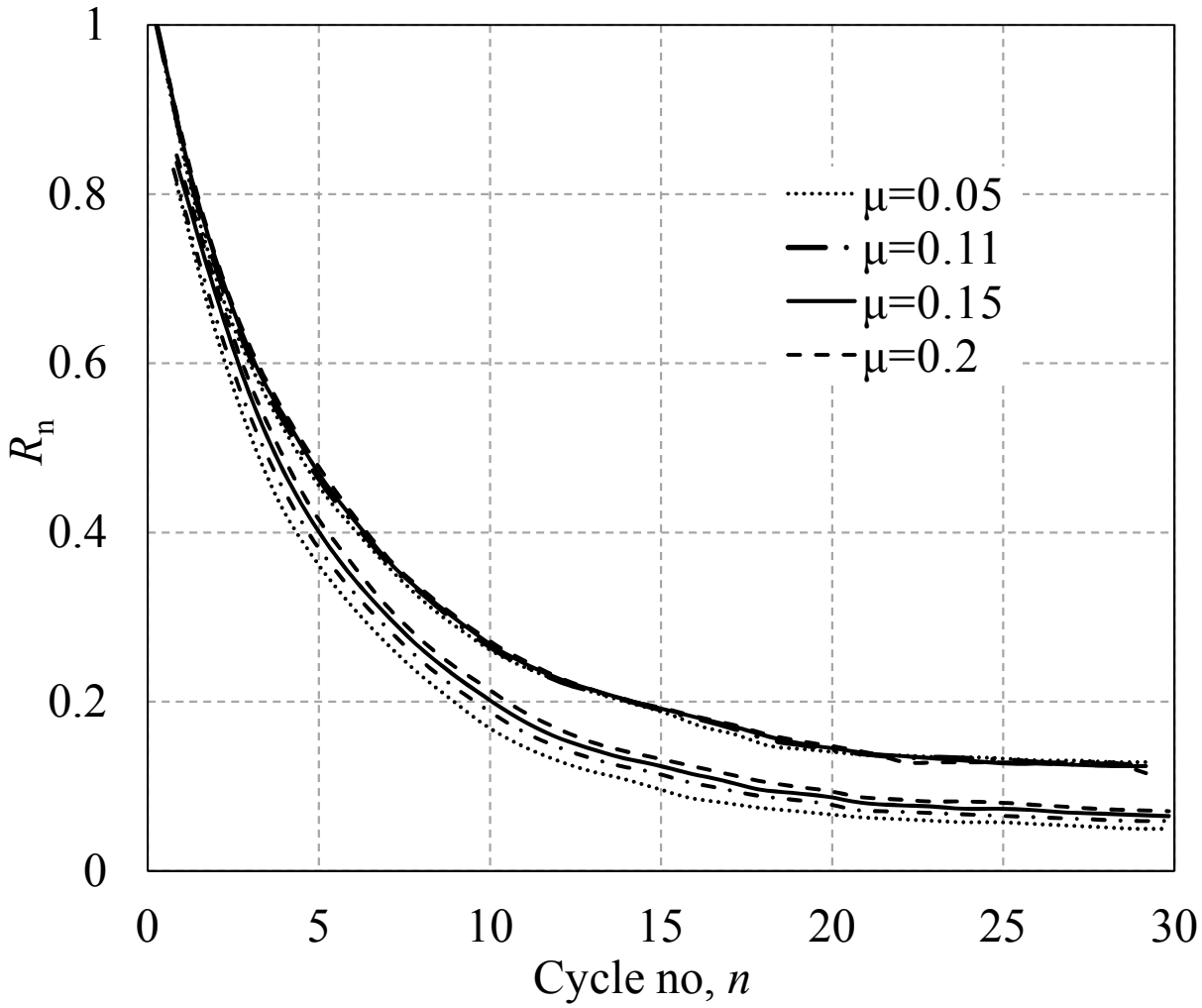

Fig. 5.9. Effect of strain rate parameter μ on normalized resistance ratio R_n

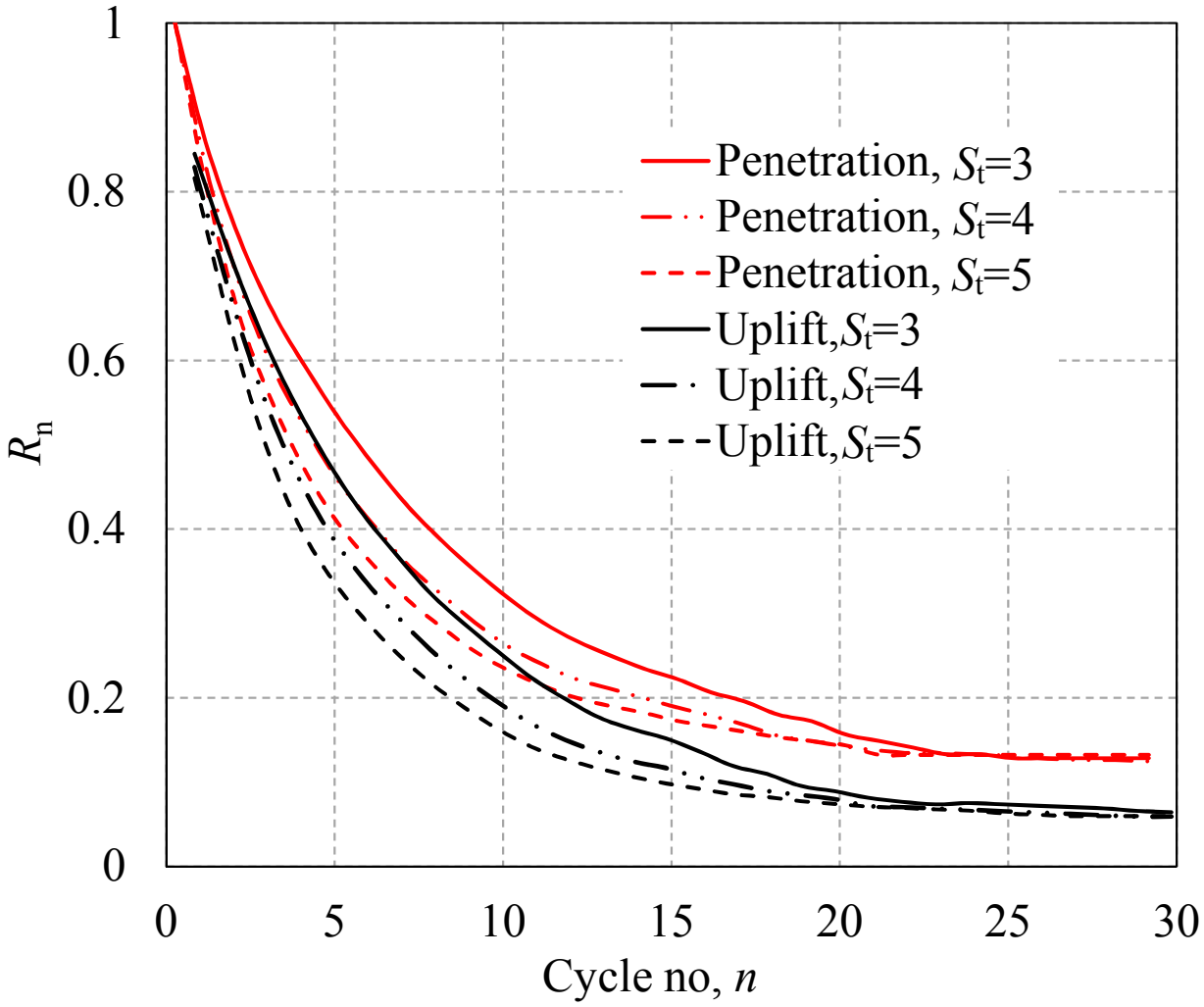

Fig. 5.10. Effects of soil sensitivity on normalized resistance ratio R_n

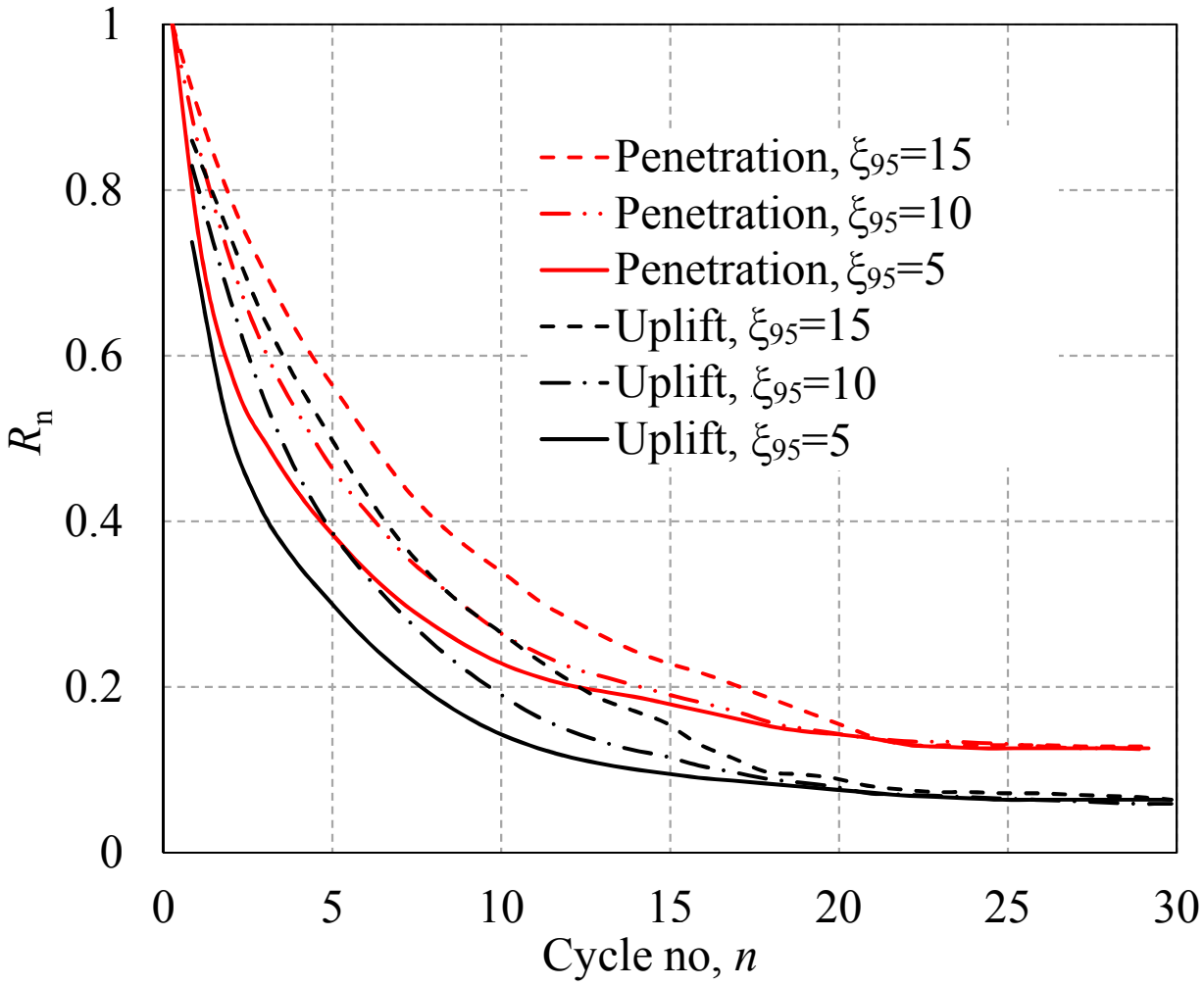

Fig. 5.11. Effects of strain softening parameter ξ_{95} on normalized resistance ratio R_n

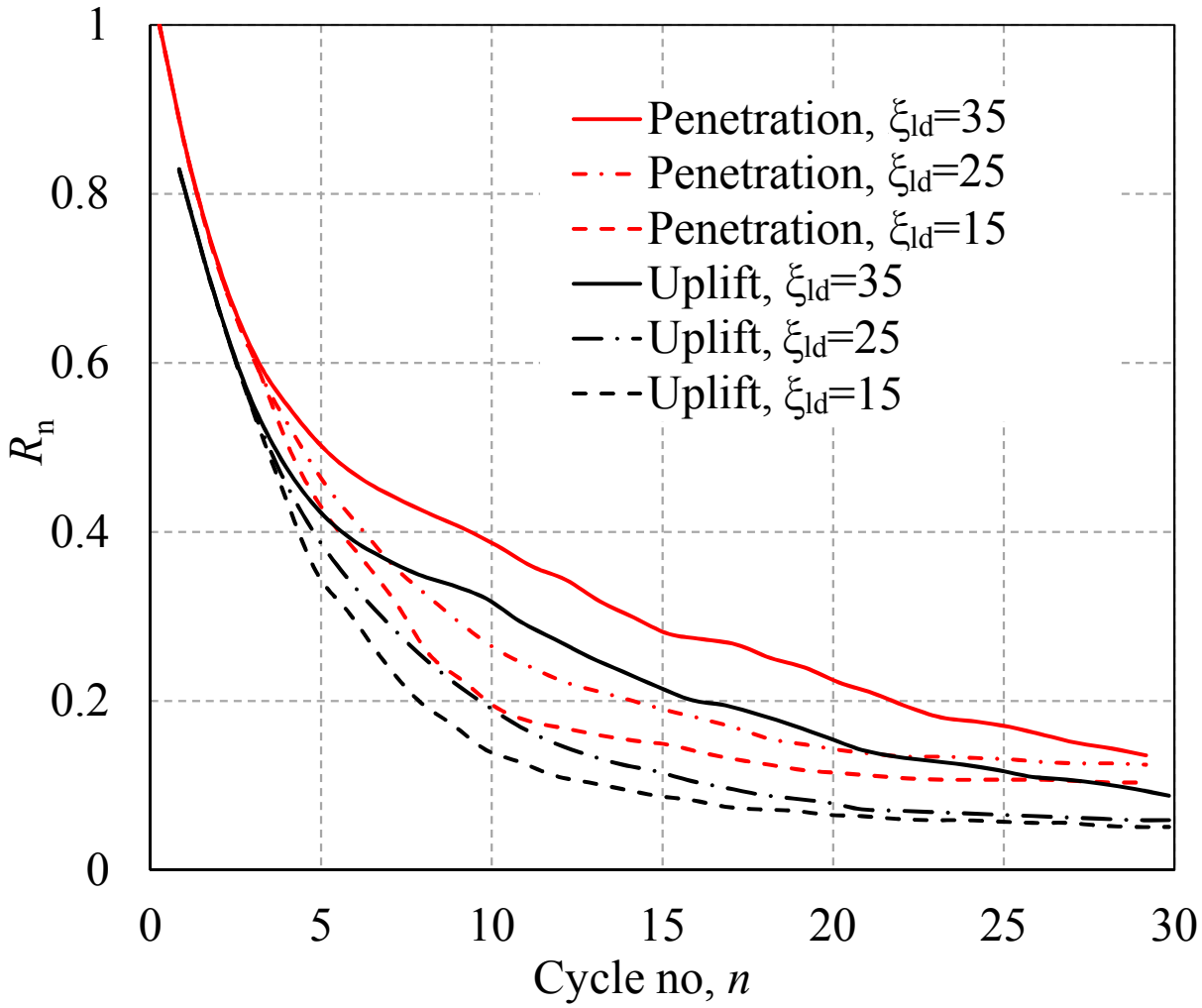

Fig. 5.12. Effects of strain softening parameter ξ_{ld} on normalized resistance ratio R_n

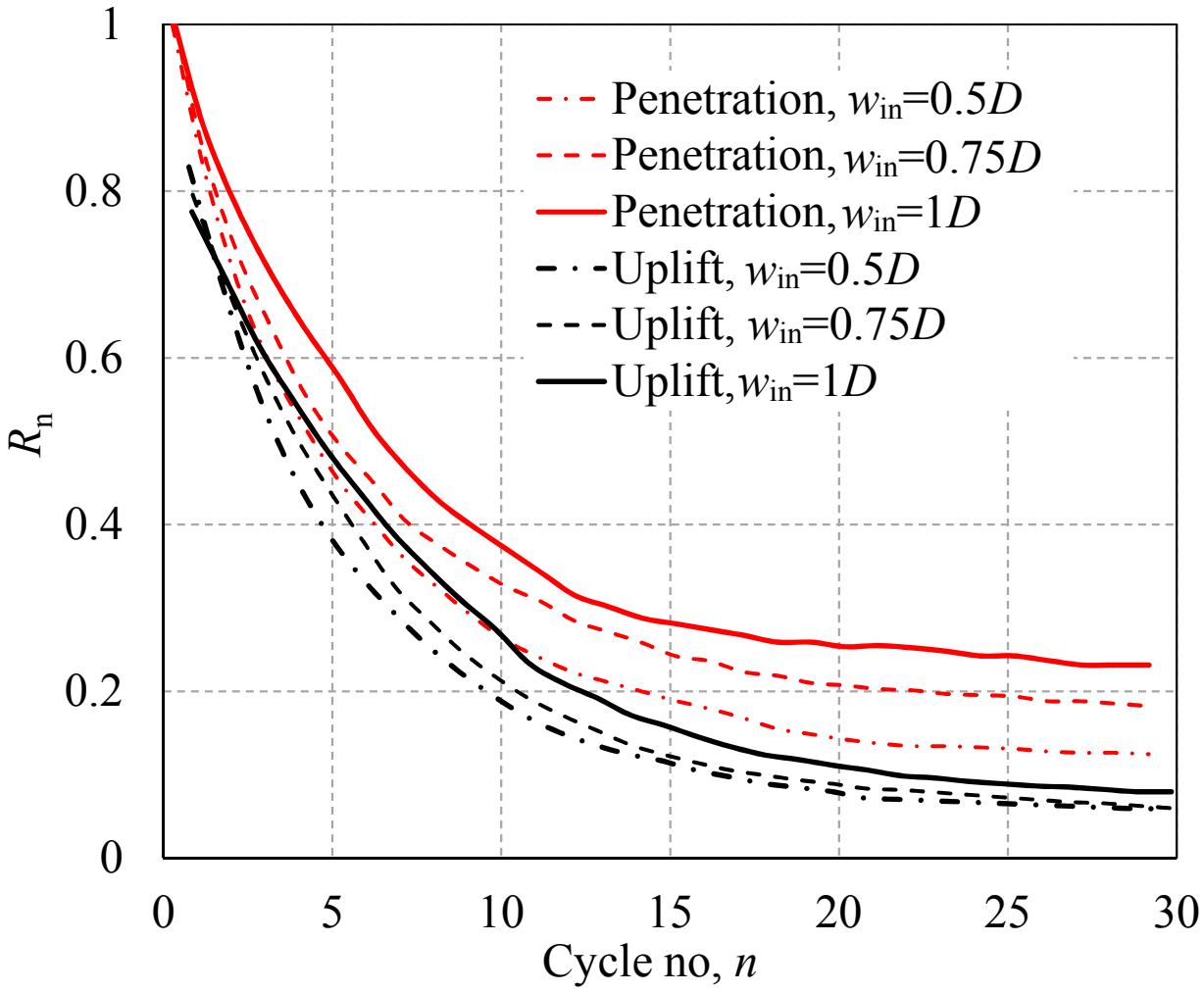

Fig. 5.13. Effects initial embedment on normalized resistance ratio R_n

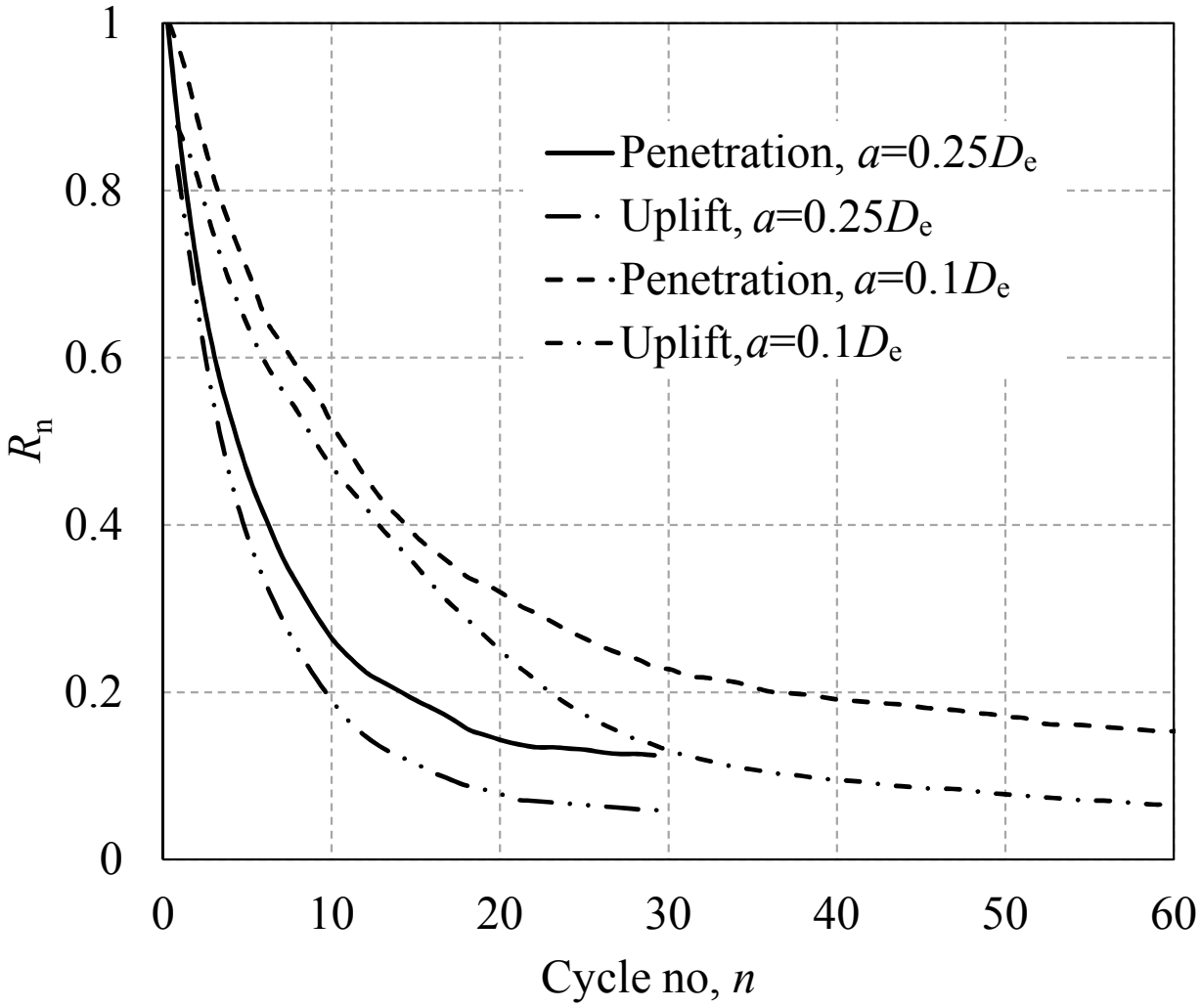

Fig. 5.14. Effects of cyclic amplitude on normalized resistance ratio R_n

Table 5.1. Geometry and model parameters for soil and water used in base case analysis

Diameter of riser, D : m	0.35
Length of riser section, L : m	0.01
Average riser velocity, v_0 : m/s	0.02
Undrained shear strength of soil, s_{u0} : kN/m^2	2.25
Submerged unit weight of soil, γ' : kN/m^3	5
Interface resistance factor, α	0.5
Remoulded sensitivity, S_t	4
Strain softening parameter, ξ_{95}	10
Shear wetting parameter, ξ_{ld}	25
Reference shear strain rate, $\dot{\gamma}_{ref}$: s^{-1}	3×10^{-6}
Shear strain rate parameter, μ	0.11
Dynamic viscosity of water : kg/m/s	0.00089

CHAPTER 6

Pipeline–Soil–Water Interaction Modeling for Submarine Landslide Impact on Suspended Offshore Pipelines

Co-Authorship: This chapter has been submitted to a journal as a technical paper for review as: Dutta, S. and Hawlader, B. (2017) "Pipeline–Soil–Water Interaction Modeling for Submarine Landslide Impact on Suspended Offshore Pipelines." Most of the research in this chapter has been conducted by the first author. He also prepared the draft manuscript. The second author mainly supervised the research and reviewed the manuscript.

6.1 Abstract

The submarine landslide is one of the major geohazards in deep water oil and gas developments. The impacts of glide blocks or out-runner blocks, which carry the geotechnical properties of the parent soil mass before the landslide, on pipelines normal to the direction of slide are investigated in this study. An efficient numerical modeling technique is developed using a computational fluid dynamics (CFD) approach, incorporating a strain-rate and strain-softening dependent model for the undrained shear strength of clay sediment, to simulate the lateral penetration of a pipe in a clay block. The role of water in the cavity and channel formed behind the pipe during the lateral penetration on drag force is successfully simulated. Numerical simulations for varying depths of the pipe explain the change in soil failure mechanisms in which the channel behind the pipe and berm play a significant role, especially at shallow depths. As the

cavity behind the pipe may not be completely filled with soil, the limitations of smooth/rough and bonded/unbonded interface conditions, as used typically in pipe–soil interaction analysis, are discussed. Based on a comprehensive parametric study, calibrated against centrifuge test results, a set of empirical equations is proposed to calculate drag force for practical applications.

Keywords: finite volume method; explicit; clay; water; strength degradation; suction.

6.2 Introduction

Deep water offshore pipelines used to transport hydrocarbons are generally laid on the continental slopes without trenching. The pipelines usually penetrate into the seabed sediments—typically clay—due to installation, weight of the pipe and hydrocarbons, and operational loading. However, on uneven seabed profiles, a number of segments of the pipeline might remain suspended between two high points and experience impact force from the downslope movement of a failed soil mass after submarine landslide (Jeanjean et al., 2005; Bruschi et al., 2006; Randolph et al., 2010). The occurrence of numerous submarine landslides of various magnitudes has been reported in the past. In some cases, the failed soil mass traveled over a large distance. For example, in the Grand Bank landslide in 1929, the failed soil mass/debris traveled more than 100 km and broke the Trans-Atlantic cable in the downslope (Piper et al., 1999). Different terminologies have been used in the past to describe the failed materials (Mulder and Alexander, 2001). The failed mass first travels as a ‘glide block’ and then as an ‘out-runner block’ until it carries the geotechnical properties similar to the parent soil, except for the sliding planes (Zakeri and Hawlader, 2013). With further downslope movement, significant remoulding and fluidization decrease the shear strength of the soil and it changes to fluid with suspended solids

and flows as ‘debris’ or ‘turbidity current.’ The present study focuses on the impact of a glide block/out-runner block, called ‘soil block’ in the following sections. The soil block might travel at high speeds when a lubricating layer is formed by hydroplaning (De Blasio et al., 2004).

The available approaches to model the drag force on a suspended pipeline resulting from submarine landslides can be divided into two groups: geotechnical and fluid mechanics approaches. In the geotechnical approach, the drag force is proportional to the undrained shear strength of the clay sediment, s_u (Audibert and Nyman, 1977; Demars, 1978; Bea and Aurora, 1982; Swanson and Jones, 1982; Summers and Nyman, 1985; Georgiadis, 1991). In the fluid mechanics approach, the drag force is proportional to a drag coefficient and square of the relative velocity between the clay block and pipeline. As the inertial component is significant when the sliding materials have low shear strength and high velocity, the fluid mechanics approach is more appropriate for modelling the impact of debris flow or turbidity current (Zakeri et al., 2008; 2009b). Combining the geotechnical and fluid mechanics approaches, and assuming that the failed clay mass fully engulfs the pipeline, Randolph and White (2012) proposed a hybrid method and showed that for typical geotechnical properties and velocity of the failed sediments—as expected in glide blocks/out-runner blocks—the drag force is dominated by the soil bearing pressure rather than the inertial component.

In the present study, a computationally efficient numerical modeling technique using ANSYS CFX is developed. The role of free water flow in the channel, suction in entrapped water, strain rate and strain-softening effects on soil strength, slide velocity and berm height effects on the mobilization of drag force are examined, simulating the response for a large lateral penetration distance. Finally, based on a comprehensive parametric study, a set of empirical equations is proposed to calculate the drag force.

6.3 Previous Studies

A large number of studies is available in the literature on buried pipelines in clay subjected to lateral loading. Generally, in physical modelling of this type of problem, a section of pipe is placed in the trench of a soil bed, covered with backfill and then dragged laterally (Paulin et al., 1998; Popescu et al., 2002; C-CORE, 2003; Phillips et al., 2004). Similarly, in numerical modelling, the pipe is placed at the desired burial depth and then displaced laterally (i.e. 'wished in place (WIP)' configuration) (Guo, 2005; Martin and White, 2012; Merifield et al., 2008). Assuming that the pipeline is fully engulfed by the soil, pre-defined pipe–soil interface behaviour is given in the numerical model.

Recognizing that the process is very different from above mentioned modeling of buried pipelines, in the current research program, physical and numerical modeling of glide block/out-runner block impact on an offshore pipeline has been performed. Developing a new experimental setup, a series of centrifuge tests were conducted where clay blocks of varying s_u impacted the pipes of diameter D, located normal to the direction of slide at 7.5–13.5D, at velocities (v_0) between 0.04 and 1.3 m/s. Further details of this experimental program have been provided by the authors and their co-workers elsewhere (Chi, 2012; Zakeri et al., 2012). The maximum drag force is found to be increased with v_0/D. Using a different experimental set-up from the one above, Sahdi et al. (2014) conducted a series of centrifuge tests where a section of pipe was vertically penetrated 2.5D into a kaolin clay bed and then dragged laterally at different velocities. Tests were conducted at varying degrees of consolidation in order to model the response for a wide range of soil behaviour—from fluid to soft clay. The lateral resistance obtained from centrifuge tests is lower than the theoretical values for deeply embedded conditions (Randolph and Houlsby, 1984), and the authors attributed this difference to depth effects.

The centrifuge tests show the formation of a channel behind the pipe when it penetrates laterally into the clay block (Zakeri and Hawlader, 2013). Channel formation is also expected in the pipe section tests during vertical penetration and lateral dragging. For example, Puech et al. (2010) showed that the channel remained open up to the depth of 13*D* when a T-bar was penetrated vertically into a clay bed having s_u=3 kPa. Under a submerged condition, the channel might be simply filled with water and provide a pathway for 'free water' outside the clay block to flow into the cavity created behind the pipe during lateral penetration. However, the flow of free water might be obstructed or stopped if the channel becomes narrow or completely closed, which depends on a number of factors such as undrained shear strength, penetration velocity and depth of the pipe, as discussed in the following sections. As the cavity may not be completely filled with soil (i.e. with no contact between soil and pipe), the assumption of a smooth/rough pipe–soil interface condition, as used in typical finite element (FE) analysis, is questionable. Moreover, the mobilized tension behind the pipe depends on suction in entrapped water in the cavity, which is again related to the flow of free water through the channel. Therefore, the use of fully-bonded (i.e. full-tension) or unbonded (i.e. no-tension) pipe–soil interface modeling techniques in FE analysis is also questionable. Moreover, the length of the failure plane behind the pipe might be influenced by suction. These issues were not examined in the physical modeling programs described above. Also, the experiments were conducted for relatively shallow (2.5*D*) (Sahdi et al., 2014) and very deep (7.5–13.5*D*) (Zakeri et al., 2012) conditions, and therefore, further studies for varying depths of the pipe are required.

Numerical modeling of pipelines buried in clay for WIP configuration has been performed by a number of researchers; however, the simulations were limited to small lateral displacements (e.g. Guo, 2005; Martin and White, 2012). For modeling soil flow around offshore pipelines

impacted by submarine landslides, Zhu and Randolph (2010, 2011) conducted large deformation FE modeling for fully embedded pipelines using a re-meshing and interpolation with small strain approach (Hu and Randolph, 1998). Their FE model could not account for inertial effects, although the authors recognized that it is significant at high v_0 and low s_u (Zhu and Randolph, 2011). In the numerical studies above, the effects of free water flow in the channel and suction in the entrapped water in the cavity were not considered; instead, the pipe–soil interface is modeled as smooth/rough and fully-bonded/unbonded conditions. Zakeri and Hawlader (2013) used a CFD approach to simulate the flow of soft clay around the pipe to calculate submarine landslide impact force. However, a number of factors, such as strain-softening, depth effects and the mobilization of tension behind the pipe, were not examined.

6.4 Problem Definition and Numerical Model Formulation

After the failure of a submarine slope, a block of failed clay mass displaces in the downslope direction at a constant speed v_0 and impacts a suspended pipeline of diameter D located at depth w from the top surface of the failed soil mass (Fig. 6.1). As typical submarine slopes are mild, neglecting the vertical component of velocity, the clay block is assumed to move at v_0 in the horizontal direction. The front face of the clay block might have an irregular shape because of its complex interaction between the water and soil beneath it; however, for simplicity it is assumed to be inclined at an angle θ to the horizontal. Because of high v_0 in the field, the undrained behaviour of clay governs the response.

6.4.1 *CFD Model Development*

The general purpose ANSYS CFX 14.0 software is used for numerical modelling (ANSYS CFX, 2012). Figure 6.1 shows the CFX model used in the present study for the ‘base case

analysis.' As CFX allows only three-dimensional modeling, the analysis is performed only for one element of 10 mm thickness in the out of plane direction. A stationary rigid pipe section of D=290 mm and L=10 mm is placed at w=885 mm. The soil and water domains are discretized into a three-dimensional mesh. Small elements are used near the pipe. Mesh deformation is not allowed and therefore the size and shape of the mesh do not change with loading. Soil and water, modeled as Eulerian material, flow through the fixed mesh. Therefore, numerical issues related to mesh distortion are avoided.

All the boundaries are placed at a sufficiently large distance from the pipe to avoid boundary effects. The bottom boundary is defined as an impermeable wall to fluid flow. The left boundary is defined as an inlet with $v_x=v_0$ and $v_y=v_z=0$, such that the soil and water enter in the domain at constant velocity, v_0. The right boundary is defined as an outlet and placed at a sufficiently large distance to model channel formation behind the pipe, as discussed later. A symmetry plane boundary condition is applied to the other two vertical faces. A free-slip boundary condition is applied to the bottom surface. The top of the domain is defined as an opening to allow water to flow in and out. The soil–water interface (abc) is created by the volume fraction tool in CFX. The volume fraction of clay is 1.0 and water is 0 in the clay block (oabc), while it is the reverse in the rest of the domain (abcdef).

The pipe is modeled as an impermeable wall with a no-slip boundary condition. Following the concept of the finite thickness interface element (Supachawarote et al., 2004; Jostad and Andresen, 2004), the shear strength of a thin zone of soil of 5 mm thickness around the pipe is modeled as αs_u, where α=0 and α=1 represent the conditions similar to smooth and rough interfaces, respectively.

6.4.2 *Shear Strength of Seabed Sediment*

Experimental evidence show that the s_u increases with shear strain rate ($\dot{\gamma}$) and decreases with accumulated plastic shear strain (ξ). Combining these two effects, Einav and Randolph (2005) proposed the following empirical equation:

$$s_u = f_1 f_2 s_{u0} \tag{1}$$

where f_1 and f_2 represent the strain rate and strain-softening effects, respectively; s_{u0} is the value of s_u at the reference shear strain rate ($\dot{\gamma}_{\mathrm{ref}}$) and prior to any softening. In this study, f_1 and f_2 are defined as (Einav and Randolph, 2005):

$$f_1 = 1 + \mu \log\{\max(\dot{\gamma}, \dot{\gamma}_{\mathrm{ref}})/\dot{\gamma}_{\mathrm{ref}}\} \tag{2}$$

$$f_2 = \frac{1}{S_t} + \left(1 - \frac{1}{S_t}\right) e^{-3\varepsilon/\varepsilon_{95}} \tag{3}$$

where μ is the rate of change of s_u per log cycle of $\dot{\gamma}$; S_t is the remoulded sensitivity; and ξ_{95} is the value of ξ at which the soil has undergone 95% of the reduction of strength due to remoulding.

The geometry and soil parameters used in the 'base case' analysis are shown in Table 6.1. A uniform s_{u0} of 5 kPa is used, although it is understood that s_{u0} might increase with depth in many cases. Typical range S_t is 2–5 for offshore sediments (Kvalstad et al., 2001). A range of ξ_{95}=10–50 and μ=0.05–0.2 have been used in the past for successful modeling of undrained remoulding and strain rate effects, respectively (Randolph, 2004; Einav and Randolph, 2005).

6.4.3 *Numerical Implementation*

Both clay and water are modeled as homogeneous multiphase Eulerian materials where the shear behaviour is defined using the dynamic viscosity (μ_d). For water, a constant value of μ_d is used (Table 6.1). Clay is modeled as rigid-plastic material, $\mu_d = s_u/\dot{\gamma}$. The CFX does not have any

direct option to define s_u as shown in Eqs. (1–3). Therefore, in each time increment, $\dot{\gamma}$ is called, which represents the second invariant of the strain rate tensor (a scalar quantity). Multiplying $\dot{\gamma}$ by the time increment (Δt), the shear strain increment $\Delta\xi$ is calculated. Summing up $\Delta\xi$ over the period of analysis, the accumulated strain ξ is calculated. The authors developed a special technique in CFX to calculate ξ. Based on the values of $\dot{\gamma}$ and ξ, s_u is calculated for each element using Eq. (1), which is then used to update μ_d.

6.5 Results of Base Case Analysis

6.5.1. *Force–Displacement Behaviour*

Figure 6.2 shows the variation of normalized force ($N=F/s_{uN}D_eL$) with normalized lateral penetration ($\hat{u}=u/D_e$) for the base case. The undrained shear strength used for normalization (s_{uN}) is $2/\sqrt{3}\,s_{u0}$ (please see Hawlader et al., 2015 a,b for further discussion). As finite thickness interface elements together with no-slip pipe–soil interface condition are used, the failure occurs through the soil instead of at the pipe–soil interface. Therefore, following the concept of Gui and Bolton (1998) and assuming that the failure occurs at a distance of half of the element thickness from the outer surface of the pipe, the value of the effective diameter (D_e) is calculated as 295 mm (=290 mm + 2×5/2 mm) for the 5-mm element size just outside the pipe. At a given time t, the lateral penetration can be calculated as $u=v_0(t-t_0)$, where t_0 is the time when the pipe touches the sloped surface and the force on the pipe starts to increase. The depth of the pipe is also expressed in normalized form as $\hat{w}=w/D_e$.

The solid line in Fig. 6.2 shows the base case results with the parameters in Table 6.1. The force N increases quickly with $\hat{u}$ up to point X ($\hat{u}$~2.0) and then the rate of increase of N decreases. The rate again increases after $\hat{u}$~4.5, and the force on the pipe reaches the maximum

(drag force) N_m (=11.8) at point Y ($\hat{u}$~12.0). The shape of the N–$\hat{u}$ curve is discussed further in the following sections. Figure 6.2 also shows the effects of strain rate and softening on N separately. When only softening is considered (i.e. f_1=1 and f_2 as in Eq. (3)), the calculated N is smaller than the base case result (e.g. N_m=7.4). However, the strain rate effects alone (i.e. f_1 as in Eq. (2) and f_2=1) give higher N than the base case (e.g. N_m=17.5). Comparison with an analysis for an 'ideal soil' case (i.e. f_1=1 and f_2=1) shows that the combined effects of rate and softening give higher N than in the ideal soil case. Note, however, that the difference of N between ideal soil and base case analyses depends on the model parameters used in Eqs. (2) and (3).

Figure 6.3 shows the shear strain rate of soil elements ($\dot{\gamma}$) normalized by the operating strain rate (v_0/D_e) (i.e. $\dot{\gamma}D_e/v_0$) at four $\hat{u}$ for the base case simulation. At $\hat{u}$=3.0, the shear strain increment mainly occurs in front (left side) of the pipe and also along an inclined plane from the top (Fig. 6.3a). The dashed line shows the location of the soil block at this time if the pipe were not there, which is found from v_0. The pipe restricts the movement of the soil significantly. The soil behind the pipe tends to collapse in the channel formed by displaced soil. At this stage, the left half of the pipe is in contact with soil that applies force on it, while the water on the right side of the pipe can flow out easily through the wide channel behind it. Between $\hat{u}$~2.0 and $\hat{u}$~4.5, pipe–soil contact does not increase significantly and also the water behind the pipe can flow easily through the channel, as it is sufficiently wide, although the thickness of the channel decreases with $\hat{u}$. Therefore, the rate of increase of N with $\hat{u}$ is small in this range of $\hat{u}$. This trend is very clear in the ideal soil case in Fig. 6.2 and in a number of cases presented in the following sections. With further penetration, the channel becomes very narrow and water cannot flow easily. Therefore, suction (-ve pressure with respect to the initial value) develops in the trapped water behind the pipe, as shown in the inset of Fig. 6.3(b) at $\hat{u}$=6.0. Because of this, the

failure pattern changes, as shown by the strain increment contours in Fig. 6.3(b), which also increases the rate of increase of N in Fig. 6.2. At $\hat{u}$=9.0, the channel size reduces and suction increases further (Fig. 6.3c), which again increases N (Fig. 6.2). At a large $\hat{u}$ (~12.0), the pipe is fully engulfed by the soil (Fig. 6.3d). The segment XY of the N–$\hat{u}$ curve represents the 'suction mobilization segment' and the horizontal distance between these two points is denoted as $\hat{u}_{\mathrm{suc}}$. After point Y, N does not change with $\hat{u}$ because the failure planes and berm size remain similar.

As the pipe is at a shallow depth ($\hat{w}$=3), the failure plane propagates upward to the top surface. Moreover, the berm above the pipe has a significant effect on drag force for small $\hat{w}$, as discussed in the parametric study section.

6.5.2 *Comparison with FE Results*

Large deformation FE analysis is also performed for the base case using the Coupled Eulerian–Lagrangian (CEL) approach available in Abaqus FE software. The clay block (oabc in Fig. 6.1) is modeled as Eulerian material with submerged unit weight (γ') while the water area is considered to be void. Geotechnical properties used in this simulation are: s_u=5 kPa (ideal soil), (γ'=6 kN/m^3, undrained Young's modulus E_u=167s_u and Poisson's ratio ν_u=0.495. Zero velocity boundary conditions are applied at the bottom and for all vertical faces. No boundary condition is applied at the top of the clay block (abc in Fig. 6.1). Similar to ANSYS CFX, Abaqus CEL allows only three-dimensional modeling. Therefore, the plane strain condition is simulated with only one element in the out of plane direction. Further details of CEL modeling are available in Dutta et al. (2014). Similar to Fig. 6.1, a rigid pipe of D=290 mm is placed at $\hat{w}$=3 in the void and then moved to the left at constant velocity, applying a displacement boundary condition at

the reference point (centre of the pipe) without any rotation. As the pipe is moving in this case, to accommodate large lateral displacement, the left boundary is placed at 20.0D from the crest of the slope (recall that in CFX modeling it is only 2.5D because the soil moves in CFX simulations while the pipe is stationary). The soil–pipe interface friction coefficient α=0.5 is used. One of the main advantages of CEL is that soil as Eulerian material flows through the fixed mesh; therefore, numerical issues related to mesh distortion are not expected, even for very large strains.

Figure 6.2 shows that N–$\hat{u}$ curves obtained from CFX and CEL analyses are comparable only at small $\hat{u}$. However, at large $\hat{u}$, CEL gives significantly lower force than CFX, because the currently available versions of CEL cannot simulate the suction behind the pipe and bonding. A void remains behind the pipe, even at large deformation. After $\hat{u}$~4, N remains almost constant in CEL simulation (N_m=6.0), which represents the penetration resistance for the unbonded condition. A fully bonded condition cannot be defined in CEL.

FE simulations are also performed using Abaqus/Explicit, by which fully bonded and unbonded interface conditions can be modeled. However, Explicit cannot accommodate a very large deformation (e.g. $\hat{u}$=15 in CFX simulations). Therefore, in order to calculate the maximum force N_m, the pipe is placed at $\hat{w}$=3.0 in a fully embedded condition (i.e. WIP) and then displaced laterally. The geotechnical properties of clay and pipe–soil interface behaviour are the same as with the CEL model. The left and right vertical boundaries of the soil domain are placed at 6.0D and the bottom boundary at 4.0D from the pipe's centre and restrained by hinge supports. In these simulations, the force on the pipe increases quickly with displacement and at $\hat{u}$~0.1 it reaches the maximum and then remains almost constant. For clarity, only the maximum value (N_m) from Explicit analyses are shown by horizontal arrows on the right vertical axis of Fig. 6.2. The bonding at the pipe–soil interface significantly influences the response—N_m=6.1 for

unbonded (point a) and N_m=10.1 for fully bonded (point b) conditions. Martin and White (2012) also calculated N_m for WIP pipes at varying depths using a finite element limit analysis (FELA) program, modeling the soil as rigid-plastic material without consideration of strain rate and strain-softening effects. The analyses were limited to the following interface conditions: smooth/rough and unbonded/fully bonded. As α=0.5 is used, N_m in the present Explicit simulations are in between the values reported by Martin and White (2012) for the smooth and rough interface conditions, having similar geometry and soil properties.

Drawing lines through the highly sheared zone, as shown in Fig. 6.3(d), the failure planes are obtained when N_m is mobilized. The inset of Fig. 6.2 shows that CFX gives asymmetrical failure planes, with a longer one on the right side. A berm also forms above the pipe. However, in Explicit analysis, the failure planes are almost symmetrical and the size of the berm is negligible for this $\hat{w}$(=3). The failure mechanisms in Explicit are similar to the FELA results of Martin and White (2012). Because of this difference in soil failure mechanisms, the CFX gives higher N_m than Explicit analysis.

Comparing N_m for the simulations presented in Fig. 6.2, the following conclusions can be drawn. Although a large deformation can be modeled using Abaqus CEL, the calculated N_m using CEL is comparable to the Abaqus/Explicit unbonded case, because the CEL cannot model the suction/tension behind the pipe. The fully bonded condition in Explicit could be used to include the effects of soil behind the pipe; however, it gives lower N_m than CFX simulation (compare point b and c in Fig. 6.2) because of the difference in failure mechanisms and berm formation. In CFX, the strain rate and softening dependent soil model gives higher N_m (point d) than for the ideal soil case (point c), which is also higher than FE results (points a and b).

In summary, numerical simulation for a very large penetration distance is required for better estimation of N_m, because the soil failure mechanisms change with penetration. The tension behind the pipe, which is related to free water flow in the channel, significantly influences the drag force. These factors also need to be considered in the design of physical experiments to obtain accurate N_m. The present CFX model can simulate this process successfully and is computationally very efficient. With a 3.4 GHz Intel Core i7 processor and 12 GB RAM, the base case CFX simulation shown in Fig. 6.2 takes only 5 hours for 15D penetration, while it takes more than 3 days in Abaqus CEL for 6.8D penetration. The difference in solution schemes and the number of elements in the model are the potential causes of a significant difference in computational time. Fine mesh is required only around the pipe in CFX because the pipe is stationary; however, in CEL, fine mesh is required over a large zone through which the pipe moves.

6.6 Parametric Study

A comprehensive parametric study is performed varying only one parameter, while the other parameters are the same as the base case (Table 6.1), unless otherwise mentioned. The N–$\hat{u}$ curves for some selective cases are presented; however, a detailed discussion on N_m is provided for all the analyzed cases.

6.6.1 *Depth of Pipe*

In offshore environments, the clay block might impact the pipe at different depths. Figure 6.4 shows that N_m increases with $\hat{w}$, and it is very significant at low $\hat{w}$. The shape of N–$\hat{u}$ curves also depends on $\hat{w}$. For $\hat{w}\geq 3$, N gradually increases and reaches the peak (N_m) at ~10D–15D

penetration. However, for shallow depths ($\hat{w}\leq 2$), N initially increases with $\hat{u}$, then remains almost constant for $\hat{w}=2.0$ and decreases slightly for $\hat{w}=1.0$, and then increases again.

A close examination of the shape of N–$\hat{u}$ curves for $\hat{w}=1.0$ is performed using shear strain increments, together with berm and channel formations (Fig. 6.5). Tension does not develop behind the pipe when the channel is wide (e.g. Fig. 6.5a); therefore, N does not increase with $\hat{u}$ between $\hat{u}=1.3$ and $\hat{u}=5.0$. The slight decrease of N is due to the change in shear surface length with formation of berm and strain softening effects. Similar to Fig. 6.3, the channel behind the pipe closes with $\hat{u}$ (Figs. 6.5(b)–6.5(d)). However, compared to Fig. 6.3, a considerably large berm forms in this case.

6.6.2 *Attack Angle*

The effects of the attack angle are investigated from 10 simulations for $\hat{w}=1.0$ and 3.0. Figure 6.6 shows that the attack angle (θ) does not have a significant influence on N_m. However, for a given $\hat{w}$, the N–$\hat{u}$ curves are different because of the difference in suction mobilization behind the pipe, as discussed before.

6.6.3 *Velocity of Clay Block*

Figure 6.7 shows that N increases with v_0, which is because of an increase in geotechnical resistance and inertia force. However, the contribution of geotechnical and inertial components to N depends on s_{u0} and $\hat{w}$, as discussed in detail in the following sections. The shape of the N–$\hat{u}$ curve also depends on v_0. The length of the suction mobilization segment (cf. Fig. 6.2) decreases with v_0, because the suction behind the pipe increases with v_0, which accelerates the closure of the channel behind the pipe. The inset of Fig. 6.7 shows that the channel is almost closed at $\hat{u}$

=3.0 for v_0=6.0 m/s while it is wide open at this $\hat{u}$ for v_0=2.0 m/s (Fig. 6.3(a)) through which water can flow out easily. For the latter case, N increases with $\hat{u}$ because of gradual closure of the channel (Figs. 6.2(b)–6.2(d)). Also, because of this variation in suction mobilization, $\hat{u}$ required to attain N_m increases with decrease in v_0, as shown by the solid squares.

6.6.4 *Undrained Shear Strength*

The undrained shear strength influences the process of engulfment and formation of channel and berm. For clarity, the results are presented separately in Figs. 6.8(a) and 6.8(b). N_m does not depend on s_{u0} for deep conditions ($\hat{w}\geq$4.0) (Fig. 6.8b). However, the suction mobilization segment of the N–$\hat{u}$ curves is different. In this segment, the normalized force increases slowly with $\hat{u}$ for high s_{u0}, because the channel behind the pipe remains open for a large penetration distance and therefore suction develops slowly as compared to the analysis with low s_{u0}. For a very deep condition ($\hat{w}$=6.0), unlike Fig. 6.3(d) or 6.5(d), a flow-round mechanism develops at large $\hat{u}$ as shown in the inset of Fig. 6.8(b).

For shallow conditions ($\hat{w}\leq$3.0), the higher the value of s_{u0}, the lower the N for the whole range penetration distance, including large $\hat{u}$. In these cases, in addition to suction, berm formation plays a significant role on N, as discussed in previous sections.

It is to be noted here that higher vertical normalized penetration resistance for lower s_{u0} has been reported at shallow depths; however, the effect of s_{u0} is not significant for deep burial conditions (White et al., 2010). The present study shows a similar trend for lateral penetration.

6.6.5 *Soil Failure Mechanisms*

The location of the failure planes for the analyses with base case soil parameters (Table 6.1) are obtained by drawing lines through the high strain zones at large $\hat{u}$, as shown by the dashed lines in Fig. 6.5(d). The failure planes, together with the berm, are shown in Fig. 6.9 for 5 different depths ($\hat{w}$=1–6). The berm height decreases with an increase in $\hat{w}$. Compared to berm height, the width of the berm is not significantly influenced by $\hat{w}$ between 1 and 4. Berm height is negligible for $\hat{w}\geq 4$.

For very shallow depths ($\hat{w}$=1), two shear planes, s1 and s2, form from the bottom of the pipe and extend almost to the end of the berm. In addition, two shear planes, s3 and s4, form from the top of the pipe. For $\hat{w}$=2 and 3 cases, the shear planes are similar to $\hat{w}$=1 case, except there are no s4 type shear planes in these cases. In a deep condition ($\hat{w}$=6), the shear planes do not reach the top surface of the clay block; instead, local flow of soil around the pipe occurs, which represents the deep flow-round mechanisms.

The effects of berm shape and failure mechanisms at shallow depths are different from vertical penetration of a pipeline, as presented in previous studies (White et al., 2010; Hawlader et al., 2015a). The failure planes are not symmetrical, as observed in vertical penetration (length of s1 is greater than that of s2). At shallow depths, the pipe is engulfed with soil while in vertical penetration the trench behind the pipe is filled with water. Moreover, the formation of s3 and s4 type failure planes is not possible in vertical penetration. However, in a deep condition, the flow-round mechanism is similar to that of vertical penetration of pipe. Therefore, considering the deep condition as a reference, a simplified model is proposed in the following sections to calculate drag force for varying depths.

6.6.6 *Proposed Simplified Equations*

The maximum force (N_m) is one of the important parameters required in design. A total of 120 simulations (including the cases mentioned above) are performed to develop empirical equations to calculate N_m. Table 6.2 shows the values of N_m for varying soil properties (s_{u0}=2–8 kPa; μ=0.05–0.2; S_t=2–4 and ξ_{95}=10–30), depths ($\widehat{w}$=1–6) and impact velocities (2–6 m/s). As the attack angle does not have an influence on N_m (Fig. 6.6), all the analyses are performed for θ=45°. The following are the general trend: (i) N_m increases with μ but decreases with S_t and ξ_{95}; (ii) N_m increases with clay block velocity; (iii) N_m increases with a decrease in s_{u0} for shallow conditions (e.g. $\widehat{w}$=1); however, N_m is independent of s_{u0} for deep conditions (e.g. $\widehat{w}$=6); and (iv) the pipe is engulfed quickly and the deep failure mechanism with a local flow-round condition develops at lower normalized depth ($\widehat{w}_{\mathrm{deep}}$)) for lower s_{u0}. These trends are somehow similar to vertical penetration of a pipeline into the seabed (White et al., 2010; Chatterjee et al., 2012) although the failure mechanisms for lateral penetration are different (Fig. 6.9).

The drag force can be estimated ($N_{m(est)}$) summing the geotechnical component (N_{m_g}) and inertial component (N_{m_I}) (Randolph and White, 2012).

$$N_{\mathrm{m(est)}} = N_{\mathrm{m\_g}} + N_{\mathrm{m\_I}} \tag{4}$$

The following equation is proposed for the geotechnical component:

$$N_{\mathrm{m\_g}} = N_{0(\mathrm{deep})} f_{\mathrm{d}}\, f_{1(\mathrm{eq})}\, f_{2(\mathrm{eq})} \tag{5}$$

where $N_{0(deep)}$ is the normalized force for deep failure mechanisms without softening and rate effects, which can be estimated from theoretical solutions and varies between 9.2 and 11.94 for smooth and rough pipe–soil interface conditions, respectively (Randolph and Houlsby, 1984;

Martin and Randolph, 2006). As α=0.5 is used in this study, $N_{0(deep)}$=10.9 is used the following sections.

The depth factor f_d is used to incorporate the effects of transition from shallow to deep failure mechanisms.

$$f_d = \left(\frac{\hat{w}}{\hat{w}_{deep}} \right)^p \text{ with } \quad \frac{\hat{w}}{\hat{w}_{deep}} \le 1.0 \tag{6}$$

The parameter p is defined as $p = a\left(\frac{s_u}{\gamma' D} \right)^b$, where a and b are constants. Note that a similar equation (Eq. 6) has been proposed for the vertical penetration pipeline (Chatterjee et al., 2012). Based on CFX simulation results, $\hat{w}_{deep}$= 5.0, 5.5 and 6.0 are used for s_{u0}=2.0, 5.0 and 8.0 kPa, respectively, to incorporate the increase of $\hat{w}_{deep}$ with s_{u0}.

In Eq. (5), $f_{1(eq)}$ and $f_{2(eq)}$ are the equivalent effects of strain rate and strain softening, respectively. Similar to Eqs. (2) and (3), the following equations are proposed for these factors:

$$f_{1(eq)} = 1 + \mu \log \left\{ \frac{(v_0 / D_e)}{\dot{\gamma}_{ref}} \right\} \tag{7}$$

$$f_{2(eq)} = \frac{1}{S_t} + \left(1 - \frac{1}{S_t} \right) e^{-3\xi_{eq} / \xi_{95}} \tag{8}$$

In Eq. (7), v_0/D_e represents the operative shear strain rate (Zhu and Randolph, 2011). Similarly, ξ_{eq} in Eq. (8) represents the equivalent ξ when N_m is mobilized.

Analyzing the simulation results shown in Table 6.2, the following values of the model parameters are obtained: a=0.35, b=0.1 and ξ_{eq}=1.7.

The inertial component can be calculated based on a fluid mechanics approach, as in Zakeri (2009b):

$$N_{m\_I} = \left(\frac{1}{2} C_D \rho v_0^2 \right) / s_{u0} \quad (9)$$

where C_D is a drag coefficient and ρ is the density of flowing material (clay in this case). For clay slurry, Zakeri et al. (2009a) showed an exponential decrease of C_D with the Reynolds number. Based on a regression analysis of experimental results, Sahdi et al. (2014) found C_D=1.06 for clay slurries and very soft clays. As geotechnical resistance is not calculated separately, a relatively large value of C_D is used in a pure fluid mechanics approach. In the combined approach, as in Eq. (4), Randolph and White (2012) used C_D=0.4 for soft clay. In the present study, C_D=0.4 is used.

Inserting the values mentioned above for $N_{0(deep)}$, a, b, $\widehat{w}_{deep}$, ξ_{eq} and C_D in Eqs. (4–9), $N_{m(est)}$ is obtained for the conditions used in the simulations listed in Table 6.2. Figure 6.10(a) shows a close agreement between $N_{m(est)}$ and N_m obtained from CFX modeling, which indicates that Eqs. (4–9) could be used for estimation of drag force on suspended pipelines.

In order to show the effects of inertia on drag force, $N_{m(est)}$ for C_D=0 (with the other parameters the same as above) is plotted against N_m in Fig. 6.10(b). As the inertial drag is neglected, the data points for the high impact velocities (e.g. v_0=6 m/s) shift below the 1:1 line and give a scattered plot, compared to Fig. 6.10(a). The estimated drag force without the inertial component is lower than simulated values at high velocities and the difference is very significant for low s_{u0}.

6.6.7 *Comparison with Physical Model Tests*

A total of 11 centrifuge tests were conducted using the geotechnical centrifuge at C-CORE. Clay blocks of 4.5 m high, 6.0 m wide and 12.0 long, prepared from kaolin clay having an

undrained shear strength between 4 and 8 kPa, impacted pipes of 0.19 m or 0.29 m diameter at velocities ranging between 0.04 and 1.3 m/s in prototype scale (Chi, 2012; Zakeri et al., 2012). The values of $N_{m(est)}$ are obtained using Eqs. (4–9) for centrifuge test conditions. As the tests were conducted at large depths ($\widehat{w}$=7.5–13.5), $\widehat{w}/\widehat{w}_{deep}$=1.0 is used (see Eq. 6). In centrifuge modeling, s_{u0} was obtained from T-bar tests, and therefore in Eq. (7), $\dot{\gamma}_{ref}$=0.2 is used (Boukpeti et al., 2012; Sahdi et al., 2014). Moreover, for kaolin clay, μ=0.1 and S_t=3 are used (Randolph, 2004). The other parameters ($N_{0(deep)}$, a, b, ξ_{eq} and C_D) are the same as above. The estimated drag force ($N_{m(est)}$) is plotted against experimental N_m (Fig. 6.10a & b), which shows that the proposed empirical equations can be used to estimate drag force on a pipeline.

6.7 Conclusions

Numerical modeling of lateral pipe–soil interaction is generally performed using FE programs in which the pipe is placed at the desired depth and displaced laterally. However, when a clay block impacts a suspended section of offshore pipeline, a channel forms behind the pipe during penetration through which free water could flow. In the present study, a numerical modeling technique is developed using a CFD approach in ANSYS CFX which can successfully simulate the role of free water flow in the channel. Developing a new technique, a strain rate and strain-softening dependent model for undrained shear strength of clay is implemented in CFX. Simplified equations are proposed for estimation of drag force for practical design. The following conclusions can be drawn from this study:

1) A large lateral penetration distance is required to mobilise the maximum force on the pipe. The flow of free water in the channel significantly influences the process.

2) The cavity behind the pipe might be filled with water, especially at shallow burial depths and high s_u. The present CFX modeling can simulate the gradual development of tension behind the pipe by modeling water pressure (suction) in the cavity. Therefore, the limitations of predefined pipe–soil interface conditions (i.e. rough/smooth and full-tension/no-tension) in this zone of pipe surface could be avoided.
3) Soil failure mechanisms change with depth of the pipe. At shallow depths, asymmetrical failure planes develop from the pipes and reach the top of the clay block, while at deeper conditions, flow-round mechanism develops.
4) The proposed empirical equations can be used to estimate drag force. The contribution of the inertial component on drag force increases with velocity and decreases with undrained shear strength of the clay block.

Acknowledgement

The works presented in this paper have been supported by the Natural Sciences and Engineering Research Council of Canada (NSERC), Mitacs, C-CORE and Petroleum Research Newfoundland & Labrador.

Notation

a, b coefficient of depth factor

C_D drag coefficient

D diameter of pipe

D_e effective diameter of pipe

F pipe resistance force

f_d depth factor

f_1 strain rate effects

$f_{1(eq)}$ equivalent strain rate effects

f_2 strain-softening effects

$f_{2(eq)}$ equivalent strain-softening effects

L length of pipe section in the out of plane direction

N normalized pipe resistance

N_m maximum normalized pipe resistance using CFX

$N_{m(est)}$ maximum normalized pipe resistance using proposed empirical equations

N_{m_g} geotechnical component for proposed empirical equations

N_{m_I} inertial component for proposed empirical equations

$N_{0(deep)}$ normalised pipe resistance at deep burial for ideal-weightless soil

p power coefficient of depth factor

s_1, s_2, s_3 & s_4 failure planes

s_u mobilized undrained shear strength

s_{u0} intact undrained shear strength

s_{u95} s_u at ξ_{95}

s_{uN} $(2/\sqrt{3})\, s_{u0}$

S_t remolded sensitivity

u clay block lateral displacement

$\hat{u}$ u/D_e

v_0 velocity of clay block

v_x, v_y,& v_z boundary velocity of CFX domain

w invert depth of the pipe

$\widehat{w}$ w/D_e

$\widehat{w}_{deep}$ deep failure mechanism at w/D_e

α pipe–soil interface factor

θ attack angle

μ shear strain rate parameter

μ_d dynamic viscosity

γ' submerged soil unit weight

$\dot{\gamma}$ shear strain rate

$\dot{\gamma}_{ref}$ reference shear strain rate

ξ accumulated absolute plastic shear strain

ξ_{eq} equivalent accumulated absolute plastic shear strain

ρ material density

References

ANSYS CFX (2012). *CFX program* (*version 14.0*) *solver theory guide*, ANSYS, Canonsburg, PA, USA.

Audibert, J. M. & Nyman, K. J. (1977). Soil restraint against horizontal motion of pipes. *J. Geotech. Engng Div*. **103**, No. 10, 1119–1142.

Bea, R. G. & Aurora, R. (1982). Design of pipelines in mudslide areas. *Proceedings of the 14th annual offshore technology conference*, Houston, TX, USA. OTC 4411 MS.

Boukpeti, N., White, D., Randolph, M. & Low, H. (2012). Strength of fine-grained soils at the solid–fluid transition. *Géotechnique* **62**, No. 3, 213–226.

Bruschi, R., Bughi, S., Spinazzé, M., Torselletti, E. &Vitali, L. (2006). Impact of debris flows and turbidity currents on seafloor structures. *Nor. J. Geol*., **86**, 317–337.

C-CORE (2003). Extended model for pipe/soil interaction. *Report No*: PR: 271-0184.

Chatterjee, S., Randolph, M. F. & White, D. J. (2012). The effects of penetration rate and strain-softening on the vertical penetration resistance of seabed pipelines. *Géotechnique* **62**, No. 7, 573–582.

Chi, K. F. (2012). *Glide block or out-runner block impact on suspended submarine pipeline*. MEng thesis, Memorial University, Canada.

De Blasio, F., Engvik, L., Harbitz, C. & Elverhøi, A. (2004). Hydroplaning and submarine debris flows. *J. Geophysical Research* **109**, No. C011002, 1–15.

Demars, K. R. (1978). Design of marine pipelines for areas of unstable sediment. *ASCE Transport. Engng J*. **104**, No. 1, 109–112.

Dutta, S., Hawlader, B. & Phillips, R. (2014). Finite element modeling of partially embedded pipelines in clay seabed using Coupled Eulerian–Lagrangian method. *Can. Geotech. J*. **52**, No. 1, 58–72.

Einav, I. & Randolph, M. F. (2005). Combining upper bound and strain path methods for evaluating penetration resistance. *Int. J. Numer. Methods in Engng*. **63**, No. 14, 1991–2016.

Georgiadis, M. (1991). Landslide drag forces on pipelines. *Soils and Found.* **31**, 156–161.

Gui, M. W. & Bolton, M. D. (1998). Geometry and scale effects in CPT and pile design. *Proceedings of the 1st international conference on geotechnical site characterization*, Atlanta, GA, USA, pp. 1063–1068.

Guo, P. (2005). Numerical modelling of pipe–soil interaction under oblique loading. *J. Geo. Geoenviron. Engng*. **131**, No. 2, 260–268.

Hawlader, B., Dutta, S., Fouzder, A. & Zakeri, A. (2015a). Penetration of steel catenary riser in soft clay seabed: Finite element and finite volume methods. ASCE *Int. J. of Geomech*. **15**, No. 6, 1–12.

Hawlader, B., Fouzder, A. & Dutta, S. (2015b). Numerical modeling of suction and trench formation at the touchdown zone of steel catenary riser. *ASCE Int. J. of Geomech*. **16**, No. 1, 1–14.

Hu, Y. & Randolph, M. F. (1998) A practical numerical approach for large deformation problems in soil. *Int. J. Numer. Methods in Engng*. **22**, No. 5, 327–350.

Jeanjean, P., Liedtke, E., Clukey, E., Hampson, K. & Evans, T. (2005). An operator's perspective on offshore risk assessment and geotechnical design in geohazard-prone areas. *Proceedings of the 1st international symposium on frontiers in offshore geotechnics* (*ISFOG*), Perth, WA, Australia.

Jostad, H. P. & Andresen, L. (2004). Modelling of shear band propagation in clays using interface elements with finite thickness. *Proceedings of the 9th international symposium on numerical models in geomechanics - NUMOG IX*, Ottawa, Canada, pp. 121–128.

Kvalstad, T., Nadim, F. & Arbitz, C. (2001). Deepwater geohazards: Geotechnical concerns and solutions. *Proceedings of the offshore technology conference*, Texas, USA. OTC 12958-MS,

Martin, C. & White, D. (2012). Limit analysis of the undrained bearing capacity of offshore pipelines. *Géotechnique* **62**, No. 9, 847–863.

Martin, C.M. & Randolph, M.F. (2006). Upper-bound analysis of lateral pile capacity in cohesive soil. *Géotechnique* **56**, No. 2, 141-145.

Merifield, R., White, D. J. & Randolph, M. F. (2008). The ultimate undrained resistance of partially embedded pipelines. *Géotechnique* **58**, No. 6, 461–470.

Mulder, T. & Alexander, J. (2001). The physical character of subaqueous sedimentary density flows and their deposits. *Sedimentology* **48**, 269–299.

Paulin, M. J., Phillips, R., Clark, J. I. & Boivin, R. (1998). An experimental investigation into lateral pipeline/soil interaction–Phase II. *Proceedings of the international conference on centrifuge*, Tokyo, Japan, pp. 699–704.

Phillips, R., Nobahar, A. & Zhou, J. (2004). Trench effects on soil/pipe interaction. *Proceedings of the international pipeline conference*, Calgary, AB, Canada, pp. 1–7.

Piper, D. J. W., Cochonat, P. & Morrison, M. L. (1999). The sequence of events around the epicenter of the 1929 Grand Banks earthquake: Initiation of debris flows and turbidity current inferred from side scan sonar. *Sedimentology* **46**, 79–97.

Popescu, R., Phillips, R., Konuk, I., Guo, P., & Nobahar, A. (2002). Pipe/soil interaction: Large scale tests and numerical modelling. *Proceedings of the international conference of physical modelling in geotechnics*, St. John's, NL, pp. 917–922.

Puech, A., Orozco-Calderón, M. & Foray, P. (2010). Mini T-bar testing at shallow penetration. *Proceedings of the 2nd international symposium on frontiers in offshore geotechnics* (*ISFOG*), Perth, WA, Australia, pp. 305–310.

Randolph, M. F. (2004). Characterization of soft sediments for offshore applications. *Proceedings of the 2nd international conference on site characterization*, Porto, Portugal, pp. 209–231.

Randolph, M. F. & White, D. J. (2012). Interaction forces between pipelines and submarine slides—A geotechnical viewpoint. *Ocean Engng* **48**, 32–37.

Randolph, M. F & Houlsby, G.T. (1984). The limiting pressure on a circular pile loaded laterally in cohesive soil. *Géotechnique* **34**, No. 4, 613–623.

Randolph, M. F., Gaudin, C., Gourvenec, S., White, D. J., Boylan, N. & Cassidy, J. (2010). Recent advances in offshore geotechnics for deep water offshore oil and gas development. *Ocean Engng* **38**, 818–834.

Sahdi, F., Gaudin, C., White, D., Boylan, N. & Randolph, M. (2014). Centrifuge modelling of active slide-pipeline loading in soft clay. *Géotechnique* **64**, No. 1, 16–27.

Summers, P. & Nyman, D. (1985). An approximate procedure for assessing the effects of mudslides on offshore pipelines. *J. Energy Resources Technology* **107**, No. 4, 426–432.

Supachawarote, C., Randolph, M. F. & Gourvenec, S. (2004). Inclined pull-out capacity of suction caissons. *Proceedings of the 14th international offshore and polar engineering conference*, Toulon, France, pp. 500–506.

Swanson, R. C. & Jones, W. T. (1982). Mudslide effects on offshore pipelines. *ASCE Transpor. Engng J.* **108**, No. 6, 585–600.

White, D. J., Gaudin, C., Boylan, N. & Zhou, H. (2010). Interpretation of T-bar penetrometer tests at shallow embedment and in very soft soils. *Can. Geotech. J.* **47**, No. 2, 218–229.

Zakeri, A. (2009a). Review of state-of-the-art: Drag forces on submarine pipelines and piles caused by landslide or debris flow impact. *J. Off. Mech. Arc. Engng* **131**, No. 1, 014001.

Zakeri, A. (2009b). Submarine debris flow impact on suspended (free-span) pipelines: Normal and longitudinal drag forces. *Ocean Engng* **36**, No. 6, 489–499.

Zakeri, A. & Hawlader, B. (2013). Drag forces caused by submarine glide block or out-runner block impact on suspended (free-span) pipelines—Numerical analysis. *Ocean Engng* **67**, 89–99.

Zakeri, A., Hawlader, B. & Chi, K. (2012). Drag forces caused by submarine glide block or out-runner block impact on suspended (free-span) pipelines. *Ocean Engng* **47**, 50–57.

Zakeri, A., Høeg, K. & Nadim, F. (2009). Submarine debris flow impact on pipelines—Part II: Numerical analysis. *Coastal Engng* **56**, No. 1, 1–10.

Zakeri, A., Høeg, K. & Nadim, F. (2008). Submarine debris flow impact on pipelines—Part I: Experimental investigation. *Coastal Engng* **55**, No. 12, 1209–1218.

Zhu, H. & Randolph, M. F. (2011). Numerical analysis of a cylinder moving through rate-dependent undrained soil. *Ocean Engng* **38**, No. 7, 943–953.

Zhu, H., Randolph, M. F. (2010). Large deformation finite-element analysis of submarine landslide interaction with embedded pipelines. *ASCE Int. J. Geomech.* **10**, No. 4,145–152.

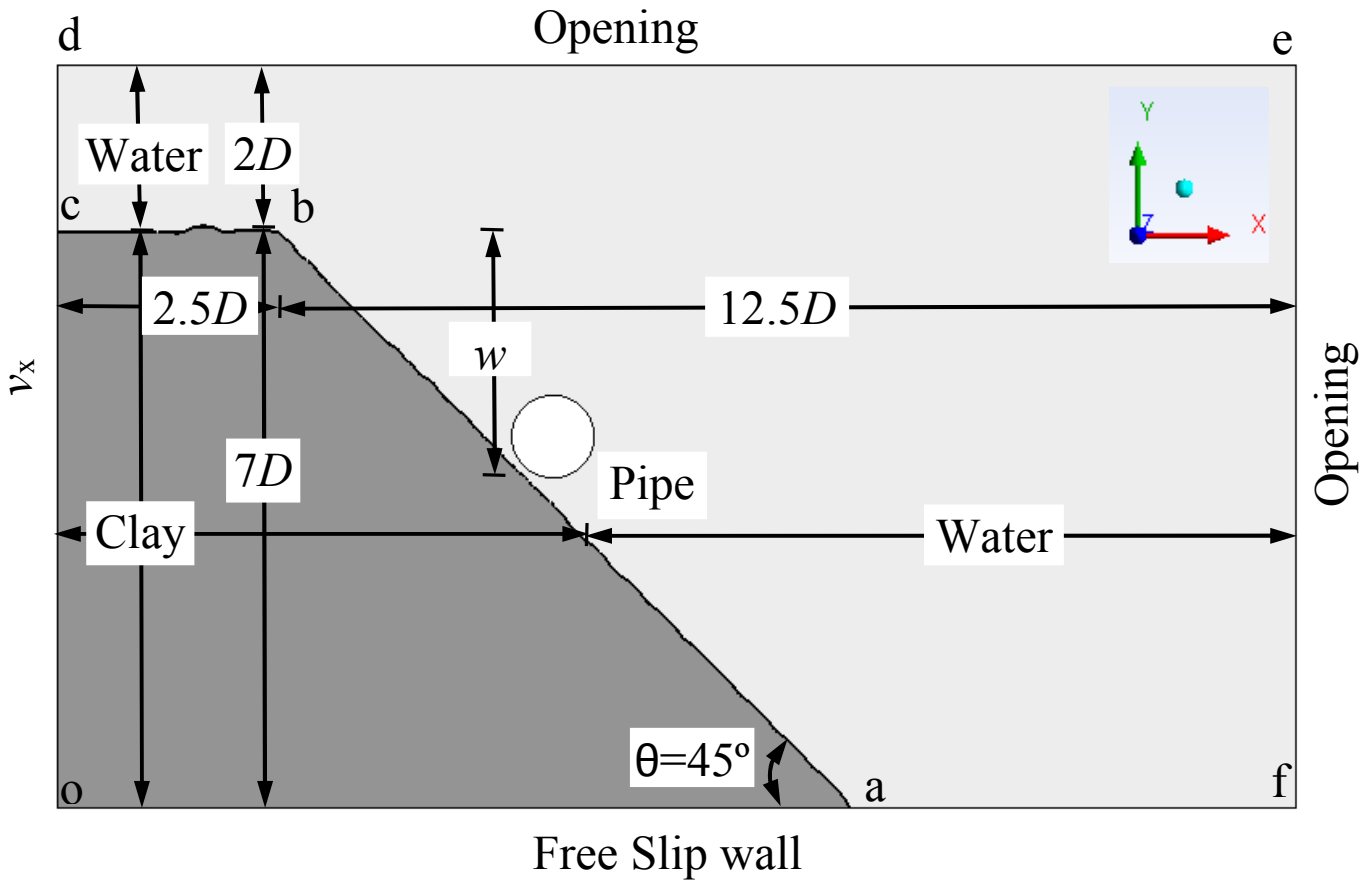

Fig. **6**.**1**. Model development for the base case

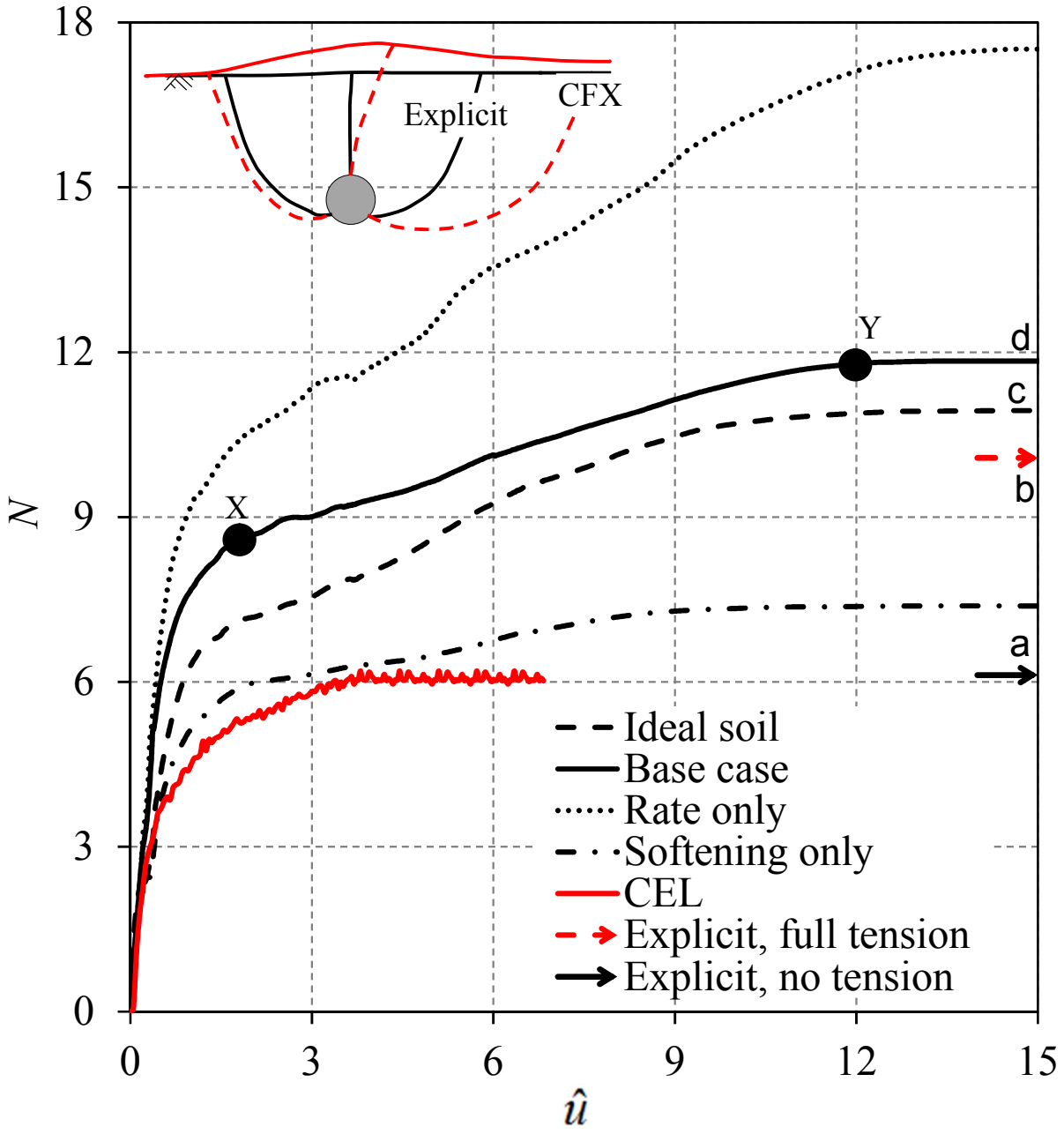

Fig. **6**.**2**. Normalized horizontal resistance with normalized displacement

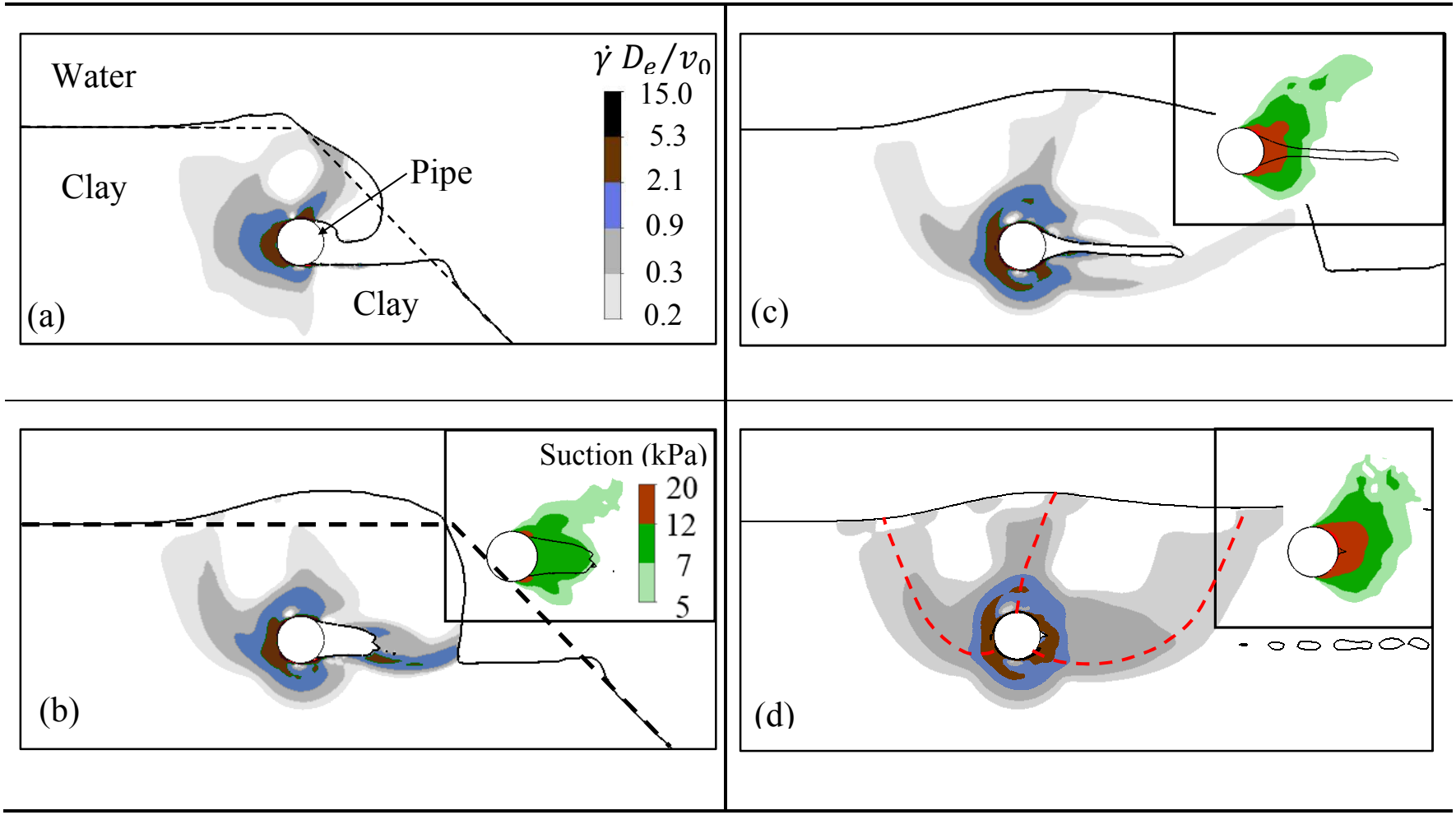

Fig. **6.3**. Normalized shear strain rate and suction around the pipe for $\hat{w} = 3$ with lateral penetration: (a) 3*D* (b) 6*D* (c) 9*D* and (d) 15*D*

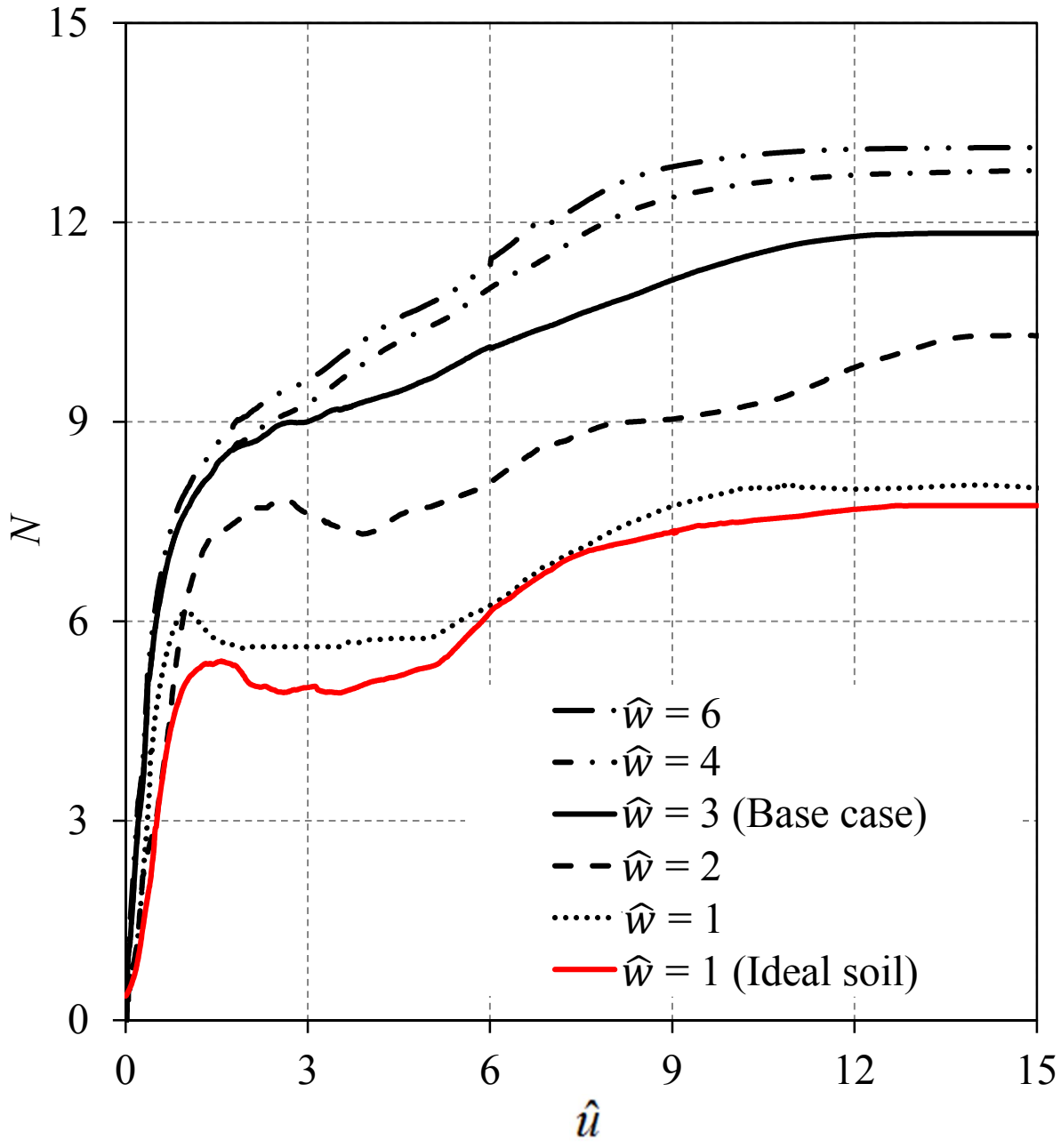

Fig. **6**.**4**. Effect of depth of pipe on *N*

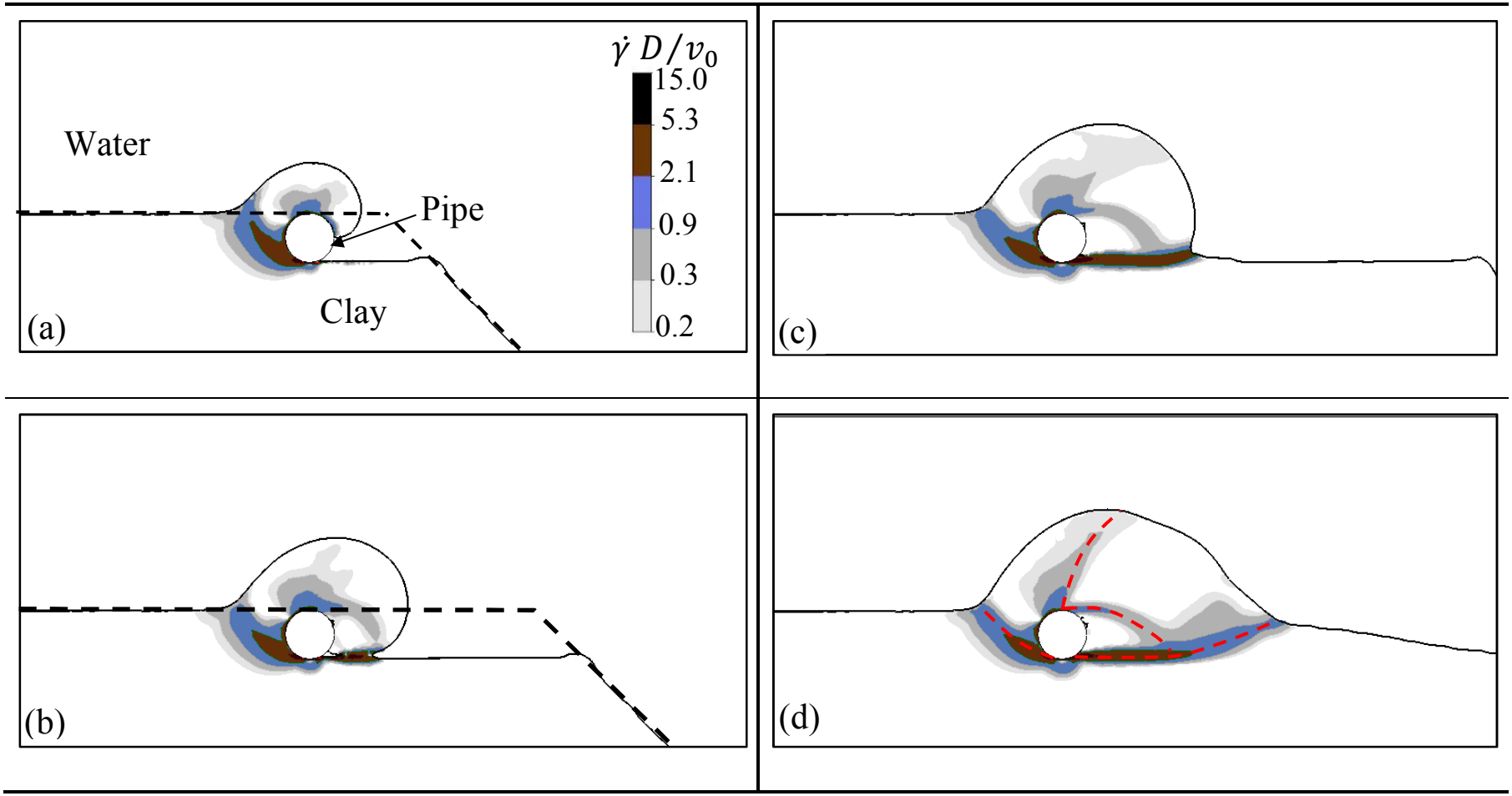

Fig. **6.5**. Normalized shear strain rate for $\hat{w} = 1$ with lateral penetration: (a) 3*D* (b) 6*D* (c) 9*D* and (d) 15*D*

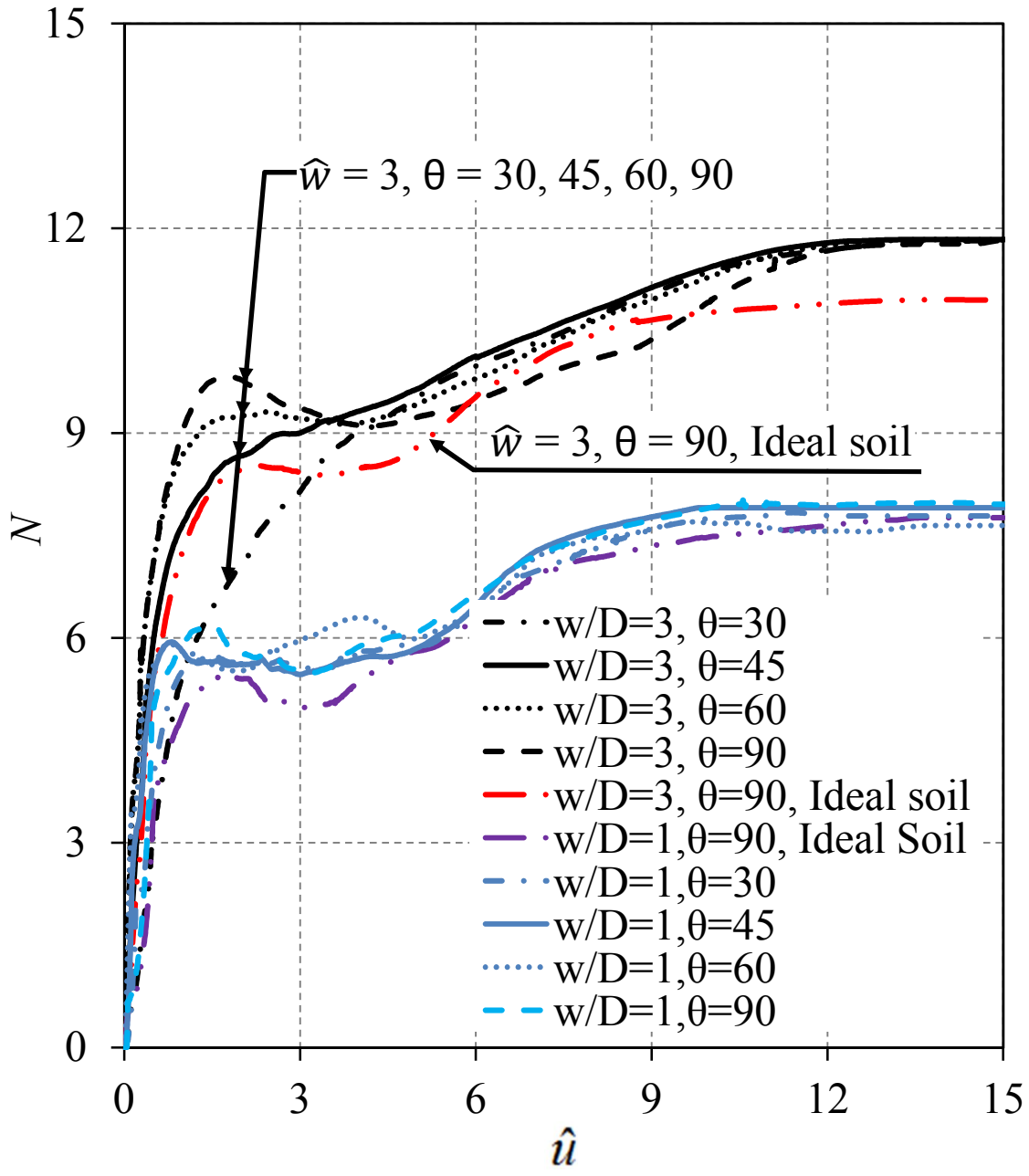

Fig. **6**.**6**. Effect of attack angle

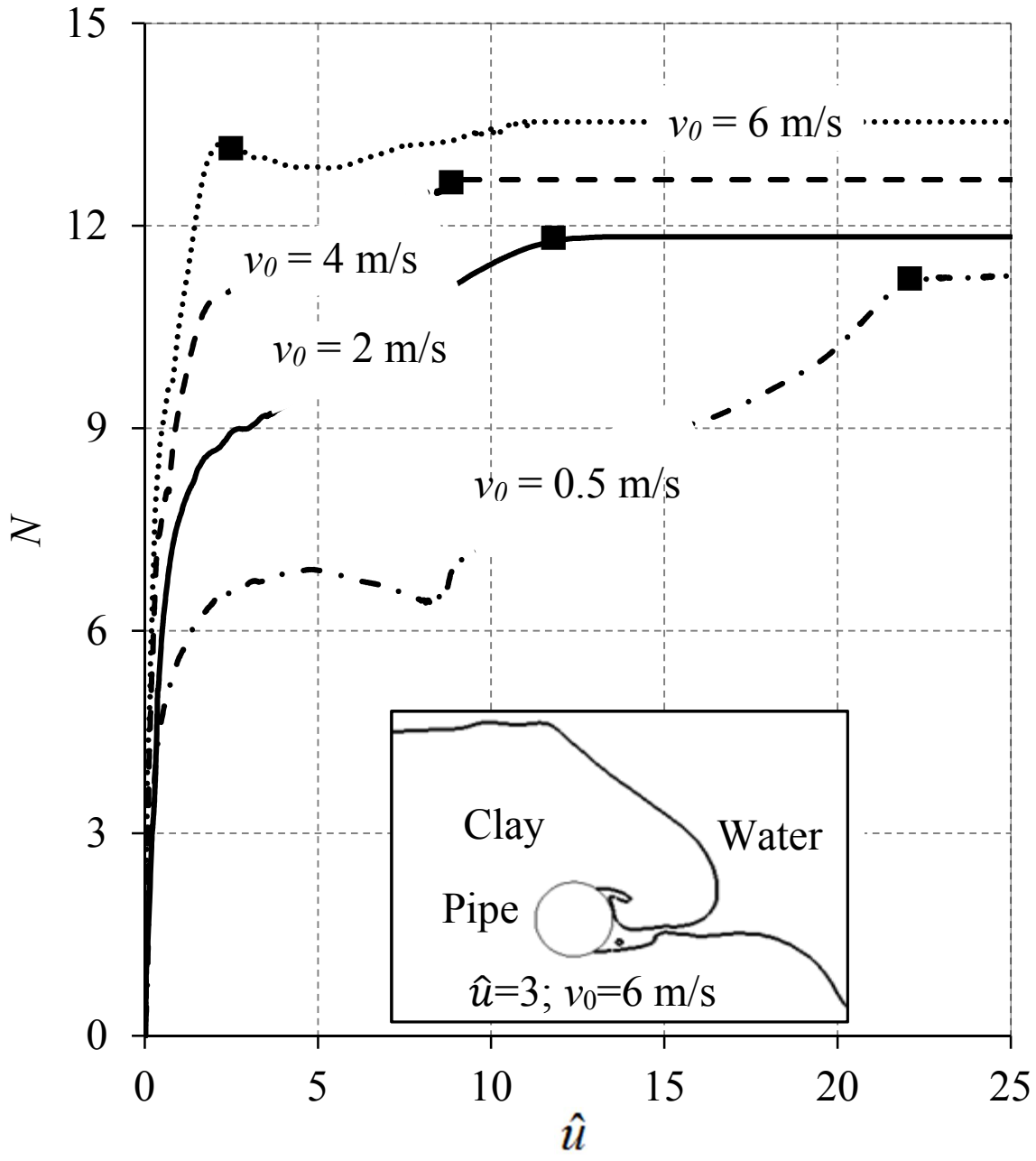

Fig. **6**.**7**. Effect of clay block velocity

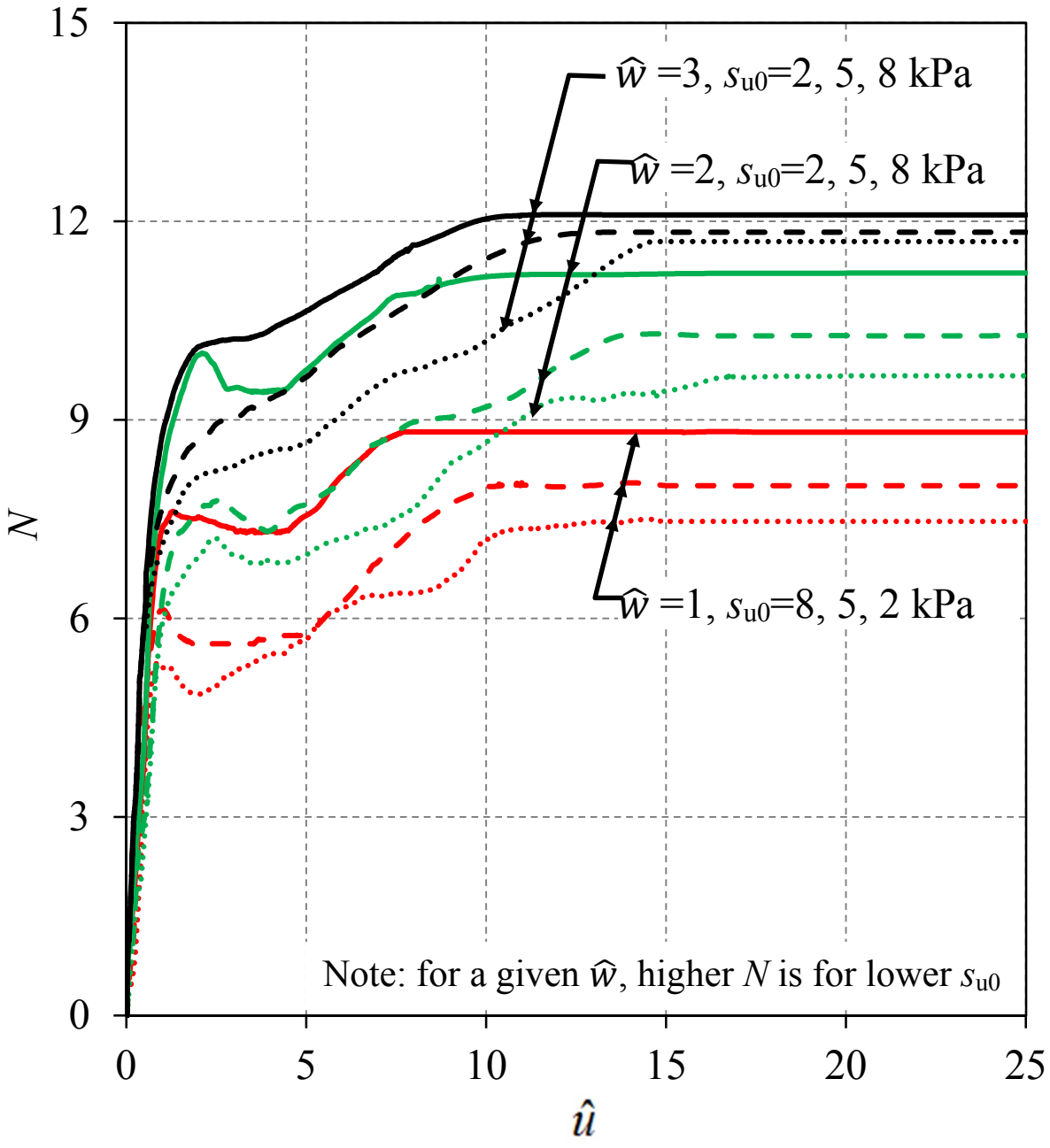

Fig. **6.8(a)**. Effect of undrained shear strength on N for $\hat{w}$ =1–3

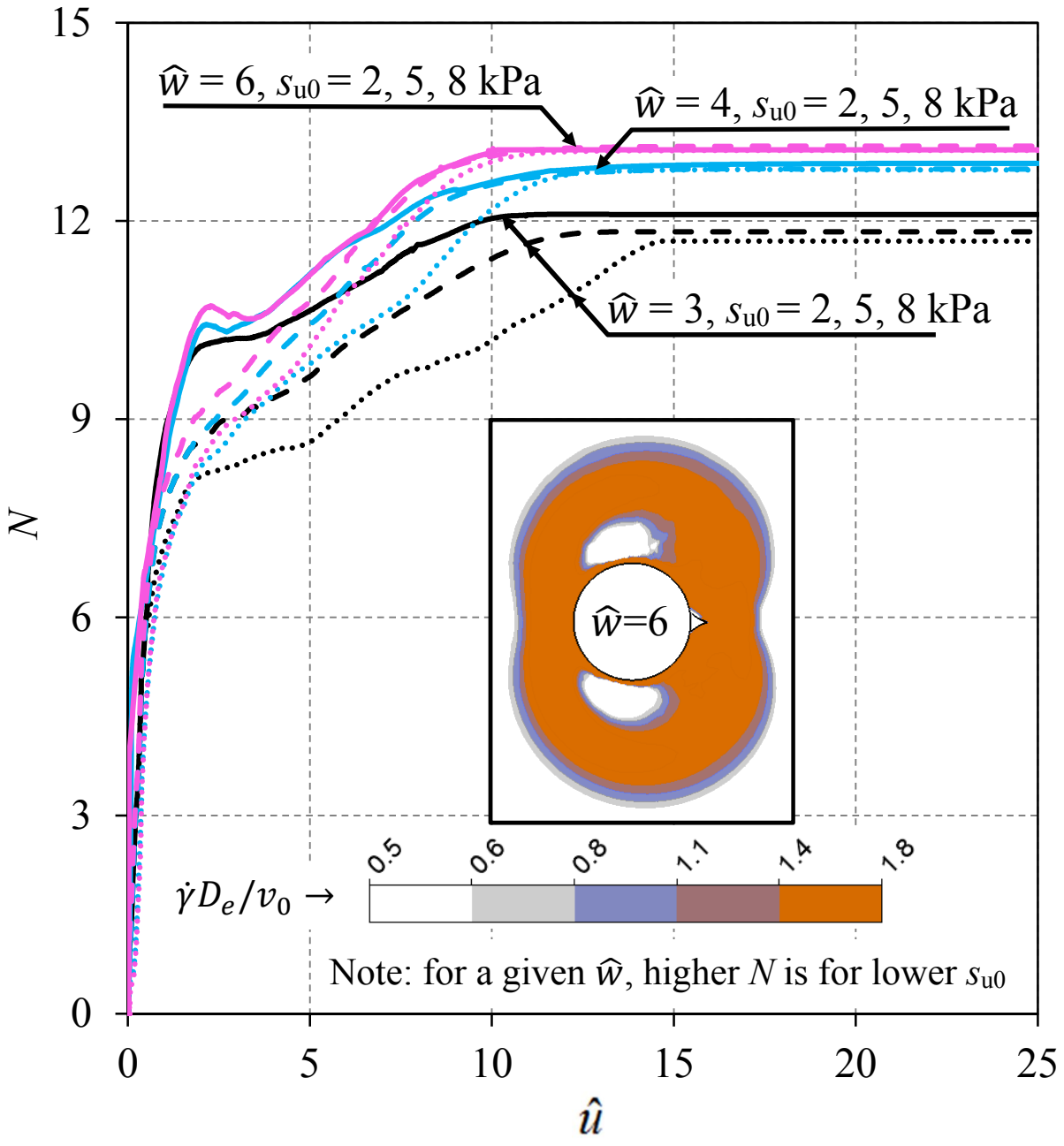

Fig. **6.8(b)**. Effects of undrained shear strength on N for $\hat{w}$ = 3–6

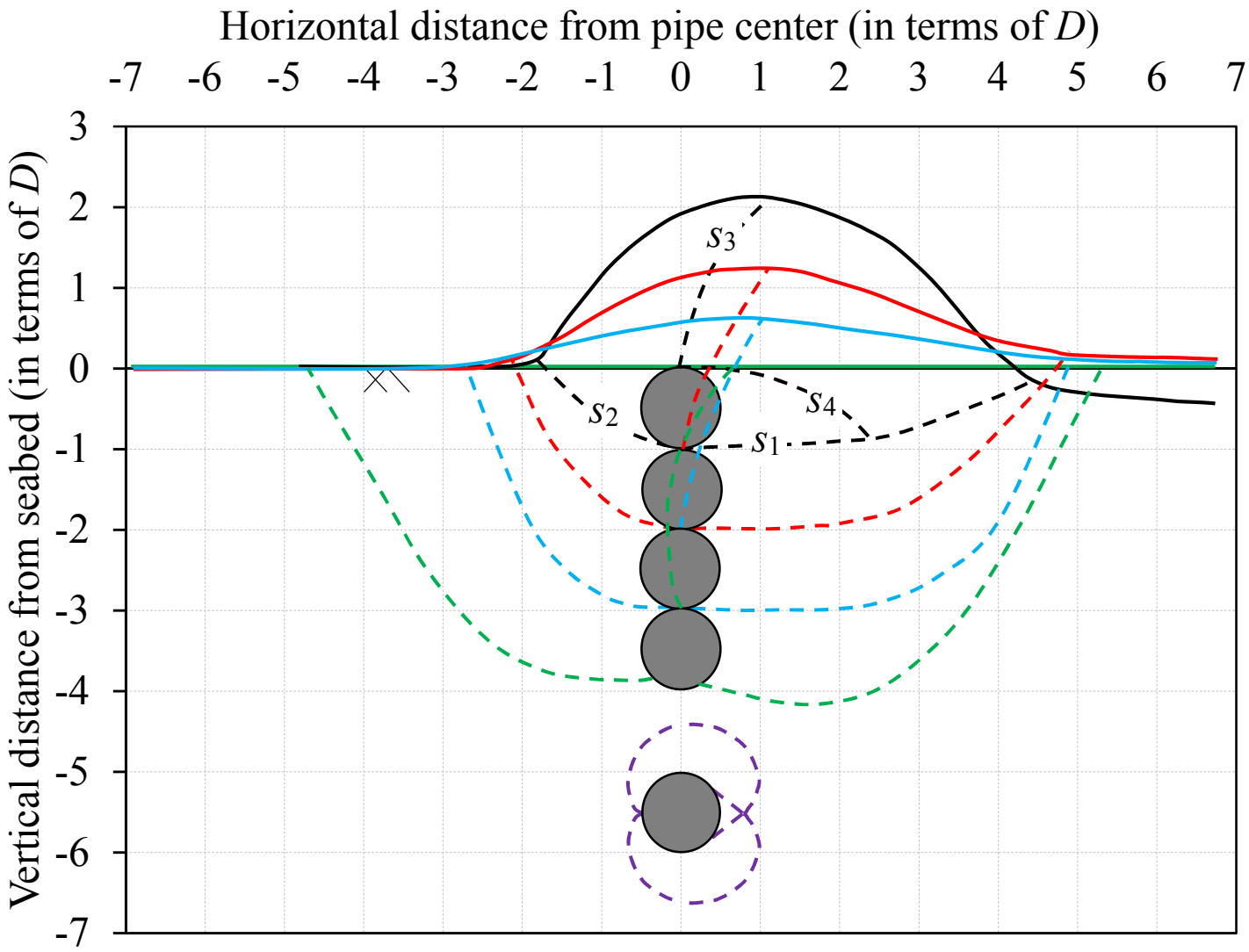

Fig. **6**.**9**. Variation of soil failure mechanisms with depth of pipe

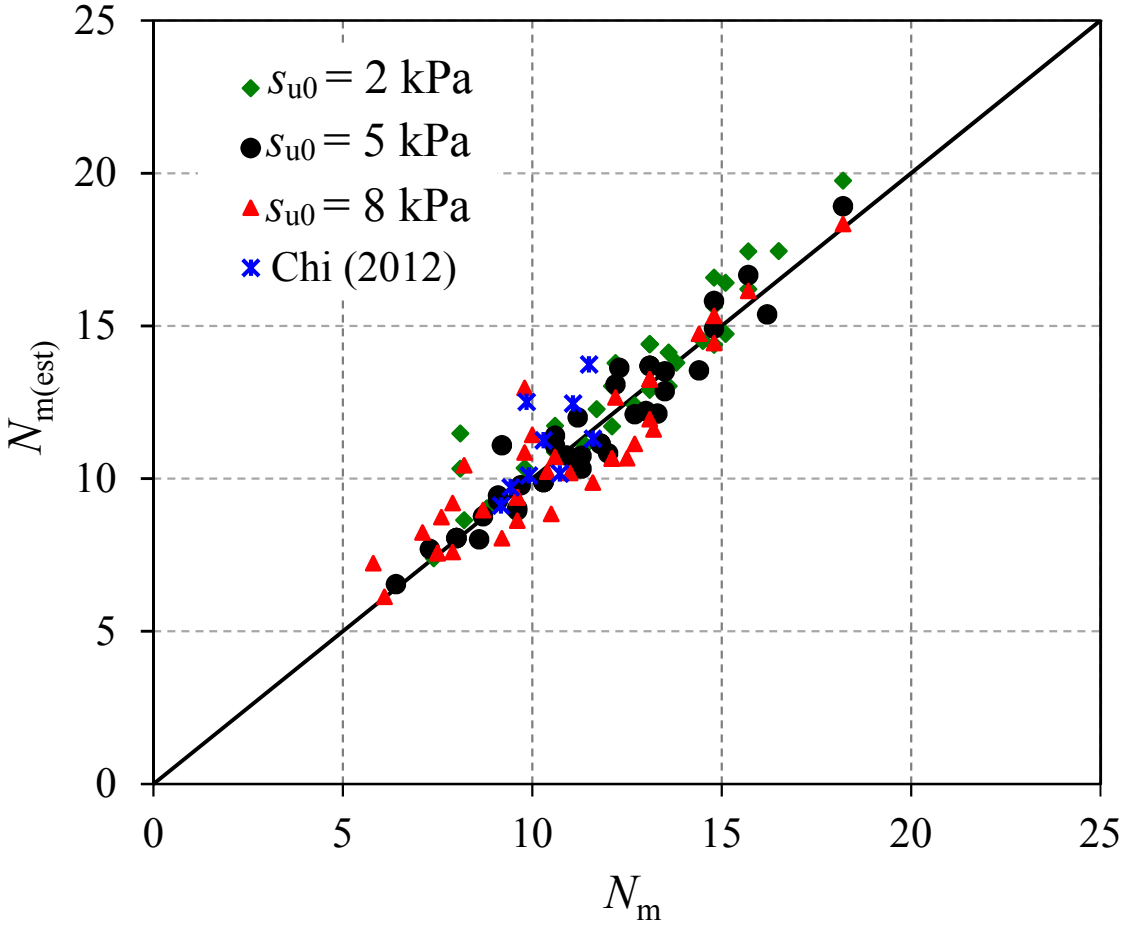

Fig. **6**.**10(a)**. Performance of combined approach for estimating N_m using empirical equations

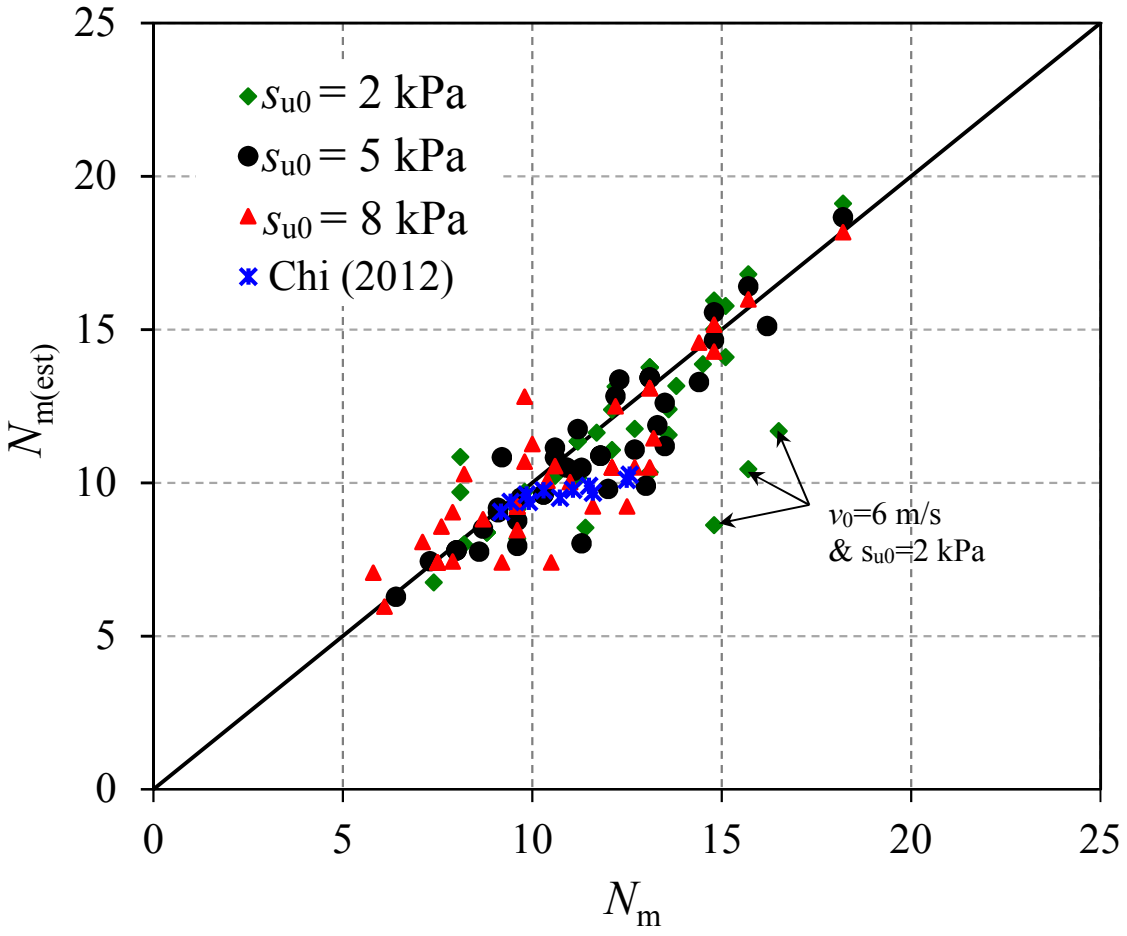

Fig. 6.10(b). Performance of geotechnical approach for estimating N_m using empirical equations

Table 6.1. Parameters used in CFX modelling for base case

Parameters	Values
Pipe diameter, D	290 mm
Saturated unit weight of soil, γ_{sat}	15.81 kN/m^3
Unit weight of water, γ_w	9.81 kN/m^3
Dynamic viscosity of water, μ_w	0.00089 kg/m/s
Soil undrained shear strength at reference shear strain rate prior to any softening, s_{u0}	5 kPa
Clay block velocity, v_0	2 m/s
Rate of increase of undrained shear strength per log cycle, μ	0.1
Reference strain rate, $\dot{\gamma}_{ref}$	3×10^{-6} s^{-1}
Soil sensitivity, S_t	3
Accumulated absolute plastic shear strain for 95% soil strength degradation (ξ_{95})	10

Table 6.2. Maximum force N_m for varying pipe depths and soil properties

μ	S_t	ξ_{95}	N_m			
			$\widehat{w} = 1$ [s_{u0} = 2, 5, 8 kPa]*	$\widehat{w} = 2$ [s_{u0} = 2, 5, 8 kPa]	$\widehat{w} = 3$ [s_{u0} = 2, 5, 8 kPa]	$\widehat{w} = 6$
0.05	3	10	7.4, 6.4, 6.1	9.6, 8.6, 7.9	10.3, 9.6, 9.6	10.6
0.10	3	10	8.8, 8.0, 7.5 {11.4, 9.6, 9.2} [14.8, 11.3, 10.5]	11.2, 10.3, 9.6 {13.1, 12.0, 11.6} [15.7, 13, 12.5]	12.1, 11.7, 11.7 {13.6, 12.7, 12.7} [16.4 13.5,13.1]	13.1
0.20	3	10	11.7, 9.2, 8.2	15.1, 12.3, 9.8	16.5, 16.2, 14.4	18.2
0.10	2	10	9.6, 8.7, 7.1	12.1, 10.9, 10.4	13.3, 13.3, 13.3	14.8
0.10	4	10	8.2, 7.3, 5.8	9.5, 9.1, 8.7	11.3, 11.1, 11.0	12.2
0.10	3	20	9.8, 9.1, 7.6	12.7, 10.6, 9.8	13.8, 13.5, 12.0	14.8
0.10	3	30	10.6, 9.7, 7.9	13.6, 11.2, 10.0	14.5, 14.4, 12.0	15.7

Notes:

* Values in columns 4–6 represent N_m for s_{u0} = 2, 5, 8 kPa, respectively

{…}: Analysis for clay block velocity of 4 m/s

[…]: Analysis for clay block velocity of 6 m/s

CHAPTER 7

Conclusions and Recommendations for Future Research

7.1 Conclusions

Pipelines and steel catenary risers (SCRs) are widely used in the offshore oil and gas industries to transport hydrocarbons. In deepwater, pipelines are usually laid on the seabed and might penetrate a fraction of their diameter into the seabed due to installation effects and the weight of pipeline and its contents. The partially embedded pipelines might displace laterally due to high internal pressure and temperature change during operation. The lateral soil resistance, which also depends on initial embedment, is a key design parameter for assessment of buckling and on-bottom stability. On an uneven seabed, sections of surface laid pipelines might be suspended which could be impacted by soil blocks moving out from submarine landslides, because these blocks can travel downslope at a high velocity. The drag force on a suspended pipeline is one of the key design issues. The SCR can be used in deepwater to transport hydrocarbons from seabed wellheads to floating platforms. The region near the touchdown point, where the SCR touches the seabed, is a fatigue hotspot. The fatigue life of the SCR depends on riser–seabed–water interaction.

Pipeline– and SCR–seabed–water interaction are large-deformation problems. In the present study, numerical models are developed for these large-deformation problems using the Coupled Eulerain–Lagrangian (CEL) approach in Abaqus finite element (FE) software and computational fluid dynamics approach in ANSYS CFX finite volume software.

The following are the general conclusions of the entire thesis. Problem specific conclusions are presented at the end of each chapter (Chapters 3–6) and in the Appendices.

Chapter 3 presents large deformation FE analyses of pipe vertical penetration into a clay seabed with subsequent lateral displacement using Abaqus CEL. A strain-rate and strain-softening dependent soil constitutive model is implemented using user subroutines. Very large displacement of the pipe, which generates large shear strain, was successfully simulated without any numerical issues using Abaqus CEL. FE results are in good agreement with centrifuge test results and previous numerical analyses. A comprehensive parametric study was performed for strain-rate, strain-softening, undrained shear strength of soil, and weight of pipe to provide further insight into soil failure mechanisms, and vertical and lateral resistance. Although commercially available FE software Abaqus CEL can simulate the large deformation behavior, it cannot simulate suction for a single-phase material.

Chapter 4 presents a comparative study between Abaqus CEL and ANSYS CFX for modeling penetration of a pipeline for a range between shallow to intermediate depths (maximum 5.0*D*). Analyses are performed for both uniform and varying undrained shear strength with depth. The vertical penetration resistances obtained from these two numerical approaches are in good agreement up to vertical penetration of 2.5*D*. After that, suction develops in water in the cavity that forms behind the pipe which gives higher penetration resistance in CFX analysis than in CEL analysis. Although Abaqus CEL can handle large-deformation problems, it cannot model suction. Detailed discussion on channel formation mechanisms, role of suction and effects of soil parameters on penetration resistance and formation of berm has been provided. It has been shown that ANSYS CFX can be used for modeling pipeline and riser penetration into soft to ultra-soft clay, including the role of the trapped water in the cavity above the pipe on penetration resistance and soil failure mechanisms.

The CFX model developed in Chapter 4 is extended in Chapter 5 to simulate the response of a SCR subjected to cyclic loading near the touchdown zone. In addition to undrained remoulding, the concept of "shear wetting" is used to further reduce the shear strength of soil. Based on a comprehensive parametric study on initial penetration depth, amplitude of displacement and geotechnical parameters, the degradation of penetration and uplift resistance with number of loading cycles are presented. The effects of these parameters on trench formation and suction during extraction are also presented. It is observed that ANSYS CFX can simulate the riser–soil–water interaction near the seabed under cyclic loading.

Modeling of drag force on a suspended pipeline when impacted by soil blocks from submarine landslides is presented in Chapter 6. Numerical analyses are performed using both CEL and CFX. It is found that ANSYS CFX can simulate landslide impact on pipeline better than Abaqus CEL and other FE modeling approaches (e.g. Explicit FE modeling). One of the main advantages of ANSYS CFX is that it can simulate the effect of water on drag force and soil failure mechanisms. Based on a comprehensive parametric study, a set of empirical equations are proposed for estimation of drag force for practical applications. Good agreement is found between drag forces obtained from CFX simulations, empirical equations and centrifuge tests.

7.2 Recommendations for Future Research

Several important features of deepwater pipe–soil–water interaction are successfully simulated in the present study. However, there are some limitations of this study which might be addressed in future.

- Because of limitations of Abaqus 6.10 for modeling interface behaviour, analyses are performed for smooth and rough interface conditions only. In the recent versions of Abaqus

(e.g. v.6.14), this issue has been resolved. Analysis could be performed using this version of Abaqus for better modeling of a range of interface condition (between smooth and rough).

- Three-dimensional FE analysis can be performed to provide better insight into the combined effects of axial/lateral/oblique movement of the pipe on lateral buckling.
- A limited number of analyses have been performed for dynamic embedment of pipeline. Further study is required for dynamic embedment.
- There is a great uncertainty in the undrained shear strength of soil near the mudline. Accurate measurement/estimation of shear strength will improve the prediction of vertical and lateral resistances.
- The drag force has been calculated for landslide impact normal to the pipeline. Simulations for axial loading and other impact angles need to be performed.
- The reduction of undrained shear strength due to water entrainment or soil water mixing is modeled empirically using shear wetting. Verification of this model with development of new experimental techniques will be useful.
- A limited number of centrifuge tests on impact loading of clay blocks on suspended pipe were performed. Additional tests are required for varying depth, soil properties and loading conditions.
- Erosion of remoulded soil occurs around the riser during cyclic motions, which could be accounted by advancing the numerical techniques developed in the present study.

REFERENCES

AGA/PRC. (1992). *Weight coating design for submarine pipeline on–bottom stability*. *Final report comparing TAMU test to SINTEF model*. American Gas Association, Report PR–178–918.

Aubeny, C. P., and Biscontin, G. (2009). Seafloor−riser interaction model. *ASCE International Journal of Geomechanics* **9**, No. 3, 133–141.

Aubeny, C. P., Shi, H. and Murff, J. D. (2005). Collapse loads for a cylinder embedded in trench in cohesive soil. *ASCE International Journal Geomechanics* **5,** No. 4, 320–325.

Aubeny, C. P., Gaudin, C. and Randolph, M. (2008). Cyclic tests of model pipe in kaolin. *Society of Petroleum Engineers* **3**, No. 4, 1–6. doi:10.2118/123131-PA.

Aubeny, C. P., White, T. A., Langford, T., Meyer, V. and Clukey, E. C. (2015). Seabed stiffness model for steel catenary risers. *Proceedings of the 3rd International Symposium on Frontiers in Offshore Geotechnics* (*ISFOG*), Oslo, Norway, pp. 351–356.

Barbosa–Cruz, E.R. and Randolph, M.F. (2005). Bearing capacity and large penetration of a cylindrical object at shallow embedment. *Proceedings of the 1st International Symposium on Frontiers in Offshore Geotechnics* (*ISFOG*), Perth, WA, Australia, pp. 615–621.

Barrett, J., Phillips, R. and Macneill, A. (2015). Comparative physical and numerical modelling of riser–seabed interaction. *Proceedings of the 34th International Conference on Offshore Mechanics and Arctic Engineering* (*OMAE*), St. John's, NL, Canada, pp. 1−8.

BostrØm, B., SvanØ, G. and Eiksund, G. (1998). Response effects of riser soil interaction modelling. *Proceedings of the 17th International Conference on Offshore Mechanics and Arctic Engineering* (*OMAE*), Lisbon, Portugal.

Boukpeti, N., White, D., Randolph, M. and Low, H. (2012). Strength of fine-grained soils at the solid–fluid transition. *Géotechnique* **62**, No. 3, 213–226.

Bransby, M.F., Zajac, P., and Amman, S. (2008). Finite element analysis of the vertical penetration of 'on-bottom' pipelines in clay. *Proceedings of the 18th International Offshore and Polar Engineering Conference* (*ISOPE*), Vancouver, BC, Canada, pp: 245–249.

Bridge, C. (2005). *Effects of seabed interaction on steel catenary risers*. PhD Thesis, University of Surrey, UK.

Briaud, J. L. (2008). Case histories in soil and rock erosion: Woodrow Wilson Bridge, Brazos River Meander, Normandy Cliffs, and New Orleans Levees. *ASCE Journal of Geotechnical Geo-environmental Engineering* **134**, N0.10, 1425−1447.

Brookes, G. and Whitmore, R. (1968). The static drag on bodies in Bingham plastics. *Rheological Acta* **7**, No. 2, 188–193.

Bruton, D.A.S. and Carr, M.C. (2011). Overview of the SAFEBUCK JIP. *Proceedings of the Offshore Technology Conference*, Houston, TX, USA. OTC 21671.

Bruton, D.A.S., Boreas, A., White, D.J., Carr, M., and Cheuk, J.C.Y. (2008). Pipe−soil interaction during lateral buckling and pipeline walking—the SAFEBUCK JIP. *Proceedings of the Offshore Technology Conference*, Houston, TX, USA. OTC 19589.

Bruton, D.A.S., Carr, M.C. and White, D.J. (2007). The influence of pipe–soil interaction on lateral buckling and walking of pipelines – The SAFEBUCK JIP. *Proceedings of the 6th International Offshore Site Investigation and Geotechnics Conference: Confronting New Challenges and Sharing Knowledge*, London, UK.

Bruton, D.A.S., White, D.J., Cheuk, C.Y., Bolton, M.D., and Carr, M.C. (2006). Pipe–soil interaction behaviour during lateral buckling, including large amplitude cyclic displacement tests by the SAFEBUCK JIP. *Proceedings of the Offshore Technology Conference*, Houston, TX, USA. OTC 17944.

Byrne, P. and Finn, W. (1978). Breakout of submerged structures buried to a shallow depth. *Canadian Geotechnical Journal* **15**, No.2, 146–154.

Cardoso, O.C. and Silveira, M.S.R. (2010). Pipe–soil interaction behaviour for pipelines under large displacements on clay soils–A model for lateral residual friction factor. *Proceedings of the Offshore Technology Conference*, Houston, TX, USA. OTC 20767.

Chatterjee, S., Randolph, M. F. and White, D. J. (2012a). The effects of penetration rate and strain softening on the vertical penetration resistance of seabed pipelines. *Géotechnique* **62**, No. 7, 573–582.

Chatterjee, S., White, D.J., and Randolph, M.F. (2012b). Numerical simulation of pipe–soil interaction during lateral movements on clay. *Géotechnique* **62**, No. 8, 693–705.

Cheuk, C.Y. and White, D.J. (2011). Modelling the dynamic embedment of seabed pipelines. *Géotechnique* **61**, No. 1, 39–57.

Cheuk, C.Y., White, D.J., and Bolton, M.D. (2007). Large–scale modeling of soil–pipe interaction during large amplitude cyclic movements of partially embedded pipelines. *Canadian Geotechnical Journal* **44**, No. 8, 977–996.

Clukey, E. C., Haustermans, L. and Dyvik, R. (2005). Model tests to simulate riser–soil interaction in touchdown point region. *Proceedings of the 1st International Symposium on Frontiers in Offshore Geotechnics* (*ISFOG*), pp. 651–658.

Clukey, E. C., Ghosh, R., Mokarala, P. and Dixon, M. (2007). Steel catenary riser (SCR) design issues at touch down area. *Proceedings of the 17th International Offshore and Polar Engineering Conference* (*ISOPE*), Lisbon, Portugal, pp. 814–819.

Clukey, E., Jacob, P. and Sharma, P. (2008a). Investigation of riser seafloor interaction using explicit finite element methods. *Proceedings of the Offshore Technology Conference*, Houston, TX, USA. OTC 19432.

Clukey, E., Young, A. G., Garmon, G. S., and Dobias, J. R. (2008b). Soil response and stiffness laboratory measurements of SCR pipe–soil interaction. *Proceedings of the Offshore Technology Conference*, Houston, TX, USA. OTC 19303.

De Blasio, F., Engvik, L., Harbitz, C. and Elverhøi, A. (2004). Hydroplaning and submarine debris flows. *Journal of Geophysical Research* **109**, No. C011002, 1–15.

Demars, K. R. (1978). Design of marine pipelines for areas of unstable sediment. *ASCE Transportation Engineering Journal* **104**, No. 1, 109–112.

Dingle, H.R.C., White, D.J., and Gaudin, C. (2008). Mechanisms of pipe embedment and lateral breakout on soft clay. *Canadian Geotechnical Journal* **45**, No. 5, 636–652.

Dunlap, W. A., Bhohanala, R. P., and Morris, D. V. (1990). Burial of vertically loaded offshore pipelines. *Proceedings of the Offshore Technology Conference*, Houston, TX, USA. OTC 6375.

Dutta, S. (2012). *Large deformation finite element analysis of partially embedded offshore pipelines for vertical and lateral motion at seabed*. MEng. Thesis, Memorial University of Newfoundland, Canada.

Dutta, S. and Hawlader, B. (2017). Pipeline–soil–water interaction modeling for submarine landslide impact on suspended offshore pipelines. (*Under preparation*).

Dutta, S., Hawlader, B., and Phillips, R. (2016c). Numerical modelling of a steel catenary riser section in the touchdown zone under cyclic loading. (*Under review*).

Dutta, S., and Hawlader, B. (2016b). Comparison of the implicit and explicit finite element methods in Abaqus based on penetration of cylindrical objects into seabed. *Proceedings of the 69th Canadian Geotechnical Conference (GeoVancouver)*, Vancouver, BC, Canada.

Dutta, S., Hawlader, B., Phillips, R. and Paulin, M. (2016a). Numerical investigations of uplift resistance of steel catenary riser near touch down zone. *Proceedings of the 11th International Pipeline Conference and Exposition* (*IPC*), Calgary, AB, Canada.

Dutta, S., Hawlader, B. and Phillips, R. (2015c). Large deformation finite element analysis of partially embedded offshore pipelines using coupled Eulerian−Lagrangian method. *Canadian Geotechnical Journal* **52**, No. 1, 58−72.

Dutta, S. and Hawlader, B. (2015b). Numerical modeling of drag force on submarine suspended pipelines using finite element and finite volume methods. *Proceedings of the 25th International Offshore (Ocean) and Polar Engineering Conference & Exhibition* (*ISOPE*), Honolulu, Hawaii, USA.

Dutta, S., Hawlader, B., and Phillips, R. (2015a). Vertical penetration of offshore pipelines: A comparative study between finite element and finite volume methods. *Proceedings of the 34th International Conference on Ocean, Offshore and Arctic Engineering* (*OMAE*), St. John's, NL, Canada.

Dutta, S., Hawlader, B. and Phillips, R. (2013). Numerical investigation of dynamic embedment of offshore pipelines. *Proceedings of the 18th International Conference on Soil Mechanics and Geotechnical Engineering* (*ICSMGE*), Paris, France.

DNV (2010). DNV-OS-F201, Offshore Standard: *Dynamic Risers*. Baerum, Norway: Det Norske Veritas.

Einav, I., and Randolph, M. F. (2005). Combining upper bound and strain path methods for evaluating penetration resistance. *International Journal of Numerical and Analytical Methods in Geotechnical Engineering* **63**, No. 14, 1991–2016.

Elliott, B. J., Zakeri, A., Macneill, A., Phillips, R., Clukey, E. C. and Li, G. (2013a). Centrifuge modeling of steel catenary risers at touchdown zone part I: Development of novel centrifuge experimental apparatus. *Ocean Engineering* **60**, No. 1, 200–207.

Elliott, B. J., Zakeri, A., Barrett, J., Hawlader, B., Li, G. and Clukey, E. C. (2013b). Centrifuge modeling of steel catenary risers at touchdown zone part II: Assessment of centrifuge test results using kaolin clay. *Ocean Engineering.* **60**, No. 1, 208–218.

Elliott, B., Phillips, R., Macneill, A. and Piercey, G. (2014). Physical modelling of SCR in the touchdown zone under three axis motions. *Proceedings of the 8th International Conference on Physical Modelling in Geotechnics* (*ICPMG*), Perth, Australia, pp. 265–270.

Foda, M.A. (1983). Breakout theory for offshore structures seated on seabed. *Proceedings of the Geotechnical Practice in Offshore Engineering* (*ASCE*), pp: 288–299.

Fouzder, A. (2015). *Modeling of riser−seabed−water interaction at touch down zone using computational fluid dynamics approach*. MEng. Thesis, Memorial University of Newfoundland, Canada.

Georgiadis, M. (1991). Landslide drag forces on pipelines. *Soils and Foundations* **31**, 156–161.

Giertsen, E., Verley, R., and Schrder, K. (2004). CARISIMA a catenary riser/soil interaction model for global riser analysis. *Proceedings of the 23rd International Conference on Offshore Mechanics and Arctic Engineering* (*OMAE*), Vancouver, Canada, pp. 633–640.

Grealish, F., Kavanagh, K., Connaire, A., and Batty, P. (2007). Advanced nonlinear analysis methodologies for SCRs. *Proceedings of the Offshore Technology Conference*, Houston, TX, USA. OTC 18922.

Hadj-Hamou, T. and Kavazanjian, E (1985). Seismic stability of gentle infinite slopes. *Journal* of *Geotechnical Engineering* **111**, No.6, 681−697.

Hawlader, B., Dutta, S., Fouzder, A., and Zakeri, A. (2015b). Penetration of steel catenary riser in soft clay seabed: Finite-element and finite-volume methods. *ASCE International Journal* of *Geomechanics*, **15**, No. 6, 1−12.

Hawlader, B., Fouzder, A. and Dutta, S. (2015a). Numerical modeling of suction and trench formation at the touchdown zone of steel catenary riser. *ASCE International Journal of Geomechanics*, **16**, No. 1, 1–14.

Hodder, M. (2009). *Geotechnical analysis of offshore pipelines and steel catenary*. PhD. Thesis, University of Western Australia, Australia.

Hill, A., White, D. J., Bruton, D, Langford, T., Meyer, V., Jewell, R. and Ballard, J-C. (2012). A new framework for axial pipe−soil interaction, illustrated by a range of marine clay datasets. *Proceedings of the 7th International Conference on Offshore Site Investigation and Geotechnics: Integrated Geotechnologies─Present and Future*, London, UK.

Hodder, M. and Cassidy, M. (2010). A plasticity model for predicting the vertical and lateral behaviour of pipelines in clay soils. *Géotechnique* **60,** No. 4, 247–263.

Hodder, M. S., White, D.J. and Cassidy, M. (2008). Centrifuge modelling of riser−soil stiffness degradation in the touchdown zone of a steel catenary riser. *Proceedings of the 27th International Conference on Offshore Mechanics and Arctic Engineering* (*OMAE*), Estoril, Portugal, pp. 1–9.

Hodder, M. S., White, D.J. and Cassidy, M. (2009). Effect of remolding and reconsolidation on the touchdown stiffness of a steel catenary riser: Observations from centrifuge modelling. *Proceedings of the Offshore Technology Conference*, Houston, TX, USA. OTC 19871

Hu, H. J. E. (2010). *Pipeline/riser soil interaction analysis*. PhD Thesis, National University of Singapore, Singapore.

Hu, H.J.E., Tho, K.K., Gan, C.T., Palmer, A.C. and Leung, C.F. (2010). Repeated loading and unloading of the seabed. *Proceedings of the 2nd International Symposium on Frontiers in Offshore Geotechnics* (*ISFOG*), Perth, WA, Australia, pp. 347–352.

Karal, K. (1977). Lateral stability of submarine pipeline. *Proceedings of the Offshore Technology Conference*, Houston, USA. OTC 2967.

Langford, T. and Aubeny, C. (2008). Model tests for steel catenary riser in marine clay. *Proceedings of the Offshore Technology Conference*, Houston, TX, USA. OTC 19495.

Langford, T.E. and Meyer, V.M. (2010). Vertical cyclic testing of model steel catenary riser at large scale. *Proceedings of the 2nd International Symposium on Frontiers in Offshore Geotechnics (ISFOG)*, Perth, Australia, pp. 803–808.

Lee, J. (2007). *Introduction to Offshore Pipelines and Risers*.

Liu, J., Tian, J., and Yi, P. (2015). Impact forces of submarine landslides on offshore pipelines. *Ocean Engineering*. **95**, 116–127.

Lyons, C.G. (1973). Soil resistance to lateral sliding of marine pipelines. *Proceedings of the Offshore Technology Conference*, Houston, TX, USA. OTC 1876.

Martin, C.M. and Randolph, M.F. (2006). Upper-bound analysis of lateral pile capacity in cohesive soil. *Géotechnique* **56**, No. 2, 141−145.

Merifield, R., White, D. J. and Randolph, M. F. (2008). The ultimate undrained resistance of partially embedded pipelines. *Géotechnique* **58**, No. 6, 461–470.

Merifield, R.S., White, D.J., and Randolph, M.F. (2009). Effect of surface heave on response of partially embedded pipelines on clay. *ASCE Journal of Geotechnical and Geo-environmental Engineering* **135**, No. 6, 819–829.

Marintek (2000). *CARISIMA, Interpretation of suction test results*. Report No. 700039.00.03, Trondheim, Norway.

Muga, B.J. (1967). Bottom breakout forces. *Proceedings of the Civil Engineering in Oceans* (*ASCE*), San Francisco, CA, USA, pp. 596–600.

Morris, D.V. Webb, R.E. and Dunlap, W.A. (1988). Self burial of laterally loaded offshore pipeline in weak sediments. *Proceedings of the Offshore Technological Conference*, Houston, Texas, USA. OTC 5855.

Morrow, D.R. and Bransby, M.F. (2010). Pipe–soil interaction on clay with a variable shear strength profile. *Proceedings of the 2nd International Symposium on Frontiers in Offshore Geotechnics* (*ISFOG*), Perth, WA, Australia, pp. 821–826.

Murff, J.D., Wagner, D.A., and Randolph, M.F. (1989). Pipe penetration in cohesive soil. *Géotechnique* **39**, No. 2, 213–229.

Puech, A., Orozco-Calderón, M. and Foray, P. (2010). Mini T-bar testing at shallow penetration. *Proceedings of the 2nd International Symposium on Frontiers in Offshore Geotechnics* (*ISFOG*), Perth, WA, Australia, pp. 305–310.

Randolph, M. F and Houlsby, G.T. (1984). The limiting pressure on a circular pile loaded laterally in cohesive soil. *Géotechnique* **34**, No. 4, 613–623.

Randolph, M. and Quiggin, P. (2009). Non-linear hysteretic seabed model for catenary pipeline contact. *Proceedings of the 28th International Conference on Ocean, Offshore and Arctic Engineering* (*OMAE*), Honolulu, HI, USA, pp. 145–154.

Randolph, M.F. and White, D.J. (2008). Upper-bound yield envelopes for pipelines at shallow embedment in clay. *Géotechnique* **58**, No. 4, 297–301.

Randolph, M. F. and White, D. J. (2012). Interaction forces between pipelines and submarine slides—A geotechnical viewpoint. *Ocean Engineering* **48**, 32–37.

Sahdi, F., Gaudin, C., White, D., Boylan, N. and Randolph, M. (2014). Centrifuge modelling of active slide–pipeline loading in soft clay. *Géotechnique* **64**, No. 1, 16–27.

Schapery, R. and Dunlap, W. (1978). Prediction of storm induced sea bottom movement and platform forces. *Proceedings of the Offshore Technology Conference*, Houston, TX, USA. OTC 3259.

SINTEF. (1986a). *Pipe–soil interaction test*, *soft clay*. STF60 F86023.

SINTEF. (1986b). *Pipe–soil interaction test*, *stiff clay*. STF60 F86072.

SINTEF. (1987). *Pipe–soil interaction test on sand and soft clay*. STF60 F7018.

Small, S.W., Tamburello, R.D., and Piaseckyj, P.J. (1971). Submarine pipeline support by marine sediments. *Journal of Petroleum Technology*. **24**, 317–322.

Summers, P. and Nyman, D. (1985). An approximate procedure for assessing the effects of mudslides on offshore pipelines. *Journal of Energy Resources Technology* **107**, No. 4, 426–432.

Swanson, R. C. and Jones, W. T. (1982). Mudslide effects on offshore pipelines. *ASCE Transportation Engineering Journal* **108**, No. 6, 585–600.

Tho, K.K., Leung, C.F., Chow, Y.K., and Palmer, A.C. (2012). Deep cavity flow mechanism of pipe penetration in clay. *Canadian Geotechnical Journal* **49**, No. 1, 59–69.

Thomas, J. B. (2004). Submarine landslides on the US continental slope: Effects on a search for the USS alligator. *Proceeding of the Capstone Seminar in Geology and GIS,* USA, 1–13.

Towhata, I. and Al–Hussaini, T. (1988). Lateral loads on offshore structures exerted by submarine mudflows. *Soils and Foundations* **28**, No. 3, 26–34.

Vesic, A.S. (1969). *Breakout resistance of objects embedded in ocean bottom*. U. S. Naval Civil Engineering Laboratory Port Hueneme, California, USA. RP: CR.69.031.

Verley, R. and Lund, K.M. (1995). Soil resistance model for pipelines placed on clay soils. *Proceedings of the 14th International Conference on Offshore Mechanics and Arctic Engineering* (*OMAE*), Denmark, pp. 225–232.

Vivatrat, V. and Chen, V. (1985). Strain rate and forces due to mud flow around piles. *Proceedings of the Offshore Technology Conference*, Houston, TX, USA.

Wagner, D.A., Murff, J.D., Brennodden, H., and Sveggen, O. (1989.) Pipe–soil interaction model. *Journal of Water Port Coastal and Ocean Engineering* **115**, No.2, 205–220.

Wang, D., White, D. J. and Randolph, M. F. (2010). Large-deformation finite element analysis of pipe penetration and large-amplitude lateral displacement. *Canadian Geotechnical Journal* **47**, No. 8, 842–856.

Westgate, Z.J., and White, D.J. (2015). Quantifying spatial variability of as-laid embedment for subsea pipeline design. *Proceedings of the 34th International Conference on Offshore Mechanics and Arctic Engineering*, St. John's, NL, Canada.

Westgate, Z.J., White, D.J. and Randolph, M.F. (2013). Modelling the embedment process during offshore pipe-laying on fine-grained soils. *Canadian Geotechnical Journal* **50**, No. 1, 15–27.

White, D.J. and Dingle, H.R.C. (2011). The mechanism of steady friction between seabed pipelines and clay soils. *Géotechnique* **61**, No. 12, 1035–1041.

White, D. J., Gaudin, C., Boylan, N. and Zhou, H. (2010). Interpretation of T-bar penetrometer tests at shallow embedment and in very soft soils. *Canadian Geotechnical Journal* **47**, No. 2, 218–229.

Yuan, F., White, D. J. and O'Loughlin, C. D. (2016). The evolution of seabed stiffness during cyclic movement in a riser touchdown zone on soft clay. *Géotechnique* (*ahead of print*).

Zakeri, A. (2009a). Review of state-of-the-art: Drag forces on submarine pipelines and piles caused by landslide or debris flow impact. *Journal of Offshore Mechanics and Arctic Engineering* **131**, No. 1, 014001.

Zakeri, A. (2009b). Submarine debris flow impact on suspended (free-span) pipelines: Normal and longitudinal drag forces. *Ocean Engineering* **36**, No. 6, 489–499.

Zakeri, A. and Hawlader, B. (2013). Drag forces caused by submarine glide block or out-runner block impact on suspended (free-span) pipelines—Numerical analysis. *Ocean Engineering* **67**, 89–99.

Zakeri, A., Hawlader, B. and Chi, K. (2012). Drag forces caused by submarine glide block or out-runner block impact on suspended (free-span) pipelines. *Ocean Engineering* **47**, 50–57.

Zakeri, A., Høeg, K. and Nadim, F. (2009). Submarine debris flow impact on pipelines—Part II: Numerical analysis. *Coastal Engineering* **56**, No. 1, 1–10.

Zakeri, A., Høeg, K. and Nadim, F. (2008). Submarine debris flow impact on pipelines—Part I: Experimental investigation. *Coastal Engineering* **55**, No. 12, 1209–1218.

Zhu, H. and Randolph, M. F. (2011). Numerical analysis of a cylinder moving through rate-dependent undrained soil. *Ocean Engineering* **38**, No. 7, 943–953.

APPENDIX A

Numerical Investigation of Dynamic Embedment of Offshore Pipelines

This paper has been published and presented in 2013 18th International Conference on Soil Mechanics and Geotechnical Engineering (ICSMGE), Paris, France. Most of the research work presented in this paper was conducted by the first author. He also prepared the draft manuscript. The other authors supervised the research and reviewed the manuscript.

Numerical investigation of dynamic embedment of offshore pipelines

Etude numérique sur ancrage dynamique de pipelines offshore

S. Dutta & B. Hawlader
Memorial University, St. John's, Canada.

R. Phillips
C-CORE, St. John's, Canada.

ABSTRACT: Pipelines are one of the key components of offshore oil and gas development programs. Deep water pipelines are often laid on the seabed and penetrate into soil a fraction of their diameter. High operating temperature and pressure generate axial stress that could buckle the pipeline laterally. The embedment and formation of soil berm have a significant effect on lateral resistance. The embedment of a pipeline depends on stress concentration at the touchdown point (TDP) and dynamic laying effects. In this study, large deformation finite element modelling of dynamic penetration of offshore pipeline is presented. The Coupled Eulerain Lagrangian (CEL) technique is used to develop finite element model. The pipe is first penetrated into the seabed followed by a small amplitude cyclic lateral motion. Results from the finite element models are compared with centrifuge test results. High plastic shear strain is obtained around the pipeline during cyclic loading which causes significant pipe embedment. The shape of soil berm is different from that of monotonic pipe penetration.

RÉSUMÉ : Les pipelines sont un des éléments clés de pétrole et de gaz programmes de développement. Conduites d'eau profonde sont souvent mis sur le plancher océanique et de pénétrer dans le sol une fraction de leur diamètre. Température de fonctionnement élevée et une pression générer une contrainte axiale qui pourraient déformer le pipeline latéralement. L'ancrage et la formation de talus sol ont un effet significatif sur la résistance latérale. L'enfouissement d'un pipeline dépend de la concentration de contraintes au point de toucher (TDP) et des effets dynamiques de la pose. Dans cette étude, une grande modélisation par éléments finis de la déformation de pénétration dynamique du gazoduc sous-marin est présenté. Le couplage Eulerain lagrangien (CEL) est utilisée pour développer le modèle éléments finis. Le tuyau est d'abord pénétré dans le fond marin suivi d'un mouvement cyclique de faible amplitude latérale. Les résultats des modèles éléments finis sont comparés avec les résultats des tests de centrifugeuses. Haut de la déformation plastique est obtenu autour de la canalisation lors du chargement cyclique qui provoque ancrage tuyau significative. La forme du talus du sol est différent de celui du tube de pénétration monotone.

KEYWORDS: pipelines, dynamic embedment, clay, large deformation analysis.

1 INTRODUCTION.

As-laid pipelines are commonly used in deepwater. During installation the as-laid pipeline could be penetrated a fraction of its diameter into the seabed (Bruton et al. 2006), and a soil berm could be formed. The soil around the pipelines provides not only the thermal insulation and hydrodynamic stability to the pipe but also resistance to pipeline walking and lateral buckling during high operating temperature and pressure. Accurate assessment of as-laid pipe embedment is extremely difficult. Depending upon sea state, vessel conditions, pipe stiffness and soil conditions, the pipeline might experience both in-plane and out-of-plane cyclic motion during installation (Westgate et al. 2010, 2012), which causes dynamic embedment of the pipeline.

The penetration of a pipeline under static load can be obtained using bearing capacity theory, analytical solution or finite element techniques. In the current engineering practice, two additional factors are used to estimate the embedment of pipelines: (a) additional vertical force near the TDP (the point where the pipe first touches the soil) due to catenary effects and (b) dynamic lay effects. A number of methods have been proposed in the past to estimate these factors (Carneiro et al. 2010, Oliphant and Yun 2011). For example, Randolph and White (2008) proposed an empirical equation to calculate the touchdown lay factor (f_{lay}) using pipe submerged weight, bending rigidity, horizontal component of effective tension, lay angle, water depth and seabed stiffness. The embedment factor for dynamic lay effects (f_{dyn}) varies between 2 and 10 (Lund 2000, Bruton et al. 2006). This wide range of variation in this factor makes the assessment of pipe embedment very difficult.

During installation, both vertical and lateral pipe motions can soften the seabed soil near the pipe. Soil softening/remolding together with water entrainment can reduce the undrained shear strength of soil. Field observation (Westgate et al. 2010) and physical modeling using geotechnical centrifuge (Cheuk and White 2011) show that the horizontal cyclic motion, although small amplitude, has a significant effect on pipe embedment.

The main purpose of this study is to conduct large deformation finite element (FE) analysis for dynamic events during the installation of pipeline. Coupled Eulerian Lagrangian (CEL) technique is adopted in the analysis using ABAQUS FE software. Four FE models are developed for two different soils: kaolin and high plasticity clays (plasticity index for kaolin is 34 and for high plastic clay is 100-130, Cheuk and White 2011). The results are compared with the centrifuge test results available in the literature.

2 PROBLEM DEFINITION.

The problem considered in the present finite element (FE) modelling is shown in Fig.1. During laying, offshore pipelines usually penetrate vertically into the seabed due to its self-weight and catenary effect near the touchdown zone (TDZ). The vessel movement from wave loading could cause small amplitude cyclic

motions in the x-direction. As the pipeline is under a vertical load (p_0), the lateral movement in the x-direction could cause additional vertical penetration as shown by Stage-II and III in Fig. 1.

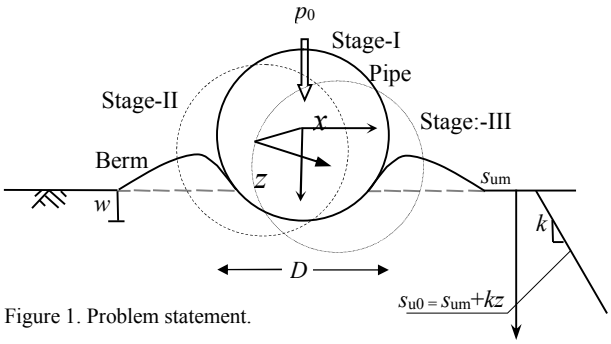

Figure 1. Problem statement.

3 FINITE ELEMENT MODELLING.

ABAQUS 6.10 EF-1 is used in the present finite element analysis. As the embedment of pipe in the seabed is large deformation problem, the conventional finite element techniques in Lagrangian approach cannot simulate the complete process realistically as numerical difficulties are generally encountered for such large displacements. Therefore, in this study the Coupled Eulerian Lagrangian (CEL) technique currently available in ABAQUS FE software is used. In CEL, the soil flows through the fixed mesh without having any numerical issues. The FE modeling using CEL for pipe embedment into the seabed is presented by the authors previously (Dutta et al. 2012 a&b). A soil domain of 8m×3m ×0.04m (length × height × thickness) is used in this study. The soil is modelled as Eulerain elements and the pipe is modelled as Lagrangian elements. The 1.5 m void space above the soil is required to accommodate the displaced soil mass (Eulerian materials) during pipe displacement. Zero velocity boundary conditions are applied at all faces of the Eulerian domain to make sure that Eulerain materials are within the domain and cannot move outside. However, at the seabed-void interface, no boundary condition is provided so that the soil can flow to the void. That means, the bottom of the model is restrained from any vertical movement, while all the vertical faces are restrained from any lateral movement. The pipe is modeled as a rigid body. During penetration, especially in cyclic loading, the remolding of soil near the pipe could cause significant reduction in undrained shear strength. Smooth pipe/soil interface condition is used for the present analysis. Mesh sensitivity analysis is also performed and an optimum mesh size of 0.04m×0.04m is used (Dutta et al. 2012 a).

The loading is performed in three different stages. First, the geostatic conditions are applied to bring the seabed to in-situ condition. Second, the pipe is penetrated applying a vertical load (p) which is the combined effect of submerged unit weight of the pipe and laying effects. In the third step, 40 cycles of small amplitude ($\pm 0.05D$) lateral displacement are applied using displacement boundary conditions under the constant vertical load p_0. Plastic shear strain develops near the pipe during penetration. In the present FE analyses the degradation of undrained shear strength as a function of plastic shear strain is adopted using the following model (Einav and Randolph 2005 Wang et al. 2009 and Zhou and Randolph 2009).

$$s_u = [\delta_{rem} + (1-\delta_{rem})\exp(-3\xi/\xi_{95})]s_{u0} \quad (1)$$

where $\delta_{rem} = 1/S_t$, S_t is the soil sensitivity, ξ is the accumulated equivalent plastic shear strain, s_{u0} is the intact undrained shear strength of soil and ξ_{95} is the accumulated plastic shear strain at 95% undrained shear strength degradation. The variation of s_{u0} with depth is shown in Fig. 1 and the von-Mises yield criteria is adopted.

In this study four cases are simulated and the results are compared with centrifuge test results of Cheuk and White (2008). Two tests (KC-04 & KC-05) are in kaolin clay and two (HP-06 & HP-07) are in high plasticity clay. Table 1 shows the parameters used in the FE analyses. The vertical load p for initial static penetration and during cyclic motion are also shown in Table 2.

Table 1. Parameters for finite element modelling.

Pipe		
Pipe diameter, D (mm)	800	
Lateral displacement during cyclic motion	$\pm 0.05D$	
Soil Properties	*Kaolin Clay*	*High Plasticity Clay*
Undrained modulus of elasticity, E_u	$500s_u$	$500s_u$
Poisson's ratio, ν_u	0.495	0.495
Undrained shear strength at mudline, s_{um} (kPa)	0.75	0.40
Gradient of shear strength increase, k (kPa/m)	1.6	2.5
Submerged unit weight of soil, γ' (kN/m^3)	6.0	3.0
Remoulded soil sensitivity, S_t	4.0	1.7
Accumulate absolute plastic shear strain for 95% degradation of soil strength, ξ_{95}	10	10

Table 2. Centrifuge test conditions (Cheuk and White 2011).

	KC-04	KC-05	HP-06	HP-07
Pipe vertical load, p (kN/m)	1.17	2.23	1.47	2.61
Initial static embedment, w_{in}/D	0.08	0.12	0.10	0.22
Pipe vertical load at cyclic motion, p_0 (kN/m)	1.13	2.17	1.43	2.52

4 RESULTS.

The pipe was initially penetrated under a static vertical load p. The initial static embedment (w_{in}) for this load is shown in Table 2. After initial penetration a small amplitude cyclic lateral load is applied (e.g. Fig. 2 for KC-05, u = pipe lateral displacement) to simulate the first 40 cycles (Stage-I) of centrifuge tests. The normalized lateral resistance for KC-05, where $s_{u0(i)}$ in the horizontal axis is the intact undrained shear strength at pipe invert, is shown in Fig. 3(a) and comapred with centrifuge test results Fig.3(b). The lateral resistance is slightly higher than that obtained in centrifuge test. This might be due to the limitation of the soil shear strength degradation model (Eq. 1). It is very difficult to measure and model the behaviour of soil near the pipeline under cyclic loading. However, using this simplified model (Eq. 1) in ABAQUS CEL the lateral resistance during cyclic movement is reasonably simulated.

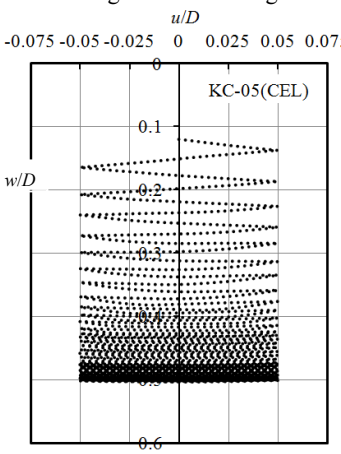

Figure 2. Pipe embedment during lateral motions

Figures 4(a),4(b) and 4(c) show the lateral resistance for other three simulations. As shown, the shape of the lateral resistance plot is

different, which mainly depends on soil shear strength profile, shear strength degradation, sensitivity of soil, and applied vertical load. The depth of the invert of the pipe normalized by pipe diameter (D) with number of load cycle is shown in Fig. 5 for comparison the centrifuge test. the present FE model reasonably simulates the embedment of the pipe with the soil parameters listed in Table 1. Figure 5(a) shows that the depth of embedment does not increase significantly after 20-30 load cycles for kaolin clay. However, the pattern is somehow different for high plastic clay as shown in Fig. 5(b) where the pipes continue to penetrate even after 20-30 load cycles.

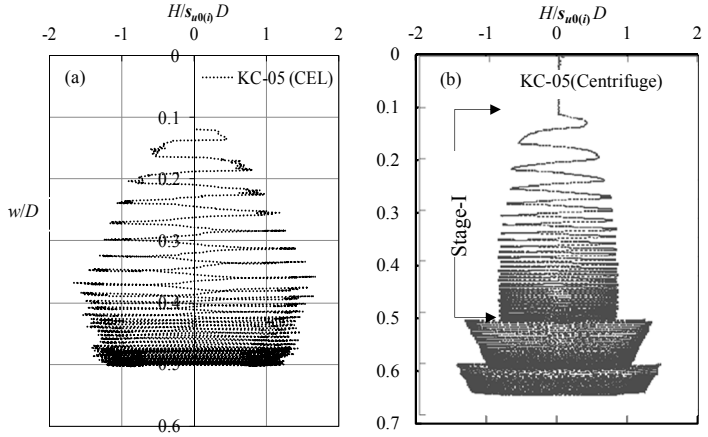

Figure 3.Test KC-05 (a) present study (b) centrifuge test.

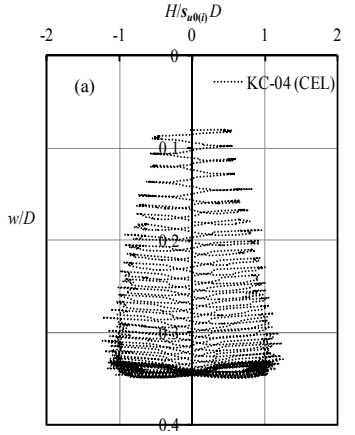

From field experience in deepwater pipeline projects in West Africa, Casola et al. (2011) suggested that the embedment of pipelines is more than $D/3$ and the lateral cyclic load has little effect on pipe embedment. Their observed behaviour might be applicable if s_{u0} and the gradient (k) of s_{u0} is high as they found in these projects. However, for the cases analyzed in the present study, the cyclic loading has a significant effect even after embedment of $D/3$ as shown in Fig. 5(b).

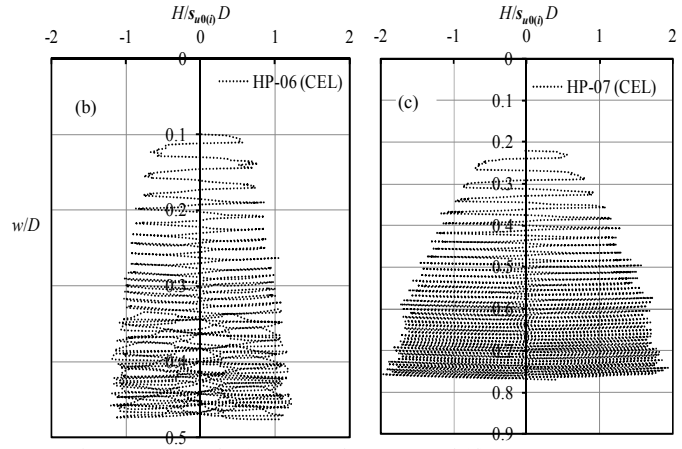

Figure 4. FE results (a) KC-04 (b) HP-06 and (d) HP-07.

5 DYNAMIC EMBEDMENT

In the current engineering practice the effects of laying and dynamic embedment are assessed separately. The lay effect on vertical load (p) is obtained by multiplying the submerged unit weight of the pipe by an empirical lay factor (f_{lay}). The monotonic embedment (w_{mon}) for this load p is calculated using the bearing capacity theory. The effect of small amplitude cyclic lateral motion is incorporated using another empirical factor known as dynamic embedment factor (f_{dyn}). Finally, the total embedment (w_f) is calculated as $w_f = f_{dyn}\ w_{mon}$. In some projects (e.g. Oliphant and Yun 2011) a combined empirical factor ($=f_{lay}\times f_{dyn}$) is also used that accounts for both laying and dynamic effects. Table 3 shows the calculated values of f_{dyn} for the four tests simulated in this study. Analyzing field data of a 200 km offshore pipeline in shallow to deep water, Oliphant and Yun (2011) showed that an average value of f_{dyn} of approximately 7 could be used for estimation of pipeline embedment. Lund (2000) suggested that the value of f_{dyn} in the field varies between 2 and 10.

6 EQUIVALENT PLASTIC STRAIN AND BERM SHAPE.

During penetration the soil around the pipeline is softened as a function of plastic shear strain as shown in Eq. 1. The equivalent plastic shear strain at the end of penetration for two cases (KC-04 and KC-05) are shown in Figs. 6(a) & 6(b). A significant plastic strain (>500%) is developed near the pipe. The white broken lines in Figs. 6(a) & 6(b) show the boundary above which the equivalent plastic shear strain is greater than ξ_{95} (=10). That means 95% degradation of undrained shear strength occurred

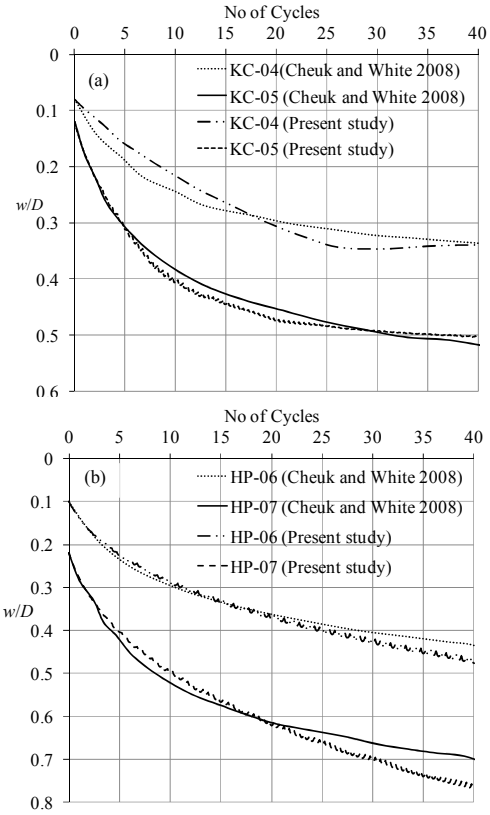

Figure 5.Pipeline embedment with horizontal cyclic motions (a) Kaolin clay (b) High plasticity clay.

in the soil above this line (see Eq. 1). In other words, the undrained shear strength of the soil in the zone above this line is almost near the remoulded undrained shear strength. In order to show the effects of lateral cyclic loading on penetration, an analysis is performed for monotonic penetration as shown in Fig. 6(c). The geometry and soil property used in this analysis is same as KC-05 in Fig. 6(b), except the pipe moved monotonically downward to the depth of final embedment in KC-05 using a displacement boundary condition. The shear strain and berm formation for monotonic penetration is shown in Fig. 6(c). the equivalent plastic shear strain near the pipe in monotonic loading is significantly lower (Fig. 6c) than that obtain in lateral cyclic loading (Figs. 6a&b). The maximum plastic shear strain developed near the pipe in cyclic loading is almost 5 times higher than that of monotonic loading. Also the maximum equivalent plastic shear strain is less than ξ_{95}, which means that the shear strenth reduction due to softening is less than 95%. The softening has a significant effect on the shape of the berm and soil movement around the pipe. the highly softened displaced soil mass formed flat berms on the top of the seabed extended over a large distance in cyclic loading. In addition, the soil is in contact with the pipe almost up to the top of the berm. However, for monotonic loading the displaced soil mass formed a berm mainly near the pipe and the berm height is more than that of in cyclic loading. That means, the soil deformation in monotonic and cyclic loading is significantly different.

Table 3. Dynamic embedment factor, f_{dyn}.

	KC-04	KC-05	HP-06	HP-07
Initial static embedment (w_{in}/D)	0.08	0.12	0.10	0.22
Final embedment (w/D)	0.34	0.50	0.48	0.77
f_{dyn}	4.25	4.16	4.8	3.5

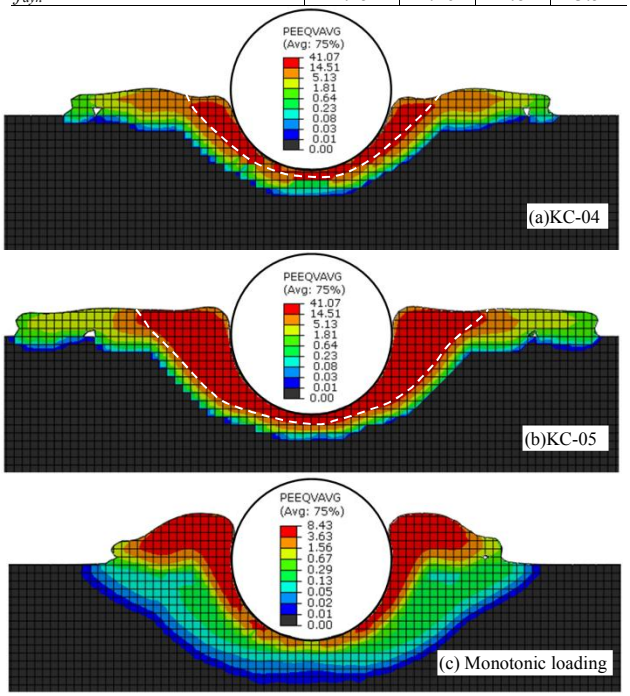

Figure 6. Equivalent plastic strain.

In a parametric study Dutta et al. (2012 b) showed that the effect of softening on the vertical penetration resistance in monotonic loading is not very significant, which is because of less plastic strain developed near the pipe. However, for cyclic loading huge plastic strain is developed in a zone near the pipe which causes significant reduction in undrained shear strength. That means, the zone of considerable softening is higher in cyclic loading. As in offshore the small amplitude lateral cyclic loading near the touchdown zone is commonly encountered from the motion of the vessel, the analyses for cyclic motion with strain softening behaviour of soil will provide more accurate results.

7 CONCLUSION

Large deformation finite element analyses are conducted to assess the embedment of as-laid offshore pipelines in clay. The effects of small amplitude cyclic lateral loading are investigated. The following conclusions can be drawn from this study.

- The Coupled Eulerian Lagrangian (CEL) method currently available in ABAQUS FE software can simulate the pipeline embedment.
- The plastic shear strain near the pipeline in cyclic loading is significantly higher than that of in monotonic loading.
- The shape of the berm depends on type of loading; spread over a large area in cyclic and mounted near the pipe in monotonic loading.
- The softening of soil in a zone near the pipe is significantly higher in cyclic loading compared to monotonic loading.
- Forty cycles of small amplitude lateral loading increased the embedment by a factor of 4-5 of initial static embedment. The embedment is higher in initial loading cycles.

8 ACKNOWLEDGEMENTS

The work has been funded by C-CORE, MITACS and NSERC Discovery grant which is greatly acknowledged.

9 REFERENCES

Bruton, D., White, D., Cheuk, C. And Bolton, M. (2006). Pipe/soil interaction behaviour during lateral buckling, including large amplitude cyclic displacement tests by the Safebuck JIP. *Proc. Offshore Technology Conference*, Houston, Texas, USA. OTC 17944.

Carneiro, D. Gouveia, J. and Parrilha, R. 2010. Feedback analysis of pipeline embedment over as-laid survey results. *Proc. Int. Conf. on Offshore Mechanics and Arctic Engineering,* Shanghai, China. OMAE2010-20410.

Casola, F., El-chayeb, A., Greco, S. and Carlucci, A. 2011. Characterization of pipe soil interaction and influence on HP/HT pipeline design. *Proc. Int. Conf. on Offshore and Polar Engineering Conference,* Hawaii,USA,pg:111-121.

Cheuk, Y.C. and White, J.D. 2008. Centrifuge modelling of pipe penetration due to dynamic lay effects. *Proc. Int. Conf. on Offshore Mechanics and Arctic Engineering,* Estoril, Portugal. OMAE2008-57923.

Cheuk, Y.C. and White, J.D. 2011. Modelling the dynamic embedment of seabed pipelines. *Géotechnique* 61 (1), 39-57.

Dutta, S., Hawlader, B. and Phillips, R. 2012a. Finite element modeling of vertical penetration of offshore pipelines using Coupled Eulerian Lagrangian approach. *Proc. Int. Conf. on Offshore and Polar Engineering Conference,* Rhodes,Greece,pg:343-348.

Dutta, S., Hawlader, B. and Phillips, R. 2012b. Strain softening and rate effects on soil shear strength in modeling of vertical penetration of offshore pipelines. *Proc. Int. Pipeline Conference,*Alberta, Canada. IPC2012-90233.

Einav, I. and Randolph, F.M. 2005. Combining upper bound and strain path methods for evaluating penetration resistance. *Int. J. Numer. Meth. Engng.,* 63:1991-2016.

Lund, K.H. 2000. Effect of increase in pipeline soil penetration from installation. *Proc. Int. Conf. on Offshore Mechanics and Arctic Engineering,* New orleans, USA. OMAE2000-PIPE5047.

Oliphant, J. and Yun, J.G. 2011. Pipeline embedment prediction using as-laid data. *Proc. Int. Conf. on Offshore Mechanics and Arctic Engineering,* Rotterdam, The Netherlands. OMAE2011-50095.

Randolph F.M. and White J.D. 2008. Pipeline embedment in deep water: Processes and quantitative assesment. *Proc. Offshore Technology Conference*, Houston, Texas, USA. OTC 19128.

Wang, D., White, J.D. and Randolph, F.M. 2009. Numerical simulations of dynamic embedment during pipe laying on soft clay. *Proc. Int. Conf. on Offshore Mechanics and Arctic Engineering,* Hawaii, USA. OMAE2009-79199.

Westgate, J.Z., White, J.D. and Randolph, F.M. 2010. Pipeline laying and embedment in soft fine-grained soils: Field observations and numerical simulations. *Proc. Offshore Technology Conference*, Houston, Texas, USA. OTC 20407.

Westgate, J.Z., White, J.D. and Randolph, F.M. 2012. Modelling the embedment process during offshore pipe laying on fine-grained soils. *Canadian Geotechncial Journal* (accepted).

Zhou, H. and Randolph, M. F. (2009). Numerical investigations into cycling of full-flow penetrometers in soft clay. Géotechnique, 59 (10), 801-812.

APPENDIX B

A Comparative Study of Advanced Numerical Methods for Large Deformation Problems using Cylindrical Object Penetration into Seabed

This paper has been published in 2016 69th Canadian Geotechnical Conference, GeoVancouver (2016). The first author conducted the research and wrote the draft manuscript. Second author mainly supervised the research and helped to prepare the draft manuscript.

A Comparative Study of Advanced Numerical Methods for Large Deformation Problems using Cylindrical Object Penetration into Seabed

Sujan Dutta and Bipul Hawlader
Department of Civil Engineering
Faculty of Engineering and Applied Science, Memorial University
St. John's, NL, Canada A1B 3X5

ABSTRACT
Finite element methods (FEM) are widely used to solve many complex geotechnical engineering problems. Generally, the implicit FEM are used to analyze small-strain problems. However, for large-deformation problems, mesh distortion and convergence are the major numerical issues if one considers small-strain finite element (FE) modeling techniques. In order to overcome these numerical issues, several FE modeling techniques have been developed in recent years, such as Arbitrary Lagrangian Eulerian (ALE), Remeshing and Interpolation Technique with Small Strain (RITSS), Coupled Eulerian Lagrangian (CEL) techniques. Among them, ALE and CEL techniques are available in the commercially available software package Abaqus. Each of these techniques has a number of advantages and limitations. In this study, the performance of four FEM (pure implicit, pure explicit, ALE and CEL) and a finite volume method (FVM) available in ANSYS CFX for geotechnical applications is investigated by simulating the penetration of a cylindrical object into the soft clay seabed. Analyses are conducted for undrained loading conditions. Good agreement is found among the FE and FV approaches for shallow pipe penetration depths. However, at large penetration depths, CEL gives lower resistance than the other FEM and also shows a good agreement between previous studies and CFX analysis. The pure implicit, pure explicit and ALE approaches cannot simulate extremely large-deformation problems.

RÉSUMÉ
méthodes d'éléments finis (FEM) sont largement utilisés pour résoudre de nombreux problèmes d'ingénierie géotechnique complexes. En général, le FEM implicite sont utilisés pour analyser les problèmes de petite déformation. Cependant, pour des problèmes de grande déformation, distorsion du maillage et de convergence sont les principaux enjeux numériques si l'on considère la petite déformation éléments finis (FE) des techniques de modélisation. Afin de surmonter ces problèmes numériques, plusieurs techniques de modélisation FE ont été développés au cours des dernières années, comme arbitraire Lagrangian Eulerian (ALE), Remaillage et interpolation Technique avec Small Strain (RITSS), Eulerian lagrangiennes (CEL) techniques couplées. Parmi eux, les techniques ALE et CEL sont disponibles dans le package de logiciels disponibles dans le commerce Abaqus. Chacune de ces techniques comporte un certain nombre d'avantages et de limitations. Dans cette étude, la performance de quatre FEM (pur implicite, pur explicite, ALE et CEL) et une méthode de volumes finis (FVM) disponible dans ANSYS CFX pour les applications géotechniques est étudiée en simulant la pénétration d'un objet cylindrique dans le fond marin de l'argile molle . Les analyses sont effectuées pour les conditions de chargement non drainées. Un bon accord est trouvé parmi les FE et FV approches pour peu profondes profondeurs de pénétration du tuyau. Cependant, à de grandes profondeurs de pénétration, CEL offre une résistance plus faible que l'autre FEM et montre également une bonne concordance entre les études antérieures et l'analyse CFX. Les approches explicites et implicites ALE pures pures ne peuvent simuler extrêmement problèmes de grande déformation.

1 INTRODUCTION

Finite element method (FEM) is one of the promising tools for analysing geotechnical engineering problems both in onshore and offshore environments. The conventional FEM cannot handle large deformation problems because of excessive mesh distortion and convergence issues. Previous studies show that the Arbitrary Lagrangian Eulerian (ALE) and Coupled Eulerian Lagrangian (CEL) techniques in Abaqus could be used for modeling large deformation problems (Qiu et al. 2010; Tho et al. 2012; Dutta et al. 2014). However, these advanced FEM still have some limitations. For example, the role of water and computational time could be the concern in Abaqus CEL modeling for some applications. The computational fluid dynamics (CFD) approach might be a better choice for those problems (Hawlader et al. 2015). Therefore, the performance of these modeling approaches need to be examined further. In the present study, a deepwater offshore problem is considered to show some limitations and advantages of these numerical methods.

One of the large deformation problems in the offshore environments is the penetration of cylindrical objects (e.g. surface laid pipelines, T-bar, steel catenary riser) into the soft clay seabed. Deepwater pipelines (water depth>300 m) to transport hydrocarbon are usually laid on the seafloor without trenching. It might penetrate into the seabed during installation. Estimation of pipe embedment is one of the key parameters for pipeline design to prevent lateral buckling. These pipelines generally transport hydrocarbons at high pressure high temperature. During operational cycles (start-up/shut down), the pipelines might displace laterally. Field observations showed that

pipeline can displace 5–20 diameters laterally (Bruton et al. 2008). The resistance to lateral displacement depends on depth of embedment (Wang et al. 2010; Dutta et al. 2014).

Theoretical, physical and numerical studies have been performed in the past to model pipe penetration behaviour. Theoretical studies include upper-bound (Aubeny et al. 2005; Randolph and White 2008) and lower-bound (Murff et al. 1989) solutions. Small-scale (Aubeny et al. 2008), full-scale (Dunlap et al. 1990; Cheuk et al. 200) and centrifuge (Dingle et al. 2008; White and Dingle 2011) tests were also conducted to understand the mechanisms further. Numerical studies include FE, FV and finite difference modelling. Analyses have been performed for wished-in-place (WIP) and pushed-in-place (PIP) pipe configurations. In WIP, the pipe is placed at a certain depth and moved small distance to estimate penetration resistance. However, in PIP, the pipe is placed near the seabed and penetrated into the soil using large-deformation numerical modeling techniques. For example, the Remeshing and Interpolation Technique with Small Strain (RITSS), developed at the University of Western Australia, have been used by a number of researchers (e.g. Barbosa-Cruz and Randolph 2005; Wang et al. 2010; Chartarjee et al. 2012).

Other applications of penetration of cylindrical objects into soft clay seabed include the penetration of steel catenary risers (SCR) at the touchdown zone (TDZ) and field T-bar penetration. Due to environmental loading, sections of SCR might penetrate several diameters into the seabed (Bridge, 2005). Similarly, T-bar is penetrated into the seabed to several diameters to determine undrained shear strength profile.

Abaqus CEL has been also used by a number of researchers for modeling penetration of cylindrical objects (Shi et al. 2011; Tho et al. 2012; Dutta et al. 2012a,b, 2014). A summary of numerical studies on pipe penetration into soft clay seabed is available in Dutta et al. (2014).

The aim of the present study is to show the performance of four FEM (pure implicit, pure explicit, ALE and CEL) and a FVM for modeling large deformation geotechnical problems. The penetration of a pipe section into soft clay seabed is considered as an example.

2 Problem statement

A section of pipe of diameter D is penetrated into the seabed at uniform velocity (v_0) (Fig. 1). Deepwater soft clay seabed is modeled using uniform undrained shear strength (s_u) and submerged unit weight (γ'). Four FEM (pure implicit, pure explicit, ALE and CEL) and one FVM are used for pipe vertical penetration into the seabed in undrained condition. Note that the undrained condition is satisfied when the non-dimensional velocity (v_0D/c_v) is greater than 20, where c_v is the coefficient of consolidation (House et al. 2001).

3 FE model development

FE models are developed using Abaqus 6.14-2 for plain strain condition. Taking the advantages of symmetry, only half of the domain is simulated. A large soil domain of 6Dx10D is considered to avoid any boundary effect on penetration behaviour (Fig. 2). Table 1 shows parameters used in the analysis. The pipe is modelled as rigid body. Adopting the von-Mises yield criteria, the undrained shear strength is implemented in Abaqus using the yield strength (=2s_u). The pipe is penetrated vertically into the seabed until the analysis stops due to mesh distortion or convergence issues, except for CEL analysis. The CEL can simulate excessive large deformation phenomena as discussed in the following sections.

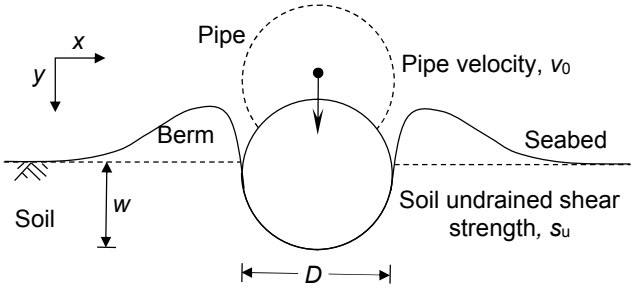

Figure 1. Problem statement

Table 1. Parameter used in FE analysis

Parameters	Value
Pipe diameter, D (m)	0.8
Pipe velocity, v_0 (m/s)	0.012
Soil undrained Young's modulus, E_u (kPa)	500s_u
Poison's ratio, v	0.495
Soil undrained shear strength, s_u (kPa)	5
Submerged unit weight, γ' (kN/m^3)	6

3.1 Pure implicit and pure explicit

The pure implicit analysis is performed using Abaqus/Standard. The pipe is placed near the seabed and penetrated using a displacement boundary condition at the center of the pipe. Roller supports are used in the left and right vertical sides, while hinge supports are used at the bottom of the domain. Plain strain condition is simulated using 4-node bilinear, reduced integration with hourglass control elements (CPE4R). Mesh sensitivity analysis is performed to select the optimum mesh size. A dense mesh of 0.04D×0.04D is used in the left side of the domain, while a coarse mesh of 0.08D×0.04D is used in the right side. Pipe-soil interface resistance is defined as $\tau_{max}=\alpha s_{u0}$, where τ_{max} is maximum allowable shear resistance at the interface and α is a coefficient (Wang et al. 2010). The value of α is zero for smooth and one for rough pipe. Smooth pipe-soil interface condition is used in FE analysis unless otherwise mentioned.

For pure explicit, the solver in Abaqus/Standard is changed to explicit from implicit keeping all other parameters same as pure implicit method described above. As the explicit scheme is for dynamic problems, dynamic and inertia effects should be minimized such that

the analysis becomes quasi-static. In the present study, all conditions for quasi-static simulation are satisfied. Further details on the quasi-static simulation could be found in previous studies (Dey et al. 2015; Wang et al. 2015).

3.2 Arbitrary Lagrangian Eulerian (ALE) technique

The FE model discussed in Section 3.1 is extended for ALE modeling. The initial mesh, soil domain, pipe diameter and boundary conditions are kept same as pure explicit/implicit analysis. The zone of smaller mesh (left side of Fig. 2) is selected for ALE adaptive meshing. In this case, adaptive mesh generation is performed by sweeping the mesh over the adaptive mesh domain. After that, state variables are remapped from old mesh to new mesh using an advection algorithm. The default options in Abaqus are used for simplicity.

3.3 Coupled Eulerian Lagrangian (CEL) technique

The CEL modeling is slightly different from previous models discussed in Section 3.1 and 3.2. Here, the mesh is fixed and material can flow through the mesh (see Section 5). The soil domain in CEL model is same as Fig. 2; however, a void region of height 3*D* is created to accommodate displaced soil mass during penetration of the pipe. The mesh configuration in the void is same as the soil domain (i.e. dense mesh in the left side and coarse mesh in the right). The CEL can handle only three-dimensional models, and therefore the plain strain condition is simulated using model thickness (in the out of plane direction) equal to the dimension of the smallest element (0.04*D*). Detailed mesh sensitivity analysis is performed to select the optimum mesh size. Zero velocity boundary conditions perpendicular to the faces are applied to the bottom and all vertical faces. No boundary condition applied at the soil-void interface such that the displaced soil can move into the void during penetration. The pipe is displaced downward using displacement boundary condition. Eulerian volume fraction (EVF) tool is used to create the initial void and soil domains. For any element, EVF=1 means that the element is filled with soil and EVF=0 means the element is void. Fractional value of EVF means that the element is partially filled with the soil. The authors presented details of the CEL modelling techniques elsewhere (Dutta et al. 2014).

4 FV model development

Figure 3 shows the FV model developed using ANSYS CFX 14.0. Similar to FE simulation, half of the pipe with the corresponding soil model is developed with a domain of 8.5*D*×20*D* where the bottom 13.3*D* represents the soil and the upper 6.7*D* represent the water above the seabed. The soil and water zone are created using the CFX expression language. The shaded zone in Fig. 3 shows an inner subdomain of 1.5*D* radial thickness where no mesh deformation is allowed but the Eulerain material can flow through it. Similar to Abaqus CEL, only three-dimensional model can be generated in CFX. Therefore, the plain strain condition is simulated using a model thickness of 10 mm in the out of plane direction. All the vertical faces of the model are defined as solid impermeable walls. No slip boundary condition is used for the bottom of the domain and pipe wall, whereas free slip boundary condition is used for right vertical wall. Symmetry plane boundary condition is used for the other three vertical walls. Pipe is displaced downward at constant velocity v_0 using the CFX expression language. Pipe-soil interface condition is defined using a finite thickness interface element around the pipe. Similar to FEM, smooth pipe-soil interface condition is defined. Further details on mesh size, mesh sensitivity, interface element thickness and boundary conditions can be found in Hawlader et al. (2015). The FV analysis is performed for the soil and pipe parameters listed in Table 1. Soil is modelled as non-Newtonian fluid whereas water is modelled Newtonian fluid. The dynamic viscosity of the soil is defined as: $\mu = s_u/\dot{\gamma}$ where s_u is the undrained shear strength of soil and $\dot{\gamma}$ is the plastic shear strain rate. For water, default parameters in ANSYS CFX are used.

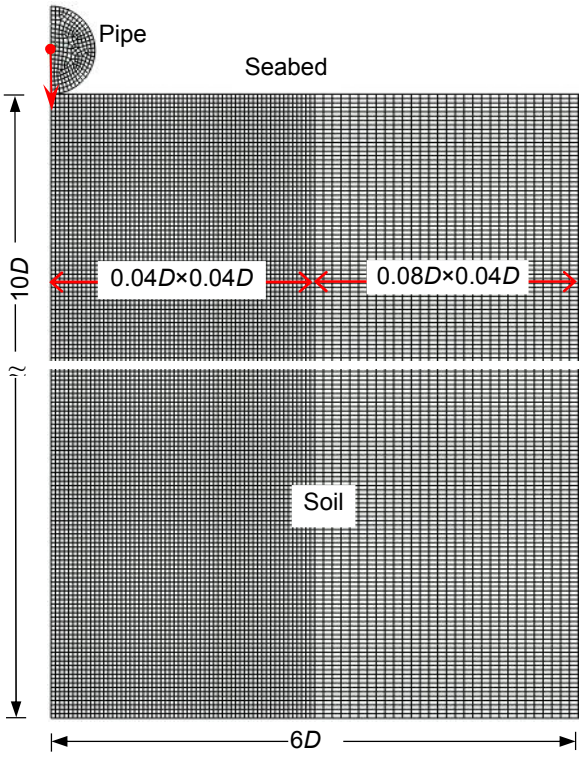

Figure 2. FE model development

5 Results

5.1 Pipe penetration resistance

Figure 4 shows the normalised penetration resistance with normalised penetration depth. It is observed that the pipe can be penetrated up to 0.7*D*, 0.13*D* and 2*D* for pure implicit, pure explicit and ALE approaches, respectively, because of significant mesh distortion. The CEL and CFX can overcome the mesh distortion and convergence issues and allows penetration of pipe at large depths. Figure 4 shows a close agreement between penetration resistances obtained from different FEM for small penetration depths. In pure explicit, the program stopped

at w=0.13*D*. Note that the time increment significantly influences the success of explicit analysis. In this analysis the default option is used. After w≈0.25*D*, the pure implicit method shows higher penetration resistance than other three approaches, which might be because of excessive mesh distortions near the pipe after this level of vertical displacement. This has been discussed further in the following sections. For higher pipe penetration depths (>0.7*D*), the ALE approach also gives higher penetration resistance than the CEL and CFX approaches. Again, it might be because of significant mesh distortion in ALE method. Good agreement is found between CEL and CFX. In order to verify the present CEL analysis, the results of Tho et al. (2012), who also used Abaqus CEL, is plotted in this figure. The readers are referred to Dutta et al. (2014) for further comparison among Abaqus CEL analysis, empirical solutions and model test results.

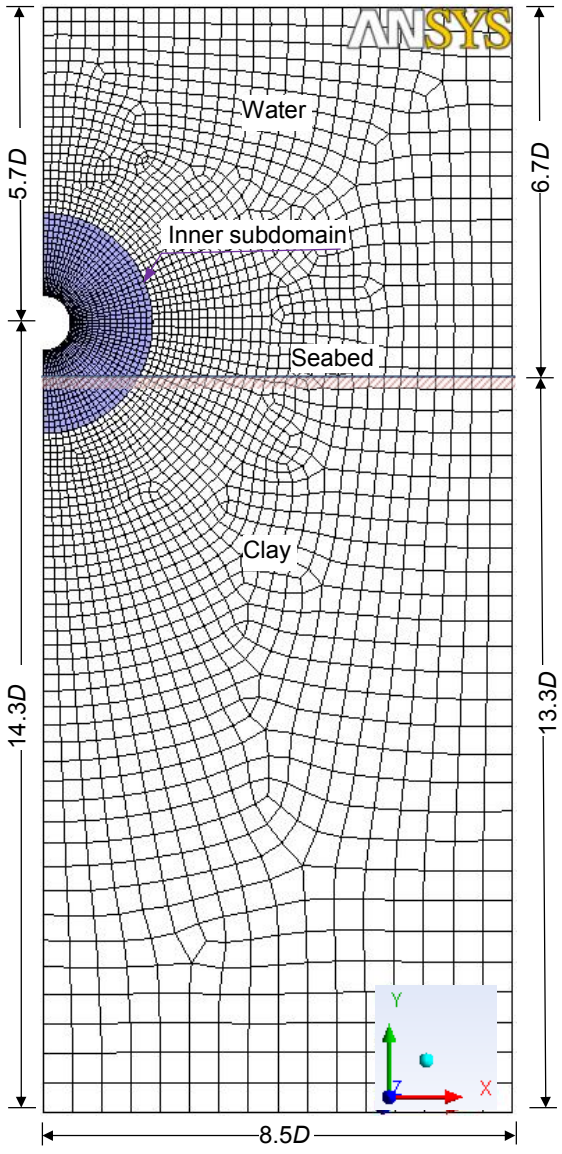

Figure 3. FV model development

5.2 Development of equivalent plastic strain (ε_q) around the pipe

Figure 4 shows that the penetration resistance is almost same for different methods of FE analysis up to 0.25*D*, except for pure explicit. In order to compare the performance of these methods further, the equivalent plastic strain ($\varepsilon_q = \sqrt{\frac{2}{3}\varepsilon^{pl}:\varepsilon^{pl}}$, where ε^{pl} =plastic strain) for three different depths (<0.25*D*) are plotted in Fig. 5. As shown, not only the penetration resistance (Fig. 4) but also the plastic strains are very comparable for these three methods of FE analysis for this range of penetration. Therefore, it can be concluded that Abaqus CEL successfully simulate the penetration behaviour.

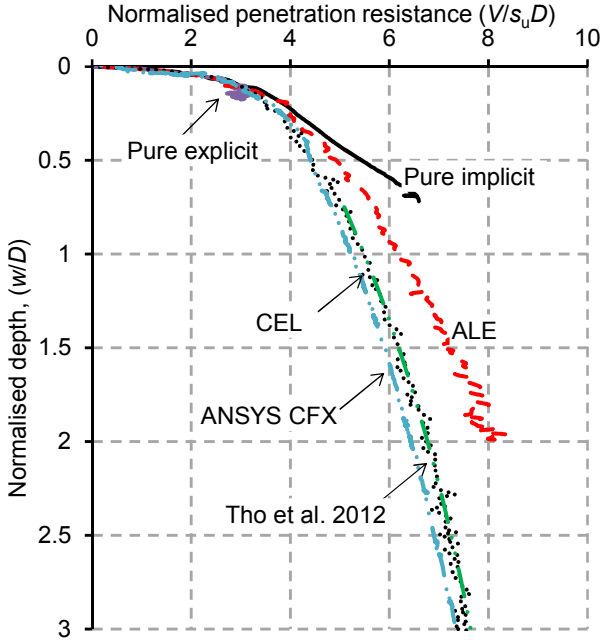

Figure 4. Normalised vertical penetration resistance

5.3 Deformation of mesh

Figure 6 shows the comparison of deformed mesh for three penetration depths. Mesh distortion is not significant for a small pipe displacement of *w*=0.08*D*, as shown in the first row of Fig. 6, for pure implicit and pure explicit analysis. Because of adaptive meshing, the distortion is even less in the ALE approach as compared to pure implicit or pure explicit approach. As the mesh remains fixed, no mesh distortion occurs in in the CEL analysis. At higher depth of penetration (*w*>0.08*D*) significant mesh distortion occurs in pure implicit and explicit analysis. In fact, the pure explicit analysis stops at *w*=0.15*D* because of mesh distortion issue.

The 3rd column of Fig. 6 shows that adaptive meshing reduces mesh distortion in ALE analysis. When penetration continued, the ALE analysis stopped at *w*=2*D*. This implies that the ALE method has some limited success for large deformation modeling. Figures 7(a), 7(b) and 7(c) show the deformed mesh when the program stops for pure implicit, pure explicit and ALE methods, respectively.

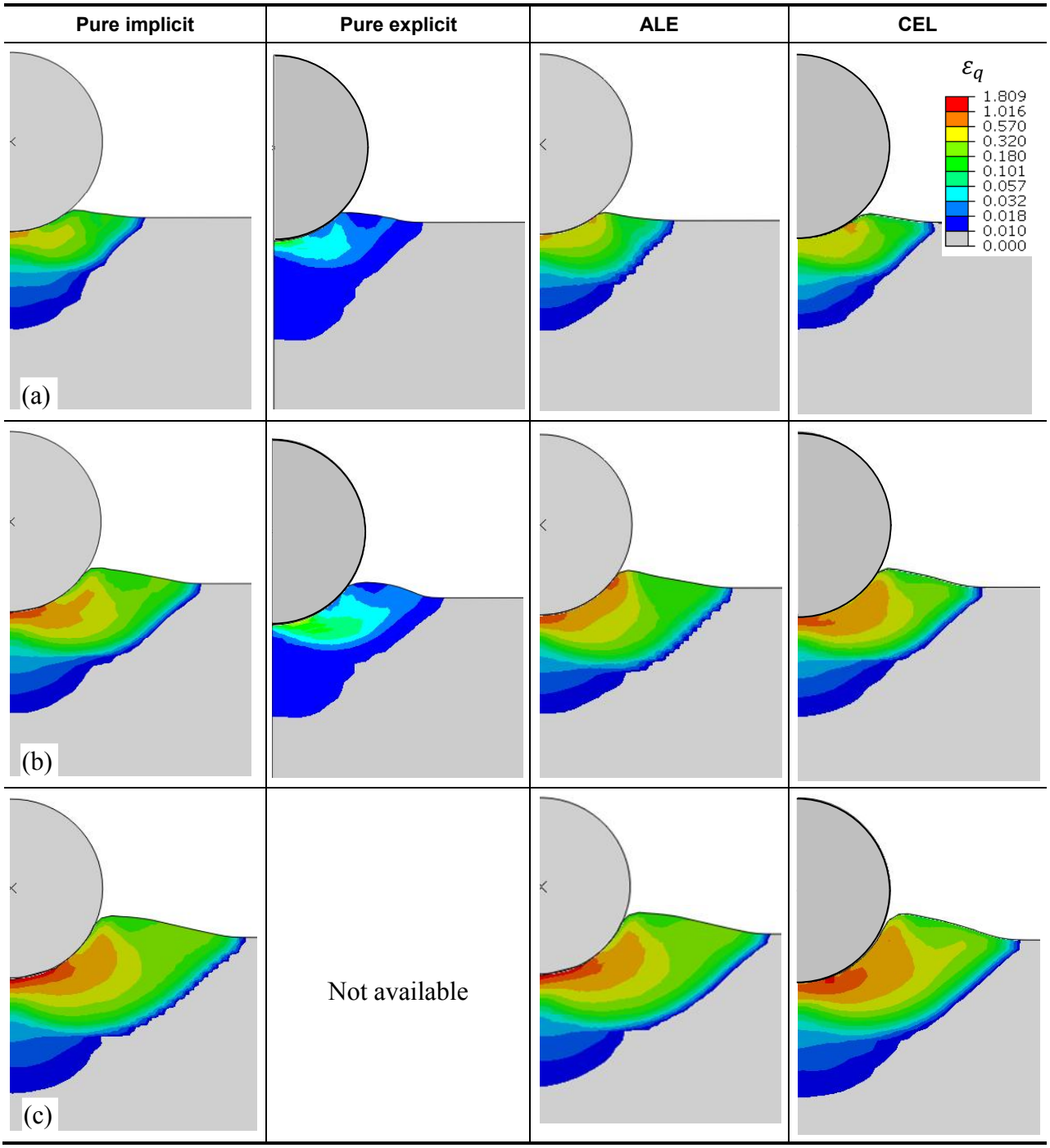

Figure 5. Comparison of developed equivalent plastic strain (ε_q) around the pipe for ideal soil at (a) *w*/*D*=0.08 (b) *w*/*D*=0.15 (c) *w*/*D*=0.23

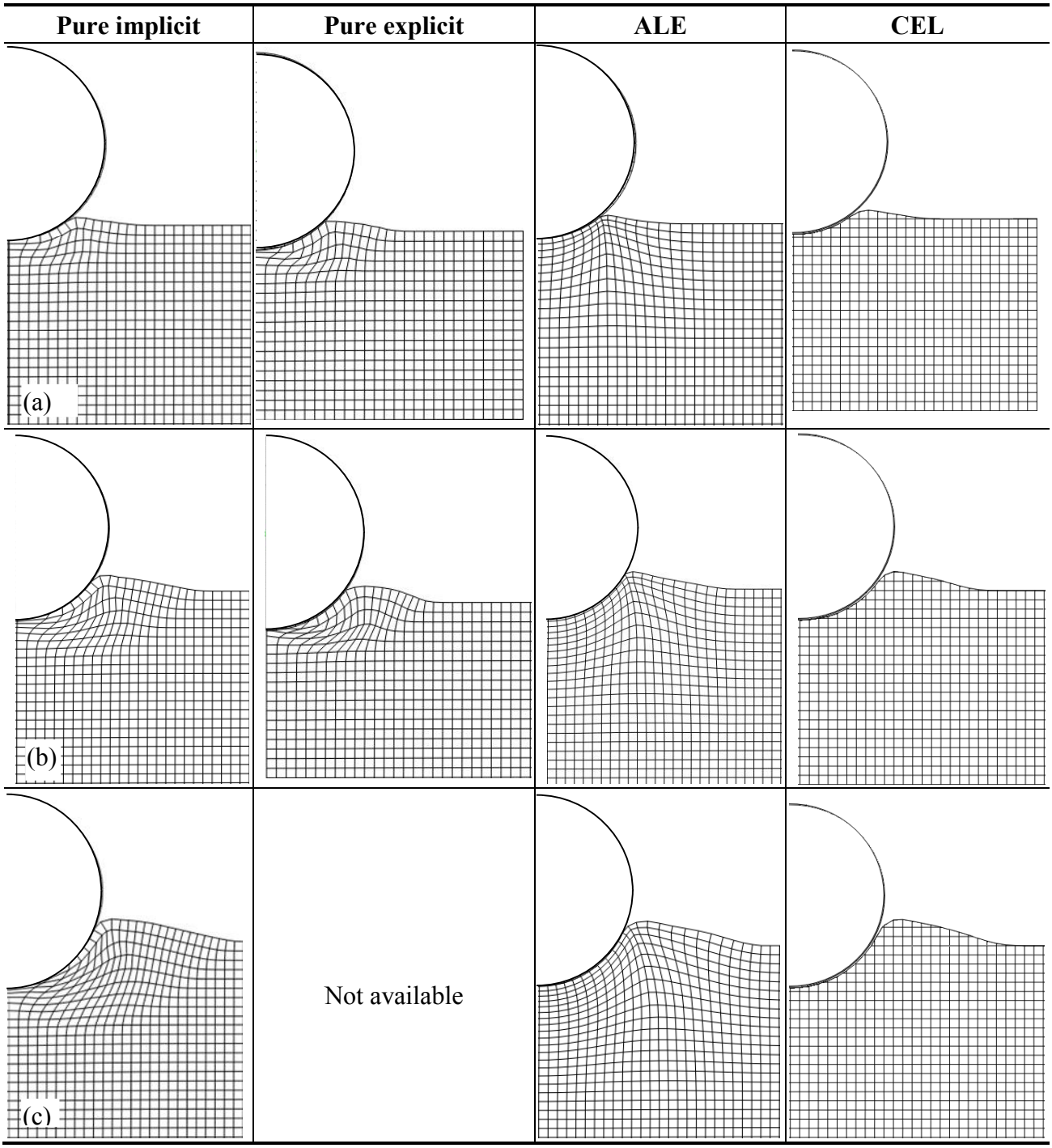

Figure 6. Comparison of mesh deformation for pipe penetration depth of (a) *w*/*D*=0.08 (b) *w*/*D*=0.15 (c) *w*/*D*=0.23

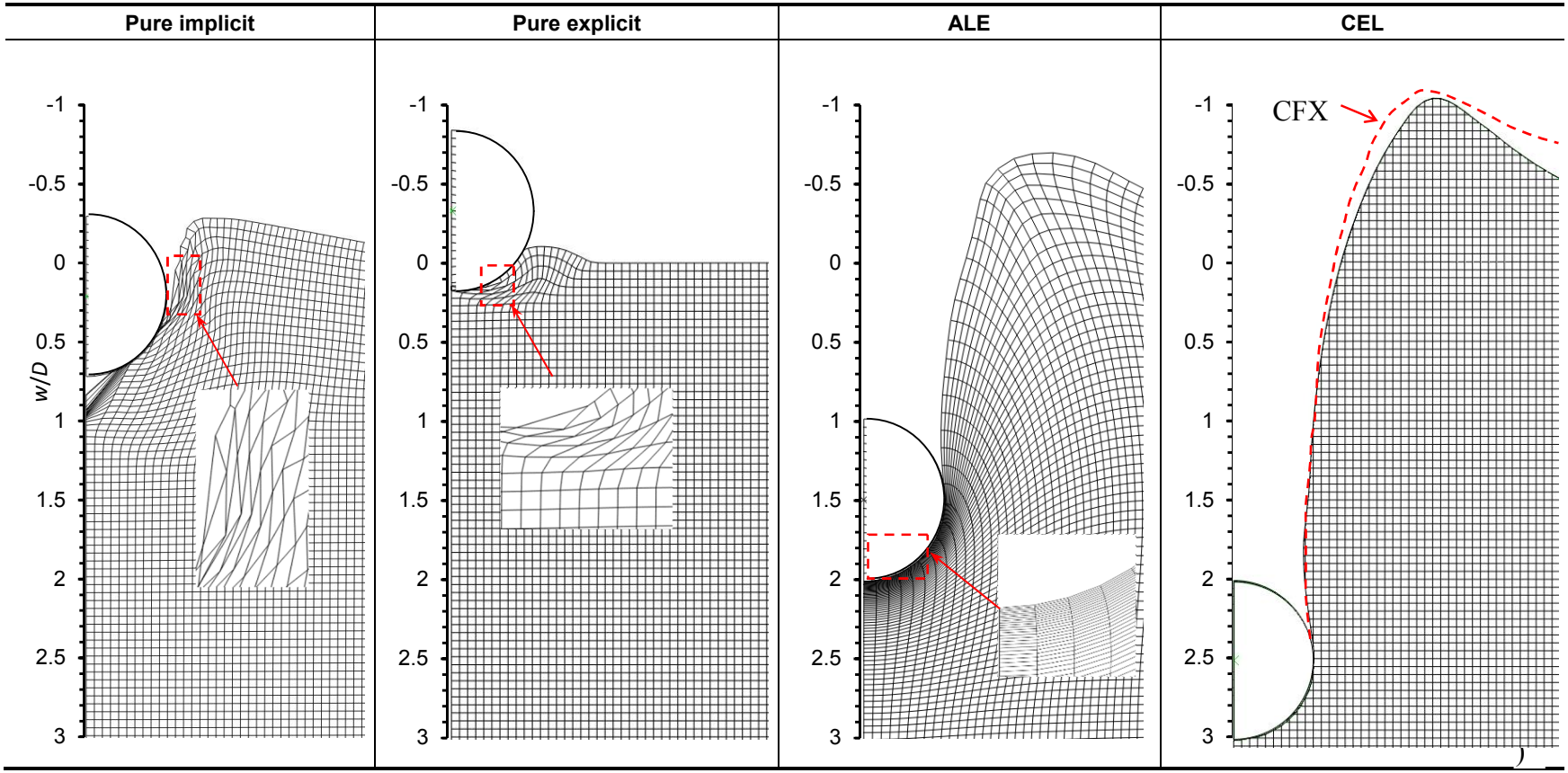

Figure 7. Deformation of mesh at the location where analysis stops for pure implicit, pure explicit and ALE, and mesh in CEL

Elements near the pipe distorted severely for pure implicit and pure explicit analysis. For ALE, the aspect ratio of the mesh increased significantly at large displacements (e.g. w=2D). However, the analysis did not stop for CEL and CFX because it can handle excessive large deformation problem. Figure 7(d) shows that the shape of the trench and berm obtained from CEL and CFX are very similar. Note the neither CEL nor CFX analysis stops due to mesh distortion, rather the analysis has been stopped by the user at w=3D.

From this comparative study, it can be concluded that CEL and CFX can better simulate the large deformation behaviour than the other FEM. The analysis takes approximately 13.8 h with a 3.2-GHz Intel Core i5 processor and 8 GB RAM where CFX takes only 63 min on the same computer (i.e., 13 times faster than CEL). Further discussion could be found in Hawlader et al. (2015).

6 Working principles

Pure implicit, pure explicit and ALE methods have been used by many researchers for FE modeling of different problems. Theoretical formulation, advantages and limitations of these techniques have been also discussed in those studies (Qiu et al. 2010). However, the use of CEL and CFX approaches for modeling geotechnical problems is relatively new. Therefore, in this section a brief description of these modeling techniques is provided.

6.1 CEL approach

In the standard Lagrangian formulation material time derivatives are used, while in the Eulerian description the equations are written using spatial time derivatives. The relation between material and spatial time derivatives can be written as:

$$\frac{\partial \varphi}{\partial t} + \nabla \Phi = S \qquad [1]$$

where φ is the field variable, Φ is the flux function, and S is the source term. There are two basic ways to solve above equation: (i) solve the non-symmetric system of equations directly (ii) decouple and solve using "operator splitting." Abaqus is based on operator split method in which a Lagrangian phase is followed by an Eulerian/convection phase that can be described by the following equations:

$$\frac{\partial \varphi}{\partial t} = S \qquad \text{Lagrangian step} \quad [2]$$

$$\frac{\partial \varphi}{\partial t} + \nabla \Phi = 0 \qquad \text{Eulerian step} \quad [3]$$

The Lagrangian step is very similar to conventional FE analysis and mesh deforms as shown schematically in Fig. 8. The solution variables are then adjusted to account for the flow of the material between adjacent elements. An explicit integration scheme based on the central difference method is used to solve the governing equations. Variables are then transferred from the old mesh to the new mesh in each advection sweep. In the present study, the second-order scheme proposed by Van Leer (1977) implement in Abaqus is used for advection. According to this scheme, a variable is remapped from the old mesh to the new mesh by defining a linear distribution of the variable in each old element. Further details about this method are available in Abaqus documentation files (Abaqus 2014). Abaqus recommended this second order advection method for quasi-static problems, as the one presented in this study.

6.2 CFX

In ANSYS CFX, the domain is discretized into three-dimensional mesh. The governing equations are solved adopting a solution methodology based on finite volume, which are constructed using the discretized mesh. The force-displacement behaviour is modeled using the Navier-Stokes equations, which has been developed applying Newton's Law (F=ma) to fluid elements. Here F is the force, m is the mass and a is the acceleration. The forcing term (F) is the sum of gravitational force (F_{grv}), pressure force (F_{press}) and viscous force (F_{visc}). The gravitational force F_{grv} (=mg) is same as it is in solid mechanics, where g is the gravitational acceleration. The last two (F_{press} and F_{visc}) are the reaction forces to the motion, which are analogous to the normal and frictional resistance in solid mechanics. The parameters required in CFX to calculate F_{grv} and F_{pres} are given by density of soil and water, and the boundary conditions including the displacement of the riser. The coefficient of dynamic viscosity (μ) is used to calculate F_{visc}. For further details please see Hawlader et al. (2015).

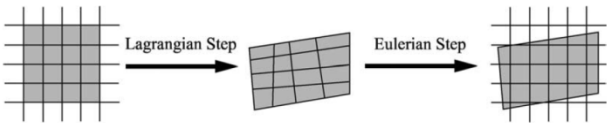

Figure 8. Lagrangian and Eulerian phases used in CEL based on operator split method (after Benson and Okazawa, 2004)

7 Conclusion

Finite element methods (FEM) are extensively used to model many geotechnical engineering problems. However, most of these methods are not suitable for large deformation problems. In this paper, a comparative study among four FEM (pure implicit, pure explicit, ALE and CEL) and a computational fluid dynamics approach is performed for modeling penetration of a cylindrical object into soft clay seabed. For shallow penetration depths (w<0.25D), a very good agreement is found between penetration resistance and plastic shear strain development around the pipe for all four FE modeling approaches. It also shows that the CEL and CFX can simulate small strain behaviour.

The program stops at shallow depths in pure implicit and pure explicit approaches because of mesh distortion. The ALE approach has some limited success in modeling large deformation problems. On the other hand, Abaqus CEL or ANSYS CFX could successfully model the behaviour even at extremely large deformation although there are some limitations of each method.

In deepwater environments, the increase in s_u with depth is commonly observed. Moreover, strain rate and accumulation of plastic shear strains significantly influence s_u. These factors are not considered in this study. Authors presented the effect of these factors elsewhere (Dutta et al. 2012b, 2014, 2015).

ACKNOWLEDGEMENTS

Funding from MITACS, Memorial University and C-CORE are gratefully acknowledged.

REFERENCES

Abaqus. 2014. Analysis user manual. Abaqus 6.14-2. Simulia Inc., Dassault Systemes.

Aubeny, C.P, Gaudin, C., and Randolph, M.F. 2008. Cyclic tests of model pipe in kaolin. Society of Petroleum Engineering Journal, 3(04): 1–6.

Aubeny, C.P., Shi, H., and Murff, J.D. 2005. Collapse loads for a cylinder embedded in trench in cohesive soil, International Journal of Geomechanics, 5(4): 320–325.

Barbosa-Cruz, E.R. and Randolph, M.F. 2005. Bearing capacity and large penetration of a cylindrical object at shallow embedment. In Proceedings of the 1st International Symposium on Frontiers in Offshore Geotechnics (ISFOG), pp. 615–621.

Benson, D.J. and Okazawa, S. 2004. Contact in a multi-material Eulerian finite element formulation. Computational Methods of Applied Mechanics and Engineering, 193:4277–4298.

Bruton, D.A.S., Boreas, A., White, D.J., Carr, M., and Cheuk, J.C.Y. 2008. Pipe-soil interaction during lateral buckling and pipeline walking-the SAFEBUCK JIP. In Proc. of the Offshore Technology Conference, Texas, USA. OTC 19589.

Chartarjee, S., Randolph, M.F., and White, D.J. 2012. The effects of penetration rate and strain softening on the vertical penetration resistance of seabed pipelines, Géotechnique, 62(7): 573-582.

Cheuk, C.Y., White, D.J., and Bolton, M.D. 2007. Large-scale modelling of soil-pipe interaction during large amplitude cyclic movements of partially embedded pipelines, Canadian Geotechnical Journal, 44(8): 977–996.

Dey, R., Hawlader, B., Phillips, R. and Soga, K. 2015. Large deformation finite-element modelling of progressive failure leading to spread in sensitive clay slopes. Géotechnique, 65(8): 657–668.

Dingle, H.R.C., White, D.J., and Gaudin, C. 2008. Mechanisms of pipe embedment and lateral breakout on soft clay, Canadian Geotechnical Journal, 45(5): 636–652.

Dunlap, W.A., Bhojanala, R.P., and Morris, D.V. 1990. Burial of vertically loaded offshore pipelines in weak sediments. In Proc. of the Offshore Technology Conference, Texas, USA. OTC 6375.

Dutta, S., Hawlader, B., and Phillips, R. 2015. Vertical penetration of offshore pipelines : A comparative study between finite element and finite volume methods. In Proc. of the 34th International Conference on Ocean, Offshore and Arctic Engineering, NL, Canada, 1–8.

Dutta, S., Hawlader, B., and Phillips, R. 2014. Finite element modelling of partially embedded pipelines in clay seabed using coupled Eulerian Lagrangian method. Canadian Geotechnical Journal, 52(1):58–72.

Dutta, S., Hawlader, B., and Phillips, R. 2012a. Finite element modeling of vertical penetration of offshore pipelines using coupled Eulerian Lagrangian approach. In Proceedings of the 22nd International Offshore and Polar Engineering Conference, Rhodes, Greece, pp. 343-349.

Dutta, S., Hawlader, B., and Phillips, R. 2012b. Strain softening and rate effects on soil shear strength in modeling of vertical penetration of offshore pipelines. In Proceedings of the 9th International Pipeline Conference, The American Society of Mechanical Engineers, Calgary, AB, Canada, 13–20

Hawlader, B., Dutta, S., Fouzder, A. and Zakeri, A. 2015. Penetration of steel catenary riser in soft clay seabed–finite element and finite volume methods. International Journal of Geomechanics, 15(6):1–12.

House, A.R., Oliveira, J.S., and Randolph, M.F. 2001. Evaluating the coefficient of consolidation using penetration tests, International Journal of Physical modelling in Geotechnics, 1(3):17–26.

Murff, J.D., Wagner, D.A., and Randolph, M.F. 1989. Pipe penetration in cohesive soil, Géotechnique, 39(2): 213–229.

Qiu, G., Henke, S. and Grabe, Jurgen. 2010. Application of a Coupled Eulerian–Lagrangian approach on geomechanical problems involving large deformations. Computers and Geotechnics, 38(1):30–39.

Randolph, M.F. and White, D.J. 2008. Upper-bound yield envelopes for pipelines at shallow embedment in clay, Géotechnique, 58(4): 297–301.

Shi, H., Sun, J., Hossain, K., Eltaher, A., and Jukes, P. 2011. Offshore pipeline embedment in cohesive soil – a comparison between existing and CEL solutions. In Proceedings of the 30th International Conference on Ocean, Offshore and Arctic Engineering (OMAE), Rotterdam, the Netherlands, pp. 1–6.

Tho, K.K., Leung, C.F., Chow, Y.K., and Palmer, A.C. 2012. Deep cavity flow mechanism of pipe penetration in clay. Canadian Geotechnical Journal,49(1):59–69. doi:10.1139/t11-088.

Van Leer, B. 1977. Towards the ultimate conservative difference scheme IV. A new approach to numerical convection. Journal of Computational Physics, 23:276–299.

Wang, D., White, D.J., and Randolph, M.F. 2010. Large-deformation finite element analysis of pipe penetration and large-amplitude lateral displacement, Canadian Geotechnical Journal, 47(8): 842–856.

Wang, D., Bienen, B., Nazem, M., Tian,Y., Zheng, J., Pucker, T. and Randolph, M. 2015. Large deformation finite element analyses in geotechnical engineering, Computers and Geotechnics, 65, 104–114.

White, D.J. and Dingle, H.R.C. 2011. The mechanism of steady friction between seabed pipelines and clay soils, Géotechnique, 61(12): 1035–1041.

APPENDIX C

Vertical Penetration of Offshore Pipelines: A Comparative Study between Finite Element and Finite Volume Methods

This paper has been published and presented in 2015 34th International Conference on Ocean, Offshore and Arctic Engineering (OMAE), St. John's, NL, Canada. Most of the research work presented in this paper was conducted by the first author. He also prepared the draft manuscript. The other authors supervised the research and reviewed the manuscript.

VERTICAL PENETRATION OF OFFSHORE PIPELINES: A COMPARATIVE STUDY BETWEEN FINITE ELEMENT AND FINITE VOLUME METHODS

Sujan Dutta
PhD Candidate
Memorial University
St. John's, NL, Canada

Bipul Hawlader
Associate Professor
Memorial University
St. John's, NL, Canada

Ryan Phillips
Principal Consultant
C-CORE
St. John's, NL, Canada

ABSTRACT

Deepwater surface laid pipelines generally penetrate a fraction of their diameter into the seabed. The near surface penetration behaviour of steel catenary risers (SCRs) is equally important in offshore oil and gas developments. Theoretical, physical and numerical investigations have been performed to understand pipeline–soil interaction during vertical penetration. The large deformation finite element (LDFE) modeling is a recent and advanced tool among different numerical modeling techniques. The authors of this study simulated the penetration of pipeline using Abaqus CEL Finite Element (FE) software [1]. They also developed a numerical modeling technique based on finite volume approach using ANSYS CFX [2] and showed some of its advantages. However, in that study an ideal soil (i.e. no softening or strain rate effects on undrained shear strength) was used. Strain rate and softening have significant effects on penetration behaviour and therefore in this study a numerical technique has been developed to incorporate these effects in ANSYS CFX. Comparison of the results shows that ANSYS CFX can also model the penetration behaviour. Moreover, ANSYS CFX has some advantages including low computational time, modeling of suction and pipeline–soil–water interaction. A parametric study is also presented to provide more insights into the pipeline–soil–water interaction.

Keywords: Pipelines, Finite element methods, Finite volume methods, Soft clay.

INTRODUCTION

In deepwater, the surface laid pipelines used to transport hydrocarbon can penetrate a fraction of their diameter into the seabed. Other than these pipelines, cylindrical objects such as steel catenary risers (SCRs) or T-bar penetrometer can also penetrate several pipe diameters vertically into the seabed. The soil near the mudline in deepwater could be soft to very-soft clay. Undrained behaviour of soft clay can be modeled using two approaches. In the first approach, as typically used in geotechnical engineering, it is characterized using undrained shear strength (s_u). In the second approach, the soil can be modeled using the fluid dynamics approach where the shear strength can be defined as a function of shear strain rate (e.g. Bingham and Herschel–Bulkley model). In this second approach, the shear resistance is defined by dynamic viscosity. In modeling of slurry, the second approach has been widely used (e.g. [3–5]). Recently, this type of model has also been used in problems involving relatively strong soils such as debris flow or glide block impact on pipelines [4&6]. If the model parameters are properly defined, both approaches might give comparable results.

The objective of this study is to present numerical simulations of pipeline penetration behaviour using two numerical techniques. In the first technique, large deformation finite element analysis is performed using Abaqus CEL where the shear strength of soil is modeled using undrained shear strength. In the second one, similar modeling is performed using ANSYS CFX where the shear resistance is defined using dynamic viscosity. In both numerical modeling tools, the effects of strain rate and strain softening due to remoulding are incorporated. Based on numerical simulations it is shown that ANSYS CFX can be also used for modeling large deformation behaviour of deepwater pipelines if the soil properties are properly defined and that this numerical tool can offer some additional advantages in some cases.

PREVIOUS STUDIES

A number of theoretical, physical and numerical analyses have been carried out to understand pipeline–seabed interactions. Theoretical analyses include upper and lower bound theorem and slip line theory. Physical modelling includes full-scale, reduced scale and centrifuge tests.

Numerical analyses include finite element (FE) and finite difference solutions. The Authors presented a comprehensive literature review of these studies in [7]. As numerical modeling is the main focus of this study, a brief literature review on numerical analyses is presented here. Small strain FE analysis by [8] estimated the penetration resistance for uniform and linearly increasing s_u profiles of the seabed for wished-in-place (WIP) pipe configuration. In their analyses, the effects of strain rate and softening were not considered. However, they proposed a set of generalized equations to calculate penetration resistance. FE and finite difference modeling of WIP pipes have also been conducted in studies by [9–12]. Several investigations have also been performed for pushed-in-place (PIP) pipes using LDFE techniques [1,2,13,14,15,16,17&18]. Among them, a large number of studies used RITSS (Remeshing and Interpolation Technique with Small Strain) technique developed at the University of Western Australia [13,14,18,19,20,21&22]. The Coupled Eulerian Lagrangian (CEL) approach in Abaqus FE software is also used with built-in soil model [17]. The authors of this study implemented strain rate and softening effects on s_u in Abaqus CEL. Recognizing some limitations of LDFE, they recently developed a numerical technique in ANSYS CFX to simulate pipeline penetration [2]. However, in that study strain rate and softening effects were not incorporated.

PROBLEM STATEMENT

A pipe of 0.8m diameter (D) is placed at a distance y_w above the mudline (Fig.1). The pipe is penetrated vertically into the seabed at a constant velocity, v_o. Horizontal displacement and rotation of pipe are not allowed. A linearly increasing s_{u0} profile defined as $s_{u0} = s_{um} + ky'$ is used, where, s_{um} = mudline undrained shear strength; k = shear strength gradient and y' = depth of the soil element below mudline.

STRAIN RATE AND SOFTENING EFFECTS ON UNDRAINED SHEAR STRENGTH OF SOIL

The undrained shear strength of clay increases with rate of shearing. On the other hand, it degrades (softening) with accumulated plastic shear strain (ξ) magnitude. In order to capture these effects, the following empirical model has been proposed by Randolph and his coworkers [19,23].

$$s_u = \left[1+\mu\log\left\{\frac{\max\left(\left|\dot{\gamma}_{\max}\right|,\dot{\gamma}_{ref}\right)}{\dot{\gamma}_{ref}}\right\}\right]\left[\delta_{rem}+\left(1-\delta_{rem}\right)e^{-3\xi/\xi_{95}}\right]s_{u0} = [f_1]\,[f_2]\,s_{u0} \quad (1)$$

Here, f_1 represents the strain rate term, f_2 represents the strain softening terms and s_{u0} represents the initial undrained soil shear strength at the reference shear strain rate ($\dot{\gamma}_{ref}$) and prior to any softening. μ is the rate of undrained shear strength increase per log cycle, δ_{rem} is the ratio of remolded to in situ undrained soil shear strength which is the inverse of remolded soil sensitivity (S_t), and ξ_{95} is the value of ξ at which soil has undergone 95% reduction in undrained shear strength due to remolding.

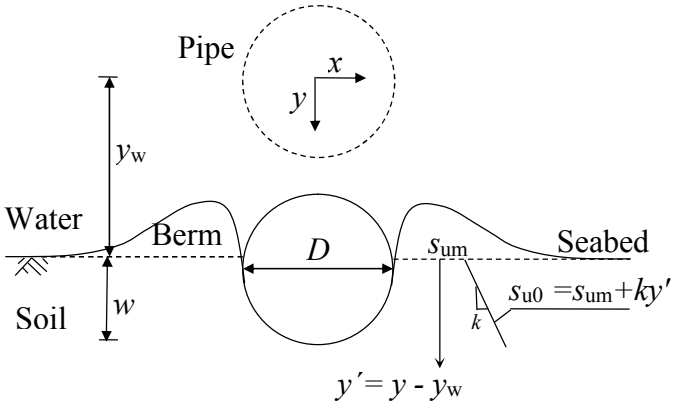

Figure 1. Problem definition

LARGE DEFORMATION FINITE ELEMENT MODEL

Figure 2 shows the FE model developed in Abaqus CEL. The details of modeling techniques can be found in [1]. In CEL analysis, the pipe is displaced vertically downward at a constant velocity (v_o) of 0.015D/s to a depth of 0.5D. With vertical penetration of the pipe, the soil around it is displaced and a berm is formed in the void space. Only 3-dimensional modeling can be performed using CEL and therefore the plane strain condition is simulated using only one element in the out of plane direction. Zero velocity boundary conditions are applied normal to all the faces. These boundary conditions keep the soil (Eulerian material) inside the domain. No boundary condition is applied at the soil/void interface and therefore the displaced soil can move into the void space. Based on previous mesh sensitivity analyses [24], cubical elements of 0.05D side lengths are used in this study.

The von-Mises yield criterion is adopted. As Abaqus does not have any direct option for modeling a linearly varying s_u profile, the numerical technique previously developed by the authors [1] is used. The pipe is modeled as rigid body to reduce the computational time. The pipeline-soil interface condition for undrained analysis is usually defined by limiting the shear stress, τ at the interface as αs_u, where α is interface roughness factor (0 for smooth and 1 for rough). Abaqus CEL 6.10 EF4 cannot limit the shear resistance at the pipeline-soil interface and therefore only smooth and rough conditions are simulated. Note that the rough condition in Abaqus CEL actually represents the full soil shear resistance at the pipeline-soil interface [25].

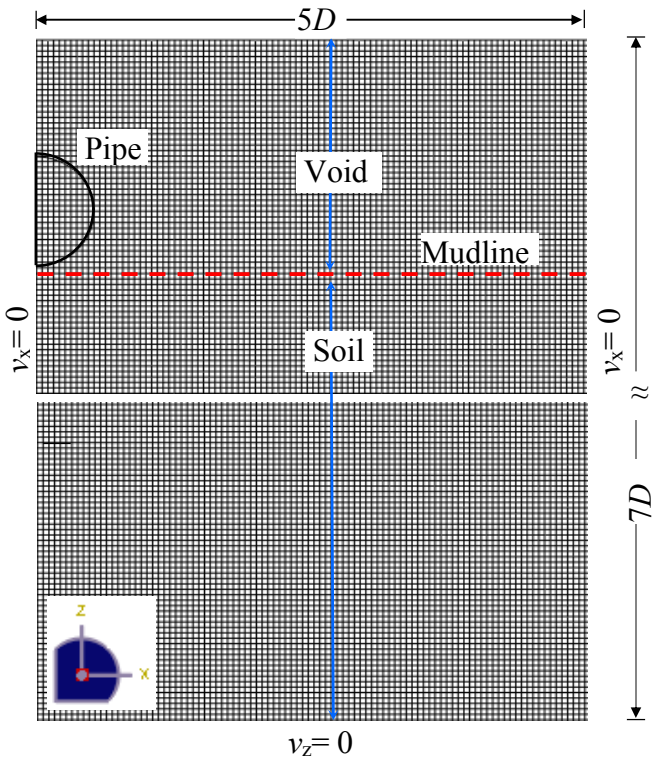

Figure 2. LDFE model in Abaqus CEL

FINITE VOLUME MODEL

Figure 3 shows the model developed using ANSYS CFX 13.0 software. Again taking the advantage of symmetry only the right half is modeled. A domain of $8D \times 20D$ is considered where the water and soil heights are $7D$ and $13D$, respectively. The pipe is placed at $1D$ above the seabed. Based on previous experience with Abaqus CEL modeling [7], the plastic shear strains in clay mainly develop within a radial distance of $4D$ [1,20]. Therefore, an inner subdomain of $4D$ diameter is created around the pipe (shaded zone in Fig. 3). The subdomain moves with the pipe at a same velocity without any mesh deformation. However, the soil or water as Eulerian material can flow though the subdomain and outside the subdomain [26].

All the vertical faces and the bottom of the model are defined as impermeable walls. No-slip boundary conditions are applied to the bottom wall and pipeline surface; however, a free-slip boundary condition is applied on the right vertical wall. The other three vertical faces are defined as planes of symmetry. The top of the water is defined as opening to allow water to flow in and out of the domain.

The maximum dimension of the mesh just outside the pipeline surface is 10 mm. With a reduced s_u in these elements, the interface behaviour is simulated as finite thickness interface elements. Note that finite thickness interface elements have been successfully used in previous studies [27–28]. Water is modelled as Newtonian fluid, while the soil is modelled as non-Newtonian fluid defining the dynamic viscosity as $s_u / \dot{\gamma}$, where $\dot{\gamma}$ is the shear strain rate.

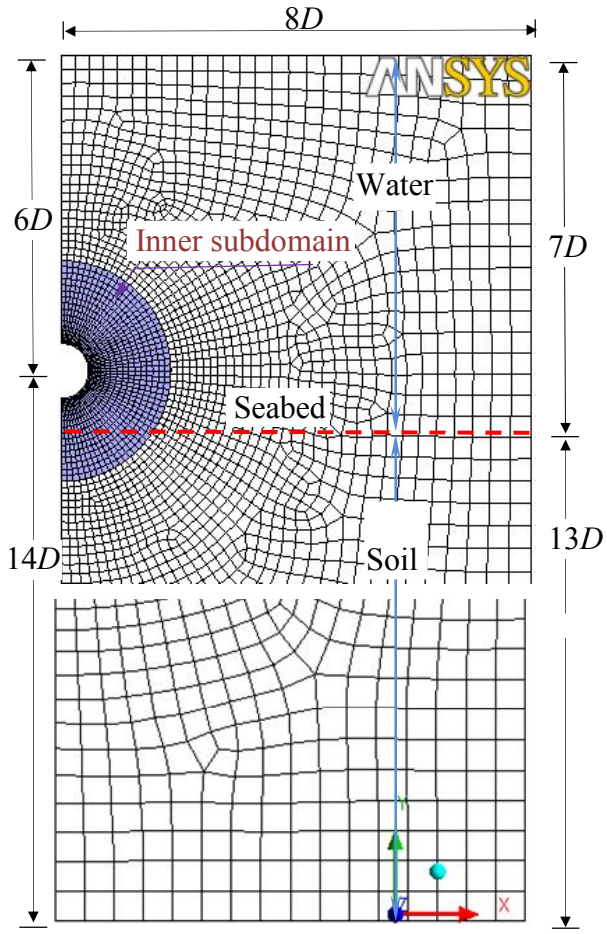

Figure 3. Finite Volume model in ANSYS CFX software

PARAMETER SELECTION

Table 1 shows the parameters used in ANSYS CFX and Abaqus CEL analyses. The parameters are selected based on the critical review of previous studies [18,19,29].

Comparison of Abaqus CEL and ANSYS CFX simulations

Figure 4a & b show the comparisons of penetration resistance with penetration depth obtained from Abaqus CEL and ANSYS CFX. The vertical axis shows the normalized penetration depth (w/D_e) and horizontal axis shows the normalized resistance ($F/s_{uo(i)}D_eL$). Here, w = distance of pipe invert from mudline, D_e = effective diameter of the pipeline, F = pipe vertical resistance, L = length of the pipe in the out of plane direction and $s_{u0(i)}$ = undrained shear strength of soil at pipe invert in triaxial condition. Following the concept of [30] and assuming that the failure occurs at a distance of half of the element size from the outer surface of the pipe, the value of D_e can be calculated as 810 mm (= 800 mm + 2 × 10 mm/2) for 10 mm element size just outside the pipe in CFX analysis. If D

is used instead of D_e, the normalized penetration resistance will be increased by only 1.25%. No strain softening and rate effects are considered (i.e. ideal soil) in the simulations shown Fig.4. Figure 4(a) shows a very good agreement between ANSYS CFX and Abaqus CEL simulation results. As an additional check the FE result from [18], where the RITSS technique is used, is also plotted. All three numerical techniques give almost similar penetration resistance curves for a smooth interface. The overlying water does not have significant role on penetration resistance at shallow depths simulated in this study; however, it has a considerable effect on failure mechanism and penetration resistance at intermediate depths as discussed in Hawlader et al. [2].

Table 1. Parameters for Abaqus CEL & ANSYS CFX analyses

Pipe	
Diameter, D (mm)	800 mm
Penetration depth, w (mm)	400 mm
Vertical penetration velocity, v_0	0.015 D/s
Clay	
Undrained shear strength at mudline, s_{um}	2.3 kPa
Gradient of shear strength increase, k	3.6 kPa/m
Submerged unit weight, γ'	6.5 kN/m^3
Rate of shear strength increase, μ	0.1
Reference shear strain rate, $\dot{\gamma}_{ref}$	3×10^{-6}/s
Remolded sensitivity, S_t	3.2
Accumulated absolute plastic shear strain for 95% degradation of shear strength, ξ_{95}	10
Clay (for Abaqus CEL)	
Undrained Young's modulus, E_u	$500s_u$
Poisson's ratio, ν_u	0.495

Figure 4(b) shows the penetration resistance for the rough pipeline-soil interface condition. The slight differences between the results might be attributed from the definition of interface condition in three programs. Overall, the penetration resistances obtained from these three numerical programs are still comparable.

ANSYS CFX modeling has some advantages such as computational time. The CEL is computationally expensive. For example, the CEL simulations shown in Fig. 4(a) take approximately 2 hours with a 3.4 GHz Intel Core i7 processor and 12 GB RAM. On the other hand, the CFX analysis shown in the same figure takes only 9 minutes on the same computer (i.e. 13 times faster than CEL). Some other advantages are discussed in [2&31]. However, one of the limitations of the CFX modeling is that the elastic behaviour is excluded. As it is a very large deformation problem, elastic deformation does not have a significant effect on penetration resistance curve. These simulations give confidence that ANSYS CFX can be used for modeling pipeline penetration. Therefore, in the following section, the discussion is focused on CFX results.

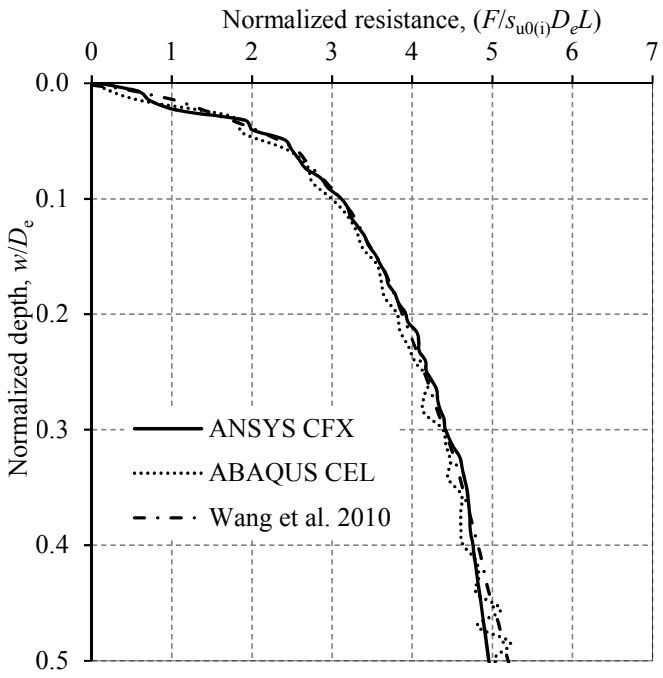

Figure 4 (a). Comparison for smooth pipeline-soil interface

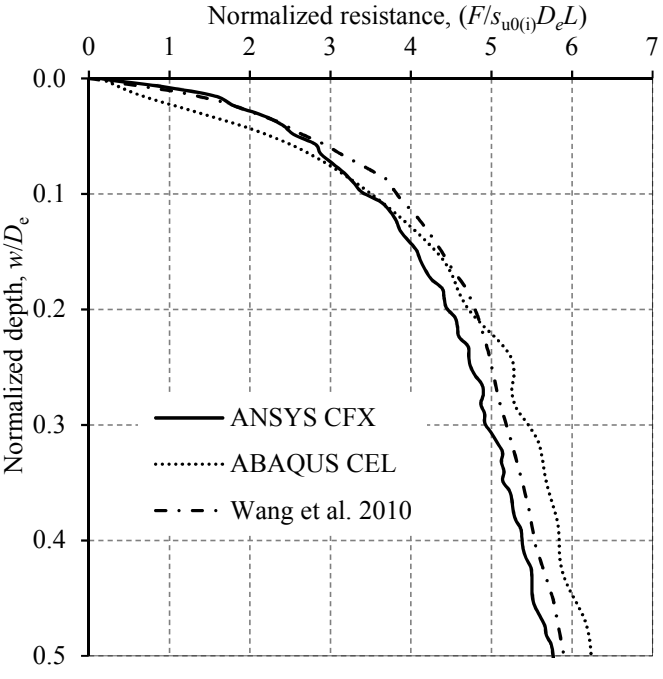

Figure 4(b). Comparison for rough pipeline-soil interface

Physical modeling & ANSYS CFX results comparison

An objective of this study is to incorporate strain rate and softening effects on undrained shear strength in ANSYS CFX, which has not been done in previous studies [16,17]. However, ANSYS CFX does not have any direct option to incorporate Eq. (1). Therefore, an in-house numerical tool has been developed to calculate accumulated strain in the ANSYS CFX platform which is then used to calculate the mobilized s_u using Eq. (1). The simulation results considering both of these effects are compared with physical model test results using a geotechnical centrifuge [29]. The parameters used in this simulation are listed in Table 1. The pipeline-soil interface roughness factor (α) of 0.6 is used by defining the shear strength in one layer of elements near the pipeline surface (finite thickness interface element) as 0.6 times of initial shear strength. The load-displacement curves in Figure 5 show good agreement between the physical model test and ANSYS CFX results.

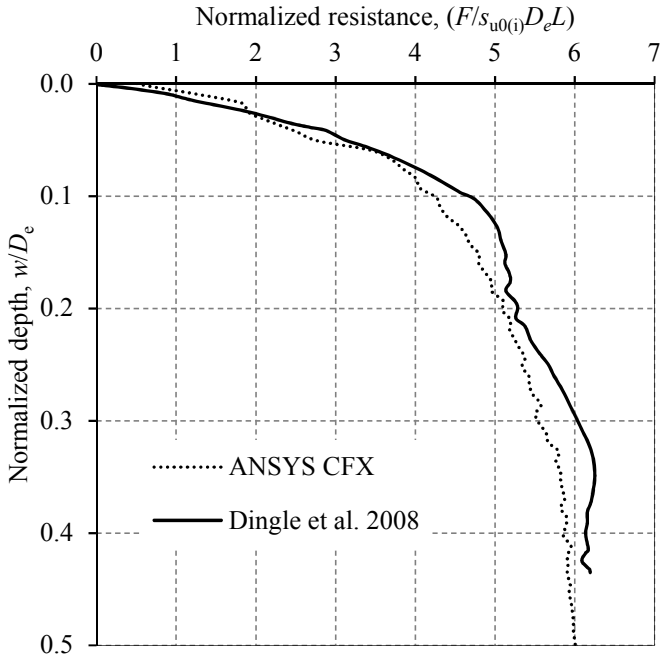

Figure 5. Comparison between ANSYS CFX and physical model test

Figure 6 shows the accumulated plastic shear strain (ξ) around the pipe at 0.5D penetration. For presentation clarity, the contours are shown over a logarithmic scale. The magnitude ξ is very high near the pipe surface which gradually decreases with radial distance. This observation is very similar to authors' Abaqus CEL analysis for both smooth and rough pipes [11]. Therefore, it can be concluded that Eq. (1) is properly implemented in ANSYS CFX. With penetration of the pipe the displaced soil forms a berm as shown in Figure 7 at w = 0.45D. The shape of the berm obtained from ANSYS CFX (right side of Fig. 7) compares very well with physical model test (left side of Fig. 7).

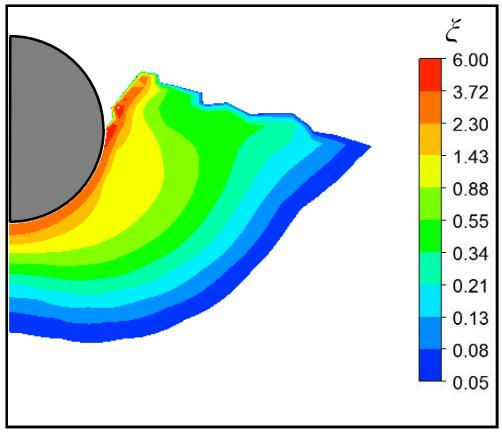

Figure 6. Accumulated plastic shear strain (ξ) in soil at pipe embedment of 0.5D

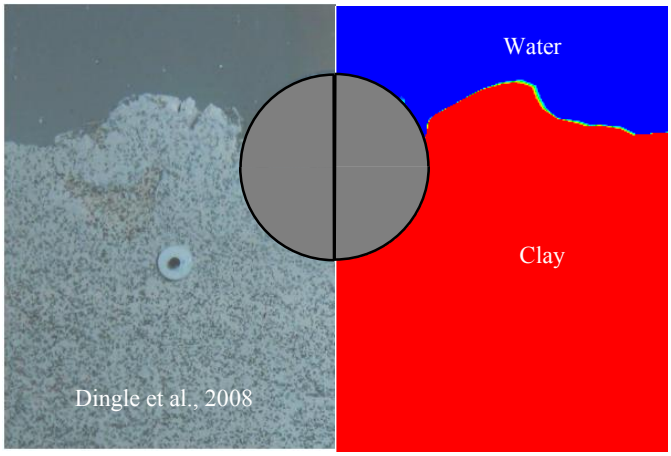

Figure 7. Comparison of developed berm around the pipe

Figures 8a–c show the instantaneous velocity vectors of soil elements and the pipe at three different depths of penetrations (right side). For comparison, physical model test results from Dingle et al. (2008) are also shown in the left side of these figures. The vertical arrows from the pipe surface represent the velocity of the pipe. Again, the velocity vectors are comparable with physical model test results.

PARAMETRIC STUDY

The parametric study was performed by varying only one parameter at a time keeping all other parameters same as Table. 1. A smooth pipeline-soil interface condition is used.

Effects of strain rate parameter μ

Undrained shear strength of clay increases with parameter μ and the value of μ can vary from 0.05 to 0.2 [23]. Figure 9

shows the effects of μ on penetration resistance. Three different values of μ (0, 0.1 and 0.2) are used. No strain softening effects are considered (i.e. f_2 = 1 in Eq. 1).The penetration resistance significantly increases with μ because of increase in undrained shear strength of clay.

Effects of soil sensitivity (S_t)

Equation (1) shows that the mobilized undrained shear strength depends on S_t. ANSYS CFX analysis is performed for three different values of S_t (1, 3.2 and 5). The strain rate effect is not considered in this analyses (i.e. f_1 = 1). Moreover, when S_t = 1, the value of f_2 equals 1.0, which represents the ideal soil in this case. Figure 10 shows that the penetration resistance decreases with increase in S_t, because s_u decreases with S_t. The observed behavior is very similar to the previous analysis conducted by the authors using Abaqus CEL [24] and LDFE analysis by others using RITSS [14].

Effects of strain softening parameter (ξ_{95})

Figure 11 shows the effects of strain softening parameter ξ_{95}. In addition to ideal soil, the penetration resistance is calculated for two more values of ξ_{95} (10 and 20). The penetration resistance increases with increase in ξ_{95} because of higher mobilized s_u. Again, these simulation results are consistent with previous studies [14,24].

CONCLUSIONS

Proper estimation of vertical penetration resistance is very important for deepwater surface laid pipelines. It is equally important in other applications such as penetration of a steel catenary riser at the touchdown zone or T-bar penetration. Large deformation finite element analyses have been conducted in the past to estimate the penetration resistance. An alternative numerical modeling technique based on computational fluid dynamics is presented. Analyses have been conducted using ANSYS CFX. Although large deformation FE modeling can simulate the penetration behaviour, the advantage of ANSYS CFX is that it is computationally efficient. The CFX simulations presented in this study considered the effects of strain rate and softening on undrained shear strength of clay which are the main improvements from authors' previous studies [2,31]. Numerical simulations using ANSYS CFX compare very well with previous physical modeling and FE results. The parametric study also shows very similar trend as obtained from large deformation finite element modeling. Therefore, it can be concluded that ANSYS CFX can successfully model pipeline–soil interaction behaviour.

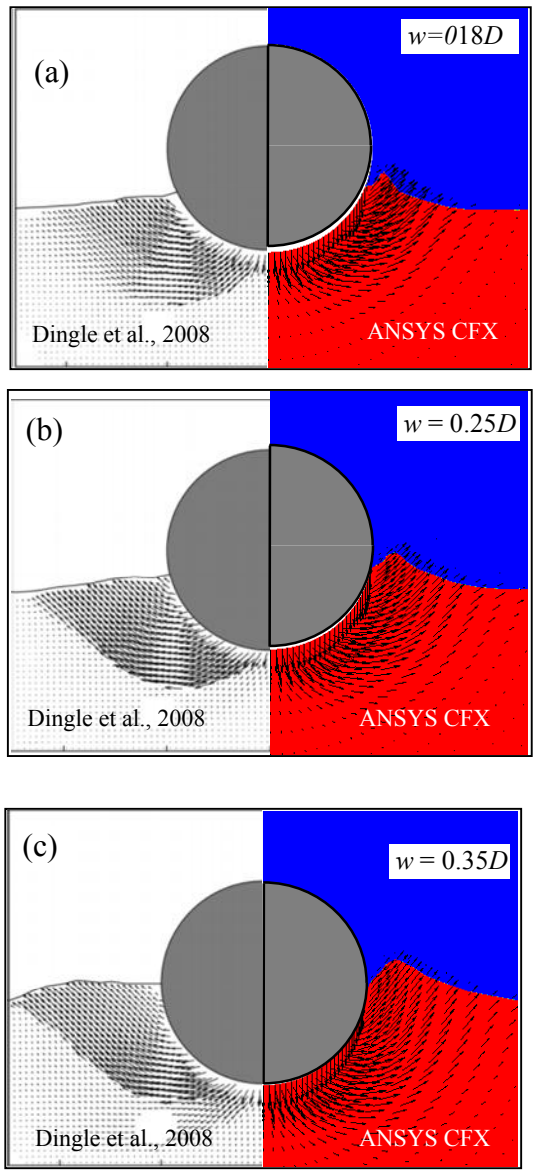

Figure 8. Comparison of instantaneous velocity between physical model test and numerical simulation using ANSYS CFX

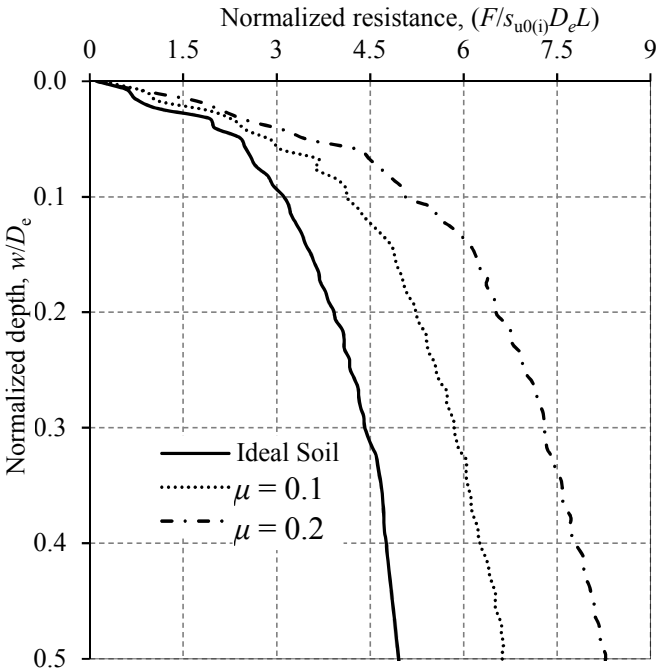

Figure 9. Effects of strain rate parameter (μ) on penetration resistance

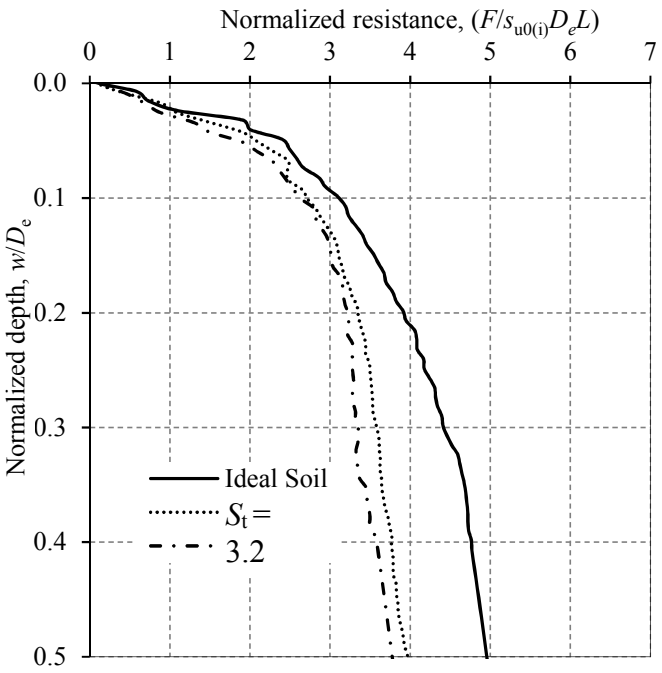

Figure 10. Effects of soil sensitivity (S_t) on pipe penetration resistance

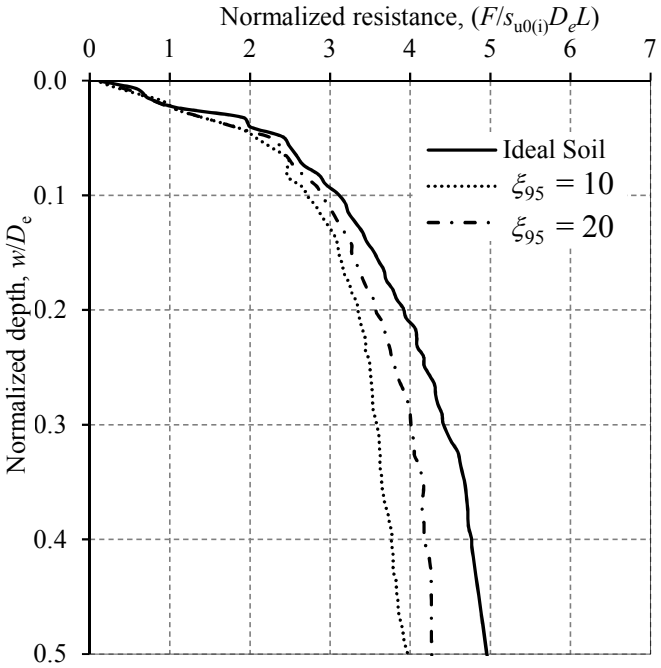

Figure 11. Effects of strain softening parameter (ξ_{95}) on pipe penetration resistance

ACKNOWLEDGMENTS

The work presented in this paper is funded by MITACS, NSERC, PRNL and C-CORE.

REFERENCES

[1] Dutta, S., Hawlader, B., and Phillips, R. (2014). "Finite element modelling of partially embedded pipelines in clay seabed using Coupled Eulerian Lagrangian method." Canadian Geotechnical Journal, 2015, 52(1): 58–72, 10.1139/cgj-2014-0045.

[2] Hawlader, B., Dutta, S., Fouzder, A. and Zakeri, A. (2015a). "Penetration of steel catenary riser in soft clay seabed–Finite Element and Finite Volume methods." International Journal of Geomechanics, ASCE (Accepted).

[3] Boukpeti, N., White, D. J., Randolph, M. F., and Low, H. E. (2012). "Strength of fine-grained soils at the solid-fluid transition." Géotechnique, 62(3): 213–226.

[4] Zakeri, A., Høeg, K., and Nadim, F. (2009). "Submarine debris flow impact on pipelines-Part II: Numerical analysis." Coastal Engineering, 56(1): 1–10.

[5] Imran, J., Harff, P. and Parker, G.(2001). "A numerical model of submarine debris flow with graphical user interface." Computers and Geosciences, 27(6): 717–729.

[6] Zakeri, A., and Hawlader, B. (2013). "Drag forces caused by submarine glide block or out-runner block impact on suspended (free-span) pipelines–numerical analysis." Ocean Eng., 67: 89–99.

[7] Dutta, S. (2012). "Large deformation finite element analysis of partially embedded offshore pipelines for vertical and

lateral motion at seabed." M.Eng. thesis, Memorial University of Newfoundland, Canada.
[8] Aubeny, C. P., Shi, H., Murff, J. D. (2005). "Collapse loads for a cylinder embedded in trench in cohesive soil." International Journal of Geomechanics, 5(4): 320–325.
[9] Bransby, M. F., Zajac, P., Amman, S. (2008). "Finite element analysis of the vertical penetration of 'on–bottom' pipelines in clay." Proc. 18th International Offshore and Polar Engineering Conference, July 6-11, International Society of Offshore and Polar Engineers, 245–249.
[10] Martin, C., and White, D. (2012). "Limit analysis of the undrained bearing capacity of offshore pipelines." Géotechnique, 62(9): 847–863.
[11] Morrow, D. R., and Bransby, M. F. (2010). "Pipe–soil interaction on clay with a variable shear strength profile." Proc. 2nd International Symposium on Frontiers in Offshore Geotechnics, ISFOG 2010, November 8–10, Taylor & Francis - Balkema, 821–826.
[12] Zhao, B., Gao, F., Liu, J., Wu, Y. (2009). "Vertical bearing capacity of a partially-embedded pipeline on Tresca soils." Proc. 19th International Offshore and Polar Engineering Conference, Osaka, Japan, June 21–26.
[13] Barbosa-Cruz, E. R., and Randolph, M. F. (2005). "Bearing capacity and large penetration of a cylindrical object at shallow embedment." Proc. 1st International Symposium on Frontiers in Offshore Geotechnics (ISFOG) 2005, 615–621.
[14] Chatterjee, S., Randolph, M. F., White, D. J. (2012). "The Effects of penetration rate and strain softening on the vertical penetration resistance of seabed pipelines." Géotechnique, 62(7): 573–582.
[15] Merifield, R. S., White, D. J., Randolph, M. F. (2009). "Effect of surface heave on response of partially embedded pipelines on clay." J. Geotech. Geoenviron. Eng., 135(6), 819–829.
[16] Shi, H., Sun, J., Hossain, K., Eltaher, A., Jukes, P. (2011). "Offshore pipeline embedment in cohesive soil–a comparison between existing and CEL solutions." Proc. ASME 30th International Conference on Ocean, Offshore and Arctic Engineering, OMAE2011, June 19–24, Rotterdam, The Netherlands, 1–6.
[17] Tho, K. K., Leung, C. F., Chow, Y. K., Palmer, A. C. (2012). "Deep cavity flow mechanism of pipe penetration in clay." Canadian Geotechnical Journal, 49(1): 59–69.
[18] Wang, D., White, D. J., Randolph, M. F. (2010). "Large-deformation finite element analysis of pipe penetration and large-amplitude lateral displacement." Canadian Geotechnical Journal, 47(8): 842–856.
[19] Zhou, H., and Randolph, M.F. (2007). "Computational techniques and shear band development for cylindrical and spherical penetrometers in strain-softening clay." International Journal of Geomechanics, ASCE, 7(4): 287–295.
[20] Zhou, H., and Randolph, M. (2009). "Resistance of full flow penetrometers in rate dependent and strain softening clay." Géotechnique, 59(2): 79–86
[21] Hu, Y., and Randolph, M. F. (1994). "A fully automated mesh generation method for large deformation problems." Proc. of Computer Methods and Advances in Geomechanics, Rotterdam, 441–446.
[22] Hu,Y. and Randolph, M. (1995). "Numerical simulation of pipe penetration in non-homogenous soil." Proc. 5th International Offshore and Polar Engineering Conference, ISOPE 1995, June 11–16, International Society of Offshore and Polar Engineers, 522–525.
[23] Einav, I., and Randolph, M.F. (2005). "Combining upper bound and strain path methods for evaluating penetration resistance." International Journal for Numerical Methods in Engineering, 63(14): 1991–2016.
[24] Dutta, S., Hawlader, B., Phillips, R. (2012a). "Strain softening and rate effects on soil shear strength in modeling of vertical penetration of offshore pipelines." Proc. 9th International Pipeline Conference, IPC2012, September 24-28, 2012, Calgary, Alberta, Canada, 1–8.
[25] Abaqus. (2010). "Analysis user manual." Abaqus 6.10-EF1.Simulia Inc., Dassault Systems.
[26] ANSYS CFX. (2010). "CFX solver modeling guide." CFX-Program (version13.0) Physical Modelling Documentation, ANSYS Inc.
[27] Jostad, H. P. and Andresen, L. (2004). "Modelling of shear band propagation in clays using interface elements with finite thickness." Proc. 9th International Symposium on 'Numerical Models in Geomechanics-NUMOG IX', Ottawa, Canada, 121–128.
[28] Supachawarote, C., Randolph, M. and Gourvenec, S. (2004). "Inclined pull-out capacity of suction caissons." Proc. 14th International Offshore and Polar Engineering Conference, Toulon, France, 500–506.
[29] Dingle, H. R. C., White, D. J., Gaudin, C. (2008). "Mechanisms of pipe embedment and lateral breakout on soft clay." Canadian Geotechnical Journal, 45(5): 636–652.
[30] Gui, M.W., and Bolton, M.D. (1998). "Geometry and scale effects in CPT and pile design." Geotechnical Site Characterization, Robertson & Mayne (eds), Balkema, Rotterdam, 1063–1068.
[31] Hawlader, B., Fouzder, A. and Dutta, S. (2015b). "Numerical modeling of suction and trench formation at the touchdown zone of steel catenary riser." International Journal of Geomechanics, ASCE (Accepted).

APPENDIX D

Numerical Investigation of Vertical Penetration of Steel Catenary Riser Near the Touch Down Zone

This paper has been published and presented in 2016 11th International Pipeline Conference and Exposition (IPC), Calgary, AB, Canada. Most of the research work presented in this paper was conducted by the first author. He also prepared the draft manuscript. The other authors supervised the research and reviewed the manuscript.

NUMERICAL INVESTIGATION OF VERTICAL PENETRATION OF STEEL CATENARY RISER NEAR THE TOUCH DOWN ZONE

Sujan Dutta
PhD Candidate
Memorial University
St. John's, NL, Canada

Bipul Hawlader
Associate Professor
Memorial University
St. John's, NL, Canada

Ryan Phillips
Principal Investigator
C-CORE
St. John's, NL, Canada

Mike Paulin
Operations Director
INTECSEA Canada
St. John's, NL, Canada

ABSTRACT

Steel catenary risers (SCR) are widely used in offshore to transport hydrocarbon from the seabed to floating or fixed platforms. The fatigue life of SCR near the touchdown zone (TDZ) is one of the main design concerns because the risers are often subjected to cyclic loading (vertical penetration/uplift, lateral and axial displacements) from various sources of environmental loadings, such as sea waves and currents. Numerical modeling of the penetration and uplift behaviour of an SCR is a challenging task. Most of the models available in the literature for uplift resistance are empirical, which h ave been developed mainly from the results of physical experiments.

In this study, numerical simulation of vertical resistance is presented. Analysis is performed using ANSYS CFX software. Strain-softening and strain-rate dependent undrained shear strength behavior of soft clay sediment has been reported by many researchers. Unfortunately, these models were not available in CFX. Numerical simulations presented in this paper are performed implementing this behavior in CFX. Numerical results are compared with available empirical models. The present CFX modeling explains some mechanisms involved in trench formation and suction development during uplift. Factors affecting uplift resistance such as the size and shape of the trench are also discussed from a parametric study.

INTRODUCTION

Steel catenary riser (SCR) is a pipe that connects the seabed with the floating or fixed platforms (Fig. 1) and considered as an economic solution for deep water (>400 m) oil and gas development [1]. The zone where SCR touches the seabed is known as touchdown zone (TDZ) (Fig. 1). Dynamic loads arising from sea state and current cause vertical displacement of the riser in the touchdown zone. Field evidence shows that a section of riser might penetrate vertically up to five diameters into the seabed during its lifetime forming a trench [2]. One of the reasons for trench formation in the TDZ is the riser cyclic motions where the riser is continuously penetrated into and uplifted from the seabed. The fatigue stress due to these cyclic motions might cause the failure of the riser [2]. One of the main components of uplift resistance is any suction generated behind the riser during upward motion. Proper estimation of uplift resistance is very difficult. Water intrusion into the soil, shear strength mobilization, suction mobilization and trench and berm formations make the whole process very complex. Because of these uncertainties, a very high level of safety factor is currently used in the design [3].

The effect of suction and trench formation on fatigue life has been investigated in some previous studies [2,28]. Giertsen et al. [28] showed a significant increase in bending moment in some locations in the TDZ when suction is considered. Bridge [2] showed that suction effect could double the stresses in riser at the touchdown point (TDP) during slow drift motions. Shiri and Randolph [29] and Ting et al. [30] showed that suction could double the fatigue damage for the parameters considered in the analyses. The effect of trench formation on riser is not well understood—while some studies show increase in fatigue life with trench formation [31,32, 33], and opposite trend has

been also reported [28, 30, 35]. Therefore, further studies are required on trench formation and suction development.

In the present study, vertical penetration and uplift behavior of a section of riser are simulated using ANSYS CFX 14.0 finite volume software [4]. A strain-softening and strain-rate dependent model for undrained shear strength is implemented in ANSYS CFX. Calculated resistances are compared to empirical models proposed by previous authors [2, 5]. One of the main advantages of the present numerical modeling is that it provides further insights into the mechanisms in addition to penetration and uplift resistances. The parametric study presented at the end shows the influence of a number of factors on suction mobilization, trench formation, role of water, strain-rate and strain-softening.

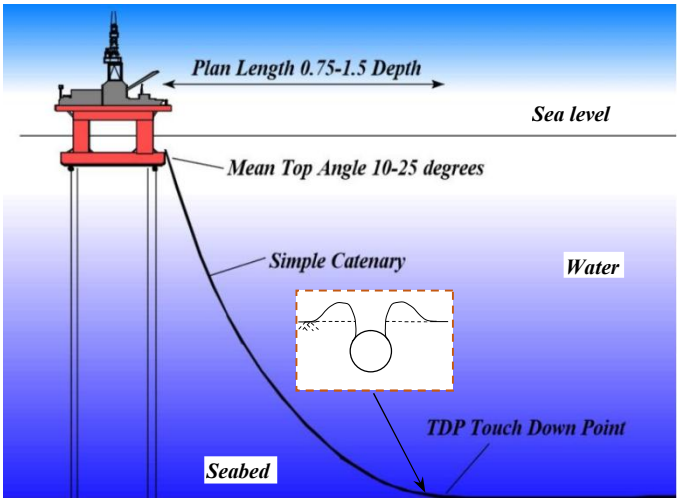

Figure 1. Typical steel catenary riser (SCR) in deepwater (modified from www.subseaworldnews.com)

PREVIOUS STUDIES

Theoretical, analytical, physical and numerical modeling have been conducted in the past to understand penetration and uplift behaviour of a cylindrical object into the seabed sediment. Dunlap et al. [6] conducted physical experiments using a section of pipe (D=0.15 m) subjected to cyclic vertical motion in a soft clay seabed of undrained shear strength of 1.5 kPa. They showed that suction force can be generated during uplift motions, and proposed a method to estimate uplift resistance. Bridge [2] reported a large number of two-dimensional laboratory tests conducted under CARISIMA and STRIDE JIPs for penetration and uplift behaviour of a section of riser for various conditions including initial penetration depth, riser velocity and shear strength profiles. Analyzing such test data, a set of empirical equations have been proposed to estimate suction and uplift resistances [2, 5]. Centrifuge tests have been also performed where a cylindrical object such as T-bar or a pipe section cycled into the seabed sediments [7–9].

Analytical models in the form of Q-z curve to estimate the riser penetration and uplift resistance have been proposed in the past [5, 10]. These models have been also used in calculating fatigue behaviour of risers.

In addition to two-dimensional modeling, three-dimensional full-scale and centrifuge modeling have been performed [2, 11, 12, 13]. The authors presented a comprehensive review of this work elsewhere [24, 25].

A very limited number of numerical studies are available on modeling of uplift behaviour. Clukey et al. [14] performed numerical investigation using LS-DYNA software and showed that Eulerian formulation can capture the kinematics of water particle in riser–seabed–water interaction. In recent studies, authors used a computational fluid dynamics approach (ANSYS CFX) and successfully simulated penetration and uplift behaviour for some idealized conditions. In the present study, an improved soil model described in the following sections, is implemented in CFX.

PROBLEM STATEMENT

A section of riser pipe of diameter D located above the seabed is displaced vertically at a constant velocity (v_0) to a depth of w into the seabed (Fig. 2). The pipe is then lifted to its starting point maintaining the same velocity v_0. Note that undrained condition is satisfied when the non-dimensional velocity (v_0D/c_v) is greater than 20, where c_v is the coefficient of consolidation [27]. Seabed sediment is modeled using initially uniform undrained shear strength (s_{u0}). However, during the displacement of the pipe, the mobilized undrained shear strength (s_u) varies with strain-rate and accumulated plastic shear strain.

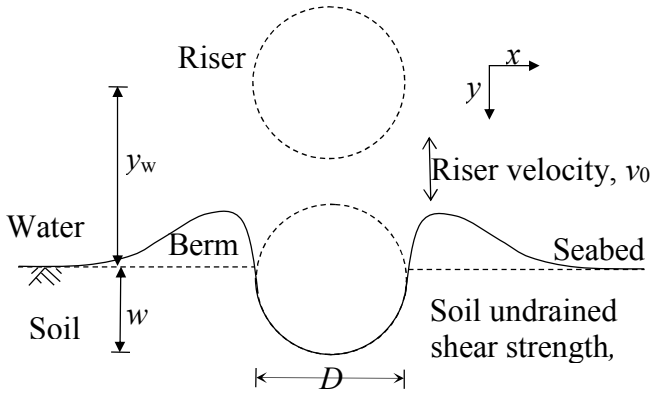

Figure 2. Problem definition

STRAIN RATE AND SOFTENING DEPENDENT SOIL CONSTITUTIVE MODEL

The undrained shear strength of soil depends on the rate of shearing and amount of accumulated plastic shear strain. The effects of shearing rate on s_u is generally expressed in terms of strain-rate ($\dot{\gamma}$) using a power law or logarithmic function. In this study, the model proposed by Einav and Randolph [15] shown in Eq. (1) is used, where f_1 represents the strain-rate effects and f_2 represents the strain-softening effects. Typical values of soil parameters for rate effects are: μ=0.05–0.2 and $\dot{\gamma}_{ref}$=1%/hr [15]. In the softening part, δ_{rem} represents the inverse of soil sensitivity (S_t), which could vary between 2 and 10 for marine clays [16]. ξ represents the accumulated absolute

plastic shear strain and ξ_{95} is the value of ξ at which 95% reduction of s_u (from peak to remoulded) occurs.

$$s_u = \left[1+\mu\log\left\{\frac{\max\left(|\dot{\gamma}_{\max}|,\dot{\gamma}_{ref}\right)}{\dot{\gamma}_{ref}}\right\}\right]\left[\delta_{rem}+(1-\delta_{rem})e^{-3\xi/\xi_{95}}\right]s_{u0} = [f_1]\,[f_2]\,s_{u0} \quad (1)$$

Undrained shear strength could be decreased further in addition to above mentioned undrained softening when water content remains constant. Water intrusion in the highly sheared layers near the water–soil interface might cause further reduction of shear strength and higher erodibility. De Blasio and his co-workers termed this phenomenon as "shear wetting" [17, 18]. A suitable model for this complex process is not currently available. However, in the problem considered in the present study, large shear strains mainly accumulate near the riser surface and soil–water interface in the trench. Therefore, in order to incorporate shear wetting effects, s_u is decreased linearly with ξ from s_{u_95} at ξ_{95} to s_{u_ld} at a large strain of ξ_{ld}. After ξ_{ld}, s_u remains constant at s_{u_ld}.

FINITE VOLUME MODEL DEVELOPMENT

Figure 3 shows the finite volume model developed using ANSYS CFX 14.0 software, where the upper 7*D* represents water and the lower 13*D* is the seabed sediment. ANSYS CFX can simulate three-dimensional condition only and therefore a thickness of 10 mm is considered in the out of plane direction to simulate the plane stain behaviour.

The riser is placed at 1.22*D* (=y_w) above the seabed and then displaced downward. After penetration to a desired depth into the seabed, the riser is lifted back to the initial position. The riser is modeled as a wall such that soil cannot penetrate into it during displacement. An inner subdomain near the riser has been defined (shaded zone in Fig. 3) where no mesh deformation is allowed; however, the soil as Eulerian material can flow through it. The use of a subdomain improves the performance of numerical modeling significantly as discussed by the authors in [24, 25]. All the faces of the domain are defined as impermeable walls. No-slip boundary condition is used for riser surface and the bottom, while a free-slip boundary is used for the right vertical face. For the other vertical faces, a symmetry-plane boundary condition is used. The top is defined as an opening. The thickness of the mesh (radial distance) just outside the riser is 10 mm. As shown in Fig. 3, the size of the mesh gradually increases with distance from the riser. Further details, including mesh sensitivity analysis, are available in Hawlader et al. [24, 25].

In deepwater, seabed sediments are mostly very soft clays. In the present study, both soil and water are modeled as homogenous Eulerian materials. Soil is modeled as non-Newtonian fluid and while water as Newtonian fluid. The undrained shear strength of soft clay sediments is implemented in CFX using the parameter dynamic viscosity which is related to s_u as $s_u/\dot{\gamma}$. In order to calculate s_u using Eq. (1), the strain rate ($\dot{\gamma}$) and accumulated plastic shear strain (ξ) need to be obtained. In CFX, $\dot{\gamma}$ could be easily obtained as it is an output variable. Authors developed a special technique to calculate ξ from strain rates, which has been discussed in detail in [19]. Now using $\dot{\gamma}$ and ξ, the value of s_u is updated at each time increment during simulation.

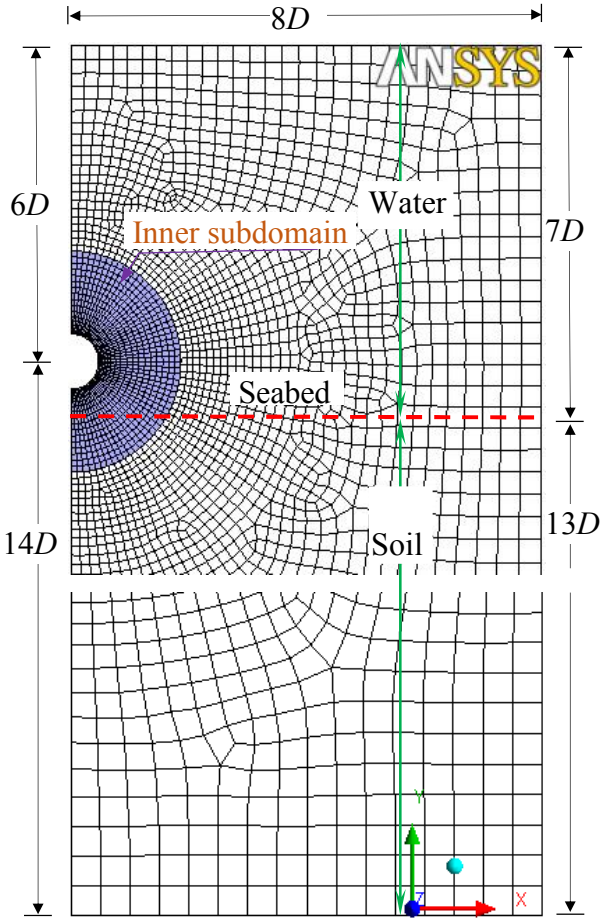

Figure 3. Finite volume model in ANSYS CFX 14.0

In order to model riser–soil interface condition, the undrained shear strength of the first row of elements around the riser is defined as αs_{u0} where α is equal to 0 and 1 for smooth and rough pipe–soil interface conditions, respectively. Further details of the material modeling, riser–soil interface conditions and CFX modeling techniques are available in Hawlader et al. [24, 25].

PARAMETERS SELECTION

Soil parameters are estimated based on a comprehensive literature review of soft clay sediment behavior in deepwater environments [20, 21]. Table 1 shows the parameters used in CFX analysis for the base-case.

NUMERICAL SIMULATION RESULTS

The simulation results for the base-case are presented in this section.

Penetration and uplift resistance

The solid line Fig. 4 shows the variation of penetration and uplift resistance with depth. In this figure, the vertical axis shows the normalized penetration depth (w/D_e) and horizontal axis shows the normalized riser resistance ($F/s_{uo}D_eL$), where w=distance of pipe invert from mudline, D_e=effective riser diameter, F=vertical resistance, L=length of the riser section in the out of plane direction and s_{u0}=initial undrained shear strength of soil in triaxial condition without any strength degradation and softening. Following the concept of Gui and Bolton [22] and assuming that the failure occurs at a distance of half of the element size from the outer surface of the pipe, the value of D_e can be calculated as 360 mm (=350 mm+ 2×10 mm/2) for 10 mm element size just outside the riser in CFX analysis. If D is used instead of D_e, the normalized penetration resistance will be increased by only 1.25%.

The left side of the Fig. 4 shows uplift resistance. For this condition (depth of embedment and soil properties) uplift resistance gradually decreases with upward movement of the pipe. At $w\approx0.1D$ pipe separates from the soil leaving a trench.

Table 1. Parameters for base-case analysis

Riser	
Diameter, D (m)	0.35
Length, L (m)	0.01
Maximum depth of penetration, w	0.5D
Penetration velocity, v_0 (m/s)	0.02
Soil	
Undrained soil shear strength, s_{u0} (kPa)	4.0 (1.0)
Undrained soil shear strength, s_{u_ld} (kPa)	0.3
Submerged unit weight, γ' (kN/m^3)	5
Riser-soil interface factor, α	0.7 (0.01, 0.1, 1)
Sensitivity, S_t	8 (4, 6, 10)
Softening parameter ξ_{95}	5 (9)
Softening parameter ξ_{ld}	9
Reference shear strain rate, $\dot{\gamma}_{ref}$ (s^{-1})	3×10^{-6}
Strain rate parameter, μ	0.15 (0.1, 0.2)
Water	
Unit weight, γ_w(kN/m^3)	9.81
Dynamic viscosity, μ_w(kg/m/s)	0.00089

Note: Numbers in parentheses in the right column show the values used for parametric study

Comparison with empirical models

As mentioned in the introduction, empirical models have been proposed in the past for penetration and uplift resistances. The model proposed by Randolph and Quiggin [5] is used for a comparison with the present numerical results. In the Randolph and Quiggin [5] model, the penetration and uplift resistances are expressed as a function of ultimate riser penetration P_u and ultimate uplift resistance $P_{u\text{-}suc}$, respectively, which are defined as: $P_u=N_cs_uD$ and $P_{u\text{-}suc}=-f_{suc}P_{u\text{-}pen}$. The bearing factor N_c is defined using the power law $N_c=a(w/D)^b$ proposed by Aubeny et al. [26] together with a correction factor for shallow depths ($w<0.1D$), where a and b are model parameters. A linearly increasing shear strength profile is considered; however, the model could be used for uniform shear strength assigning zero shear strength gradient. The initial penetration resistance (P) is defined as: $P=P_u/(1+D/yK_{max})$, where K_{max} varies between 150 and 200. Moreover, for a single uplift, f_{suc}=0.5–1.0 has been recommended. For uplift resistance, the following equation has been proposed: $P= P_0\text{-}H_{UL}(P_0\text{-}P_{u\text{-}suc})$, where $H_{UL}=(\zeta_0\text{-}\zeta)/\{A_{UL}+\zeta_0\text{-}\zeta)\}$, $A_{UL}= \{P_0\text{-}P_{u\text{-}suc}\}/P_u(y_0)$, where ζ_0= dimensionless penetration at which the latest episode of this contact mode started, y_0=penetration y at which the latest episode of this contact mode started, i.e. the value at the time the latest transition into this contact mode occurred and P_0=resistance $P(y)$ at which the latest episode of this contact mode started. For further details about this empirical model, the reader are referred to Randolph and Quiggin [5].

Now using above mentioned equations, penetration and uplift resistances are calculated. As recommended in [5], two values of f_{suc} (0.5 & 1.0) are used. Other parameters are listed in Table 2.

Table 2. Parameters used for Randolph and Quiggin [5]

Undrained soil shear strength, s_{um} (kPa)	4.0
Shear strength gradient, ρ (kPa/m)	0
Power law parameter, a	6
Power law parameter, b	0.25
Normalized maximum stiffness, K_{max}	200
Suction ratio, f_{suc}	0.5 & 1.0

Figure 4 shows that CFX simulated penetration resistance matches very well with [5]. In addition to other researchers, the authors of the present study discuss the penetration behavior in detail elsewhere [23] and therefore is not repeated here. Instead, the discussion is focused mainly on uplift behavior.

In the range of w between $0.3D_e$ and $0.5D_e$ the calculated uplift resistance is slightly lower than [5] with f_{suc}=1.0 (Fig. 4). However, with increase in upward displacement CFX calculates lower uplift resistance than [5]. The uplift resistance is approximately zero above $w\approx0.1D_e$ because the riser separates from the soil. Flow of water in the trench plays a significant role as discussed in the following sections.

Bridge [2] provides a set of empirical equations to calculate uplift resistance and its mobilization with upward displacement of the pipe. For the development of this empirical model, one set of tests were conducted in Watchet Harbor clay which has geotechnical properties similar to the Gulf of Mexico clay [2]. Hawlader et al. [25] presented a summary of this model. Using the model parameters recommended for this clay, the uplift resistance is calculated as shown in Fig. 4. Although the soil properties are different, it shows that the maximum uplift resistance from [2] is comparable with the present CFX analysis. The zone of "suction plateau" where the uplift resistance is constant is not found in CFX modeling or in Randolph and Quiggin [5]. The *breakout point*—the depth at

which pipe separates from the soil—is comparable between CFX analysis and empirical model proposed by Bridge [2].

While Fig. 4 shows the comparison between penetration and uplift resistances, further insights into the potential mechanisms as presented in the following sections help explain this behaviour.

Plastic shear strain around the riser

The first row of Fig. 5 shows the accumulated absolute plastic shear strain (ξ) around the riser for three different depths (w/D_e=0.4, 0.2 and 0.1) during penetration and uplift. The magnitude of ξ is very high near the riser, and decreases with radial distance. Figure 5(a) shows that high ξ develops only in a thin zone during penetration. Figure 5(b) shows the ξ at the same depth (w=0.4D_e) but during uplift. As the riser penetrated up to w=0.5D_e and was then uplifted, the magnitude of ξ increases due to this displacement. The increase in ξ continued with upward displacement as shown in Figs. 5(b)–5(d). The variation of ξ presented in Figs. 5(a)–(d) shows that the developed technique in CFX successfully calculates the accumulated plastic shear strains. The magnitude of ξ and the output variable $\dot{\gamma}$ are used to update mobilized s_u (Eq. 1) at each time increment.

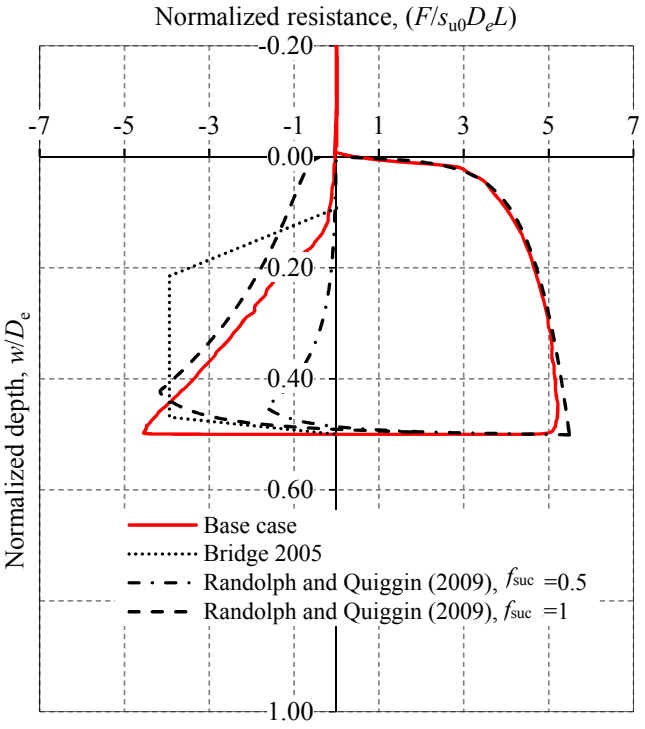

Figure 4. Comparison of riser uplift resistance for riser penetration of 0.5D_e into the seabed

Suction around the riser

The development of suction is shown in Figs. 5(e)–(h) by plotting the variation of absolute values of negative pressures. As expected, suction around the riser is not observed during vertical penetration to this shallow depth (Fig. 5e). Note that suction might be developed in the cavity above the pipe if the penetration depth is high [24]. Suction generates under the pipe during uplift as shown in Fig. 5(f) and 5(g). The zone of suction is high in Fig. 5(g) as compared to Fig. 5(f) because water can flow toward the invert of the pipe through the narrow channels formed near the pipe. At large upward displacements, suction is almost negligible (<5kPa) as shown in Fig. 5(h).

Instantaneous soil and water velocity field around the riser

Figures 5(i)–5(l) show the instantaneous velocity vectors of soil and water during penetration and uplift. During penetration, soil flows around the riser and berms form in both sides of the pipe. Water particles above the pipe move downward. Velocity vectors in opposite direction are obtained during uplift (Figs. 5(j)–(l)). With further upward displacement, a channel is formed and water flows at a high velocity toward the bottom of the pipe (Fig. 5(k) & 5(l)).

PARAMETRIC STUDY

A parametric study is conducted varying only one parameter while keeping other parameters same as listed in Table 1, unless otherwise mentioned.

Effect of maximum penetration depth (w)

Simulations are also performed for two additional penetration depths (w=0.75D_e and 1.0D_e). Figures 6 and 7 show the variation of normalized penetration resistance. Again for the purpose of comparison, calculated resistance using empirical model [5] for two values of f_{suc} (0.5 and 1.0) are shown in this figure. The shape of the resistance vs. depth curves in Figs. 6 and 7 are similar to that presented in Fig. 4. As expected, the maximum penetration and uplift resistances increase with increase in maximum penetration depth.

Effect of soil sensitivity (S_t)

Figure 8 shows the results with four different values of sensitivity S_t used in Eq. (1). The higher the sensitivity the lower the mobilized undrained shear strength. Therefore, both penetration and uplift resistances decrease with increase in sensitivity.

Effect of softening and rate parameters

In the base-case analysis, softening parameters of ξ_{95}=5 and ξ_{1d}=9 is used. To show the effect of these parameters two more analyses are performed with ξ_{95}=5 and 9 without any shear wetting. In other words, shear strength degradation in these two analyses are defined by only Eq. (1). Figure 9 shows the simulated results. A comparison between analyses with ξ_{95}=5 and 9 shows that ξ_{95}=5 gives lower uplift resistance because in this case s_u degrades quickly. When the shear wetting is considered (i.e. ξ_{95}=5 and ξ_{1d}=9) uplift resistance degreases further.

Figure 10 shows the effect of μ. Both penetration and uplift resistances increase with increase in μ, because of shear strength increase with strain rate (see Eq. 1).

To examine whether a strain-rate and strain-softening model, as the one shown in Eq. (1), is required for estimation of penetration and uplift resistances, analyses are also performed using a constant s_u (=4 kPa). Figure 11 shows the strain-rate and strain-softening dependent model gives slightly lower penetration resistance, especially at shallow depths. However, a significant difference is observed in uplift resistance. Analysis with constant s_u gives significantly higher uplift resistance as compared to the base-case analysis with strain-rate and strain-softening dependent model. Moreover, the shape of the uplift resistance curve is very different. This effect is expected to be increased with cyclic loading as encountered in the touchdown zone of the riser, because the accumulated shear strain around the riser increases with cyclic loading. In summary, the effects of strain- rate and strain-softening on s_u should be considered for successful simulation of penetration and uplift resistances.

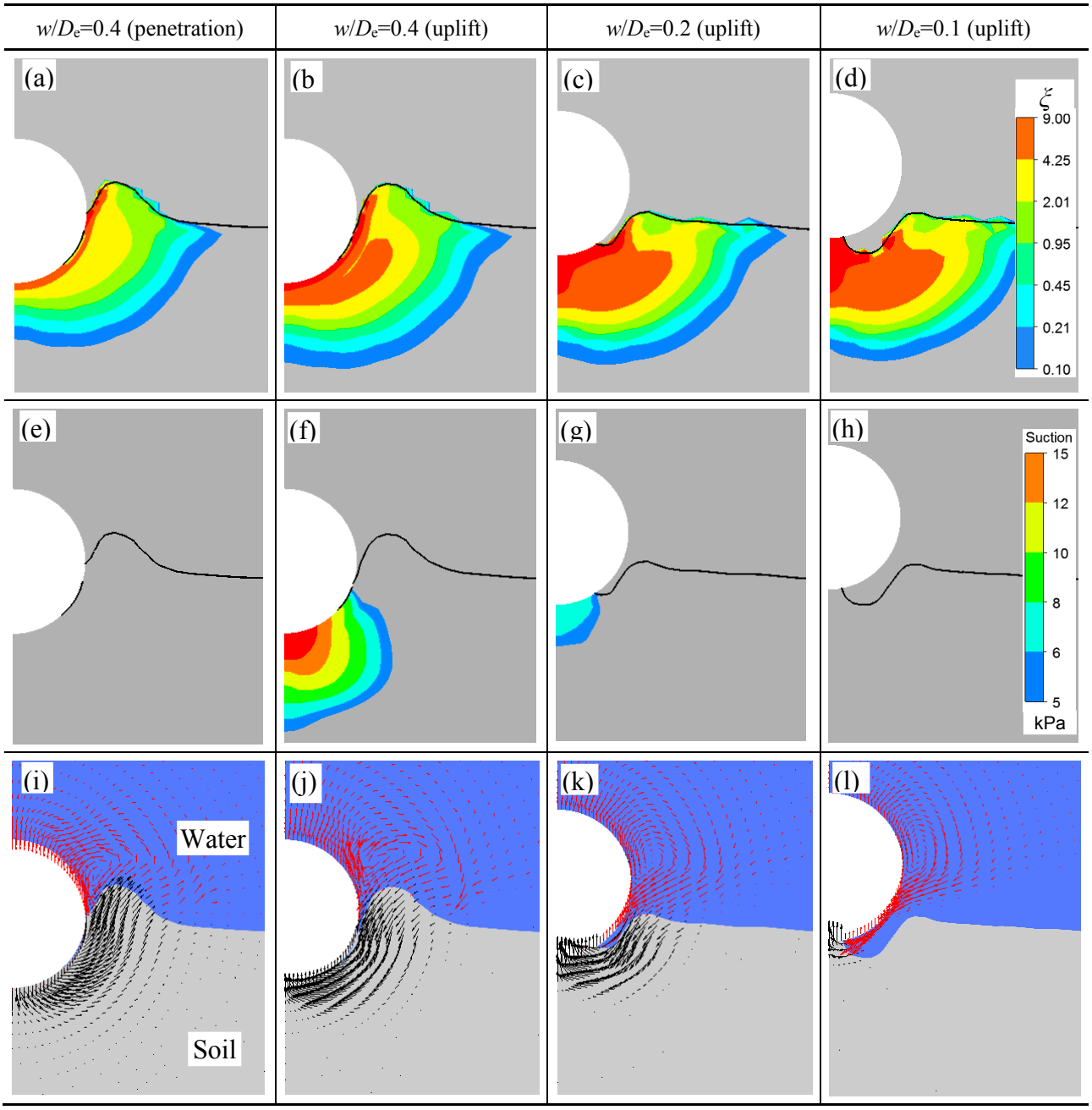

Figure 5. (a–d) Accumulated plastic shear strain (ξ) in soil; (e–h) Development of suction near riser invert; (i–l) Instantaneous velocity of soil and water

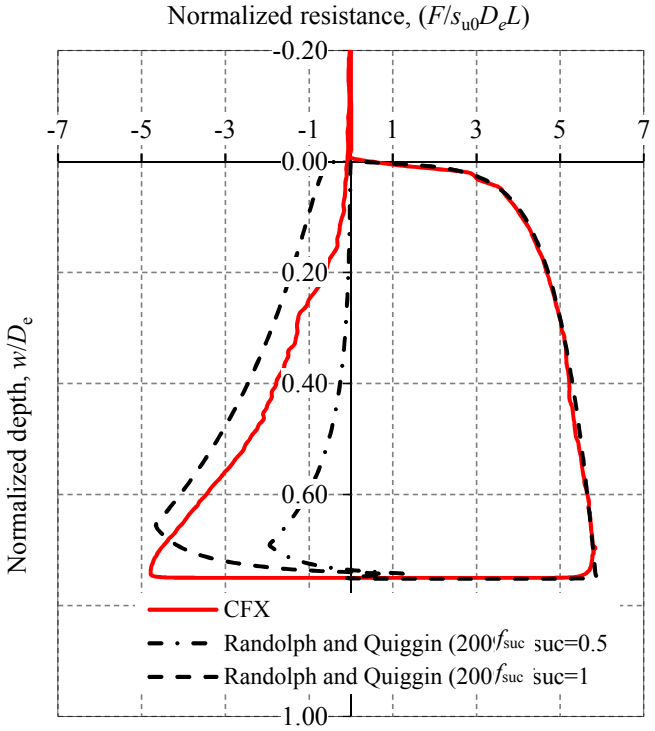

Figure 6. Comparison of riser uplift resistance for riser penetration of $0.75D_e$ into the seabed

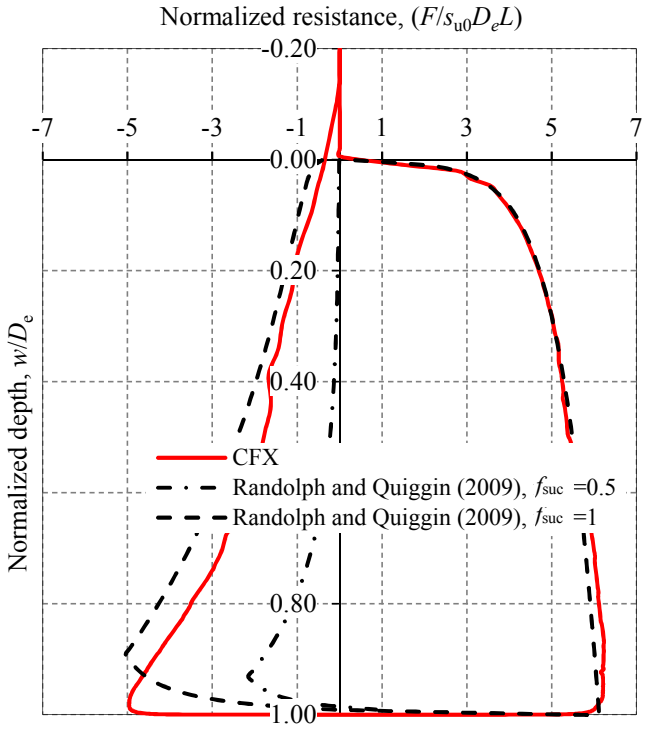

Figure 7. Comparison of riser uplift resistance for riser penetration of $1D_e$ into the seabed

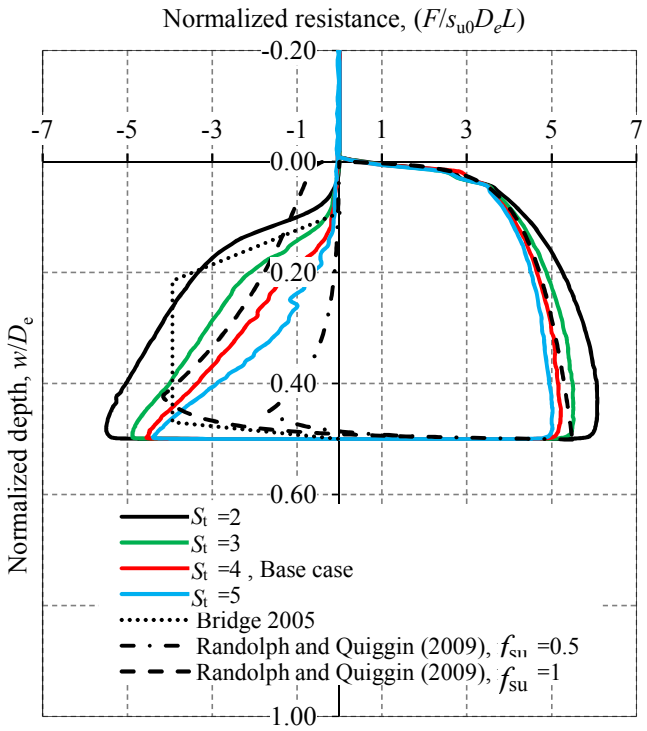

Figure 8. Effects of soil sensitivity on riser uplift resistance

CONCLUSION

Penetration and uplift resistances offered by seabed sediments near the touchdown zone have a significant influence on the design life of steel catenary risers for cyclic loading. The suction develops under the riser during upward movement is one of the main sources of uplift resistance. Currently, empirical equations in the form of *Q-z* curve are used. The suction and trench formation is influenced by kinematics of water particles. In order to capture these effects, the computation fluid dynamics approach available in ANSYS CFX is used in this study. A strain-softening and strain-rate dependent soil model is implemented in ANSYS CFX. The present CFX analysis gives penetration and uplift resistances similar to empirical models developed from laboratory experiments. Moreover, the CFX modeling provides further insight into the mechanisms including trench formation and role of water. Numerical simulations show that the combined effects of strain-softening and strain-rate on undrained shear strength reduce uplift resistance as compared to the simulations without these effects for the cases analyzed.

Riser–seabed–water interaction is a very complex process. Only one cycle of vertical loading is simulated in this study and the results are compared with an empirical model [29]. Multiple loading cycles, improved modeling of soil-water mixing and potential erosion, and comparison with field and model test results need to be considered in future studies.

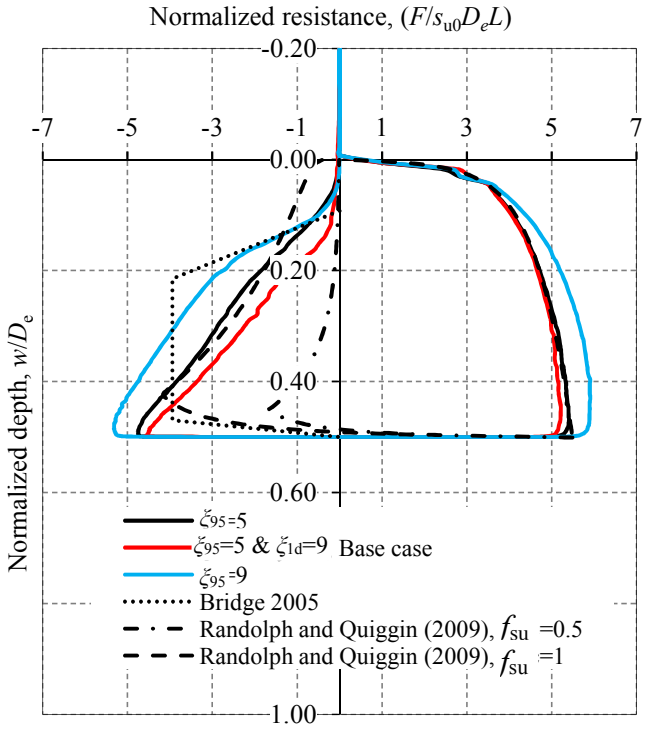

Figure 9. Effects of soil softening parameters (ξ_{95} *and* ξ_{1d}) on riser uplift resistance

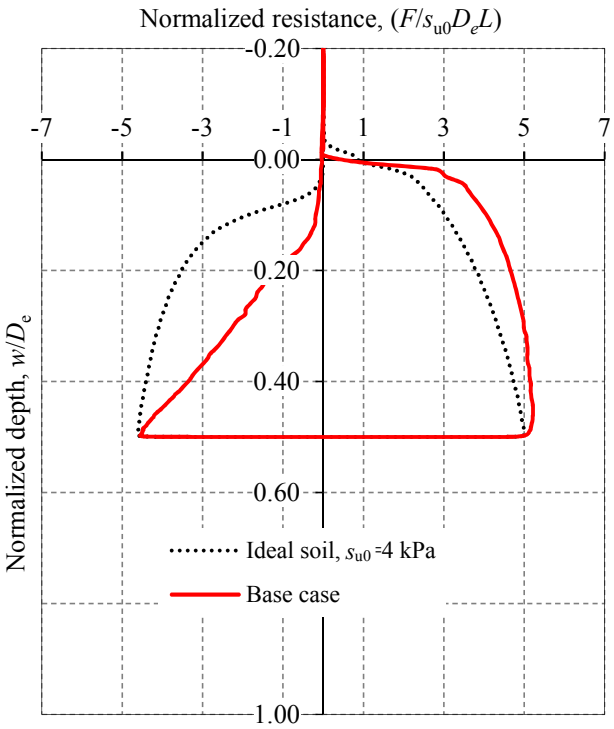

Figure 11. Combined strain rate and softening effects on riser uplift resistance

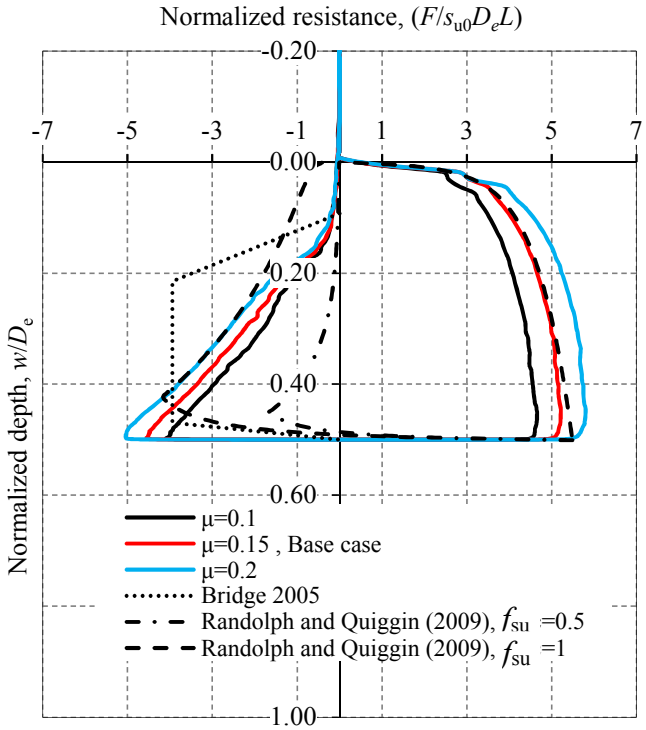

Figure 10. Effects of strain rate parameter μ on riser uplift resistance

ACKNOWLEDGMENTS

Funding from the MITACS, Natural Sciences and Engineering Research Council of Canada (NSERC), Petroleum Research Newfoundland & Labrador (PRNL) and C-CORE are gratefully acknowledged.

REFERENCES

[1] Howells, H. (1995). "Advances in steel catenary risers design." Proc. 2nd Annual International Forum on Deepwater Technology, Aberdeen, UK, pp.1–5.

[2] Bridge, C. (2005). "Effects of seabed interaction on steel catenary risers." PhD Thesis, University of Surrey, Surrey, UK.

[3] DNV–RP–204. (2010). Riser fatigue.

[4] ANSYS CFX. (2010). "CFX solver modeling guide." CFX-Program (version13.0) Physical Modelling Documentation, ANSYS Inc.

[5] Randolph, M., and Quiggin, P. (2009). "Non–linear hysteretic seabed model for catenary pipeline contact." Proc. 28th International Conference on Ocean, Offshore and Arctic Engineering (OMAE), Honolulu, HI, USA, pp. 145–154.

[6] Dunlap, W. A., Bhojanala, R. P., and Morris, D. V. (1990). "Burial of vertically loaded offshore pipelines in weak sediments." Proc. Offshore Technology Conference. OTC 6375.

[7] Aubeny, C., Gaudin, C., and Randolph, M. (2008). "Cyclic tests of model pipe in kaolin." Society of Petroleum

Engineers (SPE), Richardson, TX, USA. doi:10.2118/123131-PA
[8] Hodder, M. S., White, D. J., and Cassidy, M. J. (2013). "An effective stress framework for the variation in penetration resistance due to episodes of remoulding and reconsolidation." Géotechnique, 63(1):30–43.
[9] Hu, H. J. E. (2010). "Pipeline/riser soil interaction analysis." PhD. Thesis, National University of Singapore (NUS), Singapore.
[10] Aubeny, C. P., and Biscontin, G. (2009). "Seafloor–riser interaction model." International Journal of Geomechanics, 9(3):133–141.
[11] Elliott, B., Phillips, R., Macneill, A. (2014). "Physical modelling of SCR in the touchdown zone under three axis motions," Proc. 8th International Conference on Physical Modelling in Geotechnics (ICPMG 2014), pp. 265–270, January 14–17, Perth, WA, Australia,.
[12] Elliott, B. J., Zakeri, A., Barrett, J. (2013b). "Centrifuge modeling of steel catenary risers at touchdown zone, Part II: Assessment of centrifuge test results using kaolin clay," Ocean Engineering, 60(1):208–218.
[13] Elliott, B. J., Zakeri, A., Macneill, A. (2013a). "Centrifuge Modeling of steel catenary risers at touchdown zone, Part I: Development of novel centrifuge experimental apparatus," Ocean Engineering, 60(1):200–207.
[14] Clukey, E., Jacob, P., and Sharma, P. P. (2008). "Investigation of riser seafloor interaction using explicit finite element methods." Proc. Offshore Technology Conference, Houston, Texas, USA. OTC 19432.
[15] Einav, I., and Randolph, M. F. (2005). "Combining upper bound and strain path methods for evaluating penetration resistance." International Journal for Numerical Methods in Engineering, 63(14):1991–2016.
[16] Randolph, M.F. (2012). "Evaluation of the remoulded shear strength of offshore clays and application to pipeline-soil and riser-soil interaction," Mechanical Behaviour of Soils Under Environmentally Induced Cyclic Loads, 11, 529–573.
[17] De Blasio, F., Elverhøi, A., Issler, D. (2005). "On the Dynamics of subaqueous clay rich gravity mass flows—the Giant storegga slide, Norway," Marine and Petroleum Geology, 22(1):179–186.
[18] Elverhøi, A., Issler, D., De Blasio, F. (2005). "Emerging insights into the dynamics of submarine debris flows," Natural Hazards and Earth System Science, 5(5):633–648.
[19] Dutta et al. (2016). "Numerical investigation of soft seabed sediment flow mechanisms during cyclic loading around the touchdown zone of a steel catenary riser." (in preparation).
[20] Lunne, T., and Andersen, K. H. (2007). "Soft clay shear strength parameters for deepwater geotechnical design," Proc. 6th International Offshore Site investigation and Geotechnics Conference, London, UK .
[21] Randolph, M.F. (2012). "Evaluation of the remoulded shear strength of offshore clays and application to pipeline-soil and riser-soil interaction," Book Chapter of Mechanical Behaviour of Soils Under Environmentally Induced Cyclic Loads, Vol. 534, Series CISM Courses and Lectures, pp. 529–573.
[22] Gui, M.W., and Bolton, M.D. (1998). "Geometry and scale effects in CPT and pile design." Proc. 1st international Conference on Geotechnical Site Characterization, Atlanta, GA, USA, pp. 1063–1068.
[23] Dutta, S., Hawlader, B., and Phillips, R. (2015). "Vertical penetration of offshore pipelines: A comparative study between finite element and finite volume methods." Proc. 34th International Conference on Ocean, Offshore and Arctic Engineering (OMAE), pp. 0–10.
[24] Hawlader, B., Dutta, S., Fouzder, A. and Zakeri, A. (2015a). "Penetration of steel catenary riser in soft clay seabed–Finite element and Finite volume methods." International Journal of Geomechanics, ASCE, 15(6):1–12.
[25] Hawlader, B., Fouzder, A. and Dutta, S. (2015b). "Numerical modeling of suction and trench formation at the touchdown zone of steel catenary riser." International Journal of Geomechanics, ASCE, 16(1):1–14 .
[26] Aubeny, C. P., Shi, H., and Murff, J. D. (2005). "Collapse loads for a cylinder embedded in trench in cohesive soil." International Journal of Geomechanics, 5(4): 320–325.
[27] House, A. R., Oliveira, J. S., and Randolph, M.F. (2001). "Evaluating the coefficient of consolidation using penetration tests" International Journal of Physical modelling in Geotechnics, 1(3):17–26.
[28] Giertsen, E., Verley, R., and Schrder, K. (2004)."CARISIMA a catenary riser/soil interaction model for global riser analysis." Proc., 23rd International Conference on Offshore Mechanics and Arctic Engineering, 633–640.
[29] Shiri, H., and Randolph, M. (2010). "The influence of seabed response on fatigue performance of steel catenary risers in touchdown zone" Proc., 29th International Conference on Ocean, Offshore, and Arctic Engineering, 1–10.
[30] Ting, I. H. Y., Kimiaei, M., and Randolph, M. F. (2010)."Advanced nonlinear hysteretic seabed model for dynamic fatigue analysis of steel catenary risers." Proc., 2nd International Symposium on Frontiers in Offshore Geotechnics, 833–838.
[31] Langner, G.C. (2003) "Fatigue life improvement of steel catenary risers due to self–trenching at the touchdown point" Proc. Offshore Technology Conference, Texas, USA. OTC 15104
[32] Clukey, E., Ghosh, R., Mokarala, P., and Dixon, M. (2007)."Steel catenary riser (SCR) design issues at touch down area." Proc. 17th International Offshore and Polar Engineering Conference, 814–819.
[33] Nakhaee, A., and Zhang, J. (2010)."Trenching effects on dynamic behavior of a steel catenary riser." Ocean Engineering, 37(2–3), 277–288.
[34] Leira, J.B., Passano, E., Karunakaran, D., Farnes, K., and Giertsen, E. (2004) "Analysis guidelines and applications of

a riser-soil interaction model including trench effects" Proc. 23rd International Conference on Offshore Mechanics and Arctic Engineering (OMAE 2004), BC, Canada, 1–8.

APPENDIX E

Numerical Modeling of Drag Force on Submarine Suspended Pipelines Using Finite Element and Finite Volume Methods

This paper has been published in 2015 25th International Offshore (Ocean) and Polar Engineering Conference & Exhibition (ISOPE), Honolulu, Hawaii, USA. Most of the research work presented in this paper was conducted by the first author. He also prepared the draft manuscript. The second author supervised the research and reviewed the manuscript.

Numerical Modeling of Drag Force on Submarine Suspended Pipelines Using Finite Element and Finite Volume Methods

Sujan Dutta
Memorial University
St. John's, NL, Canada

Bipul Hawlader
Memorial University
St. John's, NL, Canada

ABSTRACT

In deepwater, pipelines are usually laid on the seabed. Depending on seabed topography, some sections of the pipeline might be suspended above the local seabed surface. Estimation of drag force on a suspended pipeline subjected to submarine landslides is a challenging task. In the present study, numerical modeling is conducted using two different approaches to calculate drag force. In the first one, large deformation finite element (FE) analyses are performed using the Coupled Eulerian Lagrangian (CEL) approach available in Abaqus FE software. In the second one, the computational fluid dynamics (CFD) approach is employed. The CFD modeling is performed using ANSYS CFX 14.0 software. In both cases, very large lateral penetration could be simulated without any numerical issues as encountered in typical FE modeling due to mesh distortion. The role of water on lateral resistance could be successfully simulated in CFX modeling. It is shown that the suction develops behind the pipe plays a significant role on calculated lateral resistance. The development of lateral resistance with penetration could be simulated better using ANSYS CFX. The calculated maximum resistance compares well with available FE simulations for idealized conditions and theoretical solutions.

KEY WORDS: Pipeline; Soft clay; Coupled Eulerian Lagrangian technique; ANSYS CFX; Suction.

INTRODUCTION

One of the major components of offshore hydrocarbon transportation is the pipeline which might traverse hundreds of kilometers. In deepwater, pipelines are generally as-laid, and therefore, depending upon topography, some sections of the pipeline might be partially embedded while some section might be suspended above the seabed. The pipeline might cross the landslide or mudslide prone areas. Once a submarine landslide is triggered, the failed soil mass can travel hundreds of kilometers (Kvalstad et al. 2001). The moving soil mass can impact the suspended pipeline either as glide block or out runner block or debris flow. A glide block represents a intact soil block that carries the soil properties of parent soil mass but travels relatively fast because of hydroplaning at the bottom of the soil block. Out-runner block means the soil block which is separated from the parent block and have same soil strength as parent soil block. Debris flow means clay rich suspension which is fully remolded and fluidized. Arnold (1967) reported 271 pipeline failures in 1958–1965 in Mississippi delta. Although the exact cause of failure is very difficult to identify, it was reported that approximately 55% failure occurred due to soil mass movements. Similarly, Demars et al. (1977) analyzed 125 pipeline failure data in 1971–1975 in the Gulf of Mexico; among them 20% failures occurred due to soil mass movements. Therefore, proper estimation of drag force on suspended pipeline from failed soil mass is essential.

The objective of the present study is to present numerical modeling of lateral force on deepwater suspended pipelines subjected to impact loading from submarine landslides. Two different numerical approaches are used to model the behaviour. In the first one, FE analyses are performed using the Coupled Eulerian Lagrangian (CEL) technique available in Abaqus FE software. In the second one, numerical modeling is performed based on the computational fluid dynamics approach using ANSYS CFX.

PREVIOUS STUDY

A number of theoretical, physical and numerical studies have been performed in the past for assessment of risk of pipeline damage associated with submarine landslides. Arnold (1967) and Denmars (1977) performed an extensive field investigation to understand offshore landslide/mudslide phenomena and its interaction with pipelines to identify potential failure criteria. Bea and Aurora (1982) discussed the pipeline design criteria in offshore mudslide prone areas and recommended advanced analysis techniques for a safer pipeline design.

Using the concept of bearing capacity, the drag force in undrained condition per unit length of the pipeline can be calculated as:

$$F = ks_u D \quad (1)$$

where F is the drag force on pipeline, s_u is the undrained shear strength, D is pipe diameter and k is a model parameter. Various approaches have been taken in the past for estimation of the value of k; however, the recommended values vary widely. For example, Brookes and Whitemore (1968) reported k value of 16.7 whereas Bea (1971) mentioned a range of 7 to 12. Scharppy and Dunlap (1978) reported a range of 9 to 21. Randolph and Houslby (1984) mentioned the rage as 9.14 to 11.94. Towhata and Al-Hussaini (1988) mentioned as 11 to 21. Vivarat and Chen (1985) showed that the value of k depends on soil velocity and proposed a generalized equation to calculate the drag force on pile. Georgiadis (1991) conducted an experiment study and showed that pipe drag force depends on the soil block velocity. A generalized equation has been proposed from his experimental data and other data

available in the literature. Zakeri et al. (2012) conducted centrifuge physical modeling and showed increase in k with velocity of the clay block impacted the pipe.

Not only the soil mechanics but also fluid dynamics approaches have been used to estimate the drag force on pipe. In fluid dynamic approach, the drag force can be calculated as

$$F = \frac{1}{2}\rho C_D U_\infty^2 A \quad (2)$$

where ρ=fluid density, C_D=drag coefficient, U_∞=free upstream velocity and A=projected area of the pipeline. Zakeri et al. (2008, 2009, 2012, 2013) performed experimental and numerical investigations to estimate debris flow/glide block induced pipeline drag force. For numerical modeling of soil, the Herschel–Bulkley model has been used.

Randolph and White (2012) reanalyzed the data of Zakeri et al. (2008, 2009) and proposed a unified approach combining both fluid dynamics and geotechnical approaches. In a recent study, Sahdi et al. (2014) verified the unified approach proposed by Randolph and White (2012) using an extensive physical test results. Liu et al. (2015) investigated drag force for debris flow and showed the effects of attack angles.

PROBLEM STATEMENT

In this study, two different pipeline-soil interaction modeling are performed.

Model-I: A section of pipe of diameter D is suspended above a certain distance from the mudline (Fig. 1(a)). A block of clay (H×L) having uniform undrained shear strength (s_u) moves towards the suspended pipe at a constant speed (v). In the finite volume analysis using CFX, the soil block is displaced to the right keeping the pipe at a fixed location without any displacement and rotation. The analysis is continued until the left side of the pipe penetrates 12D in clay. The lateral distance between the left side of the pipe and right face of the clay block is defined as penetration distance (u). In the FE analysis using Abaqus CEL, the clay block is stationary and the pipe is displaced laterally to the left at a speed of v without any rotation. As the relative velocity between the pipe and clay block is same, both modeling simulate the same problem (i.e. impact of a clay block on a suspended pipe). In CEL, the pipe is penetrated laterally in the clay block to u=4.5D.

Model-II: Both CEL and CFX analyses are performed by placing the pipe in a buried condition (Fig. 1b) in order to compare the penetration resistance with the penetration resistance obtained from Model-I (Fig. 1a).

MODEL-I: DRAG FORCE OF SUSPENDED PIPE

Finite Element Model

FE model is developed using the Abaqus 6.10-EF4 software (Fig.2). The large deformation modeling of is performed using the Coupled Eulerian Lagrangian (CEL) technique. The dimensions of the domain are 14D×10D while clay block dimensions are 10D×8D. Void spaces are created above and right side of clay block so that displaced soil mass during the analysis can move to these spaces. As CEL requires three-dimensional modeling, the plain strain condition is simulated using one element in the out of plane direction. The pipe (D=0.29 m) is placed just outside the clay block. The invert of the pipe is at 3D from the top of the clay block. Pipe is then displaced laterally to the left at a constant velocity (v). Based on authors' previous experience (Dutta et al. 2014), EC3D8R 8-noded brick elements of cubical shape having dimensions of 0.05D are used for modeling clay block. The pipe is defined as rigid body to reduce the computational time.

The pipe is moved laterally to the left using a displacement boundary condition assigned to the reference point of the rigid pipe. Zero velocity boundary conditions normal to the vertical and horizontal faces of the domain is applied to keep the materials inside. No boundary condition is applied at the clay-void interfaces such that displaced soil mass can move into the void. Smooth pipeline-soil interface condition is used.

The geotechnical parameters for the clay block are: undrained shear strength (s_u)=8 kPa; submerged soil unit weight (γ')=6.75 kN/m^3; undrained Young's modulus (E_u)=500s_u; Poisson's ratio (ν_u)=0.49.

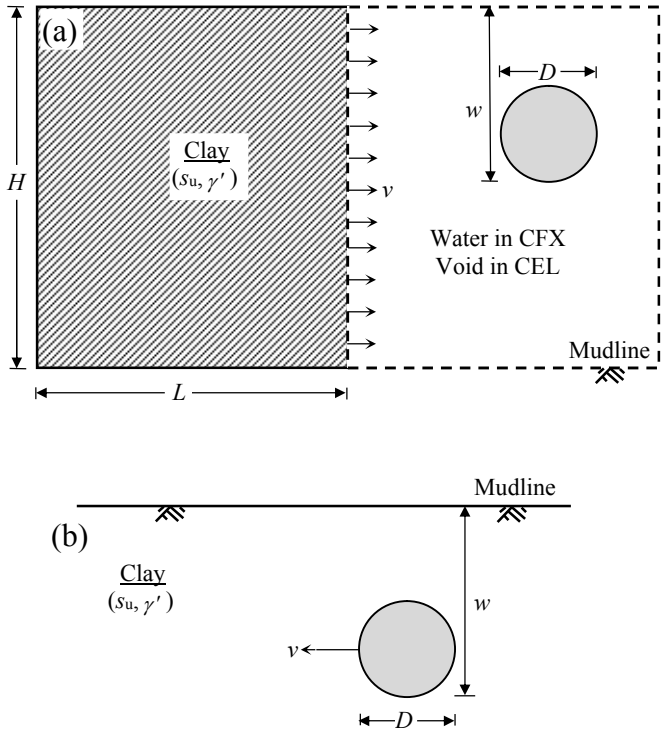

Figure 1. Problem Statement (a) Model-I: Suspended Pipe (b) Model-II: Buried pipe

Finite Volume Model

The CFX model is developed using ANSYS 14.0 CFD software (Fig.3). A domain of 15D×8.5D is considered in this analysis. In Fig. 3, the grey colored zone represents the clay block while the blue color zone represents water. The invert of the pipe is placed at 3D depth from the top surface of the clay block. Finer mesh is created near the pipeline where the shear strains are expected to be high. Similar to CEL analyses, the diameter of the pipe is 0.29 m. In this case the pipe is kept at its fixed location without any displacement or rotation. The pipe surface is defined as no-slip wall. The top and right side boundaries are defined as opening. The left vertical boundary is defined as an inlet where a uniform flow of Eulerian material (clay and water) is assigned. This implies that the size of the clay block increases with time because of inflow of clay and water from the left boundary. Therefore, at one stage clay block impacts the pipe, displaces further and finally the soil from the right face of the clay block leaves the domain through the right opening. In the out of plane directions, symmetry boundary condition is used. At the bottom of the domain, free slip boundary condition is used. Further details of CFX modeling have been discussed in Hawlader et al. (2015) and Zakeri and Hawlader (2013).

Clay is modeled as non-Newtonian fluid defining the dynamic viscosity as $s_u / \dot{\gamma}$ where $\dot{\gamma}$ is the clay shear strain rate. Water is defined as Newtonian fluid and the properties are defined using the default options in CFX. The analysis is performed for an ideal soil condition — no strain softening and rate effects on s_u. A smooth pipe-soil interface condition is defined using finite thickness element around pipeline. A mesh sensitivity analysis is also performed to select thickness of finite thickness interface element. Further details could be found in Hawlader et al. (2015).

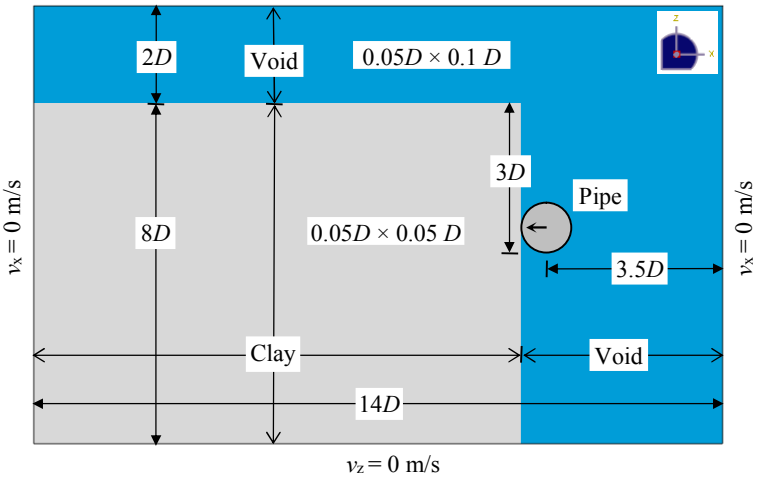

Figure 2. Finite element model for suspended pipe

Results

Figure 4 shows the load-displacement behaviour obtained from CEL and CFX modeling. The load-displacement behavior is presented in normalized form in which the drag force (F) is normalized as F/s_uDL and the lateral penetration u is normalized as u/D. Here, L is the length of the pipe section in the out of plain direction. Because a finite thickness interface element is used in ANSYS CFX, an effective diameter D_e (instead of D) is used for normalizing the drag force obtained from CFX. Assuming that the failure of soil occurs at the middle of the elements just outside the pipe and following the concept of Gui and Bolton (1998), D_e is calculated as D_e=D+2×half of average thickness of elements just outside the pipe = 0.29 + 5/1000 = 0.295 m. For CEL, D_e=D is used because smooth pipe-soil interface condition could be defined.

In the present study, CEL simulates quasi-static penetration of the pipe. In order to maintain quasi-static conditions, the pipe is penetrated slowly at v=0.01 m/s. Note that the effects of strain rate on undrained shear strength is not considered in the present study and therefore it gives the resistance for ideal soils without rate effects. Figure 4 shows that the penetration resistance obtained from CEL increases with u and at about u=3D the penetration curve becomes almost horizontal. Instead of continuing this analysis, another FE analysis is performed for a buried condition (Model-II in Fig. 1) and the penetration resistance for buried condition is compared with the maximum penetration resistance obtained at u≈3.3D, which is discussed further in the following sections.

The CFX analysis is performed for two velocities of the loading block (v=0.1 and 2.0 m/s). As shown in Fig. 4 that the load-displacement behaviour is very different for these two velocities. Starting from u=0.5D, the analysis for v=2.0 m/s gives higher resistance than that of v=0.1m/s. This difference is not because of increase in s_u with penetration speed as the increase in s_u with strain rate is not considered in these analyses. The mechanisms behind this are explained in the following sections.

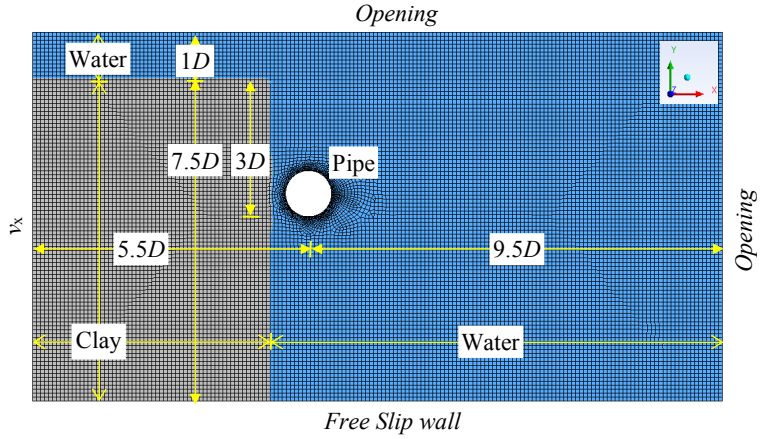

Figure 3. CFX model for suspended pipe

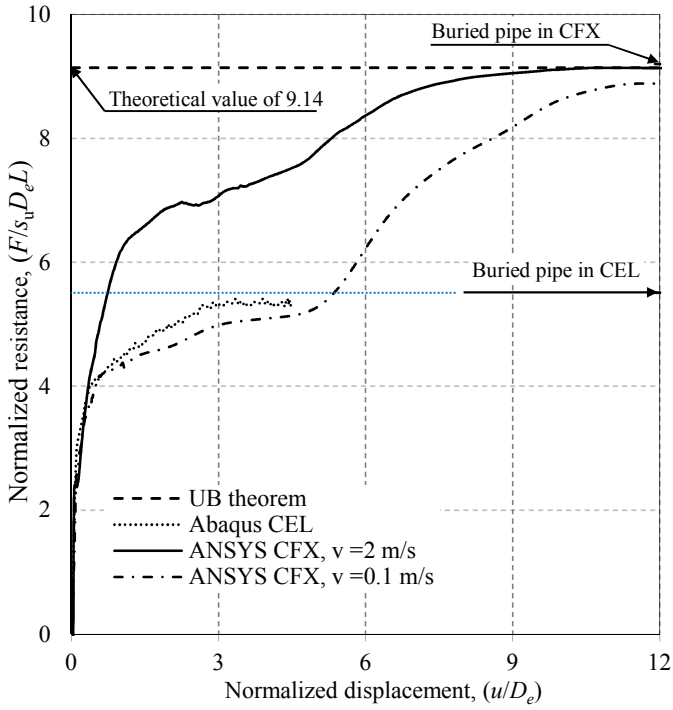

Figure 4. Load displacement plot

Figure 5 shows the deformed shape of the soil at u=3D. Figure 5(a) shows that, in Abaqus CEL simulation, the soil above the pipe is displaces upward and a V-shaped wide open channel is formed in the right side of the pipe, which has been modeled as void. Figure 5(b) shows that a similar channel is formed in CFX analysis when v=0.1/s. Unlike the voids in CEL, this channel is filled with water in this case. Figure 5(c) shows that the deformed shape of the soil for v=2 m/s is

very different from Figs. 5(b) and 5(c). The reason behind this could be explained better using suction (negative pressure) behind the pipe. As shown in Fig. 5(c) that a considerable suction is developed behind the pipe. For clarity, only the contours of considerable suction (≥10 kPa) are shown where the values in the legend represent the magnitude of negative pressure (i.e. suction) obtained from CFX. At the early stage of penetration the suction is very small even at this high velocity. With increase in penetration, the magnitude of suction increases because the suction behind the pipe at high velocity pulls the soil elements in the channel, mainly from the top in this case, and therefore the channel becomes narrow, which restricts the flow of water and increases the suction behind the pipe. This is clearly visible in the instantaneous velocity vectors plots (Figs. 5(d)-5(f)). Figure 5(b) shows that the suction behind the pipe is negligible for v =0.1 m/s).

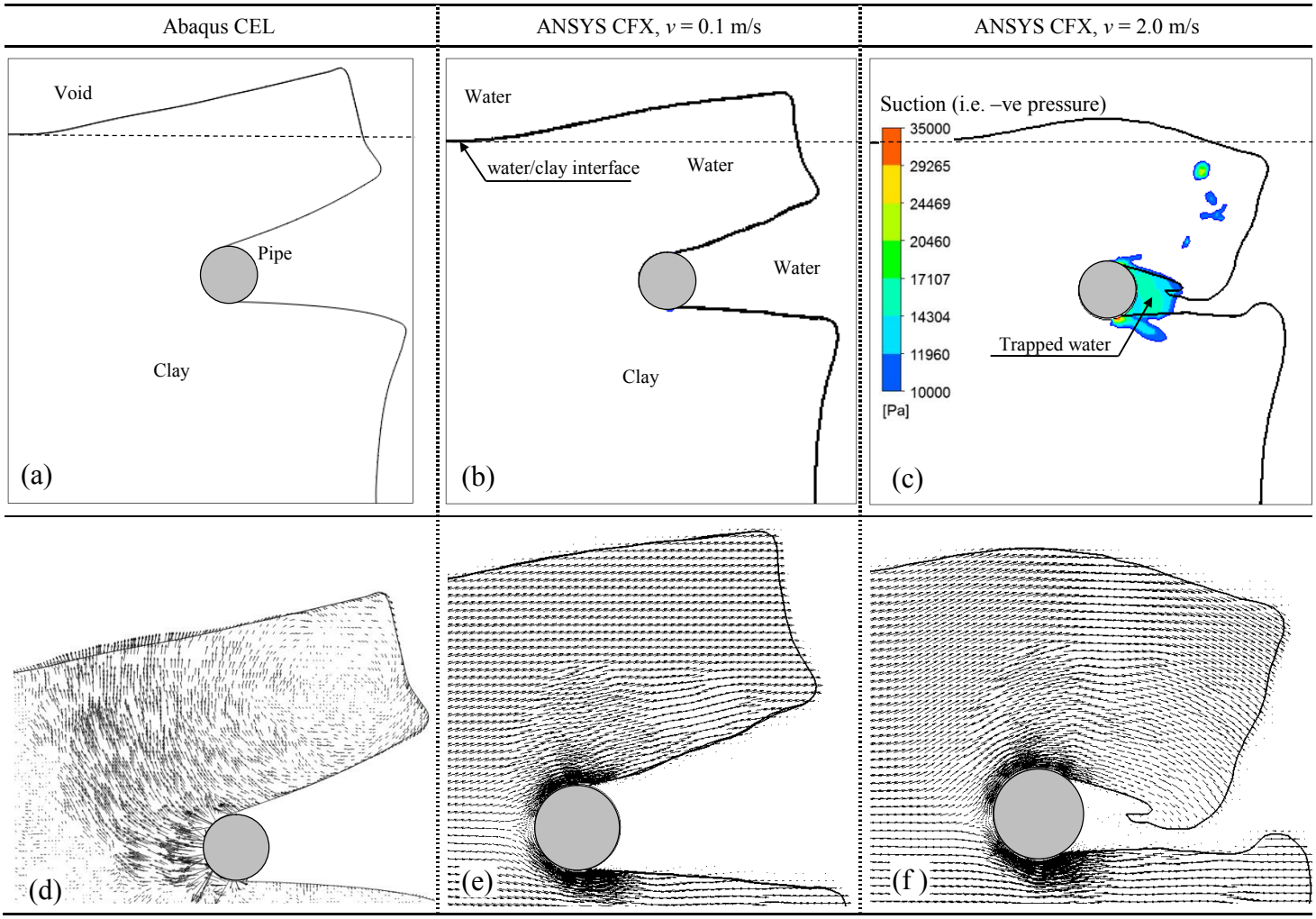

Figure 5. Deformed shape and suction at u=3D

In order to show some more comparison between CFX analysis at v=0.1 m/s and CEL analysis, the instantaneous velocity vectors at u=4.4D are plotted in Fig. 6. The red dashed lines show the interpreted failure planes. Because of shallow burial condition, a curved failure plane is developed and reached the top surface of the clay block. At a first glance, the velocity vectors in CFX (Fig. 6a) and CEL (Fig. 6b) modeling look different. This is because of the fact that in CFX modeling the clay is displaced to the right keeping the pipe fixed while in CEL modeling the pipe is displaced to the left keeping the soil block stationary. Therefore, the velocity vectors in CFX simulation far from the failure plane and deformed zone is constant (Fig. 6a) while in these zones the velocity vectors in CEL modeling is zero (Fig. 6b). The soil elements in the right side of the pipe above the channel, especially far from the pipe, displace downward showing the tendency of collapsing the cantilever portion of the soil mass. The deformed shape of the top surface of the clay block is also similar. From these two analyses, it is therefore concluded that the failure mechanisms and force-displacement curves in CEL and CFX simulations are similar for low penetration speeds up to a certain penetration distance.

The plastic shear strain can be obtained from Abaqus CEL modeling. Figure 7 shows the equivalent plastic shear strain (PEEQVAVG) at u=4.4D. Here, PEEQVAVG represents the integration of plastic deviatoric strain rate tensor over the period of analysis. As shown, significant plastic shear strain accumulates near the pipe and the faces of the channel formed due to displacement of the pipe.

As shown in Fig. 4 that in CFX analysis for v=0.1m/s the penetration resistance again increases after u=5D. In order to explain the reasons, the suction behind the pipe at three penetration distances (u=6D, 9D

and 12*D*) are plotted in Figs. 8 and 9 for *v*=2.0 and 0.1m/s, respectively.

For *v*=2 m/s, a considerable suction develops behind the pipe at *u*=3*D*, as shown in Fig. 5(c). With increase in penetration, the magnitude of suction increases because the flow channel becomes narrow. The cavity behind the pipe becomes almost hydraulically isolated as shown in Fig. 8(a). With further penetration, the suction increases and the size of the cavity just behind the pipe decreases (Figs. 8b and c). Figures 8(b) and 8(c) also show that some small cavities are created which are filled with trapped water.

The development of suction for *v*=0.1 m/s (Fig. 9) and *v*=2.0 m/s (Fig. 8) is slightly different. As shown in Figs. 5(b) and 6(b) that, for *v*=0.1 m/s, the channel is wide open up to *u*=4.4*D*, and suction behind the pipe is negligible. From *u*=5*D*, considerable suction starts to develop. Figure 9(a) shows that the flow channel becomes narrow and suction develops. With increase in penetration, the flow channel becomes narrower and suction increases (Fig. 9b). At large *u* (=12*D*), the initially formed flow channel does not have any continuous connection to the cavity behind the pipe.

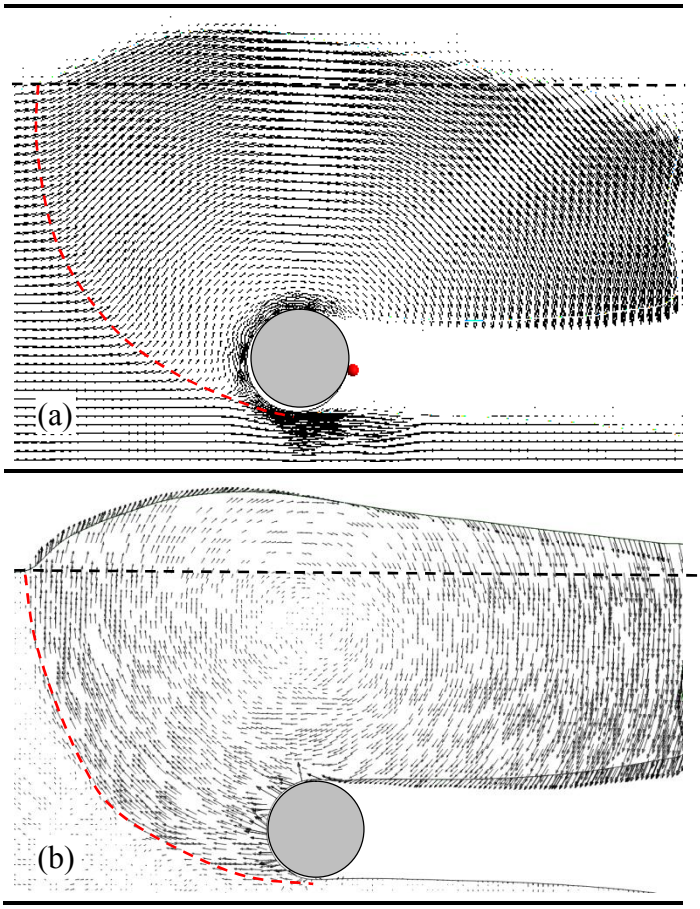

Figure 6. Soil flow mechanism (*v* = 0.1 m/s) around the pipe for pipe lateral displacement of 4.4*D* (a) CFX and (b) CEL

Comparison of suction development can explain the difference between the force-displacement curves shown in Fig. 4. Suction does not develop for *v*=0.1 m/s until *u*=5*D*, while a considerable suction develops for *v*=2.0 m/s from *u*=3*D*. Therefore, the penetration resistance for *v*=2 m/s is significantly higher than that of *v*=0.1 m/s.

As the suction starts to develop from *u*=5*D* for *v*=0.1 m/s, the penetration resistance increases with *u*. At large values of *u* (e.g. *u*=12*D*), the cavity behind the pipe becomes hydraulically isolated (Fig. 8c and 9c), and the behaviour become very similar to full-tension condition.

In modeling of penetration behaviour at intermediate depths, Tho et al. (2012) recognized the importance of drainage of water through the trench. They identified two extreme idealized scenarios: (i) open drainage, where the water in the cavity can easily drain away and (ii) closed drainage, where the water in the cavity is hydraulically isolated. They performed FE analyses using Abaqus CEL only for an open drainage condition to simulate penetration behaviour.

In the present FE analysis using Abaqus CEL, modeling is performed for open drainage condition assuming the channel as void. This implies that the suction is zero and therefore the penetration resistance obtained from Abaqus CEL is less than that of CFX simulation. However, the progressive change from open drainage to close drainage response could be successfully simulated using the present CFX modeling.

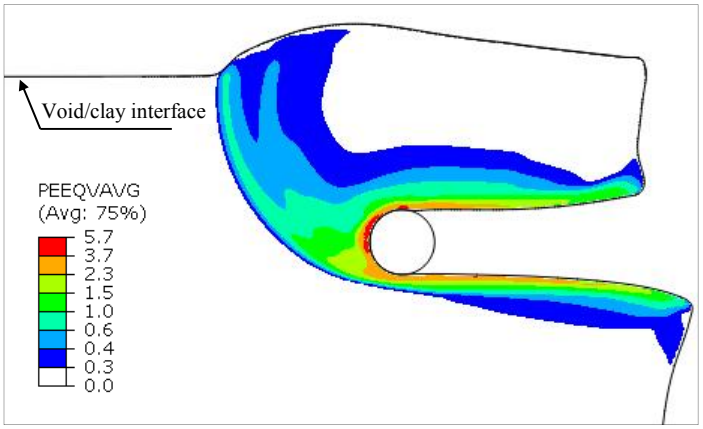

Figure 7. Equivalent plastic shear strain in FE analysis

MODEL-II: LATERAL RESISTANCE OF BURIED PIPE

As shown in Figs. 8(c) and 9(c) that the pipe is engulfed within the clay block at large lateral displacements. The drag force at this condition is compared with the lateral resistance of buried pipeline. The finite element and finite volume models are developed for buried condition in Abaqus CEL and ANSYS CFX, respectively. Similar to previous analyses, the invert of the pipe is placed at 3*D* below the top surface of the clay block.

Figure 10 shows the FE model used in the analysis. For buried condition, relatively small lateral displacement is required to reach the maximum lateral resistance, as compared to suspended pipeline modeling presented in previous section (Fig. 2). Therefore, a smaller soil domain of 10*D*×7*D* is used. A void of 2*D* is created above the soil to accommodate displaced soil. The pipe is placed at 4*D* from the right vertical face and displaced to the left. Other conditions such as mesh size, boundary conditions, pipe-soil interface (smooth), modeling of pipe, material properties are same as CEL analyses presented in the previous sections.

Figure 11 shows the CFX model developed for buried condition. As small displacement is required to reach the maximum resistance, the pipe is displaced laterally instead of clay as discussed in previous sections for suspended pipe. A domain of 10*D*×16*D* is considered

where the clay and water heights are 11.5D and 4.5D, respectively. The pipe is placed at the middle of the domain. A subdomain of dense mesh is created near the pipe. The pipe is displaced to the left. In the subdomain no mesh distortion is allowed; however, clay as Eulerian material can flow through it. Further discussion and advantages of subdomain approach have been presented elsewhere (Hawlader et al. 2015). The left, right and the bottom of the domain are defined as free-slip wall. The top of the domain is defined as an opening. Symmetry plane boundary condition is used in the out of plane direction. The pipe is defined as no-slip wall. The material properties are same as those used in CFX analyses presented in the previous sections for suspended pipe. Smooth pipe-soil interface condition is defined assigning a very low s_u to one row of soil elements just outside the pipe. Radial thickness of these elements is 5 mm.

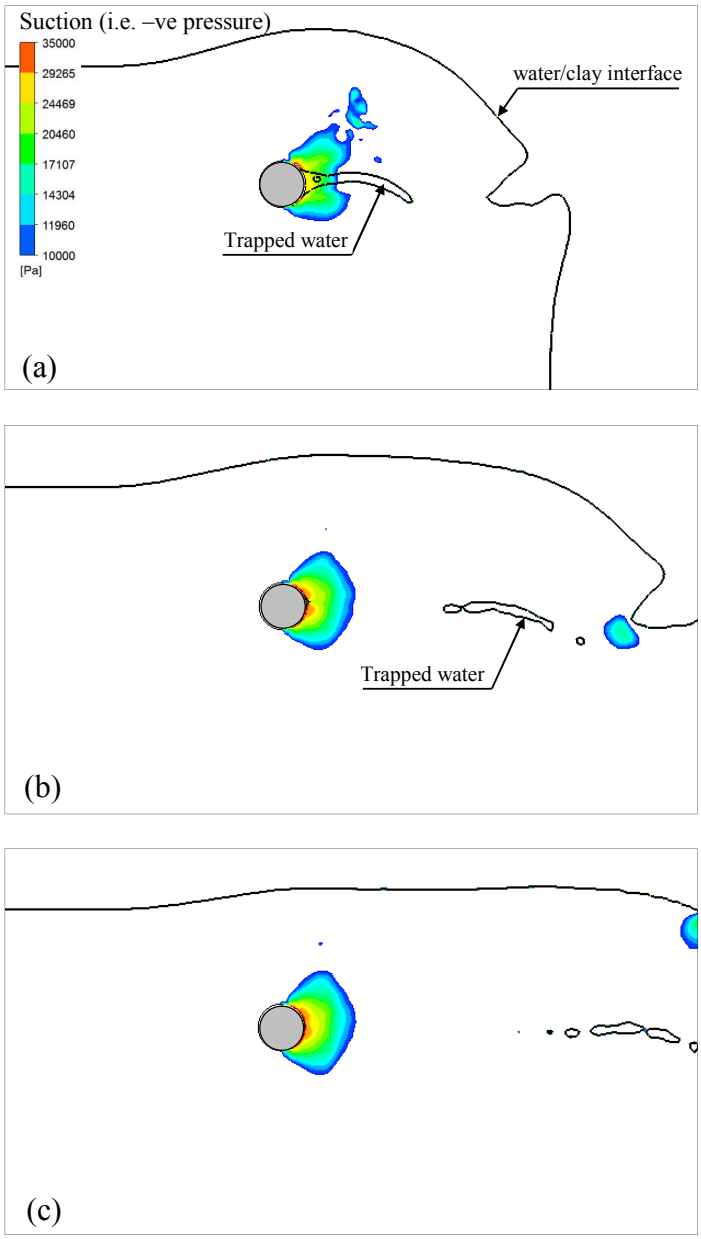

Figure 8. Mobilization of suction in CFX modeling for v = 2m/s (a) u=6D (b) u=9D and (b) u=12D

Result

Although it is not plotted here, the lateral resistance increases gradually with u and reaches the maximum normalized values of 5.51 and 9.20 in CEL and CFX modeling, respectively. These values are shown by two horizontal arrows on the right vertical axis in Fig. 4. The CFX calculated maximum normalized penetration resistance for buried conditions is slightly higher than that of plasticity solution for smooth pipe (=9.14) (Randolph and Houlsby, 1984). On the other hand, the maximum penetration resistance obtained from CEL is significantly lower than that of CFX simulation and plasticity solution, because CEL models the no-tension pipe-soil interface condition. However, the CEL simulated resistance is comparable with the calculated values reported by Martin and White (2012) for smooth and no-tension interface condition.

Figure 12 shows the developed equivalent plastic shear strain around the pipe at lateral displacement of u=0.25D for buried condition. As shown, a cavity is formed behind the pipe and there is no suction as it represents a void. The pattern of soil deformation and plastic shear strains development is very similar to Martin and White (2012).

On the other hand, a considerable suction is developed behind the pipe in CFX model (Fig. 13). Because of this suction, the soil elements behind the pipe are pulled with displacement of the pipe as shown in Fig. 14. Therefore, the maximum normalized horizontal resistance is significantly high in CFX (=9.20) as compared to CEL (=5.51) model for buried condition.

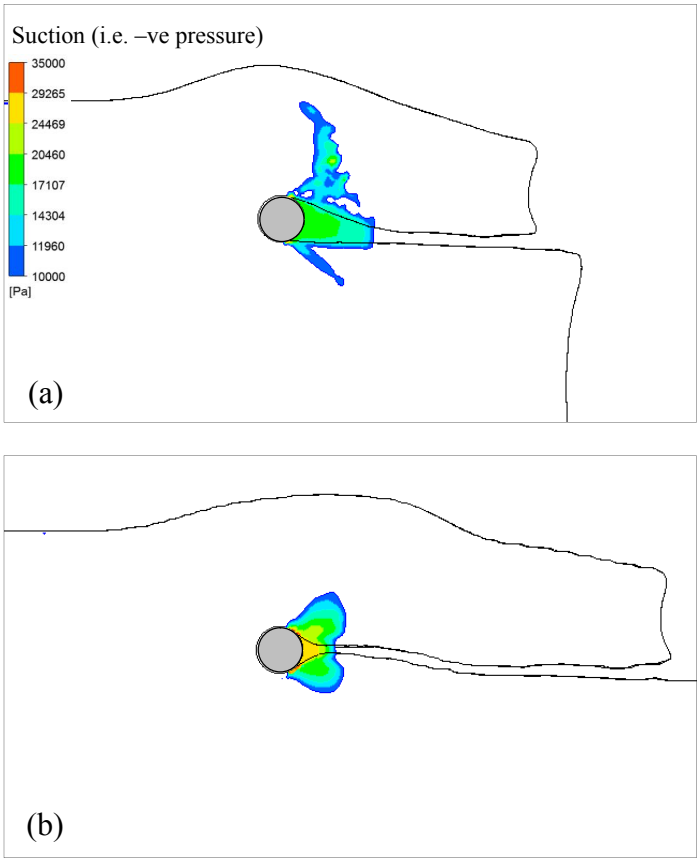

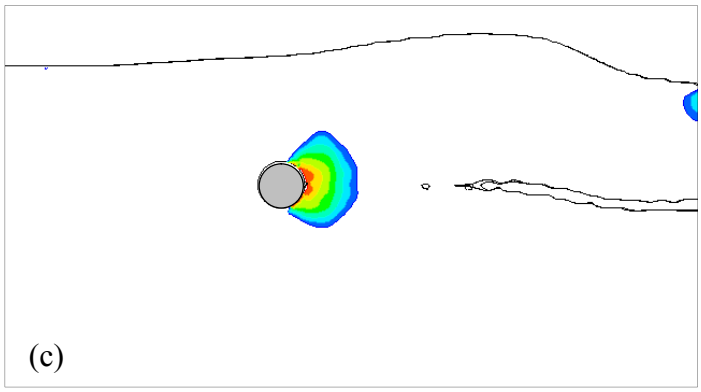

Figure 9. Mobilization of suction in CFX modeling for v = 0.1 m/s (a) u=6D (b) u=9D and (b) u=12D

CONCLUSIONS

Deepwater offshore pipelines are generally as-laid and can travel a large distance. Along its route, some sections of the pipelines could be suspended. The suspended sections of offshore pipelines can interact with failed soil masses of submarine landslides that travel at high speed. Estimation of drag force on pipeline is important for safe and economic design. In this study, numerical modeling using two different approaches are presented. The following conclusions can be drawn from the analyses presented above.

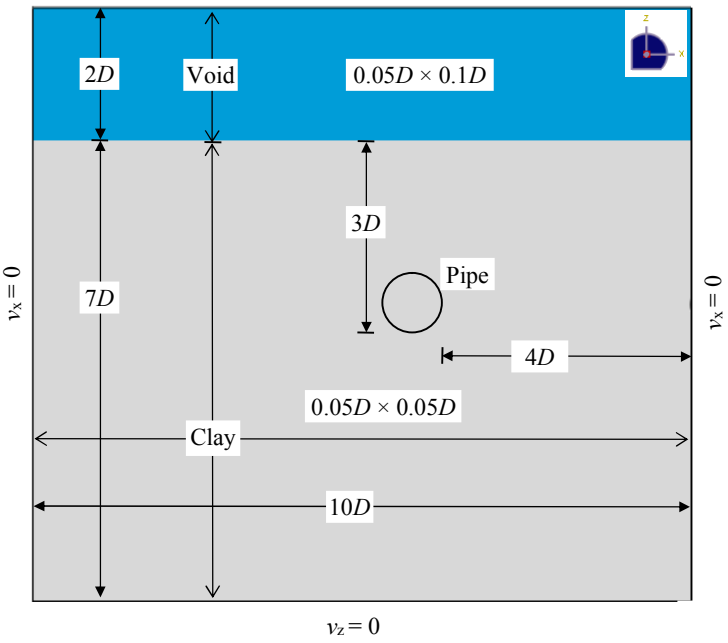

Figure 10. FE model for buried pipe

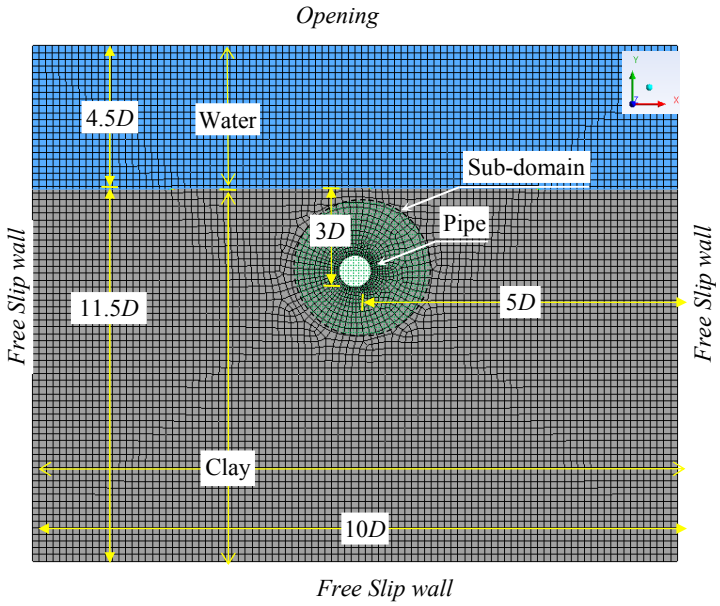

Figure 11. CFX model for buried pipe

- Both ANSYS CFX and Abaqus CEL can simulate the large deformation behaviour, as encountered in pipeline-landslide interaction events, without any numerical issues.
- The maximum resistance obtained from Abaqus CEL is

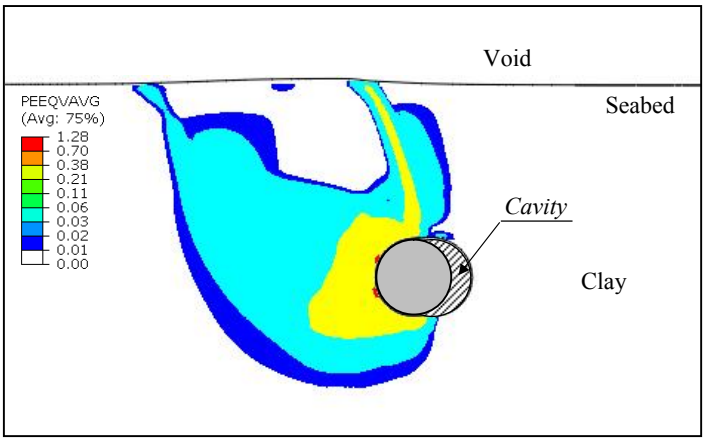

Figure 12. Equivalent plastic shear strain in FE analysis for buried pipe

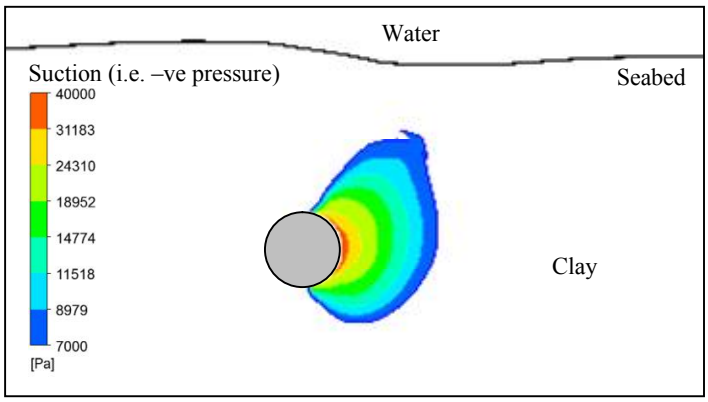

Figure 13. Suction behind the pipe in CFX modeling

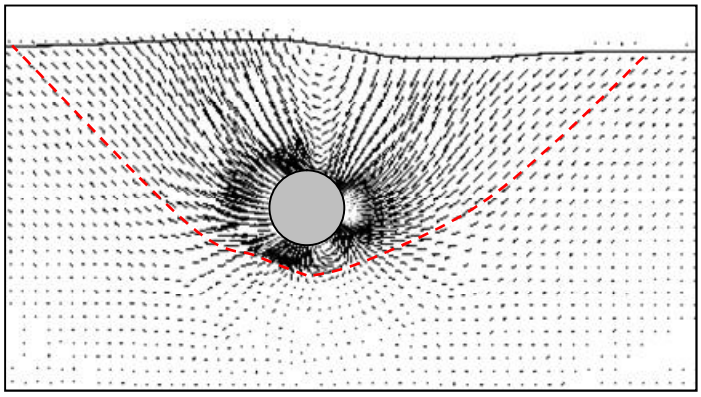

Figure 14. Velocity vectors in CFX modeling for buried condition

comparable with previous studies for smooth and no-tension interface conditions.

- In CFX analyses, suction develops behind the pipe that increases the lateral resistance. The maximum lateral resistance obtained from CFX analysis compares well with previous studies for smooth and full-tension interface condition.
- Suction development and force-displacement behaviour depends on penetration velocity.
- The maximum penetration resistance could be obtained from the simulation of buried pipeline.

One of the limitations of the present study is that the effects of strain rate and strength degradation are not considered.

ACKNOWLEDGEMENTS

Financial supports from MITACS, NSERC, C-CORE are gratefully acknowledged.

REFERENCES

Arnold, KE (1967). "Soil movements and their effects on pipelines in the Mississippi delta region," MSc. Thesis, Tulane University, New orleans, La, USA.

Bea, RG and Aurora, RP (1983). "Design of pipelines in mudslide areas," Journal of Petroleum Technology, 35(12): 1985-1995.

Brookes, G and Whitmore, R (1968). "The static drag on bodies in bingham plastics, Rheologica Acta, 7(2): 188-193.

Demars, K, Nacci, V, and Wang, W (1977). "Pipeline failure: Aneed for improved analyses and site surveys," Proc. of Offshore Technology Conference, Houston, Texas, USA. OTC 2966

Dutta, S, Hawlader, B, and Phillips, R (2014). "Finite element modeling of partially embedded pipelines in clay seabed using coupled Eulerianâ€“Lagrangian method," Canadian Geotechnical Journal, 52(1): 58-72.

Georgiadis, M (1991). "Landslide drag forces on pipelines," Soils and Foundation, 31: 156-161.

Gui, M.W., and Bolton, M.D. (1998). "Geometry and scale effects in CPT and pile design," Geotechnical Site Characterization, Robertson & Mayne (eds), Balkema, Rotterdam, Pg.1063-1068. ISBN 9054109394.

Hawlader, B, Dutta, S, Fouzder, A and Zakeri, A (2015). "Penetration of steel catenary riser in soft clay seabed – Finite Element and Finite Volume methods," International Journal of Geomechanics, ASCE (Accepted).

Kvalstad, T, Nadim, F, and Arbitz, C (2001). "Deepwater geohazards: Geotechnical concerns and solutions," Proc. of Offshore Technology Conference, Houston, Texas, USA . OTC 12958.

Liu, J, Tian, J, and Yi, P (2015). "Impact forces of submarine landslides on offshore pipelines," Ocean Engineering, 95: 116-127.

Martin, C and White, D (2012). "Limit analysis of the undrained bearing capacity of offshore pipelines, " Géotechnique, 62(9): 847-863.

Randolph, MF and White, DJ (2012). "Interaction forces between pipelines and submarine slides - A geotechnical viewpoint," Ocean Engineering, 48: 32-37.

Randolph, MF and Houlsby, G (1984). "The limiting pressure on a circular pile loaded laterally in cohesive soil," Géotechnique, 34(4): 613-623.

Sahdi, F., Gaudin, C., White, D., Boylan, N., and Randolph, M. (2014). "Centrifuge modelling of active slide-pipeline loading in soft clay," Géotechnique, 64(1): 16-27.

Schapery, R and Dunlap, W (1978). "Prediction of storm-induced sea bottom movement and platform forces," Proc. of Offshore Technology Conference, Houston, Texas, USA . OTC 3259.

Tho, KK, Leung, CF, Chow, YK, and Palmer, AC (2011). "Deep cavity flow mechanism of pipe penetration in clay," Canadian Geotechnical Journal, 49(1): 59-69.

Towhata, I and Al-Hussaini, T (1988). "Lateral loads on offshore structures exerted by submarine mudflows," Soils and foundations, 28(3): 26-34.

Vivatrat, V and Chen, V (1985). "Strain-rate and forces due to mud flow around piles," Proc. of Offshore Technology Conference, Houston, Texas, USA . OTC 4919.

Zakeri, A (2009). "Submarine debris flow impact on suspended (free-span) pipelines: Normal and longitudinal drag forces," Ocean Engineering, 36(6): 489-499.

Zakeri, A and Hawlader, B (2013). "Drag forces caused by submarine glide block or out-runner block impact on suspended (free-span) pipelines-Numerical analysis," Ocean Engineering, 67: 89-99.

Zakeri, A, Hawlader, B, and Chi, K (2012). "Drag forces caused by submarine glide block or out-runner block impact on suspended (free-span) pipelines," Ocean Engineering, 47: 50-57.

Zakeri, A, HØeg, K, and Nadim, F (2009). "Submarine debris flow impact on pipelines-Part II: Numerical analysis," Coastal Engineering, 56(1): 1-10.

Zakeri, A, HØeg, K, and Nadim, F (2008). "Submarine debris flow impact on pipelines-Part I: Experimental investigation," Coastal Engineering, 55(12): 1209-1218.